Monitoring Coastal Dune Changes with Geospatial Technology

By

Marcio Daniel DaSilva

Thesis
Submitted to Flinders University
for the degree of

Doctor of Philosophy

College of Science and Engineering
<January 17, 2024>

TABLE OF CONTENTS

DECLARATION

I certify that this thesis:

1. does not incorporate without acknowledgment any material previously submitted for a degree or diploma in any university

2. and the research within will not be submitted for any other future degree or diploma without the permission of Flinders University; and

3. to the best of my knowledge and belief, does not contain any material previously published or written by another person except where due reference is made in the text.

Signed............Marcio Daniel DaSilva...........................

Date..............October 10, 2023................................

COAUTHORSHIP

This PhD thesis is a compilation of a series of articles in peer reviewed journals. The main chapters of this thesis have been written as individual journal articles. At the time of submission, two papers have been accepted and published, while one is in the final stages of peer review.

I am the first author on all included works in this thesis, and have led all of the field work, analysis, and writing that has occurred for this dissertation.

My supervisors and co-authors have provided invaluable support, advice and editing along the way which has greatly increased the quality of all works included here. The manuscripts have been improved greatly through the peer-review process in the four journals of which I have been published in.

ACKNOWLEDGEMENTS

I would like to greatly acknowledge and thank all those who have helped me along the way in the production of this thesis.

I would not be the person that I am today without the support, nurturing and friendship of my parents Fernando and Mary DaSilva. Their example, hard work, and selfless sacrifice have given me countless opportunities that allowed me to chase my dreams across the world. Thank you.

To my dear life Partner, Jill Chmielewski, I cannot thank you enough for loving me and allowing me to be the luckiest human. Your friendship has fostered a belief that the good in our lives is always worth fighting for, and together anything is possible.

To my supervisors, Graziela Miot da Silva, Patrick Hesp, and David Bruce, I can never thank you enough for believing in me all of these years. I came upon yall at a time when I was a directionless student and found in you three a group of supporting and brilliant mentors who have pushed me to do the work that follows in this thesis. My career, my worldview, and beliefs will forever reflect that I was mentored by the three of you.

To the GIS department at Flinders, past, present, and future: thank you for allowing me to grow as part of the team. I hope those that follow will continue to keep up the good work. There is a strong foundation and I consider myself lucky to have inadvertently stumbled into all of the opportunities that abound in this place, state, country, and world.

To the BEADs lab, thanks for all of your field helps in the remote dunefields, I hope you understand I would not have been so successful without the opportunities you helped me. Specific thanks go to Joram Downes, Ben Perry, Sam Davidson, Michael Hillman, and Enya Chitty for helping my fieldwork along the way.

Thank you to my internal assessors for the constructive feedback over the years.

To my cats, Robespierre, Gwyndolyn, George (RIP) and someday Griswold: meow, meow, and meow.

This research would not have been possible without the funding from Flinders University for my PhD scholarship and SEEDs scholarship, thank you. To the Department of Environment and Water (Ali Turner and Sharie Detmar), thank you.

And finally, thank you to all of those out there who look out and think how I can leave this place, and places like this on Earth, in a better state than I found it.

SUMMARY

Coastal dunes develop across the globe on sandy coasts. Their dynamism and range reflect the world's variability in climate, sea or water levels, sediment supply, vegetation types and land uses. Their evolution through time is dependent on many inter-related, and often inseparable natural and anthropogenic variables. Shifts in environmental conditions and disturbances can trigger shifts in their form, stability and alter their evolutionary trajectory. They are managed in many places as they provide an immense protective and ecological value to human and non-human communities, but they exist as natural wild environments across most of the world.

This thesis is focused on disturbances, their evolution and the responses of remote unmanaged coastal dune systems in South Australia. These semi-vegetated and stabilised dunefields are located in temperate climates within National Parks on the Southern Ocean. The disturbances studied as part of this thesis are fire and prolonged shoreline erosion, both of which are expected to be more common, severe, and widespread in the future. These disturbances are associated with potential initiation mechanisms or catalysts for transgressive dune phases.

The thesis is comprised of three main chapters formatted as journal articles and includes additional appendices. The chapters incorporate and develop geospatial and remote sensing methods at different spatial resolutions, including *in-situ* drone surveys, high-resolution aerial imagery and multi-spectral time-series satellite analyses. The contribution of this thesis adds to the contemporary understanding of the way dunefields are studied in the following main areas: (1) fire severity from space focused on the burnt dunefields of Kangaroo Island, (2) the ecogeomorphic response of those burnt coastal dunefields following the fire, and (3) the geomorphic evolution of rapidly eroding, translating and transgressing coastal dunefields on the Younghusband Peninsula in South Australia.

Chapter 2 of this thesis explores how the predominant method of measuring fire severity from space is heavily influenced by soil brightness and canopy density leading to systematic under-assessment of fire severity of coastal dunefields. In this chapter I introduce a new application of a

disturbance index, which improves the fire severity from space as derived from a multi-spectral index of satellite imagery.

Chapter 3 examines the response of burnt coastal dunefields using 3D datasets to describe their post-fire trajectory and applies the satellite index from chapter 2. This work contributes to contemporary knowledge of coastal dunes responses to fire and shows that there is a lack of evidence for fire as an initiation mechanism for coastal dune instability and transgression, within this study and across the coastal dune literature.

Chapter 4 investigates the landscape evolution of a rapidly eroding coastal dunefield and describes its short- to medium-term response to prolonged shoreline erosion. 3D and 2D datasets are used to explore the relationship between sediment loss and its landward translation as aeolian cannibalisation drives dunefield transgression.

Overall, the components of this thesis demonstrate the resiliency and responses of these studied temperate coastal dune systems and how these dynamic landscapes respond to severe and prolonged disturbances. The application of geospatial and remote sensing methods to transgressive coastal dunes offers a dynamic approach to studying, monitoring, and understanding their evolution at the various spatial, spectral, and temporal scales.

LIST OF FIGURES

LIST OF TABLES

PREFACE.

This thesis includes a collection of three manuscripts (chapters 2-4), two published and one in press, followed by 4 appendices as described in a later section. Structurally, all chapters start with a citation and list of co-authors with individual sub-sections, figures, and tables labelled according to their chapter. Each chapter is a unique body of work that focuses on different methods or geomorphic processes and the chapters contain a review of relevant literature in their introduction sections. Chapter 1 begins with the context of the research that comprises this thesis and is followed by a section that overviews the general background of coastal dune literature to establish definitions and cover the implicit conditions that frame the relevance of their study. This is followed by the research aims of the thesis and a list of the scientific contributions from this candidature.

CHAPTER 1.

Introduction

1.1 Context

This thesis applies geospatial methods to study the effects and responses from disturbances onto two natural and remote coastal dunefields in the State of South Australia. It explores their evolution through time across different spatial scales. The focus is on two dunefields which have experienced either recent or relatively prolonged disturbances that have altered their state. I examine the effects of the 'Black Summer' bushfires of 2019/2020 on Kangaroo Island (136° 30 'E, 36°00 'S, Figure 1), and the evolution of rapidly eroding and translating coastal dunes on the Younghusband Peninsula in the Coorong region (139° 42'E, 36°18'S; Figure 1). These semi-vegetated and partially to largely stabilised transgressive coastal dunefields are in temperate climates within National Parks, exposed to the highly energetic Southern Ocean wave regime. Their landward extent reflects previous climatic conditions, sediment supply, and/or relative sea levels. The research is focused on the response of these dunefields to disturbances which, in previous research and literature, are associated with the initiation and driving of dunefield transgression/instability and may be linked with a changing climate. While this thesis studies processes potentially associated with climate change, or processes that may occur with a changing climate, it does not explicitly examine changes in local or regional climates, only the disturbance and response of the landforms and landscapes. For the course of this thesis, transgressive coastal dunefields are the object of study with the subject focus on their subsequent response, stability, and evolution as measured by remote sensing. The remainder of this section will provide a brief general overview of coastal dunes to place this study in a broader context, followed by a concise review of the methods used in the main chapters of this thesis.

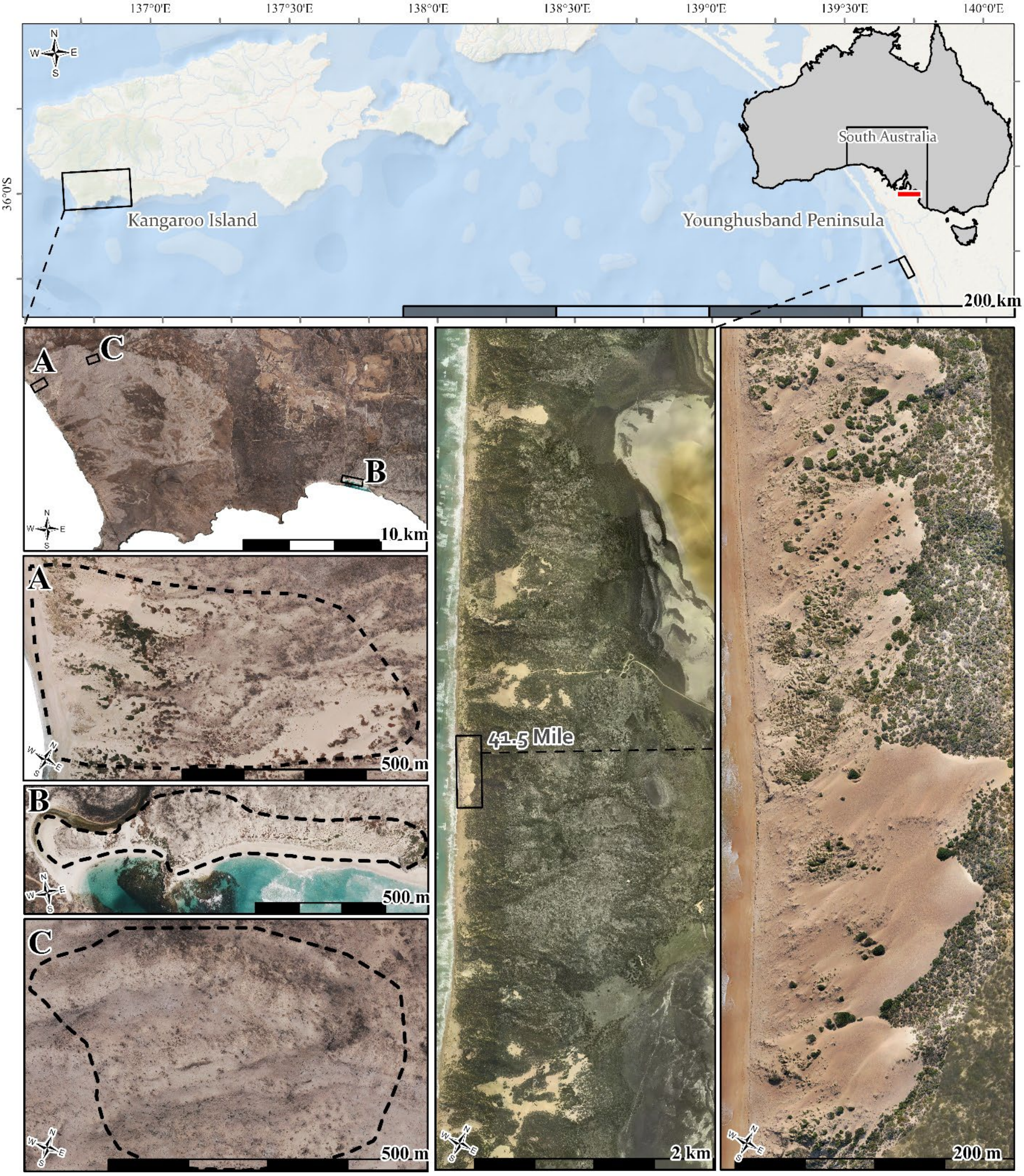

Figure 1-1 – The two dunefields in South Australia that are the focus of this thesis. The chapters are focused on changes in burnt dunefields on Kangaroo Island (Chapters 2 and 3), and on the Younghusband Peninsula coastal barrier (Chapter 4). The callout maps of (A, B, and C) on Kangaroo Island show the outlines of regions studied with drone-based surveys and satellite imagery analysis. On the Younghusband Peninsula, the extent indicator shows the focus area of Chapter 4 in a drone ortho-image from April 2022, documenting the rapidly transgressing dune system at the 41.5 Mile study site.

Coastal dunes are aeolian landforms which are characteristic of sandy shores where there is a sufficient supply of sediment and wind energy (Carter, 1988). They develop across almost all latitudes and continents and reflect their regional and local environmental conditions in form and flora (Martínez et al., 2008). Dunes and dunefields are dynamic landforms with vegetation highly adapted to their local conditions (Maun, 2009). The size, form, and complexity of coastal dunes is controlled by biotic and abiotic factors such as climate, surfzone-beach type, sediment supply, grain size, shoreline orientation relative to wind and waves, regional and local sea or lake levels, vegetation cover, and aeolian forces (Hesp and Walker, 2013, Hesp and Walker, 2022). Coastal dunes can range in size from small discrete nebkha fields and small foredunes to extensive transgressive dunefields which can reach tens of metres high and extend for kilometres along and inshore (Davidson-Arnott et al., 2019). They are generally classified into four main types; foredunes, blowouts, parabolics and transgressive dune sheets/fields (Hesp and Walker, 2022). Generally, foredunes form as sediment transported by wind is trapped by vegetation colonising the backshore, leading to the development of an incipient foredune (Hesp, 2011b). Hesp (2002) describes the process over which foredunes progress from an incipient foredune to an array of types that range from (1) stable, morphologically simple, and vegetated to (5) highly destabilised/erosional remnant knobs. Blowouts are depressions or hollows that form from wind erosion and are classified by their shape, most commonly as either a saucer, cup, or trough with the downwind depositional lobe included as part of the landform (Carter et al., 1990). They are commonly associated with beaches that are experiencing erosion or recession but also occur in stable and prograding environments (Hesp, 2002).

When blowouts advance via aeolian erosion, expansion, and cannibalisation of downwind landforms they can form parabolic dunes. Parabolic dunes are identified by the presence of trailing ridges that develop as the blowout extends and forms the identifiable U- or V- shaped depositional lobes (Hesp and Martínez, 2007). After a parabolic dune has developed from a foredune ridge or blowout, it can continue to migrate downwind regardless of upwind conditions, moving further inland until a new incipient foredune may form and close the entrance to the parabolic dune (Girardi and Davis, 2010, Hesp, 2011b). Alternatively, parabolic and blowout dunes may coalesce and form a new transgressive dune sheet/field (Yan and Baas, 2015, Pickart and Hesp, 2019, Hesp and Thom, 1990). Transgressive sand sheets (no dunes present) and dunefields are aeolian sand deposits formed by on-, oblique-, or alongshore movement of sand, and can range from relatively small features, extending over several hundred square metres, to extremely large that are similar to desert dunefields (Hesp, 1999). When active they may be devoid of vegetation and dominated by various mobile dune types, or partially vegetated, with dunes formed from deposition in or behind plants (e.g. nebkha; gegenwalle ridges, coppice dunes, shadow dunes), or erosional relics (e.g. remnant knobs, deflation ridges) (Hesp and Thom, 1990). They often contain areas previously eroded by aeolian forces (e.g. deflation plains) and can have various dominant dune types such as parabolic dunes, sand sheets, barchans, domes, barchanoids, transverse dunes, shadow dunes, coppice dunes, and/or star dunes depending on the sediment supply, climate, and wind regime (Hesp and Walker, 2013). Transgressive dunefields and sheets can become completely vegetated relict dunefields (Hesp, 2011a).

This thesis is focused on measuring and understanding changes in transgressive dunefields, a term first used by Gardner (1955) to describe sand deposits that were actively migrating and transgressing prior terrain. The term ‘transgressive dunefield’ refers to both active and stabilised dune systems (Hesp and Thom, 1990). They have been studied since at least the late 19th century (Hesp, 2002, Zenkovich et al., 1967), with more focused studies on the semi-active transgressive dunefields on the west coast of North America (Cooper, 1958, Cooper, 1967), Europe, Russia, and Australia (Ranwell, 1958, Landsberg, 1956, Jennings, 1957, Zenkovich et al., 1967). Early observations from coastal dunefields in North America (Campbell, 1915) noted that disturbances (or breaches to use their contemporary term) could cause a shift or translation of the entire dune system (Pye, 1983). Many studies have focused on the most distinctive coastal dune types forming at the foremost boundary:

foredunes and their extensive foredune plains (Hesp, 1988, Goldsmith, 1973, Bigarella, 1972, Bigarella et al., 1969, Mehrtens et al., 2023, Dillenburg et al., 2020), especially as they have a relatively stable geological (foredune ridges) record. Few studies exist on the evolution of coastal barriers dominated by transgressive dunefields due to their highly complex and dynamic nature (Pickart and Hesp, 2019, Miot da Silva and Shulmeister, 2016, Martinho et al., 2008, Martinho et al., 2010). But research into the form, structure, and changes in transgressive coastal dunefields continues due to their great extents and prominent place in the landscape. Transgressive coastal dunefields have acquired various descriptors and names from cultures across the world (Davies, 1980), but their on-going study is motivated in understanding dune activity as it relates to shifting environmental conditions, discrete events, and/or a combination of those complex interactions (Hesp and Thom, 1990). Similar to coastal studies on the world's oceans, significant research has been done in transgressive dunefields that have built up along large in-land lakes, most extensively studied in the Laurentian (Great Lakes) region of North America (Hansen et al., 2020). These extensive aeolian deposits containing multiple paleosols and relict transgressive dunefields are complex and vary across the geography of the region, with stratigraphic studies showing numerous cycles of dune building and transgression following changes in local water levels and fluctuations in climate (Arbogast et al., 2023). The observations from Holocene aeolian deposits help inform the understanding of how coastal dunefields respond to changes in water levels, as the discrete dates across millennia show that transgression and translation is a geomorphic evolutionary response (Loope and Arbogast, 2017, Anderton and Loope, 1995).

More recent studies in in coastal dunefields have involved looking at their current state, recent morphological changes, and investigating their past to explain variations in stability, form, and extent through time. Researchers study the geological past by using radiometric dating (Forman, 2015, Peterson et al., 2007, Hansen et al., 2010), and ground penetrating radar (Ye et al., 2023, Robin et al., 2021, Brooke et al., 2019, Girardi and Davis,

2010) to explore the stratigraphic form and evolution of the dunefields under previous climatic or environmental conditions. Other studies use historical aerial photography to track the vegetative cover or landform change within dunefields (Pickart and Hesp, 2019, Martinho et al., 2010, Moulton et al., 2020, Moulton et al., 2018). 3D datasets are used to explore the volumetric and morphological changes through time, ranging from short- to long-term changes (Grohmann et al., 2020). Many studies combine methods, using imagery, radiometric dating, stratigraphy, and/or LiDAR to describe their geological and/or recent evolution (Kennedy et al., 2020, Robin et al., 2023, Laporte-Fauret et al., 2022, Garcia-Romero et al., 2019a, Rodríguez-Santalla et al., 2021). The study of transgressive dunefields is important as they are highly dynamic landforms and vary considerably in size, structure, and stability across the globe in regions with an abundant supply of sand and strong winds (Hesp and Thom, 1990, Short, 1988, Hesp, 2011a). They can be diverse in structure, and, as noted above, range from highly stabilised by vegetation to fully active with mobile dunes, with most dunefields containing both stable and active areas depending on the climate and sediment supply (Hesp et al., 2021). Variations in climatic conditions alter dune stability by changing the sediment supply, vegetation cover, wind regimes, wave conditions and relative sea levels (Costas et al., 2012, Psuty and Silveira, 2010, Nicholls et al., 2007). Recent reviews have argued that there is a global trend of coastal dune stabilisation and increasing dunefield vegetation cover (Jackson et al., 2019a, Gao et al., 2020, Petrova et al., 2023, Gao et al., 2022) with many local and regional studies confirming the trend of re-vegetating and greening in coastal dunefields (Provoost et al., 2011, Delgado-Fernandez et al., 2019, McKeehan and Arbogast, 2021, Moulton et al., 2018). Given this trend, there is considerable intertest in how dunefields may evolve in the future, especially given predictions of future climate change. Transgressive dunefields generally form and/or re-activate in phases or episodes where changes in their environment such as sea-level, climate changes (especially rainfall and wind speed), sediment supply, coastal erosion, or fire regimes intensify or combine and result in a new phase characterised by landscape instability or transgression (Aagaard et al., 2007, Costas et al., 2012, Costas et al., 2016, Delgado-Fernandez and Davidson-Arnott, 2011, Feagin et al., 2005, Miller et al., 2009b, Psuty and Silveira, 2010, Gao et al., 2020, Hesp, 2011a). The reactivation triggers or mechanisms of transgressive dunefield phases are various, although many remain unproven and difficult to separate between drivers (Hesp 2013).

Two potential drivers or initiation mechanisms of transgressive dunefields are fire and shoreline erosion (Filion, 1984, Jackson et al., 2019b). The study of these potential dunefield re-activation mechanisms have been seen in the past as important drivers of coastal beach and dunefield change (Warrick et al., 2022). Their study is especially useful as a proxy for observing landform processes expected in a future with altered climatic conditions. The complexity and dynamism that characterise these boundary landscapes make them an ideal study subject for remote sensing and geospatial methods.

Fire is considered to be a potential re-activation mechanism for coastal dunefields, but, the evidence for this is largely sourced from stratigraphic interpretations in Holocene dunefields located in either North America or Europe (Boyd, 2010, Filion, 1984, Filion, 2017, Kotilainen, 2004, Seppälä, 1995, Tolksdorf et al., 2013). Stratigraphic studies have shown a relationship between fires and increased aeolian activity in buried soil horizons, suggesting that dune instability follows fires in times of a changing climate (Filion, 1984, Filion et al., 1991). Filion (1984) documents the chronology of dunefields in Quebec (56°N, North America) and that aeolian instability and fire is associated with the oscillations between conditions of cold and dry versus warm and humid that occurred in the mid-Holocene, similar to observations from Arbogast and Packman (2004). In stark contrast, contemporary studies of post-fire coastal dune responses have not observed significant morphological changes or shifts in their stability, suggesting their recovery is likely, absent atypical climatic conditions (Vermeire et al., 2005, Ward, 2006, Myerscough and Clarke, 2007, Shumack and Hesse, 2018, Shumack et al., 2017, Levin et al., 2012). Post-fire studies of aeolian driven activity in non-coastal landscapes have shown a short time of increased aeolian activity after a fire, but a decline in wind driven erosion during the recovery stage as vegetation returns (Barchyn and Hugenholtz, 2013, Ravi et al., 2012, Sankey et al., 2009b, Stout, 2012a). An important factor in their recovery and resistance to significant destabilisation is the enduring biomass left behind by dense root systems that hold soils in place as stabilising vegetation returns (Barchyn and Hugenholtz, 2013). Some authors (Barchyn and Hugenholtz, 2013, Shumack et al., 2017) argue against fire as being the sole cause of major shifts in dune systems, rather that fire plays a minor role in the reactivation of sediments and that there needs to be a combination of abnormal conditions for destabilisation to occur (drought or climate change). These contemporary studies observing insignificant changes following fires are at odds with some studies suggesting phase shifts from stable to destabilised dune systems from the stratigraphic records (e.g. Filion, 1984). However, it is possible that atypical climatic and weather conditions have not occurred during studies of post-fire change on dunefields. Less understood is the shortening of times between fire events in landscapes, as the established vegetation communities are repeatedly burned and prevented from returning to their mature state (Bennett et al., 2016). A recent analysis of fire severity and frequency on Kangaroo Island (the focus of chapters 2 and 3) has shown that the recent fire had the largest extent in recorded history and that the interval between major fires has shortened as observed since the 1930s (Bonney et al., 2020).

It is unclear as to the effect that an altered fire regime might have on the evolution of a dunefield, as shifts in fire regimes (frequency and severity) may lead to disruptions in vegetation diversity (Wright and Clarke, 2007), or landscape stability (Barchyn and Hugenholtz, 2013). The Black Summer bushfires of 2019/20 on Kangaroo Island (Figure 1) were potentially a preview of future fire conditions that will occur in temperate climates and regions like South Australia (CSIRO, 2020). It was the largest single fire event on the island in recorded history and burned for weeks during the dry, windy, and hot summer months. The fire burnt both relict stabilised and semi-active coastal dunefields across the region, removing the above ground vegetation. It was not known at the time to what degree the dunefields would respond and whether the fire would act as a catalyst for the reactivation of the extensive aeolian deposits. These mostly Holocene aged (<10,000 years) deposits range for up to 16 km in-land and were formed as large parabolic and transgressive dunefields (Short and Fotheringham, 1986). The research undertaken on Kangaroo Island draws on the established understanding and extensive literature of fire severity interpreted from multi-spectral satellite imagery (Chuvieco et al., 2019) and adapts it for the unique features of coastal dunefields (Chapter 2). Namely, these are their bright soils and discontinuous canopies which are major limitations of widely used indices for measuring fires and change (Norton et al., 2009, Parks et al., 2014, Fassnacht et al., 2021). In the years following the fire, multiple academic (Bonney et al., 2020, Hosseini and Lim, 2023) and government reports (Department of Agriculture, 2020) have released assessments that included broad severity estimates across Kangaroo Island. These applications of predominant fire severity indices are challenged with the findings of this thesis, and I illustrate why this occurred and suggest an improved method in chapter 2. Through the course of my candidature, I conducted field work at three sites within these burnt dunefields to study the landform and landscape response of these dunefields. The results of this field work are used in conjunction with a time-series analysis from multi-spectral satellite observations in chapter 3 to investigate the response trajectory of these active to fully stabilised temperate dunefields.

Chapter 4 examines the evolution of a foredune and formerly relict transgressive dunefield and their dynamics after transgression has commenced. In contrast to the studies in chapters 2 and 3, the wave driven shoreline erosion has reactivated the dunefield and the focus is on the sediment transfer across the profile as the dunefield is transgressing and translating landwards. This case study is particularly timely as global analysis has suggested that many coastal systems are presently experiencing shoreline loss from erosion (Mentaschi et al., 2018, Luijendijk et al., 2018). The cumulative effects on coastal systems from climate change are expected to further exacerbate shoreline loss trends and their effects to the adjacent communities (Hinkel et al., 2013, Ranasinghe, 2016, Ranasinghe et al., 2011, Vousdoukas et al., 2020). Coastal erosion can cause scarping and the degradation or destruction of dunes, especially in cases of prolonged retrogradation (Davidson et al., 2020). Scarping occurs when coastal dunes are exposed and eroded by significant or persistent wave energy, generally during periods of high-water levels (Davidson-Arnott et al., 2019). The magnitude of scarping is mainly a product of the duration and intensity of wave energy during episodes of high water-levels but is also affected by the presence of vegetation or debris that mitigate exposure (Davidson et al., 2020). Active dunefield transgression can be a response to shoreline erosion and retrogradation as mobilised sediments translate landwards (Hesp, 2013, Hesp et al., 2022b). There is significant interest in how coastal systems will respond to continued shoreline erosion and in a future with increased sea levels as the contrasting recent reviews by Cooper et al. (2020) and Vousdoukas et al. (2020) show. The on-going conversation on the resiliency of shorelines and coastal systems is based on their ability to translate as a response to coastal erosion (Davidson-Arnott and Bauer, 2021, Short, 2022), and central to this is whether sediments from the beach and dune system are lost during prolonged retrogradation.

On the Younghusband Peninsula (Figure 1), a contemporary example of shoreline retreat and the on-going evolution of a transgressive dunefield is documented, illustrating the sediment dynamics under fairly extreme erosional conditions. On-going recession has occurred in this region for years (Hesp et al., 2022b), with a 60m wide foredune and a significant section of the relict dunefield eroded by waves and substantial sediments lost seawards. The start of the transgressive dune phase occurred in the early 2010's (Hesp et al., 2022b), where prolonged wave driven erosion combined with aeolian forces destabilised the dune system. Dunefield transgression followed this destabilisation as aeolian forces began transporting sediment landwards. While this process has been described in the literature (Hesp, 2011a) and observed in a few cases (Robin et al., 2023, Hesp et al., 2022b, Pérez-Alberti et al., 2021), the ability to measure the 3D or volumetric transfer of sediments has largely been hindered by limitations of scale, timing, and resolution. In this thesis, I draw on regional 3D datasets that were collected prior to the start of this candidature to further explore the volumetric and morphological changes and use them as a baseline comparison for the surveys that I conducted. My field data collection began in 2020 and to my knowledge it is the first study to observe and document the rapid transgression of a dunefield at such a high level of spatial and temporal detail and significantly helps illustrate the sediment dynamics of a translating coastal system.

Walker et al. (2017), differentiate geomorphic studies of complex models between observations on a scale of the smallest to the largest: plot, landform, and landscape respectively. Applied research to coastal dunes generally range from *in-situ* local studies focusing on plot and landform changes to broader landscape changes looking at regional or global trends. This body of work examines the contemporary state and historical form of two disturbed dunefields with observations of landform and landscape changes sourced from local (*in-situ*) and remote observations. The general benefits and limitations of these methods are reviewed in the following with more in-depth reviews in their respective chapters.

Conventional terrestrial and field methods are limited in scale, usually focusing on a single landform with individual or successive surveys. The recent rise of low-cost drone technology and computing accessibility has given rise to an increase in applications of LiDAR or photogrammetry for monitoring changes in coastal environments (Casella et al., 2020, Drummond et al., 2015). The adoption of drone based methods has led to studies across the globe that range from single storm events (Gonçalves and Henriques, 2015), to long-term and geographically dispersed monitoring projects involving networks of citizen scientists (Pucino et al., 2021). Repeat photogrammetry surveys from drones have been used across many physical science applications (Anderson et al., 2019, Colomina and

Molina, 2014), and have facilitated an exceptional number of coastal dune studies looking at morphological and/or ground cover changes (Walker et al., 2023, Hilgendorf et al., 2021, Hilgendorf et al., 2022, Laporte-Fauret et al., 2020, Laporte-Fauret et al., 2022, Laporte-Fauret et al., 2019, Smith et al., 2022, Shumack et al., 2022, Konlechner and Hilton, 2022). They have been used to survey post-fires landscapes, deploying after a fire to observe the extent of burnt areas and monitor post-fire processes (Fernández-Guisuraga et al., 2018, Ellett et al., 2019, McKenna et al., 2017). Drone derived datasets include ortho-mosaic true-colour images, digital elevation models, and point clouds which in a time-series can be used to measure environmental changes.

To relate the local changes from field observation to larger scale landscape changes, aerial and satellite remote sensing methods provide an alternative and supplemental source of information. The continuous collection and improving resolutions of space-based observation technology is fostering a continually growing body of data and research that is monitoring changes across the Earth (Radočaj et al., 2020) and widely applied to terrestrial dunes (Hugenholtz et al., 2012). Researchers have used space-based sensors systems to study the environment with improvements in accuracy, frequency, and reliability following the progressive advancements in computing and resolutions (Burningham and Fernandez-Nunez, 2020, Nanson et al., 2022, Chuvieco et al., 2020, Chuvieco et al., 2019). For this thesis, the interests are fire severity and subsequent recovery as derived from multi-spectral satellite imagery, and the position of a proxy of shoreline (either the vegetation line or the waterline). The extensive global catalogue from multi-spectral Landsat (and others) imagery has facilitated time-series analyses at the continental scale of environmental changes (Jackson et al., 2019a, Nanson et al., 2022, Petrova et al., 2023) and widespread application for rapid assessments of environmental changes, both as a result of fire (Chuvieco et al., 2020) and shoreline changes like coastal erosion (Burningham and Fernandez-Nunez, 2020). To derive useful information from this catalogue, focused studies and observations are necessary to parse the signal to noise ratio that exists within mixed pixels of medium resolution satellite imagery (10-30 m pixels). Within coastal dune systems in particular, studies looking at the effects of fires from multi-spectral remote sensing is limited (Hosseini and Lim, 2023, Blake et al., 2020, Shumack and Hesse, 2018, Shumack et al., 2017) and significant limitations of predominant indices and methods are acknowledged (Miller et al., 2009a, Klinger et al., 2019). With the continued development of analytical methods and new improving sensor resolutions, remote sensing and geospatial sciences will facilitate greater understanding of environmental change in physical systems such as coastal dunefields.

1.2 Research Aims

This PhD broadly studies the response and evolution of two transgressive dunefields to disturbances associated with a catastrophic fire and shoreline erosion by applying various remote sensing applications and geospatial methods. Three separate processes are investigated, with a focus on the changes derived from the method's spectral, spatial, and temporal resolutions. The data collected and subsequent information developed here contributes to the understanding of coastal dune system's response and evolution to severe and/or on-going disturbances. Additionally, the application and development of the geospatial methods increases our capabilities in observing and measuring changes in these wild environments. The body of work specifically investigates:

i. Fire severity in the burnt coastal dunefields of Kangaroo Island in South Australia as derived from the difference in multi-spectral imagery, observing the change in spectra as an indicator of fire severity. I compare the predominant methods of fire severity from multi-spectral satellite imagery and a new application of a disturbance index with high-resolution multi-spectral aerial imagery. This chapter develops and presents that new method of assessing fire severity with the adapted index that is less affected by soil brightness and discontinuous canopy coverage, making it more suitable for large-extent fire severity assessments in heterogenous environments.

ii. The post-fire spectral and spatial response of coastal dune systems. This study examines ecogeomorphic response in the years preceding and following the fire to explore the potential for reactivation and/or dunefield transgression. Multi-spectral satellite indices and the index developed in chapter 2 are used in a time-series and related to the 3D datasets from repeat photogrammetry surveys.

iii. The evolution of a rapidly eroding, translating, and transgressing coastal dune system as a consequence of local environmental conditions and shoreline erosion. The work explores the response of the dunefield by examining the role of antecedent topography and sediment supply in the morphological evolution of the dunefield. The 3D data sets show how the differential volumetric changes from 2008 to 2022 and compared to alongshore variation in shoreline retreat. Two modified conceptual models are advanced on transgressive dunefield retreat and evolution, one being a stoss-slope model and the other a transgressive dunefield translation model.

1.3 Structure and Scientific Contributions

Chapters 2-4 were written as manuscripts for publication. At the time of submission (October 2023), chapter 2 has been published in Remote Sensing (DaSilva et al., 2021b), chapter 3 has been published in Earth Surface, Processes and Landforms (DaSilva et al., 2023), and chapter 4 has been submitted to Geomorphology with corrections returned to the journal. Chapters 2, 3, and 4 are open access articles and can be found at links listed in their respective title pages. The article's formatting have been adapted for this thesis, but their content is consistent with the final publication.

Following the main chapters of the thesis are three appendices of related and formative research that was undertaken during my PhD candidature. In Appendix 1, I adapted the methods developed in my master's thesis, expanded the research scope, and wrote a published research paper which examined the historical coastal change associated with a marina as measured from aerial and satellite imagery (DaSilva et al., 2021a). Its subject focus is not directly applicable to this thesis, but the methods used were constructive in developing the skills in all of the chapters of this thesis.

In Appendix 2 (Hesp et al., 2022b), I conducted the image and spatial analyses, the creation of figures and participated in the writing as a co-author. The work reviews the initiation mechanisms of transgressive dunefields and presents the historical evolution of the study site from chapter 4.

In Appendix 3 (Davidson et al., 2022), I assisted in a multi-day wind flow experiment to explore the dynamics of wind speed acceleration and boundary layer flow over the stoss-slope of an eroding coastal dune. This work was influential in my understanding of the role of aeolian forces, dune slope, and dunefield evolution as it is undergoing prolonged shoreline erosion. I cite and apply this knowledge in Chapter 4.

A list of all presentations that I contributed to and presented on during my Ph.D candidature is provided in Appendix 4.

There are 3 supplementary sections following the appendices which correspond to each of the three main chapters, these include tables, meta-data, and other information.e

CHAPTER 2.

Accepted article, DaSilva, M. D. (80%), Bruce, D. (10%), Hesp, P. A. (5%), & Miot da Silva, G. 2021 (5%). A New Application of the Disturbance Index for Fire Severity in Coastal Dunes. Remote Sensing, 13, 4739.

Statement of co-authorship - I lead the research design of this manuscript in this chapter. I was mentored and aided by my supervisors from the conceptualisation through to realisation. All text, figures, analysis, and final editorial changes were ultimately my decision after consulting with my PhD committee.

A New Application of the Disturbance Index for Fire Severity in Coastal Dunes

Abstract: Fires are a disturbance that can lead to short term dune destabilisation and have been suggested to be an initiation mechanism of a transgressive dune phase when paired with changing climatic conditions. Fire severity is one potential factor that could explain subsequent coastal dune destabilisations, but contemporary evidence of destabilisation following fire is lacking. In addition, the suitability of conventional satellite Earth Observation methods to detect the impacts of fire and the relative fire severity in coastal dune environments is in question. Widely applied satellite derived burn indices (Normalised Burn Index and Normalised Difference Vegetation Index) have been suggested to underestimate the effects of fire in heterogenous landscapes or areas with sparse vegetation cover. This work assesses burn severity from high resolution aerial and Sentinel 2 satellite imagery following the 2019/2020 Black Summer fires on Kangaroo Island in South Australia, to assess the efficacy of commonly used satellite indices, and validate a new method for assessing fire severity in coastal dune systems. The results presented here show that the widely applied

burn indices derived from NBR differentially assess vegetation loss and fire severity when compared in discrete soil groups across a landscape that experienced a very high severity fire. A new application of the Tasselled Cap Transformation (TCT) and Disturbance Index (DI) is presented. The differenced Disturbance Index (dDI) improves the estimation of burn severity, relative vegetation loss, and minimises the effects of differing soil conditions in the highly heterogenous landscape of Kangaroo Island. Results suggest that this new application of TCT is better suited to diverse environments like Mediterranean and semi-arid coastal regions than existing indices and can be used to better assess the effects of fire and potential remobilisation of coastal dune systems.

2.1 Introduction

Fires are an ordinary, recurring, and integral part of ecosystems around the globe and across many parts of Australia (Cary, 2003, Seidl et al., 2017, Massetti et al., 2019, Levin et al., 2021), and provide many benefits to ecosystems (Keeley, 1995, Wellington and Noble, 1985, Wright and Clarke, 2007). Shifts in fire regimes (frequency and severity) are associated with climate change, extreme weather events and drought (Barbero et al., 2020, Keeley and Syphard, 2016, Turton, 2020, Turton, 2017, Adeleye et al., 2021, Tran et al., 2020a) and may alter vegetation succession (Storey et al., 2021, Bennett et al., 2016) or landscape stability (Levin et al., 2012). Fire severity is a measurement of the effects of fire on landscapes and can be irregular within a burnt area due to variation in fuel loads, fuel type, weather conditions, topography, or maturity of the plant community (Schoennagel et al., 2009, Turner et al., 1994, Turner et al., 1999, Gibson et al., 2020). Measurements of fire severity provide data that can be used to better understand the subsequent post-fire recovery, such as shifts in ecological diversity or stability of the landscape (Collins et al., 2014, Coppoletta et al., 2016, Mathews and Kinoshita, 2020). Significant research has been applied to mapping and understanding fire severity from space (Keeley, 2009, Pérez-Cabello et al., 2021, Chuvieco et al., 2020, Chuvieco et al., 2019), but many conventional methods are influenced by soil conditions and pre-vegetation communities, or require region specific adjustments, thresholds or training data (Gibson et al., 2020, Miller and Thode, 2007, Tran et al., 2019, Klinger et al., 2019, Norton et al., 2009, Seydi et al., 2021, DeVries et al., 2016) which limit their wider application. Furthermore, the forecast of fires in Australia and globally shows a continued increase in frequency and intensity with extended fire seasons (Royal-Commission, 2020, Aponte et al., 2016, Flannigan et al., 2009) highlighting the need for the study and development of space based Earth Observation (EO) methods to assess fire severity that can be applied broadly across heterogenous environments.

In-situ assessments of burn severity estimate the effects of fire by measuring soil characteristics such as char depth, organic matter loss, colour (Boucher et al., 2017) and descriptions of vegetation loss (Russell-Smith and Edwards, 2006), while space based and airborne EO assessments of fire severity provide estimates of above ground biomass loss and ecological impact as measured from active or passive sensors (Keeley, 2009, Pérez-Cabello et al., 2021). Large extent fire severity mapping has been predominantly accomplished with passive optical spectral indices to discriminate between burnt and unburnt areas, and assessing severity from an index value (Gibson et al., 2020, Tran et al., 2018, Veraverbeke et al., 2012). Classification thresholds have been established with comparisons to *in-situ* observations and methods such as the Composite Burn Index (CBI) (Parks et al., 2014, Chen et al., 2011, Key and Benson, 2005) but are limited to the region and vegetation community for which they are optimised (Tran et al., 2018, French et al., 2008). Two of the most commonly used indices that are used to map the extent of burnt area and fire severity are the normalised burn ratio (NBR) and the normalised difference vegetation index (NDVI) (Bonney et al., 2020, Bright et al., 2019, Epting and Verbyla, 2005, Escuin et al., 2007, Hislop et al., 2018, Liu, 2016, Pickell et al., 2015, Shumack and Hesse, 2018, Shumack et al., 2017, White et al., 2017) that combine the shortwave infrared (SWIR), near-infrared (NIR) or red spectral bands of the electromagnetic (EM) spectrum. These bands are ideal for monitoring vegetation dynamics as the NIR wavelengths shows greenness and chlorophyl concentration while the SWIR wavelengths are sensitive to water content and woody biomass (Chuvieco et al., 2019, Massetti et al., 2019).

Many studies compare pre-fire with post-fire-pixel values to assess the impact and recovery of areas and produce a differenced measurement of change (dNBR or dNDVI) that can be interpreted as fire severity (Hayes and Robeson, 2011, Klinger et al., 2019, Lanorte et al., 2013, Lutz et al., 2011). dNBR and dNDVI were developed for use in landscapes with continuous canopy cover (Key and Benson, 2006) and under-assess fire effects in regions with heterogeneous and/or sparse vegetation communities (Norton et al., 2009, Parks et al., 2014), as the resulting absolute difference is directly related to the amount of chlorophyl of the pre-fire vegetation community and fraction of canopy consumed (Miller et al., 2009a, Fassnacht et al., 2021, Miller and Thode, 2007). Ideally, absolute differenced analysis rasters need independent calibration for different vegetation and landscapes to adjust the thresholds for fire severity (Miller et al., 2009a, Miller and Yool, 2002). Miller et al. (2009a) developed the relative dNBR (rdNBR) to standardise severity values, reduce the effects of diverse vegetation types, and account for variations in soil conditions. Comparisons of efficacy of the rdNBR have shown varying results in certain landscapes (Soverel et al., 2010, Veraverbeke and Hook, 2013, Klinger et al., 2019), but the index is commonly used in studies in semi-arid conditions (Shumack et al., 2017, Klinger et al., 2019, Wang and Glenn, 2009, Shumack and Hesse, 2018, Norton et al., 2009) to minimise effects of heterogenous landscapes and discontinuous canopy coverage (Miller et al., 2009a). Although Klinger et al. (2019) showed that there was no significant improvement between dNBR and rdNBR for assessing severity within fires in their desert study sites. Dual-band indices do not use the full spectral resolution available within multi-spectral imagery and are influenced by the sensitivities of individual bands. There is potential in methods that utilise additional parts of the EM spectrum in multi-spectral imagery that exhibit changes due to fire.

The Tasseled Cap Transformation (TCT) was developed by Kauth and Thomas (1976) to model the spectral trajectory of agricultural crops as monitored from Landsat Multispectral Scanner (MSS) data with outputs of brightness, greenness, yellowness and non-such components. Crist and Cicone (1984) adapted the TCT yellowness output to target soil moisture and formed the widely applied 3 TCT outputs: brightness (TCB), greenness (TCG), and wetness (TCW). These outputs represent values of the three principal surface components: brightness with albedo, greenness with vegetation and wetness with soil and vegetation moisture (Shi and Xu, 2019). TCT outputs are derived from linear combinations of imagery bands weighted with sensor specific coefficients sourced from representative global samples on a rotated principal component axis (Marcos et al., 2021). Healey et al. (2005) developed the Disturbance Index (DI) to track both short and long-term changes in forests by exploiting the differences between brightness compared to greenness and wetness in a cleared forest. TCT outputs are normalised to mean and standard deviation values of pre-disturbance pixels and combined into a single value that represents the normalised difference from a representative mean value (Huang et al., 2020, Baumann et al., 2014, DeRose et al., 2011, Liu et al., 2018, Masek et al., 2008). The full spectral resolution of an image that is combined with TCT and the normalised DI helps to minimise the effects of different soil spectra and varying vegetation types or phenology that can be influential in multi-band indices (Axel, 2018, Masek et al., 2008, Khodaee et al., 2020). The DI has been shown to be effective at tracking disturbances in forests and assessing severity in landscapes that are characterised by a dense and continuous canopy, as normalisation values are influenced by non-tree or forest pixels (Masek et al., 2008, Khodaee et al., 2020). Non-forest pixels, such as bare ground or mixed areas, reduce the effectiveness of DI as they increase the variance within the representative mean pixel values and therefore this diminishes the ability to detect disturbances in a tree canopy with less vigour due to disease or a low intensity fire. Masek et al. (2008) used DI in a time series analysis to track deviations from annually aggregated representative pixels terming it the ΔDI, with significant deviations suggesting disturbances or regeneration over time. To date, there has been one publication that has applied the DI as a differenced temporal index, highlighting the change over time between two dates as a result of a disturbance. Axel (2018) used the difference in pixel values between two DI images to conduct burn scar mapping in the dry forests of Madagascar, utilising local mean and standard deviations to illustrate the effects of fire. The requirement for locally derived statistics has limited the application of DI to forests and discrete study areas and reduced its precision for heterogenous landscapes.

Coastal dune systems are diverse in structure, ranging from highly stabilised, vegetation covered systems to fully active systems with mobile sand, with most dunefields containing both stable, semi-stable or partially vegetated, and active areas (Barchyn and Hugenholtz, 2013) depending on the climate (Hesp et al., 2021) and stage of evolution (Hesp, 2013, Hesp and Martínez, 2007). The long-term stability of coastal dune systems can be altered by anthropogenic factors or variations in climate that alter the sediment supply, vegetation cover, wind regimes, wave conditions, water table and relative lake or sea levels (Aagaard et al., 2007, Costas et al., 2012, Costas et al., 2016, Delgado-Fernandez and Davidson-Arnott, 2011, Feagin et al., 2005, Gao et al., 2020, Hesp, 2013, Miller et al., 2009b, Psuty and Silveira, 2010). The destabilisation or reactivation of previously stabilised coastal dunes may occur after a short-term disturbance, such as fire or storm driven wave and/or wind erosion (Barchyn and Hugenholtz, 2013, Hesp, 2013) but contemporary evidence for fire as the initiator of destabilisation or dune transgression is lacking (Shumack et al., 2017, Shumack and Hesse, 2018). Post-fire dune stability has been shown to be influenced by type of vegetation (Ravi et al., 2012), burn severity (Sankey et al., 2009b) and climatic conditions (Barchyn and Hugenholtz, 2013, Mangan et al., 2004, Whicker et al., 2006). Although dune destabilisation directly following fires has been suggested in the literature, currently the evidence is limited to observations from the stratigraphic record (Boyd, 2010, Cordova et al., 2019, Filion, 1984, Filion, 2017, Filion et al., 1991, Mann et al., 2002, Matthews and Seppälä, 2013, Rich et al., 2015, Seppälä, 1995, Shumack and Hesse, 2018, Shumack et al., 2017, Tolksdorf et al., 2013). Central to these inferences is that the fires are followed by increased aridity or drought conditions, and that fire acts as an initial catalyst for dune reactivation (East and Sankey, 2020, Nelson and Pierce, 2010). The severity of fire may affect the recovery of landscapes as dormant seeds or re-sprouters may not survive above certain temperature thresholds (Shumack et al., 2017, Bell, 2001, Pammenter et al., 1985, Myerscough and Clarke, 2007, Klinger and Brooks, 2017, Keeley, 2009, Pierce and Cowling, 1991, Bradstock, 2008).

Coastal dune landscapes have characteristics that limit the effectiveness of many remotely sensed fire severity indices: heterogeneity, discontinuous canopies, and bright soils. While research has shown alternatives to the widely used indices, region specific adjustments and statistics, training data and thresholds limit their wider application. This study uses the TCT outputs of brightness, wetness and greenness from Sentinel 2 imagery and computes a differenced Disturbance Index (dDI) based on pre- and post-fire pixels to assess fire severity in coastal dune areas. dDI measures the severity of a disturbance as it computes the transformed spectral difference between, before, and after an event at the per pixel scale. This allows it to scale in an automated process for wider geographical applications and potentially provides an improved estimation of disturbance severity in heterogenous environments. The 2019-2020 Australian fire season resulted in thousands of burnt hectares across Australia (Levin et al., 2021), with a significant portion of Kangaroo Island’s stabilised and semi-stabilised coastal dune systems affected (Royal-Commission, 2020, Bonney et al., 2020). This case study explores the effect of an intermittent canopy and soil variability on widely used burn severity indices and presents a new application that aims to improve severity assessments.

2.2 Materials and Method

2.2.1 Study Area

Kangaroo Island (KI) is in South Australia, southwest of its capital city, Adelaide (Figure 1). It has a coastline of approximately 458 km in length and a total area of 3890 km2 (Bourman, 2016). More than one-third of the island lies within a protected wilderness or national park area and holds important ecological value due to its geographical isolation (Peace, 2012). The proximity and exposure to the Southern Ocean and its cold waters have a unique meteorological effect on the island's weather, climate, and subsequent fire patterns (Peace, 2012). KI has a Mediterranean climate characterised by hot dry summers and wet winters with most rain occurring outside of the summer months (Short and Fotheringham, 1986). Fires are common and occur annually, primarily as a result of intentional burn offs and dry lightning strokes (Peace, 2012). In December of 2019, lightning strokes ignited multiple fires that burned until January 21, 2020, affecting nearly half of the island. The fire spread throughout the national park on the western side of the island and swept east into the agricultural region and was the largest recorded fire in contemporary records (Bonney et al., 2020). Historical records date to the 1930s (Bonney et al., 2020) with anecdotal records from early Europeans suggesting a dramatically increased and altered fire regime from the 19th century after colonisation (Bauer, 1959). Bauer (1959) suggests that fires were widely and repeatedly used to clear land and that by the 20th century it was likely that no parts of the island or its vegetation remained unaffected.

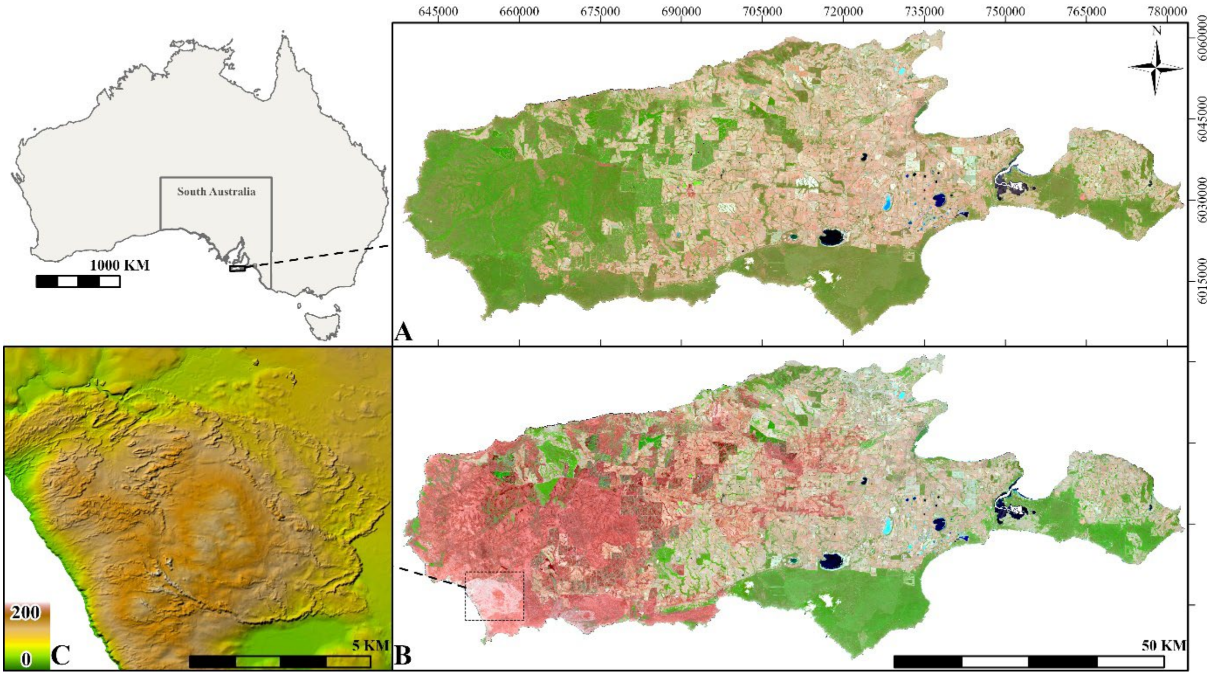

Figure 2-1- Kangaroo Island in South Australia as shown by Sentinel 2 MSI (L2A) satellite imagery from 16 December, 2019 (A) and 30 January 2020 (B). S2 imagery is shown in bands 4,8 and 12 (BGR)to highlight fire affected areas. Inset (C) shows exaggerated (2*elevation) relief map (metres) of the Holocene transgressive dunefield.

The extent of modern land and agricultural use (pastoral and forestry) on the eastern portion of the island is a result of poor soils that discouraged earlier development, with the other 46% of the island under tree, mallee or shrub cover (Figure 2) (Ball, 2002). Native vegetation can be generally grouped into eucalyptus woodland, eucalypt mallee, and sparse shrubland communities(Ball, 2002). The vegetation and landscape is broadly characterised by three major regions, the interior raised plateau/tableland, the lowland plains and coastal formations (Table 1) (Northcote, 2002). The plateau is dissected by riverine systems which have formed narrow valleys through pre-Quaternary bedrock characterised by eucalyptus woodland and dark soils coloured by humus and iron oxides (Northcote, 2002). Along the coastline, late-Cambrian granite and Pleistocene aeolian calcarenite cliffs form headlands and capes (Northcote, 2002). The south and west coast of the island is exposed to the full force of the Southern Ocean and is characterised by high wind and wave energy, actively eroding cliffs, pocket beaches and embayments (Bourman, 2016). Northern and eastern coastlines are sheltered from the predominant wind and wave energy and characterised by high cliffs, pocket beaches and tidal inlets (Bourman, 2016). Sandy beaches occupy 34% of the coast which are backed by Quaternary aeolian sediments rich in carbonate; indurated Pleistocene calcarenite and unconsolidated Holocene sands form exposed isolated units (Short and Fotheringham, 1986, Bourman, 2016). The Holocene sands form complex transgressive and parabolic dunefields that are mostly stabilised by vegetation (Figure 1C), with some areas actively transgressing and fully destabilised (Short and Fotheringham, 1986, Northcote, 2002). Coastal dune vegetation is highly heterogenous; sparse shrubland in areas with active aeolian sediment transport and dominated by densely populated mallee in stabilised or sheltered regions (Northcote, 2002).

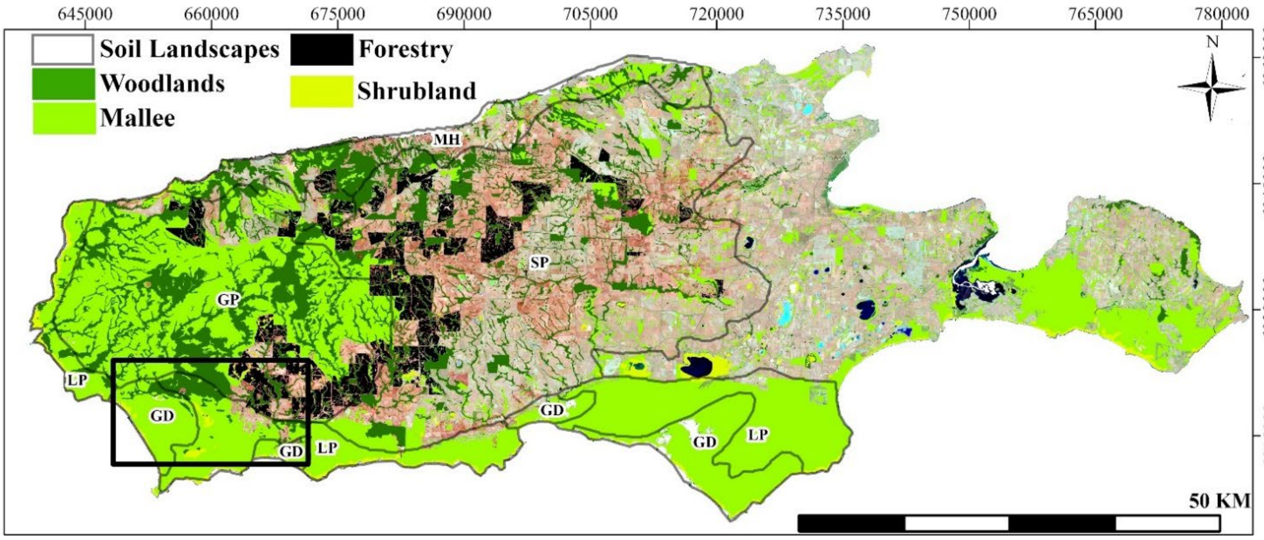

Figure 2-2 Landscape unit classifications of Kangaroo Island from Northcote (Northcote, 2002), dominant native vegetation communities and plantation forests of hardwood and softwood species. Extent indicator in the SW part of island refers to figure 3.

Table 2-1 – Landscape units associated with soils in fire affected regions of Figure 2. Dominant soils reflect classification used by Northcote (Northcote, 2002).

Unit	Landscape	(Classification) Dominant Soils
Linois Plains - LP	Calcarenite lowlands	(E10) Calcarenite and dune limestone with pockets of red sandy soils.
Gosse Plateau - GP	Dissected tableland	(Wa1) Acid duplex soils. Leached sands, high organic and alluvial soils.

Gantheaume Dunes - GD	Coastal dune	(A1) Carbonate rich sands on dune limestone, calcarenite
McDonnel Hills - MH	Steep hilly upland	(D2) Shallow grey-brown acidic soils containing ironstone gravel.
Seddon Plateau - SP	Dissected tableland	(Wb2) Duplex soils. Leached sands, ironstone gravel and high organics alluvial soils.

2.2.2 Datasets and Pre-processing

Data management, image analysis and figure generation was primarily carried out in ArcGIS Pro (2.8), ERDAS Imagine 2020 and python environments. Sentinel 2 (S2) imagery and aerial imagery were used to assess fire severity (Table 2). High resolution aerial imagery with 4 spectral bands (RGB, NIR) for 2016 and 2020 was sourced from the most recent ortho-images from the State Government of South Australia. Pre-fire aerial imagery was resampled via cubic convolution to geometrically match the spatial resolution of 2020 aerial imagery. S2 imagery was sourced from the European Space Agency's Copernicus Open Access Hub (https://scihub.copernicus.eu). Cloud free S2 imagery was acquired for before and after the fire event as well as to coincide with the dates of the high-resolution aerial imagery in 2016 and 2020. S2 imagery was resampled to the highest spatial resolution of 10m via cubic convolution. Level 2A imagery was acquired for the 2019 and 2020 imagery and Sen2Cor was used to apply atmospheric corrections for 2016 imagery (Gascon et al., 2017). All datasets were analysed in the Geocentric Datum of Australia 1994 (GDA94) with a Universal Transverse Mercator (UTM) datum in zone 53 South.

Table 2-1 - Imagery used to assess fire effects from 2016-2020. Table shows date or range of dates for satellite (L2A) and aerial ortho-imagery collected, number of spectral bands and respective pixel size.

Platform	Date	No. of Bands	Pixel Size
Aerial	18-22 December 2016	4	40 cm
S2A	11 December 2016	12	10 m-60m
S2A	16 December 2019	12	10 m-60m

S2B	30 January 2020	12	10 m-60m
Aerial	30 January 2020	4	10 cm

2.2.3 Index Design

To transform imagery to the orthogonal TCT axes, bands are scaled to individual coefficients developed from representative imagery sets and combined in a linear equation. At the time of writing, specific coefficients for all bands within S2 ground reflectance imagery have not been published. Recently, some authors (Lastovicka et al., 2020, Wittke et al., 2019) have used coefficients developed for Landsat at-sensor reflectance products on S2 level-2A imagery. Others (Wang et al., 2020, Brandolini et al., 2020, Valenti et al., 2020, Tridawati et al., 2020, Li et al., 2021) have applied TCT coefficients to S2 level-2A data that were developed for at-sensor S2 (level-1C) imagery (Nedkov, 2017, Shi and Xu, 2019). The spectral range and similarities of bands from Landsat and S2 bands is well documented (Claverie et al., 2018, Mandanici and Bitelli, 2016, Sofan et al., 2020), and the coefficients as developed by Crist (1985) have been used in various studies using surface reflectance Landsat imagery (Kennedy et al., 2010, DeVries et al., 2016, Viana-Soto et al., 2020, Hislop et al., 2018, Axel, 2018). For this study, coefficients were applied to S2 L2A bands (2_{490}, 3_{560}, 4_{665}, 8_{842}, 11_{1610}, 12_{2190}) and sourced from Landsat derived coefficients for atmospherically corrected imagery (Crist, 1985) to derive TCB, TCG and TCW.

dDI (Equ.1) combines the Tasseled-cap indices (brightness, greenness and wetness) into a single index value of transformed spectral distance and temporal change. In this application, a pre-disturbance image is used to assess the transformed spectral change that has occurred as a result of a fire.

Equation 2-1

$$dDI = \frac{(TCG' + TCW' - 0.5 * TCB')}{10{,}000}$$

Where TCB', TCG', and TCW' (Equ. 2) respectively represent the transformed spectral difference in brightness, greenness and wetness indices between the image dates.

Equation 2-2

$$TCB' = preTCB - postTCB$$

The change in brightness values was found to be disproportionately high compared to the combined greenness and wetness in regions where the tree canopy was fully consumed and had bright soils, so a scaling factor (0.5) was applied to the TCB' output in the dDI calculation. Index values are rescaled to represent change in transformed reflectance values (Gascon et al., 2017) by dividing by 10,000. The order of the equation has been shifted relative to the previously published DI equation (Healey et al., 2005) to ensure that areas disturbed resulted in a positive value. Larger index values indicate a likely disturbance event, with higher brightness and lower greenness and wetness giving greater positive values and severity. Low positive (<0.1) values indicate minimal changes in relative transformed spectral change with negative values or values close to 0 suggesting that brightness decreased or was unchanged relative to greenness and wetness and that disturbance was unlikely.

2.2.4 Satellite Fire Severity

The normalised burn ratio (NBR) (Equ. 3) was developed by Key and Benson (2005) and is the standard index used for burn severity and burnt area research and for large extent monitoring programs (Szpakowski and Jensen, 2019). dNBR (Equ. 4) and rdNBR (Equ. 5) were calculated to compare conventional fire severity indices with the dDI. To align with the spectral resolution of Landsat (Sofan et al., 2020) and previous applications of the index, NBR was computed with the bands 8_{842} and 12_{2190} of S2 imagery.

Equation 2-3

$$NBR = \frac{NIR - SWIR}{NIR + SWIR}$$

Pre- and post-fire NBR were combined to calculate the differenced NBR (dNBR). dNBR values are the absolute change between images with positive pixel values indicating burnt areas and higher values often interpreted as higher fire severity (Soverel et al., 2010).

Equation 2-4

$$dNBR = preNBR - postNBR$$

Miller and Thode (2007) developed the relativised dNBR (rdNBR) to better assess fire effects in pixels where pre-fire vegetation cover is low and an absolute measure of change would result in low values, regardless of total vegetation loss. Similar to dNBR, positive values indicate burnt areas and negative values represent areas with increased vegetation cover or vigour (Miller et al., 2009a). The dNBR value is relativised by dividing by square root of the absolute preNBR value and was calibrated based on *in-situ* comparisons to fire severity (Miller and Thode, 2007).

Equation 2-5

$$rdNBR = \frac{dNBR}{\sqrt{|preNBR|}}$$

As acknowledged in its development (Miller and Thode, 2007), low preNBR values will cause exceptionally large burn severity estimations in the resulting rdNBR index due to the division by a small value, causing significant overestimations of fire severity. For comparisons and visualisations in this analysis, the pixel values outside of 3 Standard Deviations (STDs) from the mean of rdNBR were considered outliers and removed.

2.2.5 High Resolution Aerial Assessment of Fire Severity

2.2.5.1 Representative dune sites

High spatial resolution aerial images provides a source of data that can be used to estimate burn severity, help track the recovery of vegetation (Arkin et al., 2019, Carvajal-Ramírez et al., 2019, Fernández-Guisuraga et al., 2018, Fraser et al., 2017, McKenna et al., 2017, Pádua et al., 2020, Pérez-Rodríguez et al., 2020, Samiappan et al., 2019, Shin et al., 2019, Tran et al., 2020b) and corroborate observations from satellite imagery (Alvarez-Vanhard et al., 2020, Gray et al., 2018, Mazzia et al., 2020, Morgan et al., 2020, Pádua et al., 2020). Aerial imagery from 2016 and 2020 (Table 2) was used to extract and measure vegetation loss in representative coastal dune systems (Figure 3 and Table 3). For further review of coastal dune types see Hesp and Walker (2013). Sites A and B are a mix of active and stabilised dune systems, characterised by high exposure to wave and aeolian energy. Both sites (A and B) were burnt in all regions except in the foredune areas (foremost depositional dune landward of the waterline). Before the fire event, Sites C and D were fully stabilised parabolic dunes characterised by thick mallee vegetation cover. The extent of site D was derived from the boundary of soil groups between Holocene sands and Pleistocene lowlands (GD and LP Table 1).

Table 2-2 - Representative coastal dune sites used to assess fire severity with aerial and satellite imagery.

site	State	Description	% burnt
A	Active	Foredune blowout complex backed by active parabolic dunes	~80%
B	Active	Foredune blowout complex backed by stabilised parabolic dunes	~80%
C	Stabilised	Parabolic dunes	100%
D	Stabilised	Parabolic dunes	100%

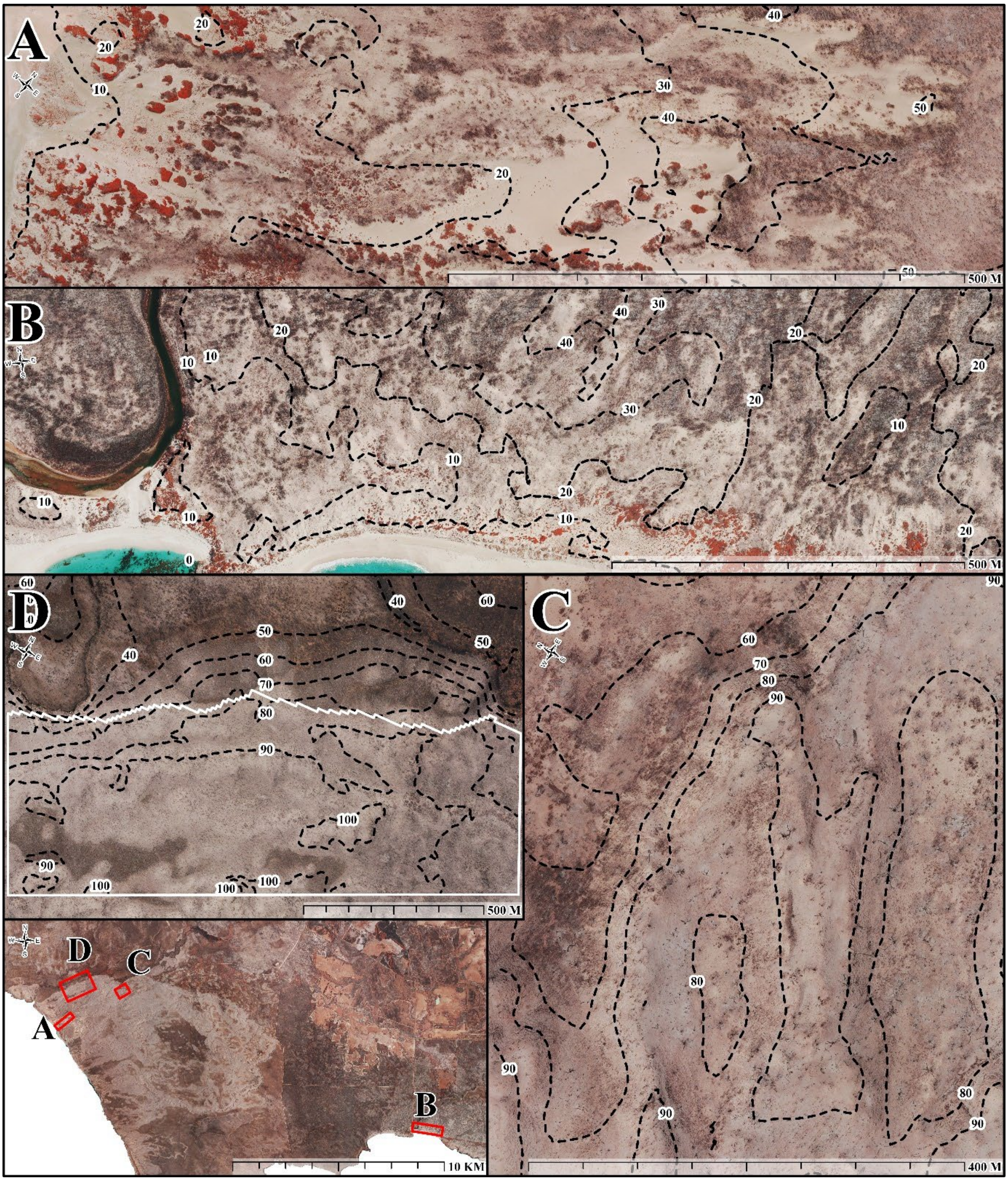

Figure 2-3 – Sites for comparing satellite and aerial derived burn indices. Aerial imagery is from 30 January 2020 and is displayed in colour infrared. Sites A-D are described in table 3 and extent of analysis area is shown in Figure 2. Site D has a mask outline (white) based on the soil boundary between Holocene dune (CDC) in the southern portion and Pleistocene lowlands in the northern section (GD and LP table 1). Interactive perspective web map of locations can be viewed at this link. Black dotted lines show 10m contours.

2.2.5.2 Measuring Fire Severity from Aerial Imagery

The Modified Excessive Green Index (MEGI) (Equ. 6) was calculated for the 2016 aerial imagery to distinguish between sand/soil and vegetation pixels in areas with a discontinuous canopy and exposed soils. MEGI emphasises the height of the green reflectance peak (McKenna et al., 2017) and was used to isolate exposed soil and sand pixels after it was found that MEGI derived a larger spectral difference between sand and non-sand pixels (including green vegetation and woody bio-mass) than other NIR/RGB indices.

Equation 2-6

$$MEGI = 2 * \text{Green} - \text{Red}$$

The non-sand classes, representing vegetation and other surface biomass were merged to form an analysis mask. This focused the spectral analysis to pixels that contained vegetation pre-fire in 2016, excluded previously active dune features or exposed soils and gave a measurement of percent sand per pixel for satellite index comparisons.

NDVI (Equ. 7) was calculated for 2016 and 2020 aerial images and differenced to show change in greenness and vegetation loss, producing a dNDVI (Equ. 8). The dNDVI image was masked to the MEGI derived analysis mask to estimate canopy and vegetation loss, independent of exposed soil in the pre-fire image. An absolute measure of change (dNDVI) was chosen because non-vegetation pixels were excluded and did not necessitate the use of a relative index. Zonal statistics from the aerial imagery were taken according to the pixel size (10 m) and location of S2 imagery to produce average dNDVI values per pixel.

Equation 2-7

$$NDVI = \frac{NIR - Red}{NIR + Red}$$

Equation 2-8

$$dNDVI = preNDVI - postNDVI$$

2.2.6 Comparisons of Satellite Derived Fire Severity

Satellite indices were extracted to a focused analysis mask, comprised of the extent of a thresholded dNBR image (> 0.2) to remove unburnt pixels and a thresholded rdNBR image (3 STDs) to remove outliers. Spatial statistics were generated for satellite indices grouped by Landsystem (LS) Soil classifications (Water, 2000) in regions with the highest burn severity indices, in dune formations, and within the protected National Park regions (Figure 4). Means and STDs of individual LS groups were compared to show differences between soil groups and the aggregate of all high burn severity LS groups (Figure 4). To compare the separability of index populations, a Welch's t-test using Z-scores was completed comparing soil groups. Z-scores for individual soil groups were calculated based on aggregated mean and STDs from the total population of LS classes.

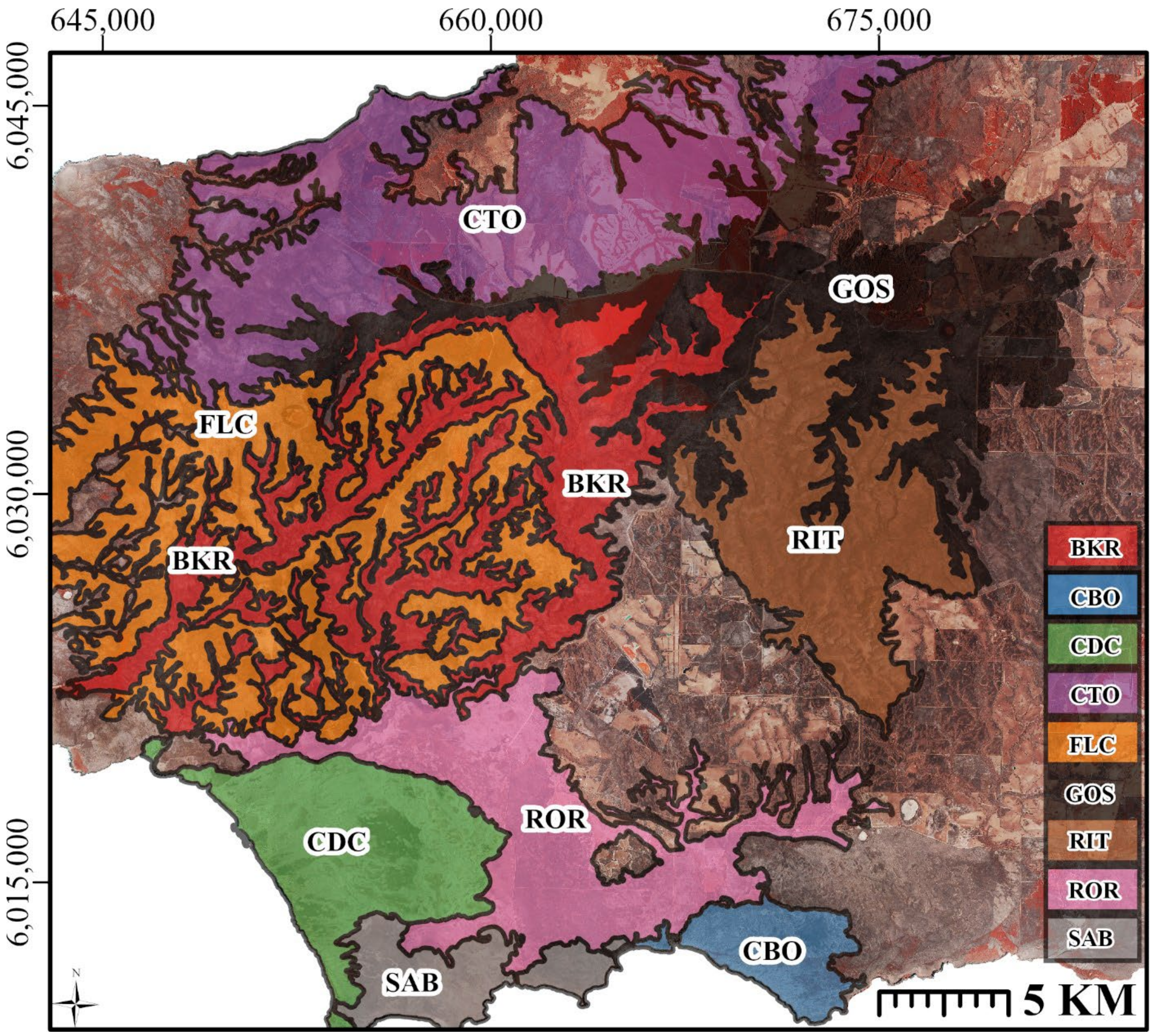

Figure 2-4 - Locations of Landsystem (LS) soil units used for comparing statistics of fire severity indices. Soil groups are chosen based on areas with highest severity and within regions of Flinders Chase National Park and Ravine des Casoars Wilderness Protection Area.

2.2.7 Comparisons to Aerial Fire Severity

Satellite and aerial fire severity index values were compared to the four representative dune sites in the fire grounds on Kangaroo Island (Table 3 and Figure 3). The high-resolution aerial imagery provided the absolute measures of greenness lost from dNDVI values and the percent of exposed sand per pre-fire pixel. Trend lines and coefficient of determination (r^2) values were generated to show the relationship between satellite derived indices and the information extracted from aerial imagery: the absolute measure of greenness and vegetation loss independent of exposed sand and the total percent per pixel of sand exposed pre-fire.

2.3 Results

2.3.1 Differenced Disturbance Index

The outputs from dDI show the difference in transformed spectral distance between two dates, with a larger index value indicating a greater spectral difference and a larger deviation from previous pixel values. Figure 5 shows the results of two separate dDI calculations between two distinct time periods, 2016 to 2019 (panel A) and 2019 to 2020 (panel B). From 2016 to 2019, few large disturbance events are detected with most areas showing low dDI values. The largest dDI values between 2016 and 2019 are in agricultural areas and are likely a result of irrigation and land use changes. Panel B shows the results of the 2019/2020 fires, with high index values shown in darker pixels. Panels B1 and B2 of figure 5 show the dDI values across different soils and landscape types. The clear boundary between light and darker soils is visible in B2 and shown in figure 2 as the border between the landscape units of Northcote's Gantheaume Dunes and Gosse Plateau.

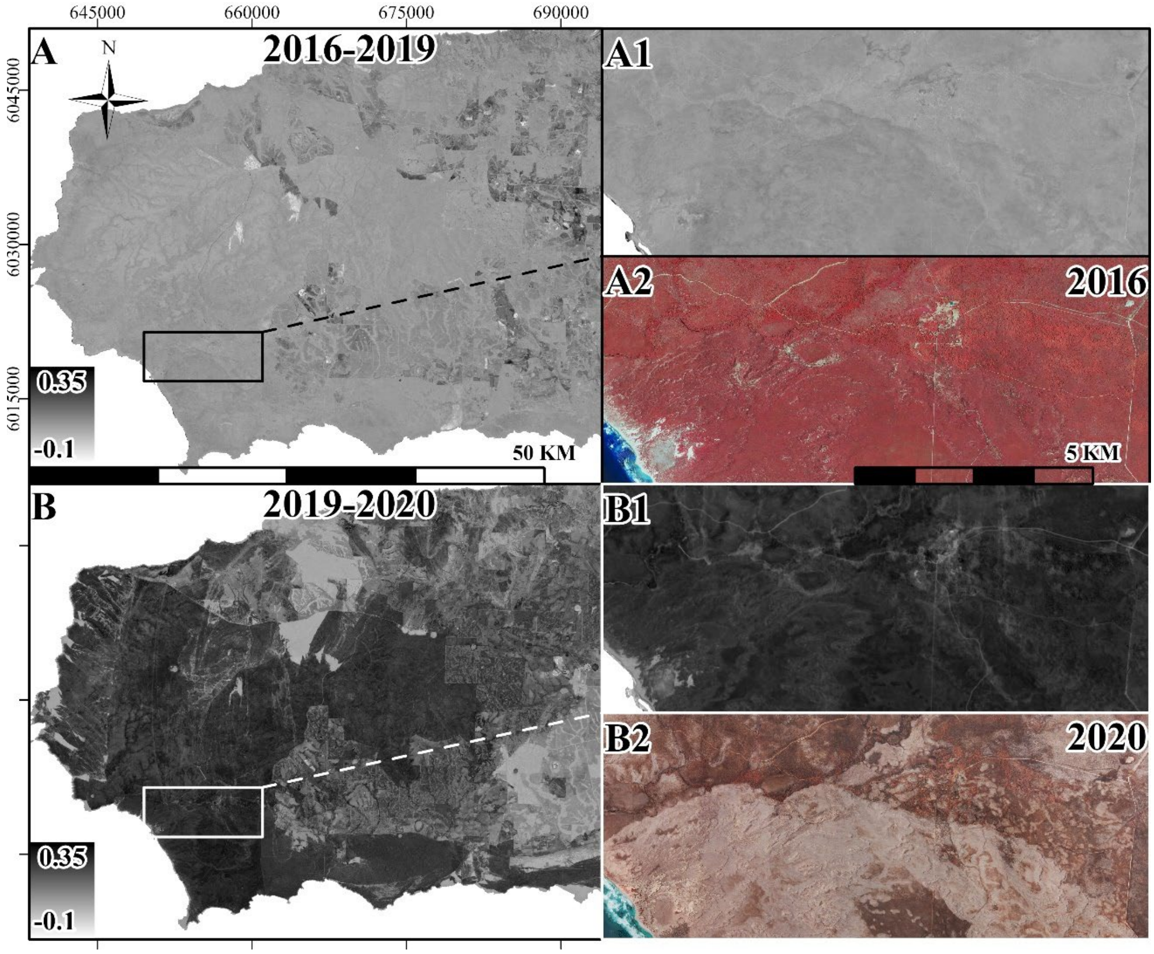

Figure 2-5 – Differenced Disturbance Index taken from Sentinel 2 imagery from December 2016 to December 2019 (A) and December 2019 to January 2020 (B). Index symbology (white to black) and scale is set from 3 standard deviations of B image, showing the high burn severity values from the 2019/2020 fires and relatively low dDI values for A and A1. A2 and B2 are colour infrared insets of area of A1 and B1, showing the landscape before and after the fire.

2.3.2 Comparisons of Satellite Fire Severity

To illustrate the differences in fire severity, imagery from 2020 and change over time indices from 2016 and 2020 are shown in figure 6. Fire severity is derived from the two forms of NBR, with its absolute and relative version and a dDI image. All indices are extracted to the extent of a dNBR threshold (>0.2) and presented in 3 STDs from white to black, showing low to high fire severity. In the inset maps of figure 6 the boundaries between the brighter and darker soils (Figure 7) are visible in both NBR fire severity indices, showing a lower relative value as a result of soil brightness. Compared with the index output from dDI, the effects of soil brightness have been removed and there is a consistent measure of high fire severity between the two soil groups and across the fire-grounds. In the left-hand panels of figure 6B, the highest values in dNBR correspond to the riverine soils, seen in the dendritic pattern of the dissected tableland and in areas of agroforestry in the centre of the panel.

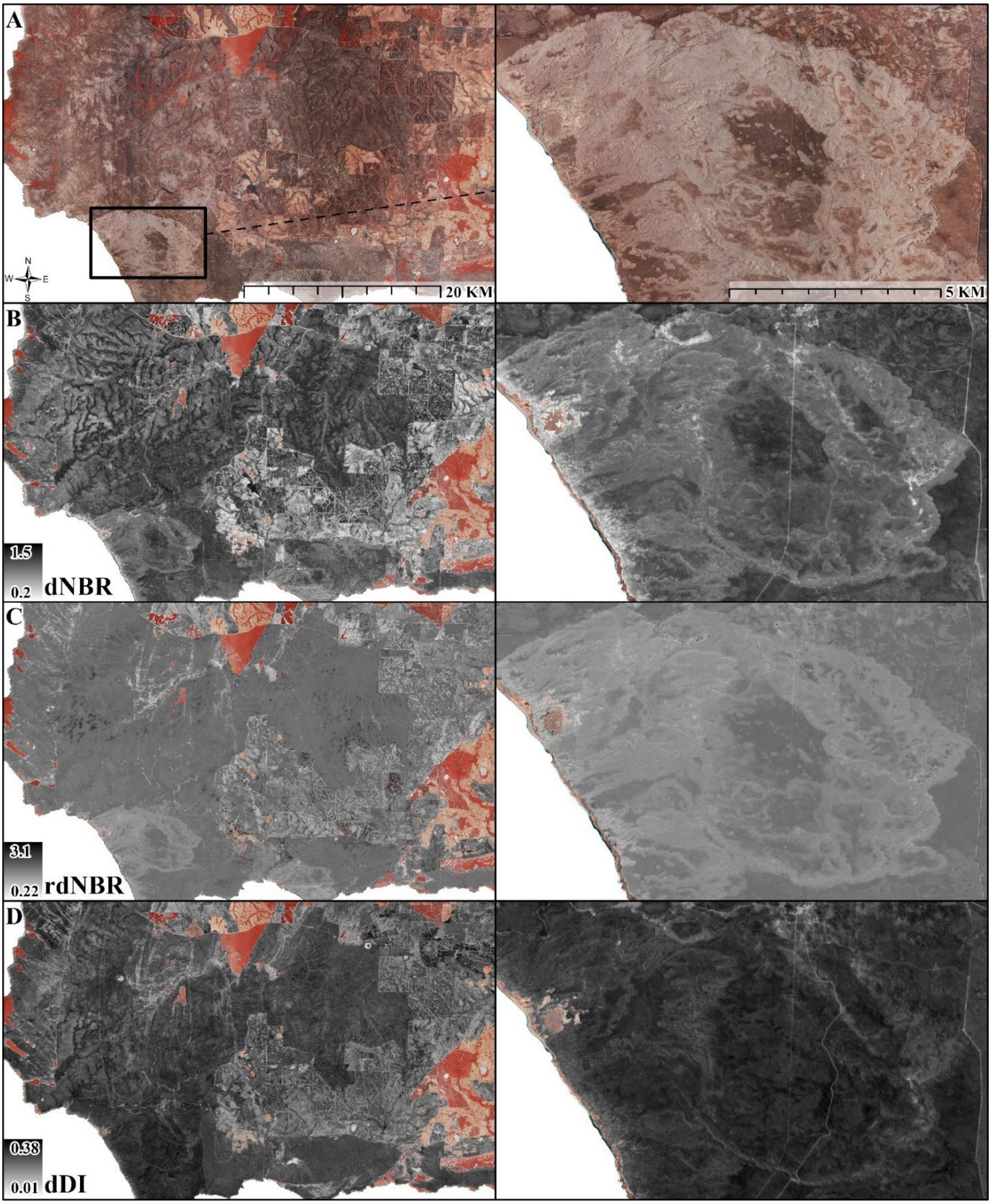

Figure 2-6 – Top row of figure (A) is colour IR imagery from January 2020 with inset map showing extent of burned dune soils (CDC) and the border of the darker soils from the low-land Pleistocene formation (ROR). Rows 2-4: Comparison of fire severity values from dNBR (B), rdNBR (C) and dDI (D). Darker values are showing higher relative index values and severity. Enlargements on the right-hand side showing the effect of soil brightness on dNBR

and rdNBR values. Imagery is masked according to a dNBR threshold (>0.2) with all indices displaying data 3 STDs from mean with 1.5 Gamma.

Figure 2-7– Oblique aerial photograph (taken 16/01/2020) showing clear boundary in soil groups between the brighter Holocene sands and the darker brown Pleistocene lowlands in the foreground. This boundary corresponds to lower fire severity in both NBR derived fire indices with dDI giving a more uniform estimation of very high severity in these regions with a fully consumed canopy.

Figure 4 shows the extent of each Landsystem (LS) soil classification used in figure 8 to show the spatial variability of means and standard deviations per LS group. Even at the aggregated LS unit, soil brightness decreases the severity of both NBR indices in the bright dune soils. The SAB LS group is considered a dune formation although it is characterised by darker Pleistocene calcarenite overlain by shallow sandy Holocene deposits (Water, 2000), meaning its soil reflectance is considerably darker than adjacent dune formations. The resulting NBR indices suggest higher severity (Figure 8) in these regions due to its predominant darker soil profile (and therefore surface colour). dDI shows similar relative fire severity for the tableland and riverine soil groups, with the dune soils reflecting the complete loss of canopy and vegetation across the dune soils of CDC and SAB. The results of a Welch's t-test indicate that all compared indices exhibit significant differences in their population's mean, with the Pearson's correlation showing their divergence presented in Appendix A, table 4A.

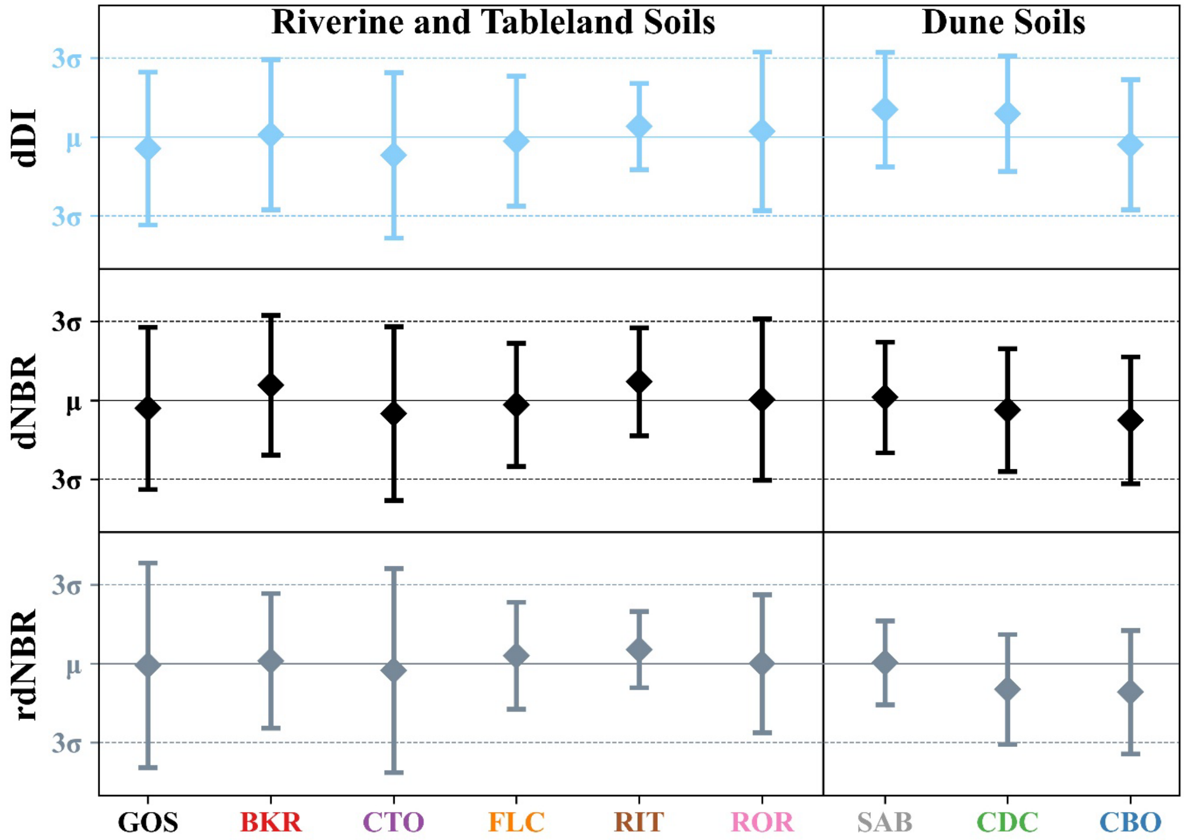

Figure 2-8 – Showing mean (μ) and standard deviations (σ) of burn indices, differenced Disturbance Index (dDI), differ-enced Normalised Burn Ration (dNBR) and relative differenced Burn Ration (rdNBR), grouped by Landsystem soil unit. Indices have been thresholded according to dNBR threshold (>0.2), with outliers above 3 STDs re-moved from individual soil groupings.

2.3.3 Comparison to Aerial Fire Severity

Figure 9 illustrates the positive association between dNDVI and satellite fire severity indices in the representative dune sites A-D (figure 3), suggesting that all 3 indices track loss of greenness with increasing index values. The negative association of index value and increasing percent sand per pixel in figure 9 shows that all severity values decrease as the percent of sand per pixel increases.

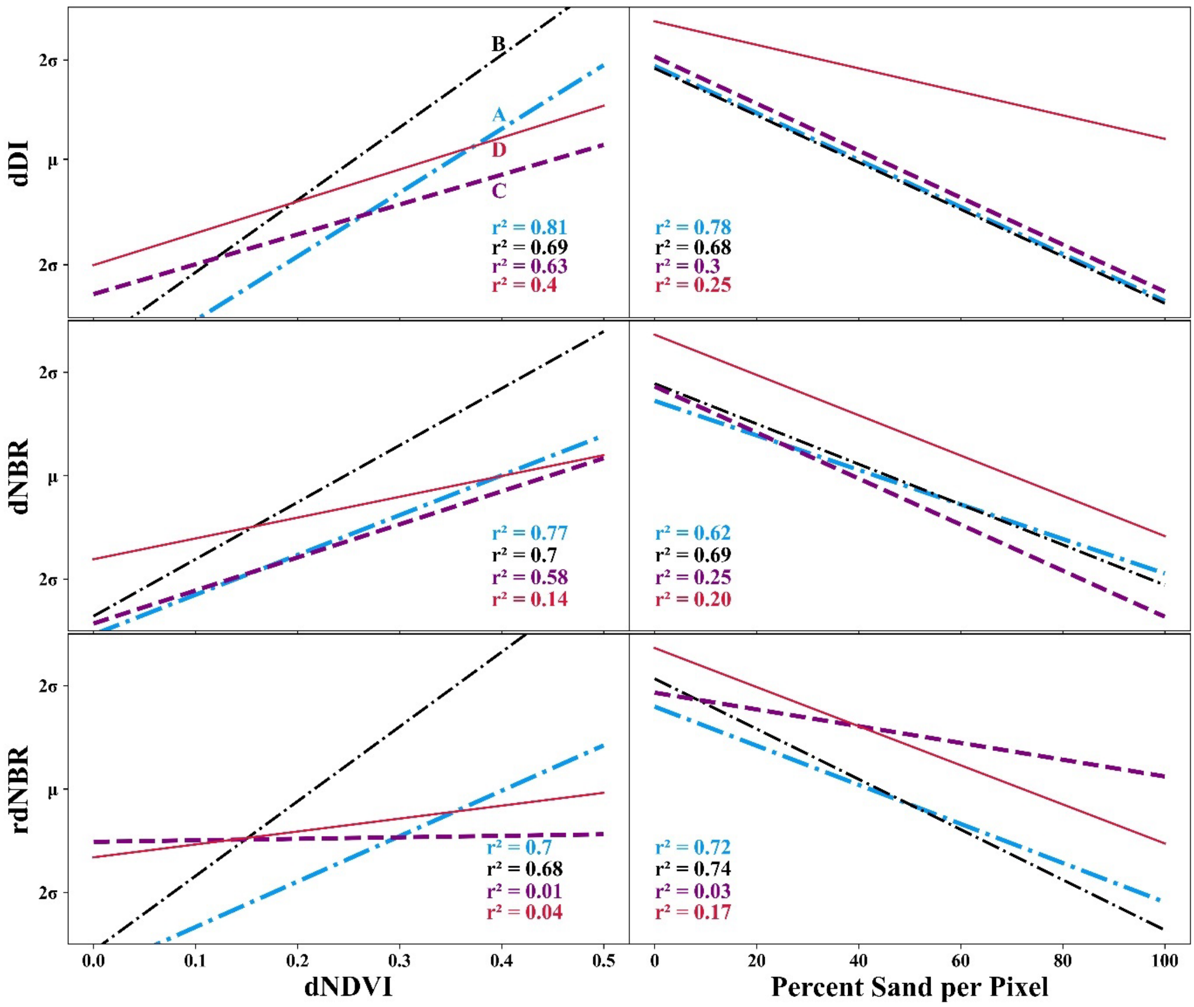

Figure 2-9 – Trend lines and coefficient of determination (r2) values showing the relationship between satellite derived indices and aerial derived fire severity from dNDVI (greenness and vegetation loss independent of exposed sand) and the total percent per pixel of sand exposed pre-fire. Indices are compared at representative dune sites A-D with a direct comparison between S2 pixel locations and aggregated statistics (mean dNDVI and Percent Sand Per Pixel).

Figure 10 demonstrates the resulting effects of soil brightness on index value within site D. Interdune swales are low points in dune landscapes that are more sheltered environments, characterised by increased moisture, higher humus and organics surface deposits, lower wind areas, accumulation and trapping of surface water, and commonly a different vegetation community than in adjacent higher areas, often resulting in darker soils (Barrineau et al., 2015). The canopy loss is uniform within this area according to the high-resolution aerial imagery, suggesting very high severity throughout site D. The darker soils located within the interdune swale have substantially higher index values in both NBR

(Figure 10) indices, contrasted to the more consistent rating of fire severity from dDI that aligns with full canopy consumption.

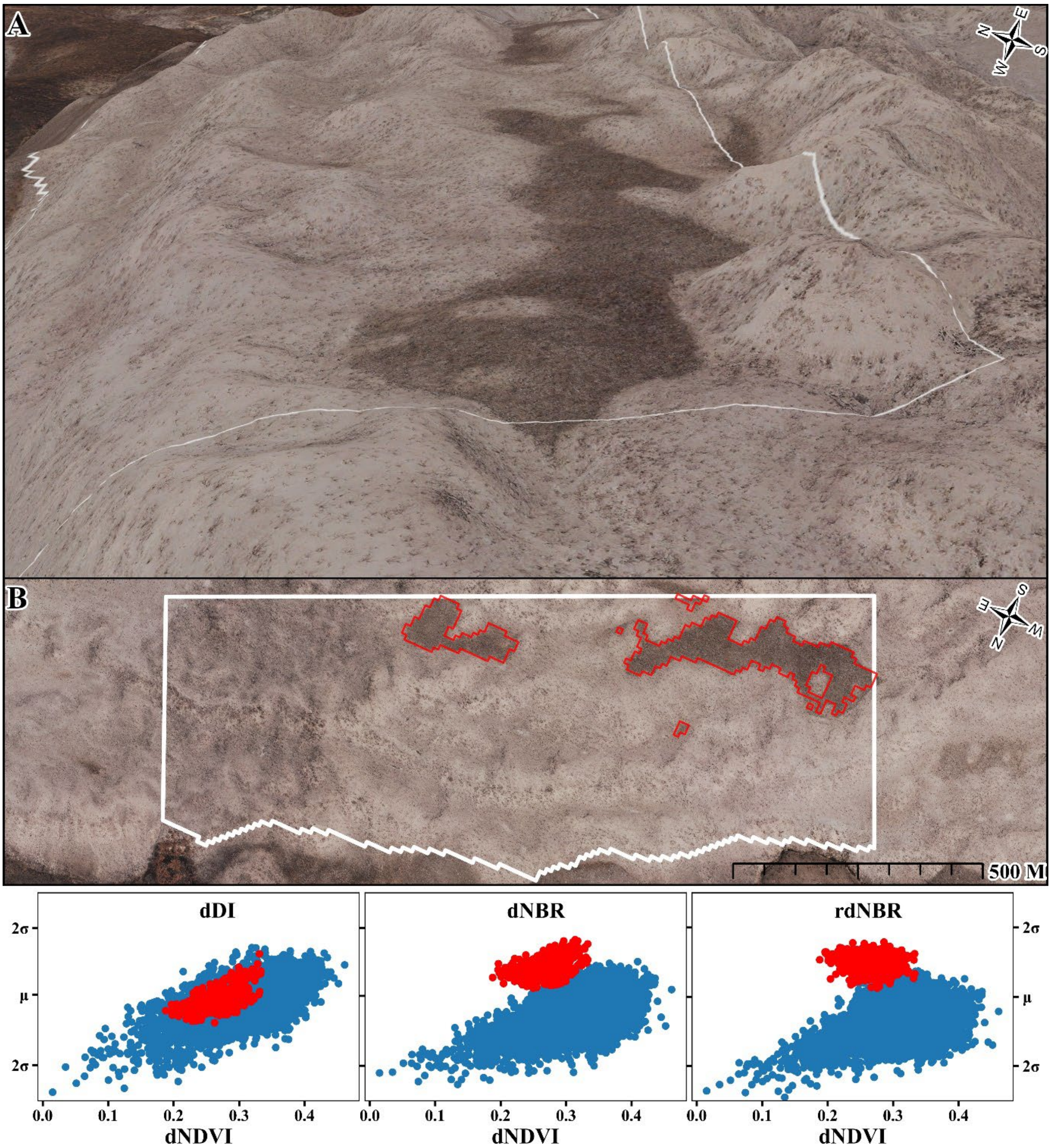

Figure 2-10 - 3D view of site D with an elevation exaggeration (3x), (B) Nadir view of site D with red outlined pixels shown in 3 indices compared against dNDVI. The clear effects of soil brightness on index values (dNBR and rDNBR) are shown by the higher severity in darker soil areas (red points in plot) compared to the lighter coloured soils (blue points in plot). All plots are set to mean and 2 Stds of their respective index per the CDC soil grouping (Figure 4).

2.4 Discussion

Kangaroo Island is a highly heterogenous landscape, exhibiting multiple broad soil groups and vegetation communities. The fire in the summer of 2019/2020 affected large swathes of the island and many of the predominant vegetation communities and soil groups. Desktop studies of the effects of the fire have shown that large portions of the island exhibited very high fire severity (Bonney et al., 2020, Department of Agriculture, 2020), although those studies assessed the fire impacts on the Holocene dunes (Figure 1) to be relatively less severe due to fixed severity thresholds. It has been well documented that NBR values are influenced by changes in soil colour, often attributed to residual char or ash and differing soil types (Chuvieco et al., 2020, Lanorte et al., 2013, Turner et al., 1994) [18,26,56]. The results of this work show that the fire severity values from NBR are influenced by soil type and brightness, both at the local level (Figure 10) and across the broad soil groups (Figures 4 and 8). The border between the bright carbonate rich sands of the Holocene dune formations and the darker Pleistocene lowland soils with verdant riverine woodlands is clearly visible within the imagery (Figures 6 and 7) and NBR based indices (Figure 6), resulting in differential classifications of fire severity in Government reports (Department of Agriculture, 2020). The results of this work show that uncalibrated coarsely applied severity thresholds will result in differential fire severity more closely aligned with differences in soil brightness and predominant vegetation communities than actual effects of fire.

The differenced Disturbance Index (dDI) presented in this work computes the transformed spectral difference between two dates, measuring the effects of a disturbance such as fire. The results show that dDI is less affected by soil brightness and corresponds to the absolute measures of greenness loss irrespective of varying canopy cover. dDI allows for the effects of soil brightness to be mitigated with a scaling factor to reduce its overall contribution to the resulting index, and the applied factor (0.5) shows good results for the heterogenous soils and landscapes of Kangaroo Island. While others have successfully applied the normalised version of DI (Axel, 2018, Healey et al., 2005, Baumann et al., 2014, DeRose et al., 2011, Huang et al., 2020, Liu et al., 2018, Masek et al., 2008, Pickell et al., 2015, Healey et al., 2006), the prerequisite information of representative pixel values of target landscapes for normalisation limits its broadscale application. The dDI presented here is a direct pixel to pixel comparison, requiring no region-specific adjusted thresholds or mean values for normalisation. The index output of dDI denotes the magnitude of change between two dates, with the highest index values indicating a complete consumption of canopy and removal of vegetation. The three outputs from the Tasseled Cap Transform; TCB, TCG, and TCW represent the three surface components of brightness, greenness and wetness. The linear combination of these three surface components models the vegetation stand replacing nature of severe fires by an increase in brightness and non-vegetation reflectance and decreases in greenness and wetness or spectra associated with vegetation's reflectance. dDI incorporates all spectral information transformed with TCT coefficients within satellite imagery, harnessing the benefits of the enlarged spectrum from SWIR, NIR and RGB bands. Combined, SWIR and NIR bands are sensitive to the characteristic effects of fires showing changes in forest structure, soils, and moisture content (Veraverbeke et al., 2012) and the variations in greenness or chlorophyl from the NIR (Tran et al., 2018, Massetti et al., 2019). The RGB regions of the EM contains often discarded data showing the effects of disturbances which can be helpful for Mediterranean or semi-arid to arid environments or areas with lower NIR reflectance, illustrated in pre- and post-disturbance comparisons of true colour imagery.

Certain limitations of dDI have been shown by the methods and results of this work. These are reviewed below with suggested areas for improvement resulting from uncertainty around TCT coefficients, large spectral changes resulting from non-disturbance (land use) changes, and the decreasing severity index value as a result of discontinuous canopy coverage.

As reviewed in section 2.3, TCT coefficients have not been published for atmospherically corrected S2 imagery, and Landsat's surface reflectance coefficients (Crist,

1985) does not cover all S2 bands. While certain authors have used at-sensor derived coefficients on surface reflectance S2 imagery (Wang et al., 2020, Brandolini et al., 2020, Valenti et al., 2020, Tridawati et al., 2020, Li et al., 2021), in a multi-temporal change application the ever-changing effects of atmosphere will result in inconsistent indices of brightness, greenness and wetness that are directly a result of fluctuating atmospheric conditions. Although the exact effects onto index values such as dDI are not fully understood, Crist and Cicone (1984) suggests that changing atmospheric conditions will alter subsequent results derived from TCT indices. The development of coefficients for all S2 (level-2a) bands will improve the consistency of spectral information derived from combinations of TCT indices such as dDI and ensure its fidelity when compared to other sensor's surface reflectance products in a time series.

The high-resolution aerial imagery used in this work (<.4 m), quantifies the spectral differences between burnt and unburnt pixels and provides an estimation of the absolute greenness and canopy loss following fire. Due to its 2D resolution, it is unable to provide a detailed estimate of vegetation structural changes or net amounts of biomass loss which would improve severity estimates. Additionally, in regions that have experienced large spectral changes resulting from shifts in land use (Figure 5A), dDI values suggest a disturbance due to the large spectral difference between dates. Indices of change to vegetation from passive optical sensors, such as Sentinel 2, are derived from changes in the spectral reflectance of pixels and measure differences in object chemistry before and after a fire. However, changes observed in near simultaneously acquired SAR imagery, particularly in cross-polarized backscatter, indicate changes to object structure resultant of fire (Addison and Oommen, 2018, Tanase et al., 2015, Ban et al., 2020). Thus, it is likely that a combination of indices such as dDI with differences in calibrated cross polarized backscatter from sensors such as Sentinel 1, NovaSAR1 and the future NISAR are likely to improve an understanding of the impact of fire on natural landscapes like those in coastal dunes. The addition of simultaneous texture information could greatly increase the ability of severity estimates in areas with sparse canopies and reduce the effect of decreasing pre-fire canopy coverage and post-fire severity estimates as shown in figure 9 and section 3.3. Additional datasets such as the fractional cover products from Digital Earth Australia (DEA) (Gill et al., 2016) could be used to adjust or scale severity indices according to the pixel's percentage of pre-fire exposed soils, improving severity estimates in areas with sparse vegetation cover. Fractional cover is derived from endmembers of representative pixels and spectral unmixing, deriving percent per pixel of bare ground, green vegetation and woody biomass (Guerschman et al., 2015). If sufficiently validated and calibrated, there is significant potential to implement a fire severity mapping method that measures the severity of a fire as a result of its spectral and textural changes and leverages the vast datasets and processing capabilities available through initiatives such as DEA's Open Data Cube (ODC) (Lucas et al., 2019, Ticehurst et al., 2019).

The suitability of fire severity indices are often evaluated by comparisons to local observations of the CBI (Parks et al., 2014, Chen et al., 2011, Key and Benson, 2005, Tran et al., 2018, French et al., 2008), a linear combination of up to 23 *in-situ* factors of which the effects of soils is only one component (Miller and Thode, 2007). Further investigation of the suitability of satellite derived spectral indices to varied landscapes requires studies to validate and calibrate their accuracy and precision for diverse vegetation communities and soil variability. The inclusion of structural estimates from active sensors on airborne platforms could provide high-resolution validation datasets for diverse calibration sites and reduce the inherent subjectivity of conventional *in-situ* burn severity estimates. Research has shown that active sensors on airborne platforms, either in the form of airborne LIDAR (Hillman et al., 2021) or airborne synthetic aperture radar (SAR) (Hinkley and Zajkowski, 2011), can significantly increase the understanding of structural and 3D changes as a result of fire. Within diverse and representative calibration sites, these sensors could assess net structural changes caused by fire and improve the accuracy of space-based fire severity estimates in heterogenous environments.

Coastal dunes are dynamic and resilient systems that are continually adjusting to disturbances and extreme events (Hesp and Martínez, 2007). The stratigraphy-based research suggesting dune destabilisations after fires (Boyd, 2010, Cordova et al., 2019, Filion, 1984, Filion, 2017, Filion et al., 1991, Mann et al., 2002, Matthews and Seppälä, 2013, Rich et al., 2015, Seppälä, 1995, Tolksdorf et al., 2013) has not been confirmed by contemporary observations (Shumack et al., 2017, Shumack and Hesse, 2018, Barchyn and Hugenholtz, 2013), but the consequences of increasing frequency (Bonney et al., 2020) and severity (Tran et al., 2020a) of fires may result in altered landscape morphology and dominant vegetation communities (Bennett et al., 2016). Specific to Kangaroo Island, the highly fire-adapted vegetation community is likely a result of the evolution in its fire regime since colonisation. The pre-European fire regime of Kangaroo Island is thought to be driven by dry lightning strokes characterised by infrequent but severe fires (Northcote, 2002), as the archaeological record indicates the island was uninhabited by humans for at least 400 years (Robinson et al., 1999, Lampert, 1981) with others suggesting closer to 2500 years BP (Draper, 2015). Bauer (1959) suggests that fire intensity and frequency was dramatically scaled up after European colonisation to facilitate land clearance and that non-developed areas of the island may be a modern artifact reflecting a shift in fire regimes. The implications of this suggest that the island's vegetated areas may be less susceptible to landscape destabilisation from fires as the vegetation communities are highly adapted to frequent and severe fire.

2.5 Conclusions

This paper provides a new application of a temporally differenced Disturbance Index (dDI) based on the Tasseled Cap Transformation (TCT) features of brightness, greenness and wetness, which improves burn severity measurements for heterogeneous environments. Satellite derived fire severity indices are compared to high resolution multi-spectral aerial imagery to show the relationship between loss of greenness and canopy consumption and fire severity in representative dune sites across Kangaroo Island. dDI calculates, at the pixel level, the transformed spectral difference between two image dates and quantifies severity within burnt areas. Comparisons to both versions of the Normalised Burn Ratio (NBR) indicate that dDI is less affected by soil brightness at local and regional scales, and therefore is able to detect and measure high burn severity in dunes on Kangaroo Island.

Fire severity is suggested to be one possible trigger for landscape instability and a possible initiation mechanism for transgressive dune phases, but coastal dune landscapes have characteristics that display the precise limitations of the conventional NBR derived indices: heterogeneity, discontinuous canopies, and bright soils.

It is unclear as to what effect the widespread use of NBR based severity estimates influence the responses of Governments or decision makers for recovery and fuel load management decisions. If resource allocation or response plans are shaped by broadly applied uncalibrated fire severity thresholds, then there is a significant risk of under-assessing areas that have experienced a high severity fire.

Improving the estimations of fire severity in coastal dune and other heterogenous systems will better illustrate the true effects of fires in these landscapes and aid in studies of their subsequent recovery or destabilisation.

CHAPTER 3.

Accepted article, DaSilva, M. D. (80%), Bruce, D. (5%), Hesp, P. A. (10%), Miot da Silva, G. (5%), & Downes, J. 2023. Post-wildfire coastal dunefield response using photogrammetry and satellite indices. Earth Surface Processes and Landforms, 1-24.

Statement of co-authorship - I lead the research design of this manuscript in this chapter. I was mentored and aided by my supervisors from the conceptualisation through to realisation. I received field assistance on the 6 multi-day field trips for the data collected for this manuscript from my co-authors but personally led all research field excursions. All text, figures, analysis, and final editorial changes were ultimately my decision after consulting with my PhD committee.

Post-Wildfire Coastal Dunefield Response using Photogrammetry and Satellite Indices

Abstract

Fire has been suggested to be an initiation mechanism of landscape instability and coastal dune transgression, but modern evidence showing a shift to a transgressive dune phase is lacking. Following the largest wildfire in historical records on Kangaroo Island, South Australia, bimonthly Uncrewed Aerial Vehicle (UAV) surveys were conducted on three coastal dune sites to study their post-fire responses. The three sites studied here represent the landscape diversity of the temperate dunes of Kangaroo Island with both active coastal and inland relict stabilised dune fields studied. UAV surveys were used to reconstruct landscapes with Structure from Motion (SfM) photogrammetry and compared over time to illustrate significant changes in the landscape. The geomorphic and vegetation changes are compared in net and intra-survey comparisons to illustrate the post-fire dunefield response and trends toward stabilisation. Due to a lack of reliable baseline pre-fire data, satellite geomedians are used to compute spectral indices to show the trajectory of ground cover in the study sites in the years preceding and following the fire. Satellite indices are used to

separate 3D changes according to ground cover types and show their differing post-fire responses. Local and regional wind, temperature and rainfall records are presented to provide weather patterns of the years preceding and following the fire, illustrating the wet and mild post-fire weather. The overall results indicate no significant landscape instability across the studied sites and that the ground cover of vegetation is nearing pre-fire baselines, showing that a severe fire has not caused a transgressive dunefield to develop.

3.1 Introduction

Coastal dunes evolve as a result of gradual or abrupt changes in environmental conditions and as a response to episodic disturbances (Hesp and Martínez, 2007). Disturbances are a key driver of aeolian erosion and landscape destabilisation as they remove or destroy stabilising vegetation and microbial soil crusts (Ravi et al., 2011) as well as decrease the threshold velocity for wind erosion (Ravi et al., 2009). The transition of coastal dunes from stabilised systems to fully active transgressive dunefields has been observed in some cases (Hesp, 2013) and is a continuing area of study (Hilgendorf et al., 2022, Fisher et al., 2021, Gao et al., 2020, Hesp and Walker, 2021). Fire has been suggested to be an initiator of a transgressive dune phase when paired with extreme weather or periods of atypical climate or climate change (Matthews and Seppälä, 2013, Filion, 1984, Filion et al., 1991). The research suggesting significant dune reactivations and transgressive dune phases following fire are largely based on observations of stratigraphic data from dunes in North America and Europe (Boyd, 2010, Filion, 1984, Filion, 2017, Kotilainen, 2004, Seppälä, 1995, Tolksdorf et al., 2013) although contemporary studies of post-fire coastal dunes have not observed significant morphological changes or shifts in their stability (Vermeire et al., 2005, Ward, 2006, Myerscough and Clarke, 2007, Shumack and Hesse, 2018, Shumack et al., 2017, Levin et al., 2012). Some works have shown short-term increases in aeolian activity after fires in continental dunefields, particularly in semi-arid grasslands or sagebrush steppes (Stout, 2012b, Sankey et al., 2012, Sankey et al., 2010, Sankey et al., 2009a), and in arid deserts (Thomas and Leason, 2005, Wiggs et al., 1995, Ash and Wasson, 1983, Wasson and Nanninga, 1986, Fisher and Hesse, 2019).

While many vegetation communities benefit from fires (Keeley, 1995), shifts in fire regimes (frequency and severity) may lead to disruptions in vegetation diversity (Wright and Clarke, 2007) or landscape stability (Barchyn and Hugenholtz, 2013). Fires are a common and natural occurrence across the world, including most of the Australian continent (Levin et al., 2021) but climate change is driving shifts in weather patterns and aridity which may exacerbate fires and their effects on the landscape (Van Oldenborgh et al., 2021). With the forecast of a warmer climate that is conducive to more frequent and severe fires, it is unclear as to what extent previously stabilised and semi-stabilised dunefields may be reactivated or altered, especially in temperate climates. Further study is necessary to show how these complex natural environments respond in the short- to medium-term following disturbance by fire.

Uncrewed aerial vehicles (UAVs) are used in many disciplines across the physical sciences (Anderson et al., 2019), and in coastal dune research (Walker et al., 2023, Hilgendorf et al., 2021). Geomorphic studies use UAV platforms and spatial data to produce 2D and 3D datasets to track landform, topographic or ground cover changes over time (Gonçalves and Henriques, 2015, Shumack et al., 2022). UAVs have been used to survey post-fires landscapes, deploying after a fire to observe the extent of burnt areas and monitor post-fire processes (Fernández-Guisuraga et al., 2018, Ellett et al., 2019). UAVs equipped with imaging cameras can be used to systematically capture overlapping images and construct 3D models of landscapes using the tenets of Structure from Motion (SfM) photogrammetry (Fonstad et al., 2013). Ortho-images and point clouds can be generated with varying resolution, precision, and accuracy, depending on the methods and hardware used (G. Poley and J. McDermid, 2020). Certain steps in respect to camera calibration and flight design (Luo et al., 2020, Nesbit and Hugenholtz, 2019, Sanz-Ablanedo et al., 2020) tied with spatial location data ensure accurate and repeatable surveys (James et al., 2019, James et al., 2017a). Spatial data is used for georeferencing, often collected with high accuracy Real Time Kinematic/Extended Global Navigation Satellite Systems (RTK/X-GNSS) and used as ground control or check control points (GCP and CCP). GCPs ensure robust geometry for the model, while CCPs provide an independent assessment of accuracy (James et al., 2017a).

The expected resolution limit for confidently detecting change from surface differencing is the level of detection (LoD), which is determined from estimated error, both systematic and random (James et al., 2017b). Research methods and sensors must account for their expected LoD to definitively show significant changes. 2D surface differencing from Digital Elevation Models (DEM) is limited in topographically complex landscapes with high relief, overhanging areas and/or surfaces with significant roughness such as vegetation (Lague et al., 2013). 3D point clouds can be used to measure change along axes unique to the surface normal, therefore preserving the local shape, texture and complexity (Williams et al., 2021). Lague et al. (2013) developed the Multiscale Model to Model Cloud Comparison (M3C2) algorithm that computes the difference between point clouds in the horizontal (X and Y) and vertical (Z) directions. M3C2 uses a vector orthogonal to the surface and calculates the difference between the mean position of points of each cloud and has been used extensively in geomorphic studies (Williams et al., 2021). James et al. (2017b) further improved M3C2 by estimating the spatially variant error from photogrammetric and georeferencing uncertainties to generate precision maps (M3C2-PM) to vary the levels of detection across the point clouds.

In this study, post-fire coastal dunefield response was explored using 3D datasets from *in-situ* surveys and 2D spectral changes from satellite images. The *in-situ* UAV surveys were conducted across 3 representative dune types to capture landscape level dynamics and describe them in relation to their local topography in the year following a severe wildfire.

Significant changes are described according to the drone surveys hardware and method's respective error (LoDs) by quantifying changes in derived point clouds. Similar to recent studies (Konlechner and Hilton, 2022, Walker et al., 2023, Hilgendorf et al., 2021, Hilgendorf et al., 2022), both vegetation and surfaces changes are of research interest as they show the post-fire ecogeomorphic response of landscapes and indicate stability, dynamism, or transgression. Satellite indices are used to separate landcover types and to assess the 3D changes between pre-fire sandy active areas, and regions that were burnt or unburnt. For a pre-fire temporal context, satellite imagery is used to calculate pixel-based geomedian images (Roberts et al., 2017) for a time-series analysis to illustrate changes in ground cover. Three separate spectral indices are computed for the years preceding and following the fire to show the post-fire spectral response.

The 2019–2020 Australian wildfire season burned thousands of hectares across Australia (Levin et al., 2021), with a significant portion of South Australia's Kangaroo Island's (KI) coastal dune systems severely affected. The Black Summer wildfires on KI were the largest fires according to contemporary records that also show an increase in recent fire frequency (Bonney et al., 2020). The broader aim of this paper is to test whether a severe fire has triggered any significant landscape instability or a shift to a transgressive dune phase in temperate South Australian dunefields. Although this study focuses on local coastal dune changes, it provides insights into the resiliency of landscapes to wildfire events and explores the short-term changes following a disturbance that has been suggested to initiate landscape instability and dunefield transgression.

3.2 Study Sites

This study focuses on three coastal dune sites on the southern coast of KI which burned in the Black Summer wildfires (Figure 1) from December 2019 to January 2020. These are chosen to represent the landscape diversity of temperate dunes on Kangaroo Island, including both active coastal and inland relict dunes. Sites are named according to their relative location on the island; Maupertuis Bay is Site A; Hanson Bay is Site B and Snake Lagoon is Site C (Table 1) and described in following sections.

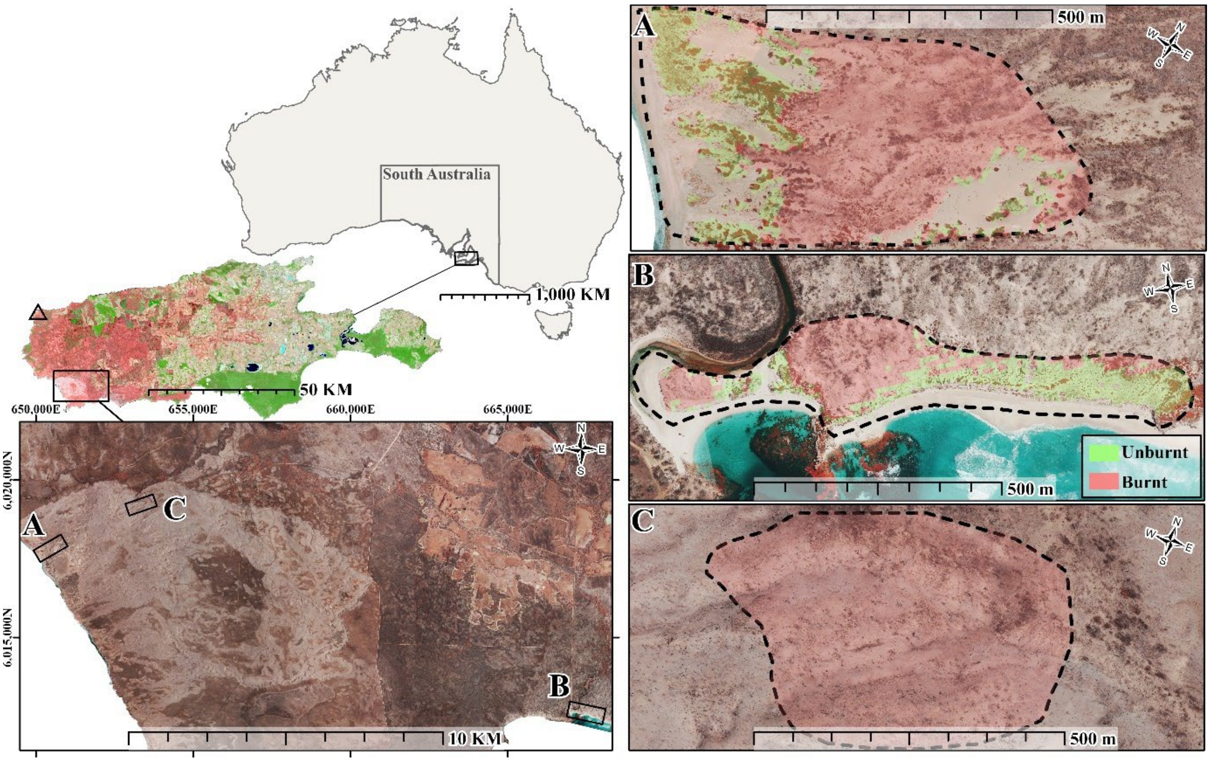

Figure 3-1– Sites of analysis for this study on the dunefields of Kangaroo Island (KI). Sentinel 2 (S2) satellite image from January 30, 2020, shows KI in the bands 12, 8 and 4 highlighting regions burnt in the 2019/20 Black Summer wildfires. Black triangle in Northwest corner of satellite image indicates location of Cape Borda weather station. Inset maps of A, B and C show the extent of drone surveys in the dotted lines, with near-transparent overlays of burnt, unburnt and sand classifications (S2) as explained further in the methods. Survey sites bounding box locations included in Table 9 in the supplementary data.

Table 3-1 - descriptions of dune sites, showing their site name and labels in this study, their state of stability before the fire, a description of the dominant landscape features and area.

Site Name	State	Description	Area (Hectares)
A – Maupertuis Bay	Active	Foredune blowout complex backed by active parabolic dunes	26
B – Hanson Bay	Active	Foredune blowout complex backed by stabilised parabolic dunes	15
		Relict parabolic dune ridges	

C – Snake Lagoon	Stable	17

3.2.1 Geography and Climate

In all three sites, and along the southern coast of KI, indurated Pleistocene aeolian calcarenite is overlain by Holocene aged unconsolidated sands (Bourman, 2016). Study sites are located amongst complex transgressive and parabolic dunefields that, pre-fire, were mostly stabilised by vegetation, but contain active areas closer to the coast (Short and Fotheringham, 1986). Sediments are predominately sands, fine to medium grained and carbonate rich.

The vegetation in the dune sites is highly heterogenous and patterned based on its relative exposure to aeolian and coastal forces. Vegetation surveys were conducted throughout this study during site visits, with dominant vegetation species noted in Table 2 for each site. Exposed regions of the coastal sites (A and B) were dominated by rhizomatous grasses (*Spinifex longifolius*) and invasives (*Euphorbia paralias* and *Thinopyrum junceiforme)* with predominantly woody varieties from the *Acacia*, *Melaleuca,* and *Eucalyptus* genus in the stabilised or sheltered regions (Table 2). The in-land site C was characterised by the epicormic re-growth of dense mallee Eucalyptus species (plants with multiple stems from an underground lignotuber) within relatively low-lying regions as described in later sections. See Northcote (2002) for additional descriptions of vegetation communities pre-fire.

Table 3-2 – ***Presence of vegetation species according to vegetation surveys conducted during this study. Species included here were considered to be dominant in-field surveys. Both Natives and Invasives are shown according to their presence in sites A, B and C (Table 1).***

Natives	**A**	**B**	**C**
Acacia longifolia	x	x	
Acacia uncifolia	x	x	x
Actites megalo carpus	x	x	
Adriana quadripartia			x
Carpobrotus rossii	x	x	

Dianella brevicaulis		x	
Eucalyptus albopurpurea			x
Eucalyptus diversifolia	x		x
Eucalyptus rugosa			x
Ficinia nodosa	x	x	
Haloragis eichleri			x
Helichrysum leucopsideum	x	x	
Ixodia achillaeoides		x	
Leucopogan parviflorus	x		
Melaleuca lanceolata	x	x	x
Muehlenbeckia adpressa	x	x	x
Myoporum insulare	x	x	
Olearia axillaris		x	
Orthrosanthus multiflorus			x
Pelargonium littorale			x
Poa poiformis		x	
Scaevola crassifolia	x		x
Spinifex longifolius	x	x	
Swainsonia lessertifolia		x	
Tetragonia implexicoma		x	
Invasives			
Cakile maritima	x	x	
Euphorbia paralias	x	x	
Thinopyrum Junceiforme	x	x	

Weather information was sourced from several locations due to inconsistent long-term records and destruction following the fire. For the study period, local wind data was sourced from a permanent weather station, installed in December of 2020 at Maupertuis Bay, with additional wind observations sourced from the station at Cape Borda which is maintained by the Bureau of Meteorology (BoM, see location in Figure 1). Monthly mean temperature and rainfall (1960-2019) were sourced from the BoM's datasets from Cape Borda and Flinders Chase at Rocky River, respectively. These monthly means were compared to the observation data at Cape Borda (2019-2021) and modelled rainfall monthly totals from interpolated rainfall gauge data (Beutel et al., 2019) across the UAV survey regions. Wind and weather patterns are influenced by the island's proximity to the Southern Ocean and its cold waters (Peace, 2012), with a complex multi-directional wind system (Figure 2).

According to the Koppen-Geiger classification (Beck et al., 2018) the climate is classified Csb, indicating a temperate climate with warm and dry summers with most rain occurring outside of the summer months. Fires are common and occur annually, principally from intentional human initiated burn offs and dry lightning strikes (Peace, 2012). For further information on KI, DaSilva et al. (2021b) provides a review of the island's geography as it relates to fire severity and Bonney et al. (2020) reviews its recent fire history.

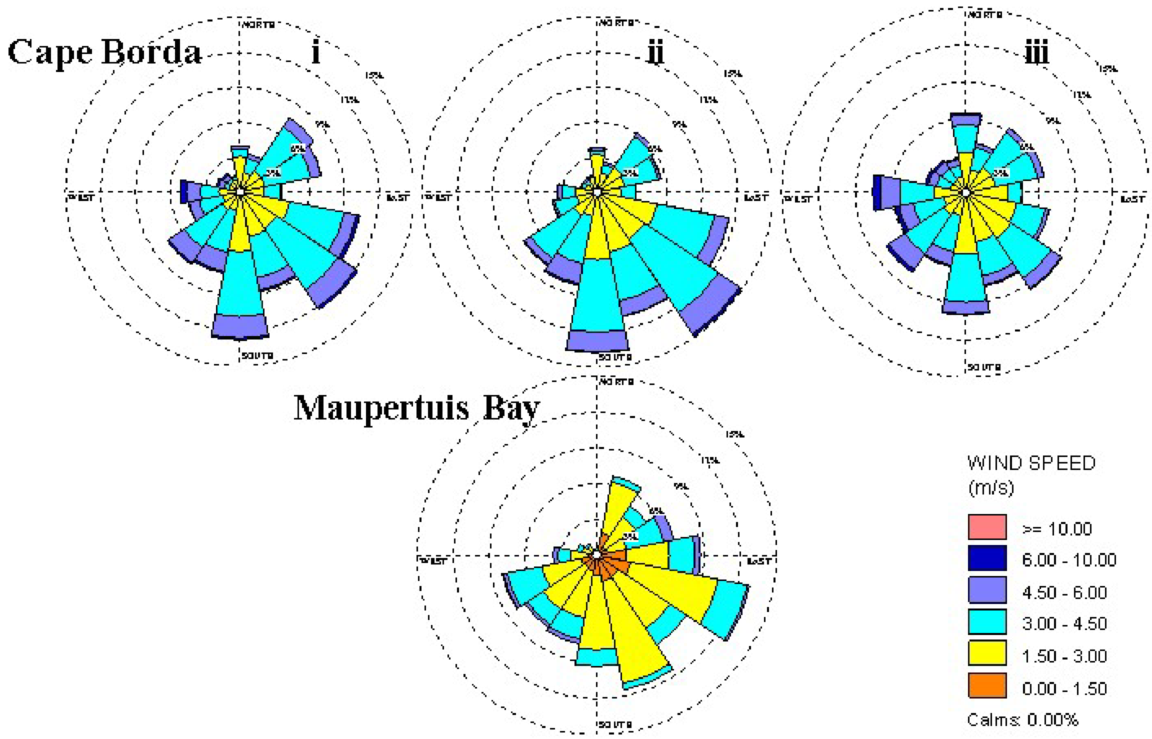

Figure 3-2 - Wind roses for Cape Borda for three time periods: (i) August 2020 to May 2021, (ii) December 2020 to May 2021, and (iii) September 2002 to May 2021 and from a weather station at Maupertuis Bay (December 2020 to May 2021).

3.2.2 Maupertuis Bay - Site A

Site A, located on the southwestern coast of Flinders Chase National Park comprises a foredune-blowout complex backed by an active and vegetated dune complex of parabolic dunes and transgressive dunefield. The foredune portion closest to the waterline, visible in Figures 3 and 4 (grid columns Z and X), were mostly unburnt and reflect pre-fire vegetative cover (Figure 1). Throughout the rest of the site, vegetative cover was highly heterogenous with species presence/absence strongly driven by the degree of exposure. The parabolic dunes, characterised by their trailing ridges and U or V shapes (Figures 3 and 4), have developed according to the multi-directional wind regime (Figure 2). Significant sediment is supplied from a high energy surfzone-near-shore wave environment.

To illustrate the changes that occurred in these sites, landform units are described in representative panels with changes shown between multiple time-series groups. Within Maupertuis Bay, these are shown in Table 3. These five regions are comprised of landforms units on both previously active dunes and stable or accretionary areas (Table 3, Figure 3 & 4). Active dunes are shown by panels A and E, illustrating a foredune-blowout complex, and an active blowout on the crest of a parabolic dune. Pre-fire, panels C and D were fully stabilised illustrating a relatively low elevation sheltered area in a sand plain and a high point on a relict parabolic dune ridge. Panel B shows an accretionary slipface of a parabolic dune, where transgressing sediment accumulates and builds in the predominant wind direction onto the adjacent sand plain.

Table 3-3 – Representative landscape descriptions of units for illustrating net and intra survey changes for Figures 10 and 11.

Landform Panels	Description
A	Active Foredune-Blowout Complex
B	Slipface of parabolic dune, sand plain
C	Sand Plain
D	Dune Ridge
E	Blowout on Parabolic Dune Crest

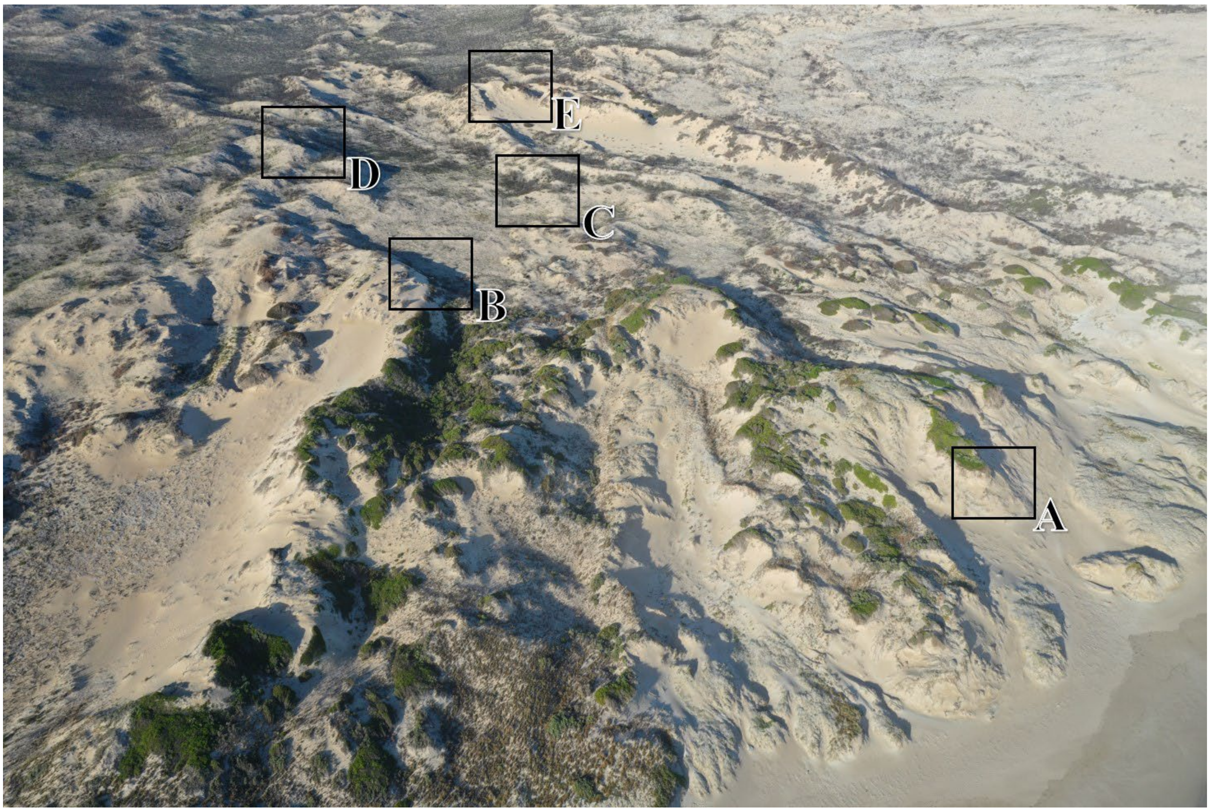

Figure 3-3 - Photograph of site A, Maupertuis Bay in August 2020. Approximate location and orientation of photo is shown below in Figure 4 with photo icon in top left. A-E extent indicators are drawn to show landform units of dunefields from Table 3 and explored in Figure 4 and subsequent results sections.

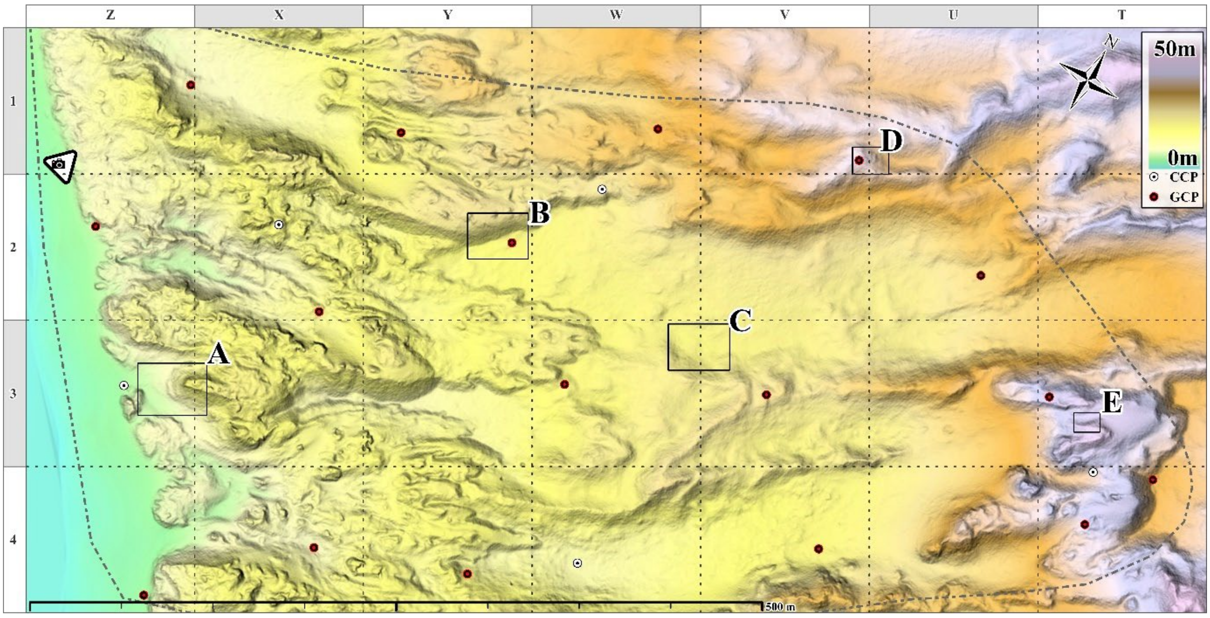

Figure 3-4 – Coloured shaded relief map of site A at Maupertuis Bay on Kangaroo Island. Elevations for digital ground model are sourced from May 2020 Lidar and resampled to 1 m. Dotted outline shows extent of change analysis done from UAV surveys, with locations of Ground Control Points (GCPs) shown in red and the Check Control Points (CCPs) shown in

white. Photo point of Figure 3 shown at grid location (1/Z) in top left. A-E extent indicators are described in Table 3, shown in Figure 3 and subsequent result Figures.

3.2.3 Hanson Bay - Site B

Site B, located on the southern coast of KI (Figure 1) at Hanson Bay comprises a foredune-blowout complex backed by a stabilised or relict parabolic dune and transgressive dunefield complex pre-fire. Most of the site was burnt including parts of the highly dynamic foredune shown in Figure 5 and through the grid row 2 of Figure 6. Pre-fire vegetation cover reflected the high exposure at the site, with areas immediately landward of the foredune largely scarified.

Landform units of Hanson Bay are shown in Table 4. These five regions are comprised of landform units on both previously active dunes and stable sheltered areas (Table 4, Figures 5 & 6). Active dunes are shown by panels A, B and D, illustrating a foredune near the intermittent mouth of an estuary, a blowout cutting across the estuarine barrier, and a foredune-blowout complex. Pre-fire, panels C and E were semi-stabilised illustrating a dune ridge within a relatively sheltered sand plain and a higher dune ridge behind the primary foredune-blowout complex.

Table 3-4 - Representative landscape descriptions of units A-E for illustrating net and intra survey changes for Figures 13 and 14.

Landform Panels	Description
A	Foredune
B	Blowout
C	Dune Ridge, Sand Plain
D	Foredune-Blowout Complex
E	Dune Ridge

Figure 3-5 - Photograph taken of site B, Hanson Bay in August of 2020. Approximate location and orientation of photo is shown below in Figure 6 in photo icon in bottom left. A-E extent indicators are drawn to show landform units of dunefields from Table 4 and explored in Figure 6 and subsequent results sections.

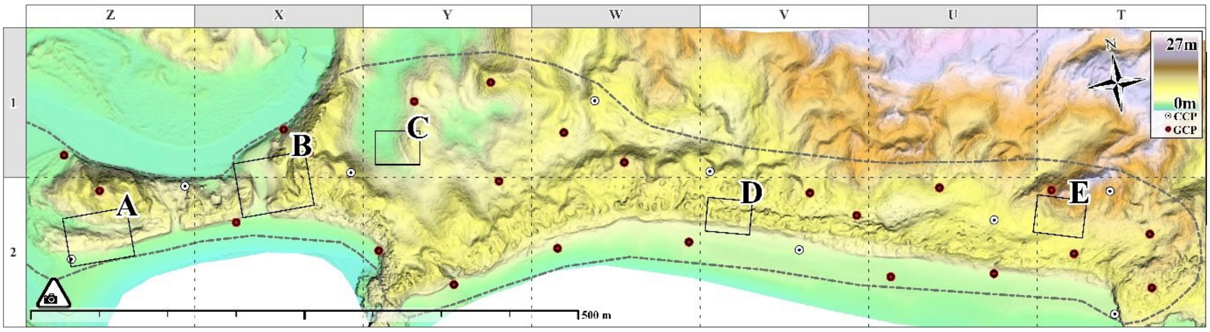

Figure 3-6 - Coloured shaded relief map of site B at Hanson Bay. Elevations for digital ground model are sourced from May 2020 Lidar and resampled to 1 m. Dotted outline shows extent of change analysis done using UAV surveys, with locations of Ground Control Points (GCPs) shown in red and the Check Control Points (CCPs) shown in white. Photo point of Figure 5 shown at grid location (2/Z) in bottom left. A-E extent indicators are described in Table 4, shown Figure 5 and subsequent result Figures.

3.2.4 Snake Lagoon - Site C

Site C is located ~7 km inland from Maupertuis Bay in Flinders Chase National Park (Figure 1). It is located within the Gantheaume Dunes formation (Northcote, 2002), with the study site covering a Holocene stabilised relict parabolic dune (Figures 7 and 8). Pre-fire vegetation was characterised as dense mallee Eucalyptus, with differential vegetation cover according to the relative location within the landscape.

The representative landform units of Snake Lagoon are shown in Table 5 and Figures 7 and 8. The units are chosen to represent the topographic variability within the site, with relatively high and low-lying regions. Dune ridge sites are explored with panels B and D and show the response of the relative high points within this study area. Low-lying areas are shown with panels A, C, and E representing relatively sheltered areas of accumulation characterised by increased moisture, humus, and organic surface deposits and generally different vegetation community than adjacent higher areas (Barrineau et al., 2015). Additionally, panels A and D show North and South facing slopes which have been shown to have differential regrowth patterns in post-fire dune landscapes (Cowling and Pierce, 1988, Vestergaard and Hastings, 2001).

Table 3-5 - Representative landscape descriptions of units for illustrating net and intra survey changes for Figures 14 and 15.

Landform Panel	Description
A	Bottom of Parabolic Dune Slope (North Facing)
B	Parabolic Dune Ridge
C	Sand Plain
D	Parabolic Dune Ridge (South Facing)
E	Inter-dune swale

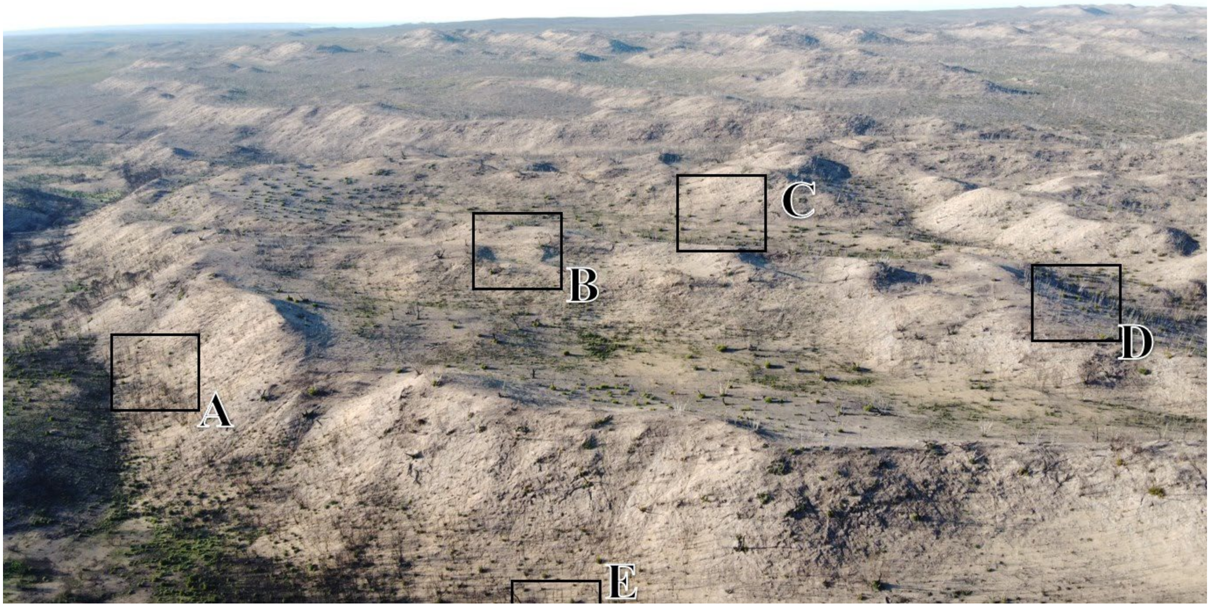

Figure 3-7 - Photograph taken of site C, Snake Lagoon in August of 2020. Approximate location and orientation of photo is shown below in Figure 8 in photo icon in top left. A-E extent indicators are drawn to show landform units of dunefields from Table 5 and explored in Figure 8 and subsequent results sections.

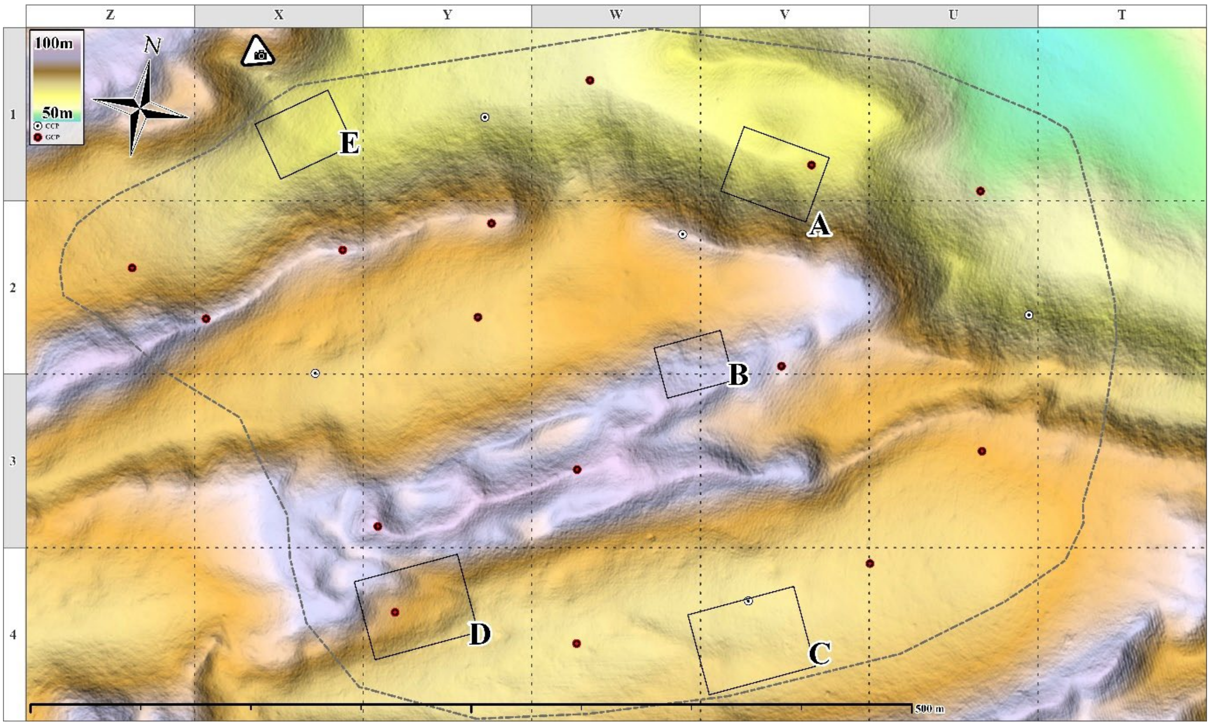

Figure 3-8 – Coloured shaded relief map of site C at Snake Lagoon. Elevations for digital ground model are sourced from May 2020 Lidar and resampled to 1 m. Dotted outline shows extent of change analysis done from UAV surveys, with locations of Ground Control Points (GCPs) shown in red and the Check Control Points (CCPs) shown in white. Photo point of Figure 7 shown at grid location (1/X) in top left. A-E extent indicators are described in Table 5, shown Figure 7 and subsequent result Figures.

3.3 Methods

3.3.1 Structure From Motion Methods

The SfM methods workflow is presented in Figure 9, with detailed parameters of individual surveys (Table 6) and processing in Tables 7 and 8. The software used was Agisoft Metashape v. 1.8.4 (MS), CloudCompare v. 2.13 (CC) and ArcGIS Pro v. 3.0. Metashape processing workflow follows guidelines from Over et al. (2021) with error metric reporting according to James et al. (2019).

3.3.1.1 Flight Design and Spatial Data Acquisition

UAV flight surveys were designed to cover the three sites (Table 1) with specific flight information presented in Table 6. Variations in photos, control, and weather conditions reflect the uncontrolled dynamic field conditions in remote locations. A DJI Mavic 2 Pro was used for all flights, equipped with a 3 band (RGB) Hasselblad camera. The camera has a 1” CMOS sensor with 20 Megapixels (MPs), 28 mm (35 mm format equivalent) focal length (FL) and uses an electronic (rolling) shutter. DJI Ground Station Pro was used for flight design and operations, with the sensor collecting images using automatic ISO and focus settings and saving in JPEG format. In one August (Site C) survey, some images were collected with a Mavic 2 Enterprise (1/2.3" CMOS, 12 MPs, 24mm, 35 mm equivalent, FL) as noted in Table 6.

UAV image collection consisted of multiple flight lines at 50 metres above flight location in a crosshatch pattern with nadir and off-nadir (70 degree) imagery using a hover and capture flight mode. Multiple mission start locations within each site were utilised, to maintain line of site of the UAV and to ensure that the starting flying height above ground was maintained. Site C’s take-off location was centrally located within the study, next to the GCP in Figure 8 (grid 2/Y), which resulted in reduced photo overlap on the surrounding higher points. The effects of the reduction in photo overlap will be discussed in further sections. Forward and lateral overlap of missions was set to a minimum of 75/60 respectively, with two orthogonal blocks forming a double grid. Variable image totals between surveys (Table 6) are attributed to dynamic survey conditions and shifting target areas which were ultimately extracted to coverage according to spread of ground control. Local lighting conditions are summarised, and average wind speed sourced from nearest operating weather station as described in Table 6.

The location of Ground Control (GCPs) and Check Points (CCPs) was generally standardised across surveys (Figures 4, 6 and 8), exact locations are provided in the supplementary data. Spatial data was collected with a Trimble RTX-GNSS in the Geodetic Datum of Australia (GDA94) within UTM zone 53S and Australian Height Datum using AusGeoid09. Estimates of precision for GNSS points were generated from Trimble Business Center and used for individual GCP and CCP precision.

Table 3-6 - Information on surveys flown over site A, B and C (Figure 1). Showing the survey date, total number of images acquired (†Indicates 525 images from Mavic 2 Enterprise.), total number of Ground Control, and independent Check Points (in Bold). Ambient conditions during survey reported as Lighting and the average wind speed during survey time from local weather station at Maupertuis Bay where available and closest weather stations where available. ‡Indicates wind record sourced from Stenhouse Bay, SA. §, Indicates wind records sourced from Cape Borda.

Site	Date	Images	GCP|CCP	Lighting	Wind (m/s)
A	28/08/20	1951	17|5	Mostly Sunny	*8.4‡*
	13/10/20	1926	16|6	Mostly Sunny	*8.3§*
	08/12/20	1942	16|5	Sunny	8.4
	13/02/21	2137	18|4	Mostly Overcast	6.9
	03/05/21	2333	17|5	Mostly Overcast	9.6
B	31/08/20	1444	24|9	Mostly Overcast	*4.5‡*
	12/10/20	1605	22|9	Sunny	*14.9 §*
	09/12/20	1525	21|8	Sunny	9.5
	15/02/21	2020	22|9	Mostly Sunny	16.2
	02/05/21	1800	22|8	Mostly Sunny	11.9
C	31/08/20	1192 †	15|4	Mostly Overcast	*5.2†*
	14/10/20	1400	15|4	Overcast	*28.5 §*
	09/12/20	1492	15|4	Sunny	6.8
	14/02/21	1930	15|5	Mostly Overcast	8.6
	04/05/21	1706	15|5	Overcast	8.8

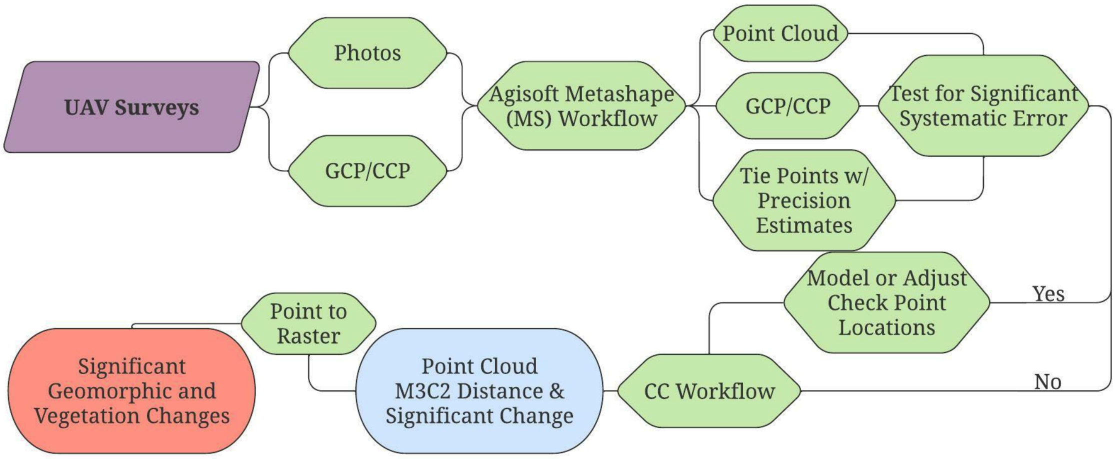

Figure 3-9 – ***Illustration of the workflow used in this study. The details of the subsections MS workflow and CC workflow are presented Tables 7 and 8.***

3.3.1.2 Structure from Motion Processing

Surveys were processed in Metashape with uniform processing parameters (Table 7). Georeferencing was prioritised on control points in images where targets were centrally located to reduce edge distortions. There is uncertainty on the optimal camera calibration corrections for SfM surveys processed in Metashape due to variations in sensor capabilities and pre-processing of JPEGs for geometric adjustments (Cooper et al., 2021, Gonçalves et al., 2021, Bertin et al., 2022, Senn et al., 2022). Camera optimisation parameters or internal orientation parameters (Table 7) were chosen after extensive testing and according to works using a similar sensor (Cooper et al., 2021, Zhou et al., 2020).

Table 3-7 - Outline of workflow and processing parameters for Agisoft Metashape (MS 1.8.4) with internal Orientation Parameters (IOP).

MS Workflow	Parameters	Values
Align Photos	Accuracy	Medium
	Generic Preselection	Source
	Key/Tie Points Limit	60,000/10,000
	Rolling Shutter Compensation	True
	Adaptive Camera Model Fitting	False

Gradual Selection	Reconstruction Uncertainty	10
	Projection Accuracy	5
	Reprojection Error	0.4
Camera Alignment	IOP (f, cx, cy, k1, k2, k3)	True
	Rolling Shutter XYZ	True
	Adaptive Model Fitting	False
	Image Quality	>0.7
	UAV GNSS Measurements	Disabled
Build Dense Cloud	Quality	High
	Depth Filtering	Mild
Export Data	Reference Data	GCP/CCP
	Point Cloud	Dense Cloud
	Precision Coordinates	Sparse Cloud

3.3.1.3 Structure From Motion Error

Clear and comprehensive error reporting shows the significance of observations with respect to the limits of spatial resolution and precision of the sensors and methods used. Following the guidelines of James et al. (2019), the error metrics in this work were designed to illustrate both the inherent systematic (bias) and random errors present in this work. Care was taken to conservatively interpret significant changes between surveys due to uncertainties arising from the methods used, as discussed in further sections.

Measurements of accuracy are from Metashape's total error, which includes individual RTX point precisions, and generated from the distance between control/check and its resulting modelled position in space giving the Root Mean Square Error (RMSE).

Precision estimates were generated from bundle block uncertainties across the surveys, exported with tie-points from Metashape and doubled as suggested by James et al. (2020). These spatially variant precision estimates were interpolated to point clouds in CC and used as X, Y, and Z Precision Maps (PM) within the CC workflow (Table 8). M3C2-PM (James et al., 2017b) interprets significant changes between surveys with a confidence interval of 95% ($LoD_{95\%}$) given by

Equation 3-1

$$LOD_{95\%} = \pm 1 \cdot 96(\sqrt{\sigma_{N1}{}^{2} + \sigma_{N2}{}^{2}} + reg\ )$$

where subscripts N1 and N2 denote surveys with error of one sigma (σ) around points that are aligned to corresponding axes (X, Y or Z). In Equation 1, *reg* corresponds to an optional expression that gives absolute spatial registration error. *Reg* was calculated from a combination of check point errors given by

Equation 3-2

$$reg\ = \sqrt{\sigma_{N1}{}^{2} + \sigma_{N2}{}^{2}}$$

where $\sigma_{N1}{}^2$ and $\sigma_{N2}{}^2$ was the total error of X, Y and Z directions of check points (RMSE) from Metashape.

Residual errors from GCPs were tested for systematic error according to James et al. (2020). The dense cloud, reference data and sparse cloud as exported from Metashape were tested in Matlab 2020b. Where significant error was detected through check points, selections of CCPs were adjusted to areas exhibiting errors to adequately reflect realistic error propagation bounds into Equation 2.

3.3.1.4 Structure From Motion Change Detection

To measure significant surface and vegetation changes between surveys the M3C2-PM plugin of CC was used. M3C2 was developed by Lague et al. (2013), to perform a direct change comparison between point clouds, with Precision Maps (PM) added by James et al. (2017b) to assess significant changes according to spatially variant error. M3C2 calculates the distance between point clouds, forming a mean circular surface of a set diameter (D) and computes the change along a cylinder oriented to the normal. For this study, change was measured to the orientation of normals according to a Ground Surface (GS) sourced from an aircraft-based LIDAR Digital Ground Model (DGM) collected in May 2020. The orientation to the GS standardises the axis on which change was detected in the time series analyses and ensures results reflected canopy and surface changes. The airborne LIDAR dataset was sourced from the State Government of South Australia's Department of Environment and Water with the following methods applied as summarised in Table 8. LIDAR ground returns were projected into GDA94 UTM Zone 53S, imported into CC and converted into a 2D Delaunay mesh to form a continuous ground surface. Further in CC, the sample points tool was run with a subsequent subsampling at 5 cm to create a DGM with a uniform point spacing. Normals were computed for the DGM to orient M3C2 to surface changes according to topography.

SfM point clouds were subsampled in CC to 3 cm spacing to reduce computation size and ensure uniform spacing. The D for M3C2 was set to 30 cm with orientations used from the DGM ground surface. M3C2 results were exported to ArcGIS Pro for visualisation and volumetric calculations. To show change between surveys within error thresholds, the following tools were used to extract M3C2 distance; XY table to point, point to raster, and extract by mask to the extent of significant changes.

Table 3-8 - Processing parameters for CloudCompare (2.13)

CC Workflow	Parameters	Values
Ground Surface (GS)	LIDAR Ground Returns	
	2D Delaunay Mesh	
	Sample Points	1,000
	Subsample	0.05
	Calculate Normals	Quadric (0.15) knn (6)
SfM Point Clouds	Subsample	0.03
	Interpolate X, Y, Z PM	knn (6), Median
	M3C2-PM	GS Normals/ D = 0.3

3.3.2 Ground Cover Changes

Satellite derived indices were used to show the baseline spectral values of dune sites, contrast the fire's effects on ground cover, and show the subsequent post-fire response. Geomedians are derived from a stack of multi-temporal images that represent the geometric median value of a pixel. The resulting composite image retains the between band spectral fidelity, reduces the impacts of thin cloud/smoke, and facilitates analyses such as index calculations (Roberts et al., 2017). Cloud-free Sentinel 2 (S2) level 2A, atmospherically corrected, images were aggregated into 4-month geomedians in the Digital Earth Australia (DEA) sandbox to the extent of the UAV surveys for each site (Krause et al., 2021).

Three spectral indices used in fire severity studies were calculated from S2 geomedians and compared in pre- (November 2015 to December-2019) and post-fire groups (January 2020 to May 2022). Indices were chosen due to their widespread application (Chuvieco et al., 2020) and according to related work in burnt coastal dune environments (DaSilva et al., 2021b). The Normalised Burn Ratio (NBR) using bands 8_{842} and 12_{2190} of S2 imagery, given by:

Equation 3-3

$$NBR = \frac{NIR - SWIR}{NIR + SWIR}$$

NBR uses the combination of near infrared (NIR) and shortwave infrared (SWIR) bands as they are sensitive to water content, woody biomass and greenness. The Normalised Difference Vegetation Index (NDVI) using bands 8_{842} and 4_{655} given by:

Equation 3-4

$$NDVI = \frac{NIR - Red}{NIR + Red}$$

NDVI uses the NIR and red bands to estimate greenness and chlorophyl concentrations. The Brightness Adjusted Disturbance Index (BADI) given by:

Equation 3-5

$$BADI = TCG + TCW - 0.5 * TCB$$

where TCG, TCW and TCB are the Tasselled Cap transformed (TCT) products of Greenness, Wetness and Brightness as derived by the linear combination of Landsat surface reflectance (SR) bands (Crist and Cicone, 1984) and used in this analysis for the similar SR S2 bands (2490, 3560, 4665, 8842, 111610, 122190). BADI uses all available spectral information and facilitates landscape specific variables such as soil brightness to be mitigated (DaSilva et al., 2021b).

Geomedian pixels within survey areas were masked to burnt areas according to a differenced NBR (dNBR) threshold of 0.2, calculated by the cloud-free images before and after the fire. Pre-fire minimum and maximum index values were calculated to show the relative range and index trajectory of dunefields as seen from satellite indices.

To analyse the M3C2 changes according to the pre-fire ground-cover types, spectral thresholds were used to separate pixels into three sub-analysis groups: bare sand and burnt or unburnt vegetated surfaces. To segment pre-fire exposed sand areas, an NDVI image was thresholded (0.15) on a cloud-free Sentinel-2 image from 16/12/2020, these areas corresponded to sandy beach regions and pre-fire active sandy areas. This segmented image was then separated according to the dNBR (0.2) mask of burnt and unburnt vegetated surface. Grouped results (Sand, Burnt and Unburnt) are presented according to significant changes, with total pixel area (m2) and volumetric (m3) loss and gain showing the response of the dunefields.

3.4 Results

Results are divided into five sections: the first gives an overview of errors associated with the SfM processing and field data collection. The next three sections illustrate the net and gross changes that occurred between the surveys. The SfM comparisons are presented in two time-series figure styles, one showing the total change that occurred within each site with another presenting the intra-survey changes measured from bi-monthly re-visits. The layout of results figures corresponds to their respective relief figures from the methods section, with Figures 4,6 and 8 matching the spatial extent of Figures 10, 13 and 16. Results for SfM surveys are shown and described according to representative landscape units, to illustrate post-fire response of the burnt dunefields and emphasise the seasonal dynamics and short-term response. M3C2-PM changes are presented according to segmented areas of satellite classifications (sand, burnt and unburnt) to show the resulting 3D responses in the time series. The fifth section shows the trajectory of ground cover in the three sites according to the satellite spectral responses in the years preceding and following the fire.

3.4.1 Structure From Motion Error

The error between SfM surveys is a product of equation 1 (LoD95%) and used to interpret significant changes between dates, including the estimated precision (Precision Maps) and measured accuracy (CCP RMSE) errors. The measured errors from SfM surveys are presented in Table 9. Measures of the GCP and CCP error were sourced from Metashape total errors which include individual RTX-GNSS precisions. The range of RMSE shows close alignment with RTX average horizontal and vertical precisions (1.5/3 cm), suggesting that the majority of surveys were relatively good fits without significant systematic error. All surveys were tested for systematic doming or dishing errors (James et al., 2020), with no surveys presenting significant error that could be modelled ($P < 0{\cdot}05$). Spatially distributed check points (CCPs) were used, instead of GCPs, to quantify accuracy between surveys to include within error propagation (Equation 2).

The final survey of site C presented considerable check point errors in certain regions, located along high points within the survey. The areas with increased error correspond to regions with reduced photo overlap as flight plans had a constant height above take-off location, as described in methods. Additionally, substantial vegetation re-growth reduced reliable tie-points and network geometry across the survey.

Table 3-9 - Root Mean Square Error (RMSE) for each survey Date is shown in centimetres according to control and check points in bold

Site	Date	RMSE (cm)
A	28/08/20	1.4|4.6
	13/10/20	0.6|4.5
	08/12/20	1.2|2.7
	13/02/21	1.7|3.4
	03/05/21	2.9|6.1
B	31/08/20	2.2|5.6
	13/10/20	1.2|4.5
	08/12/20	0.9|3.2
	13/02/21	1.4|4.6
	02/05/21	1.6|4.9
C	31/08/20	1.7|5.3
	14/10/20	1.4|5.3
	09/12/20	1.0|3.1
	14/02/21	1.7|4.0
	04/05/21	1.5|13.1

3.4.2 Maupertuis Bay

Maupertuis Bay (Site A) is a semi-stabilised coastal dunefield in the southwestern corner of Flinders Chase National Park. Its southwestern orientation is directly in-line with the prevailing wave climate from the Southern Ocean, with a substantial Holocene sediment supply. This site was nearly completely burnt, with fire completely removing above-ground live vegetation and biomass across the site (Figure 1) as shown in the western side of the Figure grid rows Y-T of Figures 4 and 10. Changes that occurred in the site are shown and described in representative landform units in panels A:E (Table 3) with net change in Figure 10, intra-survey gross changes in Figure 11 and volumetric totals in Figure 12.

The results show little evidence of geomorphic surface changes outside of highly exposed regions as shown in panels A and E of Figure 10. Most negative surface changes, interpreted as aeolian erosion, occurred in the regions immediately landward of the foredune as shown in the grid columns of Z and X of Figure 10. Sheltered areas (Figure 10, Panel C and grid columns W, V, U and T) show substantial positive M3C2-PM distances, interpreted as vegetation growth. M3C2-PM distances for Panel B, located on the slip face of a parabolic dune lobe, suggests positive surface and vegetation change as a result of sedimentary accretion and regrowth of burnt areas.

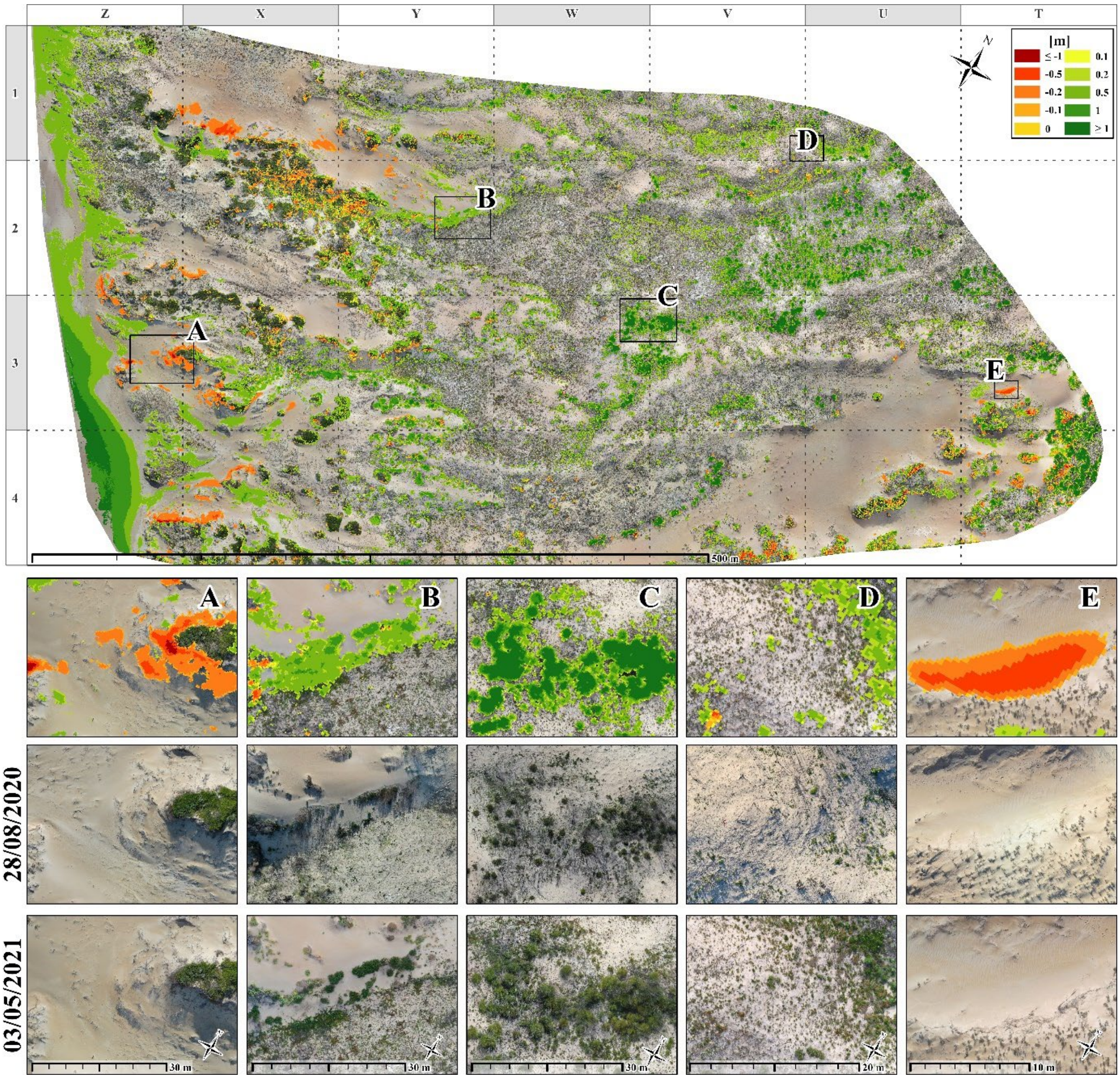

Figure 3-10 – Changes in M3C2-PM distance as extracted for areas with significant changes above error thresholds. These results show the total changes measured in this study site as per the first and last survey conducted. The grid columns Z:T and grid rows 1:4 correspond to the spatial extent of Figure 4 with the extent indicators showing panel regions A:E as described in Table 3.

Figure 11 shows the detailed intra-survey surface and vegetation changes that occurred during this study. Panels A and E of Figure 11 show the differential rates of erosion within this study’s duration. The majority of negative surface changes occurred in the first four months post first survey, corresponding to the spring and early summer months. Conversely, panel C of Figure 11 shows an increased rate of vegetation regrowth in sheltered areas in the latter two frames of summer and early autumn. Dune ridge areas (Panel C, D of Figure 10, 11) show little detectible net changes and less seasonal changes, suggesting that vegetation growth or surface changes within these regions has not occurred.

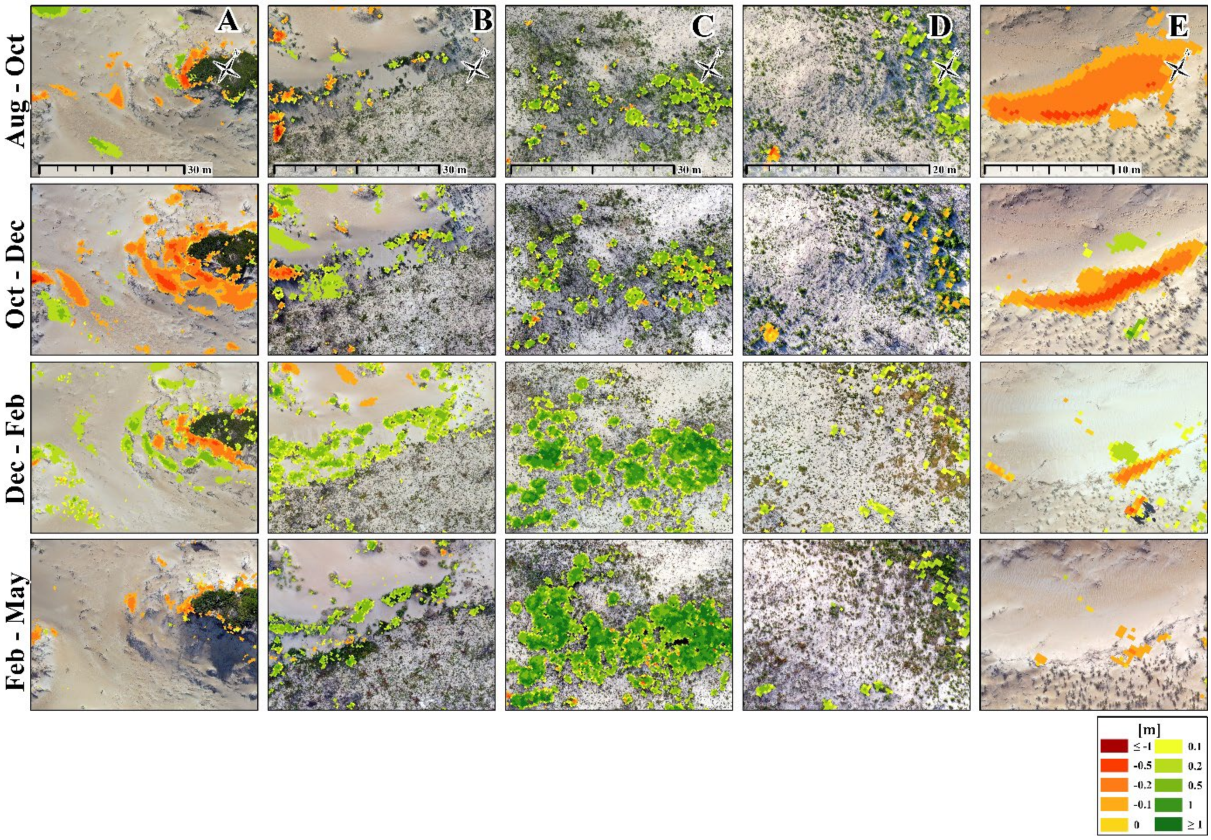

Figure 3-11 – Changes in M3C2-PM distance as extracted to areas with significant changes above error thresholds between surveys. The panels A:E correspond to the same spatial extent of the panels in Figure 10 with descriptions in Table 5.

Figure 12 shows the volumetric totals from M3C2-PM of surface and vegetation changes across Maupertuis Bay for the total time period (Figure 10) and intra-survey periods (Figure 11). Pixels were classified according to satellite derived classifications as bare sand (27%), and burnt (55%) or unburnt (18%) vegetated surfaces (Figure 1). Grouped M3C2-PM results show the differences in volumetric changes based on their pre-fire state and the changes that occurred in burnt areas. The sand pixels show peaks of negative volumetric changes in the first months of the study period, which corresponds to the negative surface changes shown in the exposed dune areas of Figure 11 (Panels A and E). Conversely, all three pixel-groups show an increase in volumetric changes in the latter months of this study corresponding to the increased regrowth of vegetation (burnt) and continued supply of sediment (sand and unburnt) in the summer and autumn months. Overall, the net volumetric changes illustrate the trend of predominant positive surface and vegetation gains across all classes during this study. Additional summary results are given in the supplementary information (Tables 10 and 11).

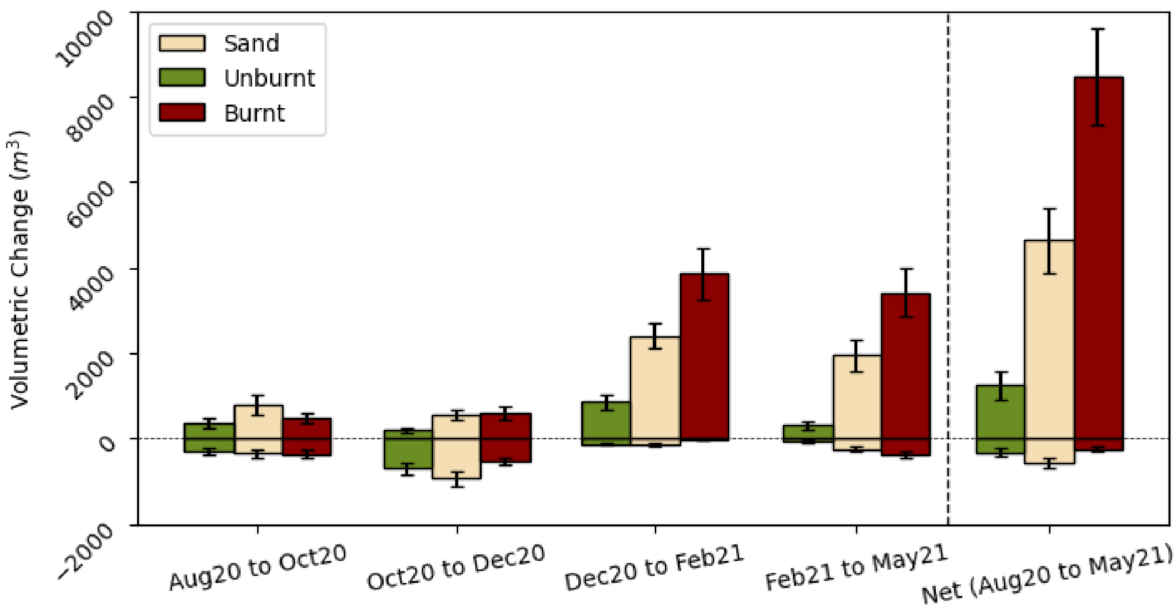

Figure 3-12 – Shows the M3C2-PM surface gain (>0) and loss (<0) from significant changes according to satellite derived classifications of pre-fire sand, burnt or unburnt pixels. Exact volumetric change (m^3) totals and area summary statistics are provided in the supplementary Tables 10 and 11.

3.4.3 Hanson Bay

Hanson Bay (Site B) is a semi-stabilised coastal dunefield on the southern coast of KI. This site was mostly burnt, with fire removing above-ground biomass and vegetation across the site (Figure 1), and with just a few relatively small patches unburnt on the stoss side of the foredune. Changes that occurred in the site are shown and described in representative landform units in panels A:E (Table 4) with net change shown in Figure 13, intra-survey changes in Figure 14 and volumetric totals in Figure 15.

Net results across Hanson Bay suggest no significant change in the stability of the foredune-blowout complex or in the regions behind the foredune. The beach width has increased with M3C2-PM distances showing positive significant values across grid row 2 of Figure 13. The net increase in beach width corresponded to the build-up of foredunes, shown by the panels A and D of Figure 13. Panel D shows the aeolian erosion of a foredune-blowout complex, with negative values suggesting the continued development of blowouts in the mid to upper sections of the foredune. A large blowout that cut across the estuarine barrier (grid column X, Figure 6) showed continued geomorphic changes (Panel B, Figure 13) with both erosion and accretion occurring during this study. Results from relatively sheltered areas behind the foredune suggest little to no negative surface changes (Panels C, E Figure 13), with positive values in areas indicating total vegetation growth. The 3D changes suggested by Panel C of Figure 13 show significant negative values, showing M3C2-PM distances detecting the displacement or dropping of remnant burnt branches and trunks.

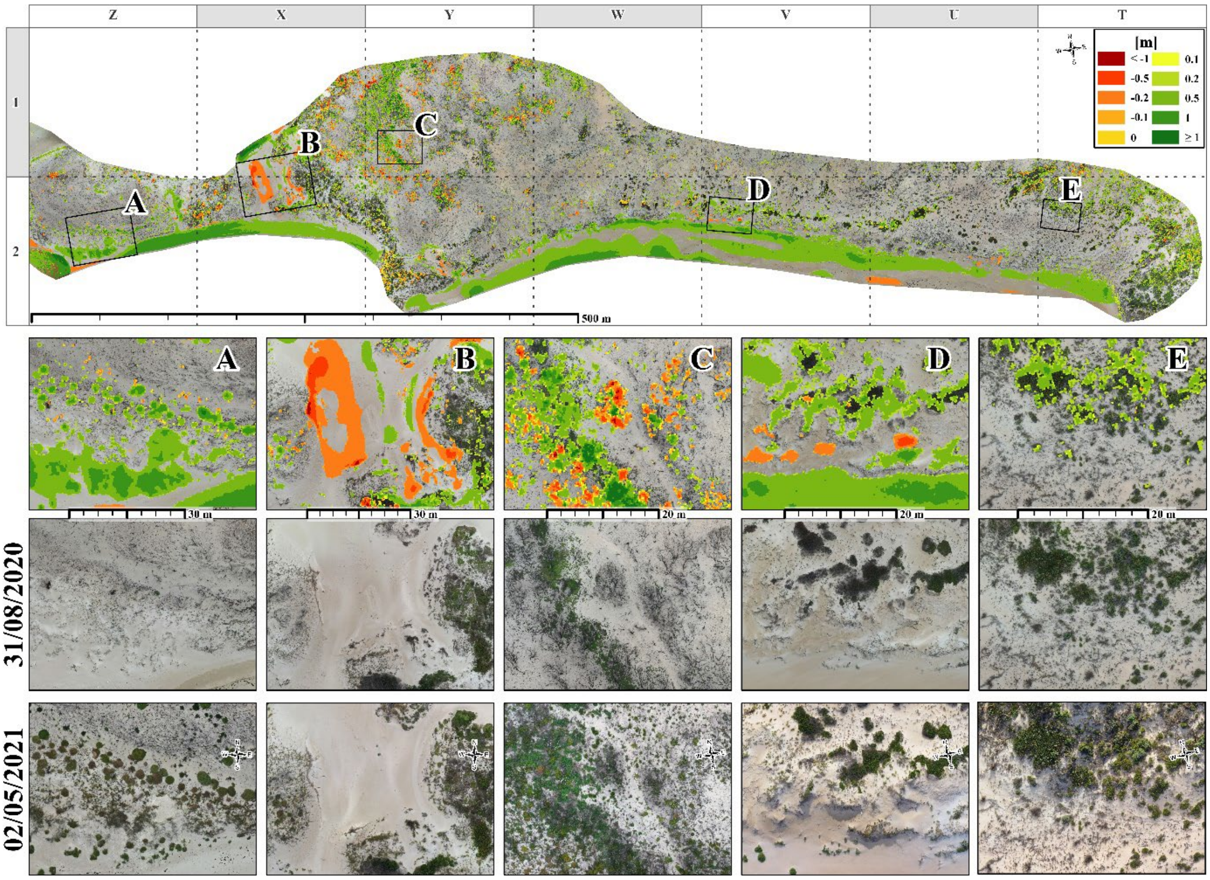

Figure 3-13 - Changes in M3C2-PM distance as extracted to areas with significant changes above error thresholds between the first and last survey. These results show the total changes measured in this study site. The grid columns Z:T and grid rows 1:2 correspond to the spatial extent of Figures 5 and 6 with the extent indicators showing panel regions A:E as described in Table 3.

Figure 14 shows the intra-survey surface and vegetation changes. Panels A and D of Figure 14 show the shifting trends of positive and negative surface changes that occurred during this study. Considerable surface changes occurred in panel B of Figure 14 during the summer-late spring-summer months, showing the continued response of a blowout across the drier seasons. The lack of significant M3C2-PM distance detected in Panel E of Figure 14 shows how incremental changes may not be detected in dense time-series, but also represents the absence of vegetation cover returning amongst dune ridges landward of the foredune.

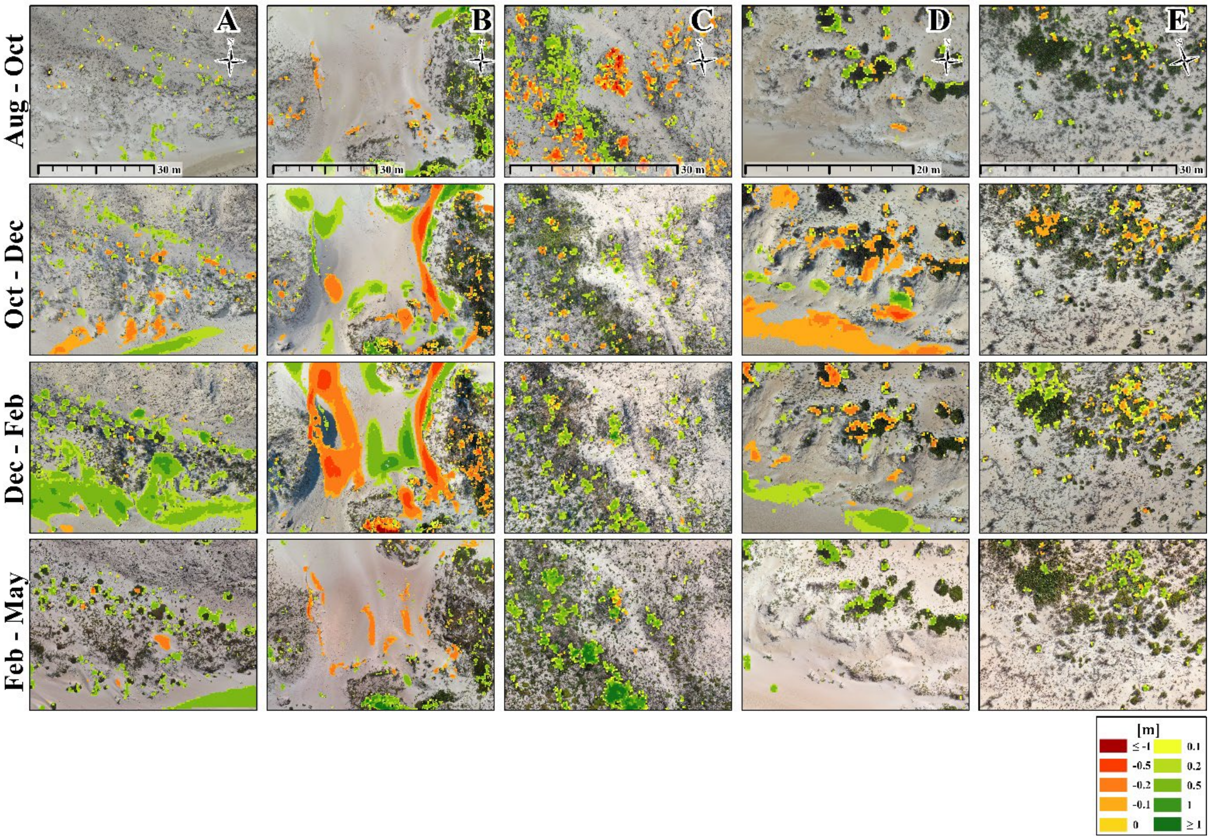

Figure 3-14 - Changes in M3C2-PM distance as extracted to areas with significant changes above error thresholds between surveys. The panels A:E correspond to the same spatial extent of Figures 5, 6 and 13 with descriptions in Table 4.

Figure 15 shows the volumetric totals from M3C2-PM of surface and vegetation changes across Hanson Bay for the total time period (Figure 13) and intra-survey (Figure 14). Pixels were classified according to satellite derived classifications as sand (28%), burnt (41%) and unburnt (30%) (Figure 1). The grouped M3C2-PM results illustrate the changes based on their pre-fire state and the changes that occurred in burnt areas. Similar to Maupertuis Bay, sand pixels show highest magnitudes of negative volumetric changes in the first months of the study period, which corresponds to the negative surface changes shown in the exposed dune areas of Figure 14 (Panels B and D). Overall, the net volumetric changes illustrate the trend of predominant positive surface and vegetation gains across all classes during this study. Additional summary results are given in the supplementary information (Tables 12 and 13).

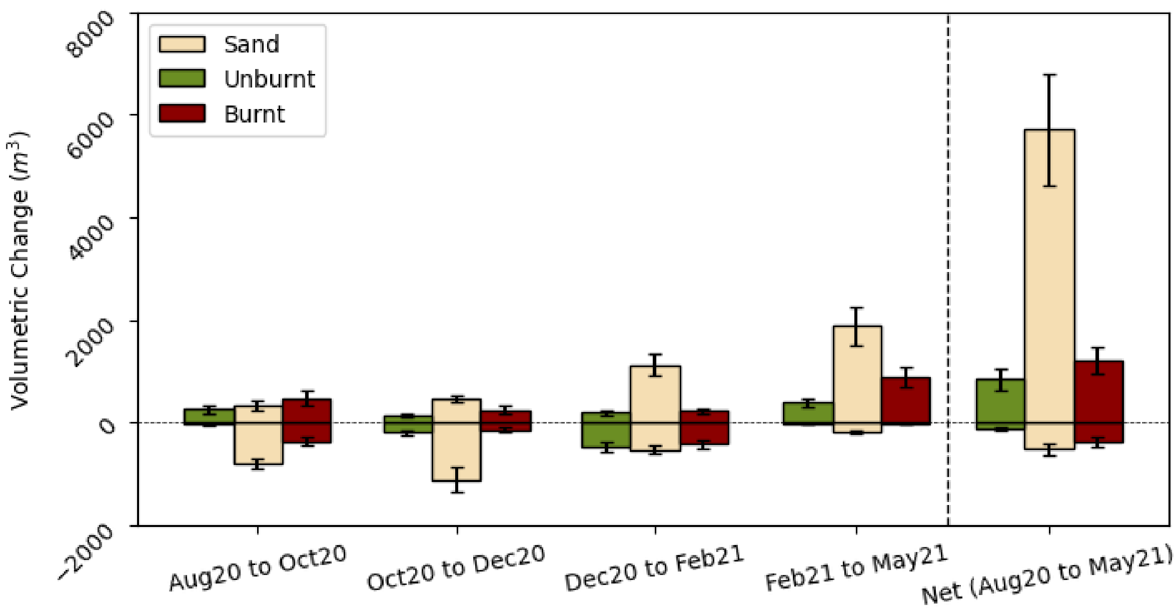

Figure 3-15 - Shows the M3C2-PM surface gain (>0) and loss (<0) from significant changes according to satellite derived classifications of pre-fire sand, burnt or unburnt pixels. Exact volumetric (m^3) totals and area summary statistics are provided in the supplementary Tables 12 and 13.

3.4.4 Snake Lagoon

The Snake Lagoon dunes are the landward portion of the Maupertuis dunefield. Before the fire, Snake Lagoon (Site C) was described as a stabilised transgressive-parabolic dunefield complex. All vegetation was completely burnt as shown in Figure 1. Changes that occurred in the site are shown and described in representative landform panels A:E (Table 5) with net change shown in Figure 16, intra-survey changes in Figure 17 and volumetric totals in Figure 18.

The results show no evidence of significant surface changes that suggests instability, with differential regrowth of vegetation across the study site. Figure 16 shows mostly positive M3C2-PM distances indicating that the net change is predominantly vegetation regrowth or accretion of sediments. Overall, net changes suggest differential regrowth rates, with distinct regions within the study area exhibiting varying degrees of positive changes. As shown by panels A and E of Figure 16, the lower slopes and inter-dune areas show higher positive distance values and indicate higher regrowth when compared to the higher elevation areas of the survey. Results of change over dune ridges show comparatively less regrowth compared to lower elevation areas. This is unsurprising given the high elevation portions of these large parabolic dune ridges (between 20-50 metres above the adjacent deflation plains) are more exposed and significantly drier than the lower slopes and interdune/deflation plain regions. There are no significant results showing negative surface changes with the negative 3D changes in Panels B, C and D of Figure 16 showing the displacement or dropping of remnant burnt branches.

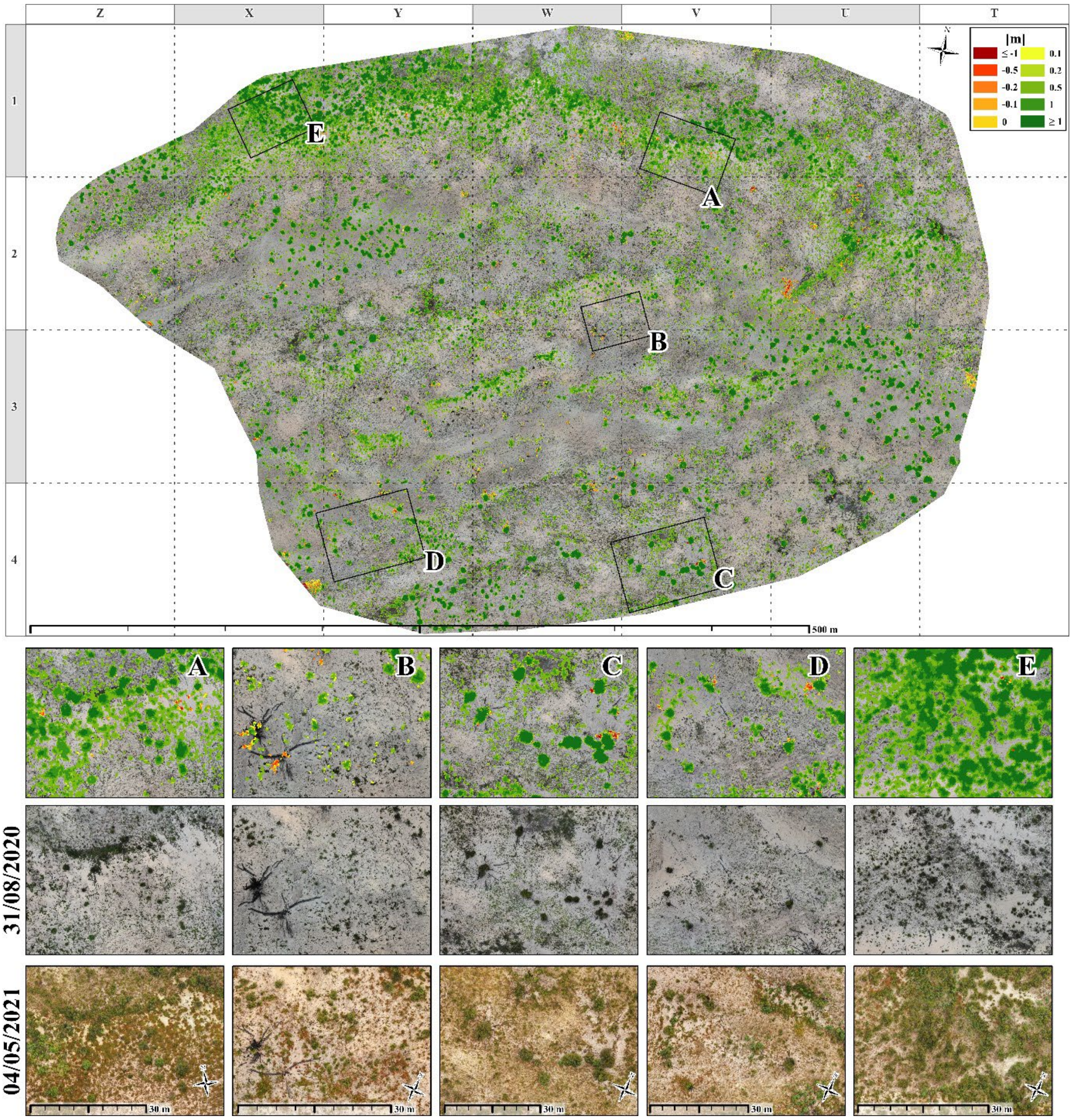

Figure 3-16 - Changes in M3C2-PM distance as extracted to areas with significant changes above error thresholds between the first and last survey at Snake Lagoon. The grid columns Z:T and grid rows 1:2 correspond to the spatial extent of Figure 5 with the extent indicators showing panel regions A:E as described in Table 5.

Figure 17 shows the intra-survey surface and vegetation changes that occurred. Results of panels A and E of Figure 17 show that rates of positive surface and vegetation changes increase in the late summer and early autumn months from December through to May. The relatively lower regions within the site (panes A, C, E, Figures 16, 17) show increased ground cover compared to the higher elevation areas of the dune ridges of panels B and D. Of the two panels (A and D) of Figure 17 on slopes, the north facing slope shows higher overall re-growth during this study period. Negative M3C2-PM values paired with positive changes suggests the displacement of remnant burnt branches as vegetation regrows epicormically from the trunk (all panels, Figure 17).

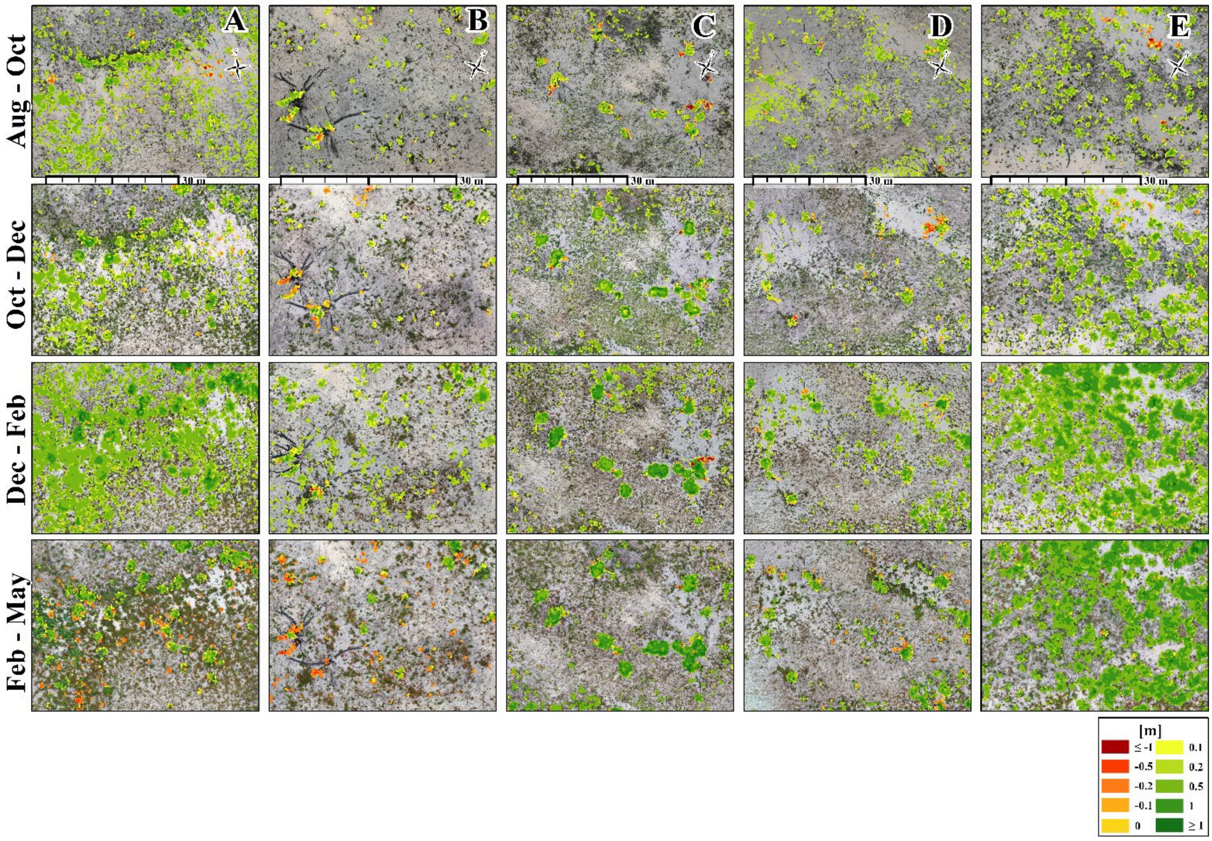

Figure 3-17 - Changes in M3C2-PM distance as extracted to areas with significant changes above error thresholds between surveys. The panels A:E correspond to the same spatial extent of Figure 16 with descriptions in Table 5.

Figure 18 shows the volumetric totals from M3C2-PM of surface and vegetation changes across Snake Lagoon for the total time period (Figure 16) and intra-survey (Figure 17). The increases in volumetric changes in the later months of the surveys reflect vegetation growth which corresponds with Figure 17. The lack of significant negative volumetric change further suggests that there is not widespread landscape instability. Overall, the net volumetric changes illustrate a clear trend of predominant positive surface and vegetation gains during this study. Additional summary results are given in the supplementary information (Tables 14 and 15).

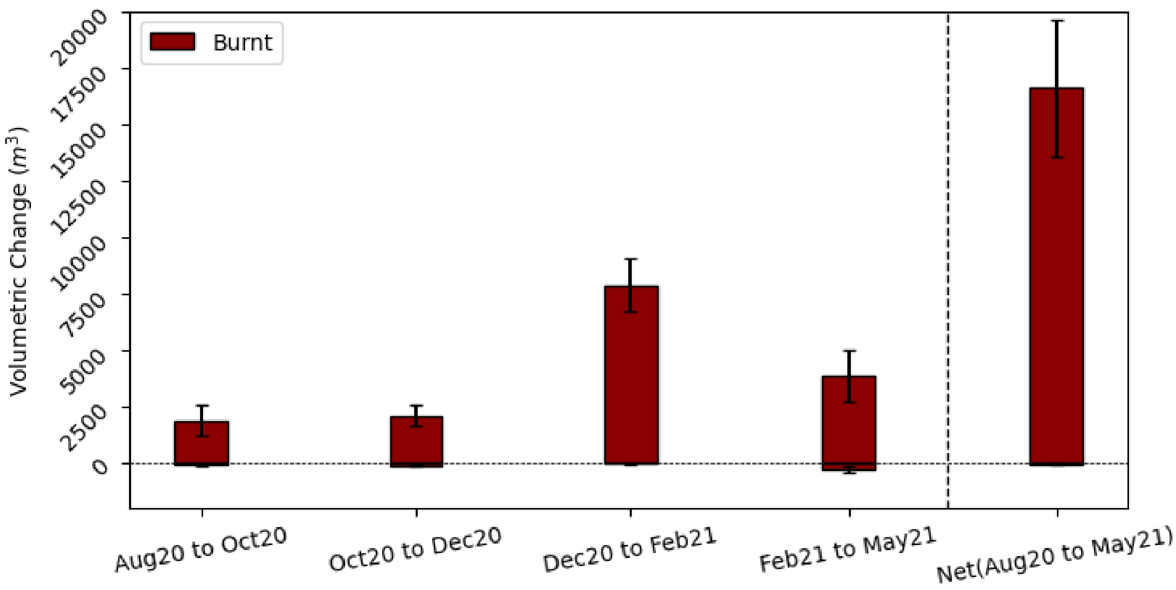

Figure 3-18 - Shows the M3C2-PM surface gain (>0) and loss (<0) from significant changes according to burnt pixels of site C. Exact volumetric (m^3) totals and area summary statistics are provided in the supplementary Tables 14 and 15.

Figure 19 shows the responses of the optical satellite indices used to illustrate ground cover changes. The Sentinel 2 time-series is calculated from available imagery and grouped into four-month geomedians to show their baseline spectral index values and post-fire trajectory. The seasonal influence on spectral indices is shown from the relative mid-year increases in index values, reflecting the temperate climate with predominantly wet and mild weather through the winter months. In the months leading up to the fire, a decrease in index value is shown across all three indices, with site C showing the largest decrease in its spectral signatures. The minimum and maximum values from the pre-fire time-series gives the range of their spectral indices and is interpreted here as a baseline of the unburnt landscape. Comparing the spectral trajectory following the fire, all indices show continued recovery between the first and last survey, with recent seasonal highs approaching the pre-fire minimum ranges.

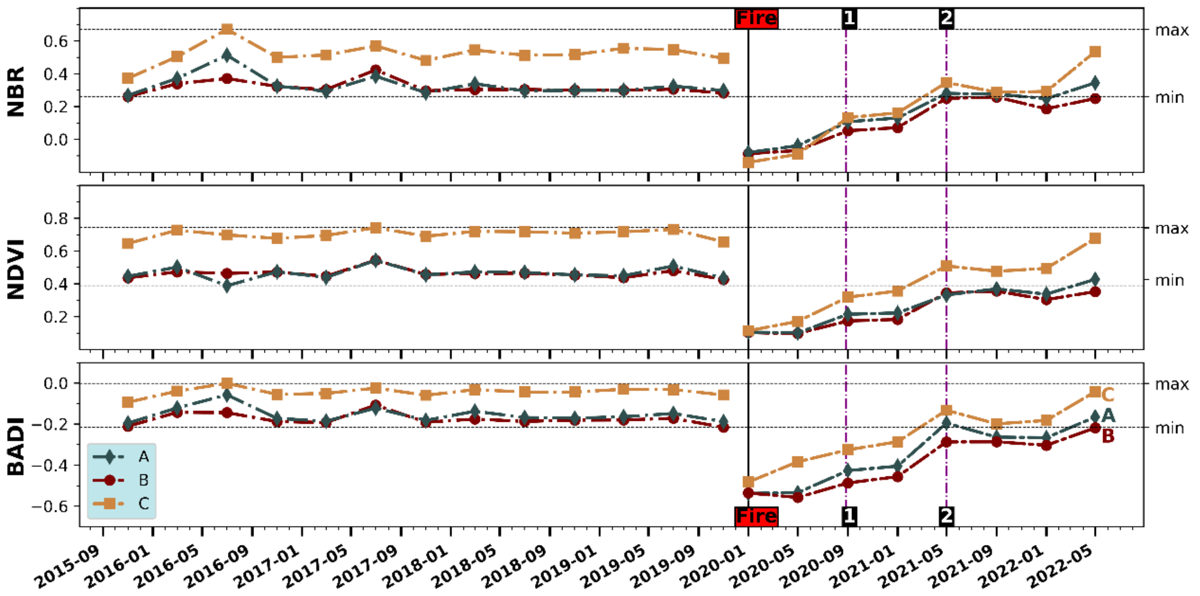

Figure 3-19 - Three optical satellite indices are computed from Geomedians, the median of 4-month time periods, over the three study sites represented by the red (A), brown (B) and gold (C) plotlines. The minimum and maximum values of the pre-fire indices, the Normalised Burn Ratio (NBR), Normalised Difference Vegetation Index (NDVI) and Brightness Adjusted Disturbance Index (BADI), are displayed by the horizontal lines from the right side of the plot to indicate the pre-fire indices' range. Vertical lines indicate the date of the fire in December 2019, the dates of the first (1) and last (2) survey.

3.5 Discussion

The fires of 2019/2020 burned coastal dunefields across Kangaroo Island, altering the vegetation cover on both semi-stabilised and fully vegetated dunefields. Fire has been suggested to be a potential initiation mechanism for dune transgression in the literature (Matthews and Seppälä, 2013, Filion, 1984, Filion et al., 1991, Hesp et al., 2022b, Barchyn and Hugenholtz, 2013), but following the severe fires of the Black Summer season of 2019/2020, the dunefields of this study clearly show a trend of stabilisation. The dune sites studied here are representative landscapes of burnt dunefields across Kangaroo Island (Figure 1), with results illustrating the post-fire response of semi-stabilised foredune-blowout complexes (Sites A and B) and previously stabilised parabolic dune/transgressive dunefield sites (Sites A, B and C).

The majority of detected surface change interpreted here as aeolian erosion is observed in the two near-coastal sites of Sites A and B with negative changes occurring in the first four months (panels A, E, Figures 11, panels B, D, Figure 14) predominantly in the spring and early summer months. Most positive 3D changes were associated with increases in vegetation with differential regrowth in the sheltered regions of coastal sites (panels C, Figures 10, 13) and in the relative low-lying areas of Snake Lagoon (panels A, C, and, E Figure 16) compared to higher sites in the landscape in similarity to the results from post-fire dune research (Cowling and Pierce, 1988, Vestergaard and Hastings, 2001), north and south facing slopes show distinct differences in vegetation regrowth and ground cover. The intra-survey results show the variable regrowth rates related to seasonality, with higher 3D changes observed in the late summer to early autumn months (Figures 11, 17) which is supported by the seasonal increases seen in the spectral signatures (Figure 19). The trend of increasing M3C2-PM totals from burnt pixel areas in the later months of the survey (Figures 12, 18) correspond to the seasonal increases in vegetation growth of the sheltered and low-lying areas shown in Figures 11 and 17.

3.5.1 Vegetation Cover Changes from Optical Satellites

A time-series of three space-based optical indices is presented to show the relative spectral index trajectory before, during, and after the time-series of UAV surveys, to place the index values in context to pre-fire patterns (Figure 19). While spectral change interpreted as ground cover change is not able to illustrate the diversity or health of an ecosystem, it provides a spectral-temporal baseline of vegetation that is used here to demonstrate the progression of these dunefields as they return to a post-fire state.

Results show the increasing trend of ground cover that occurred during this study, with all sites approaching pre-fire index minimums according to 4-month geomedians. Geomedians retain the spectral relationships between bands and facilitates the computation of indices in time-series (Roberts et al., 2017). Two spectral indices are chosen to align with established research methods (Hislop et al., 2018) and an additional spectral index developed for coastal dune and heterogenous landscapes, BADI (DaSilva et al., 2021b). The three sites exhibit patterns in index values representing their differences in dominant vegetation, relative exposure, and stability with varying canopy coverage or exposed soils. The near-coastal sites (Sites A and B, Figure 1) show lower index values throughout the time-series with the exposure of bright dune soils lowering NBR and NDVI compared to the inland site of Snake Lagoon. There is a decrease in spectral index value in the months leading up to the fire, shown prominently by the indices from the in-land relict dunefield, site C. These lower values suggest a relative decrease in vegetation greenness, vigour and indicate possible drought conditions. Indices show seasonal influences with mid-year highs in index values and a distinct increase in magnitude occurring during the UAV survey time frame.

Limitations of Sentinel 2 imagery need to be acknowledged when compared with high resolution ortho-imagery, principally the differing spatial resolutions which result in the mixing of landcover in the resampled 10-20 metre pixels. The insets of Figure 1, show pixels which were either burnt or with sparse vegetative cover and at times contradicting satellite classifications of burnt, unburnt or sand. While thresholds of indices are imperfect, the calibrated sensors facilitate consistent objective time-series analysis (Gascon et al., 2017) in contrast to non-metric UAV sensors which are limited by inconsistent illumination in orthomosaics and spectral resolutions (Eltner and James, 2022).

The increases in spectral indices, interpreted as increasing vegetation cover (Figure 19), corresponds with the results from the UAV surveys. The trend of dunefield revegetation and landscape stability after severe fire follows similar findings of other post-fire dune studies who have found little evidence of dunefield reactivation post-fire (Shumack and Hesse, 2018, Shumack et al., 2017, Barchyn and Hugenholtz, 2013). Evidence of dunefield destabilisation following fires is limited to interpretations of the stratigraphic record (Boyd, 2010, Filion, 1984, Filion, 2017, Filion et al., 1991, Kotilainen, 2004, Seppälä, 1995, Tolksdorf et al.,

2013) and central to the suggestion of fire and landscape instability is a coincident increase in aridity or drought conditions post-fire acting as a catalyst for reactivation (East and Sankey, 2020, Fisher and Hesse, 2019). Figure 20 shows the monthly mean maximum temperature for Cape Borda and monthly mean rainfall totals for Rocky River between 1960 and 2019, plotted against modelled rainfall and observation data for the corresponding 2016-2022 period in Figure 19. Modelled rainfall monthly totals were interpolated from rainfall gauge data (Beutel et al., 2019) across the extents of the UAV surveys. Following the fire, rainfall totals shows mean precipitation was high while temperatures were below average, and thus, a wet and mild summer occurring throughout the time of the UAV surveys. The rainfall data shows a wet month following the fire, which likely resulted in removal of surface sediments. Six months later, significant sheet-flows and gullying of sediments within the burnt landscape, provide direct evidence of the impacts of rainfall-induced erosion (Figure 21). Studies have shown that fire drastically alters the susceptibility of landscapes to surface water erosion, showing that even short duration rainfalls with moderate intensities can trigger significant post-fire surface water erosion (Lopes et al., 2020). The high rate of recurrence of fire in Australian landscapes may reduce the geomorphological role of wildfires in producing significant sediment mobilisation, as suggested by Shakesby et al. (2007).

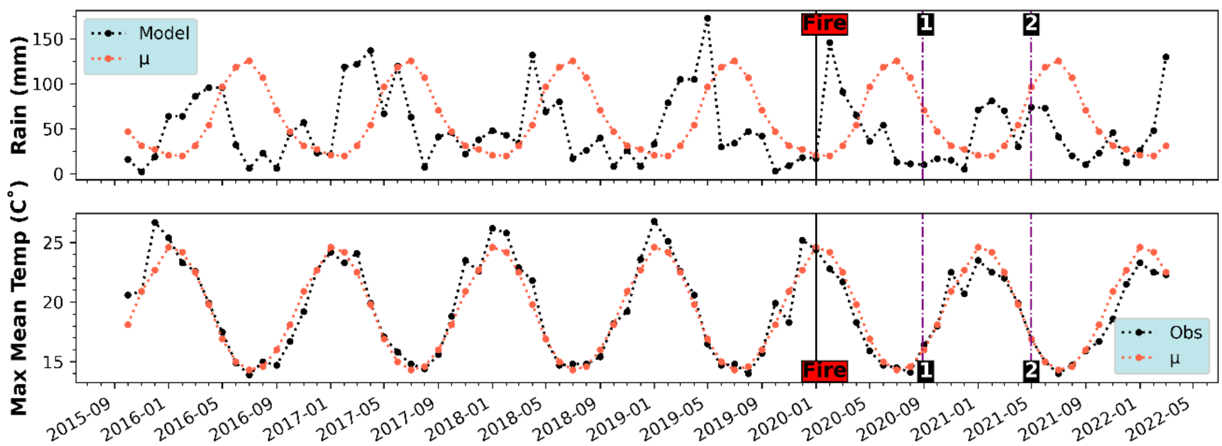

Figure 3-20 - Monthly mean (μ) values of rainfall and max temperature (C˚) observed by the Bureau of Meteorology for Flinders Chase (Rocky River) and Cape Borda from 1960-2019 plotted against the monthly interpolated (Model) data of rainfall (mm) for the survey extents

and the mean max temperature (Obs) from Cape Borda. Time period is set to match Figure 19 with vertical lines indicating the date of the fire in December 2019, the dates of the first (1) and last (2) survey.

3.5.2 Structure From Motion Change Detection and Error

The change detection workflow used here is based on two central assumptions: (i.) that positive M3C2-PM changes indicates an increase in vegetation canopy or sediment accretion. Similarly, (ii.) that negative M3C2-PM surface change indicates erosion or loss of vegetation canopy. Given these assumptions, dunefield reactivation or transgression would show widespread negative surface changes as sediments are mobilised and cannibalise previously stable regions (Barchyn and Hugenholtz, 2013). Barchyn and Hugenholtz (2013) describe a stabilised dunefield as retaining a protective skin, encompassing all biomass including above-ground vegetation, surface litter and sub-surface root systems. Dunefield reactivation occurs as this protective skin is removed or degraded and erosional dune types such as blowouts develop, expand, and coalesce. M3C2-PM changes detected in this work were oriented to the surface normals from a LIDAR ground model, standardising the axis on which change detection occurred across the time-series. This standardisation ensures both canopy and surface changes reflect the baseline orientation derived from ground, instead of a shifting reference cloud. Although M3C2-PM (Lague et al., 2013) and its precision maps (James et al., 2017b) were developed for surface changes, the workflow used here and above assumptions benefit from its ability to robustly detect changes across point-clouds with spatially-variant errors as in the case of SfM generated datasets. Additionally, SfM datasets are widely used for vegetation related applications, such as calculating above-ground biomass (Cunliffe et al., 2022) and in multi-temporal studies of canopy changes (Zhang et al., 2021). For this study, the increases in vegetation height reduced the efficacy of SfM point cloud generation but also illustrated the lack of dunefield instability or transgression following severe fire.

The principal limitations of the methods used here are attributed and reviewed according to the following: reduction of functional photo-overlap due to vegetation regrowth, sensor specific hardware issues and operational from inconsistent above-ground flying heights.

The increasing surface roughness of regrowing leafy vegetation reduces effective overlap, tie-point precisions and subsequent point-cloud reconstructions (James et al., 2020). Through the Metashape (MS) workflow outlined in Table 7, tie-points were iteratively reduced according to their error or uncertainty, with point precisions over high roughness regions representing the highest values of uncertainty in precision maps. As uncertainty increases, tie-points are reduced and reconstruction in regions of dense vegetation is less robust. Figure 21 shows remnant branches and trunks with epicormic regrowth in August of 2020 in an inter-dune swale in site C. These remnant branches caused significant reduction in tie-point certainty and residual errors due to their height and susceptibility to wind movement. During this study's duration, inter-dune swales, deflation plains, low-lying areas or sheltered areas displayed both the highest rates of positive intra-survey changes and highest uncertainty values. Between surveys, negative changes were detected as these branches were displaced from wind or dropped, as shown in the results of Figure 13 and 16.

Figure 3-21 - Epicormic regrowth on the dominant vegetation, Mallee Eucalyptus diversifolia occurring at Site C at the intersection of the lowermost portion of a steep parabolic dune slope and interdune depression. Sheet wash and gullying are evident in the image taken 6 months after the fire. Image corresponds to location of panel E in Figures 7, 8, and 17.

Additional limitations of this study arose from the use of the Mavic 2 Pro. Its rolling shutter sensor has been shown to reduce image clarity and is not recommended for monitoring environmental changes (Eltner and James, 2022, Stark et al., 2021). Although the precise magnitude of error directly from the rolling shutter is difficult to isolate, the use of rolling shutter corrections attempts to model sensor movement within the bundle block adjustment and has been shown to improve results (Zhou et al., 2019).

After iterations of reducing uncertain tie-points (Table 7), camera calibration coefficient correlations displayed high correlations between focal (f) and radial (k1-k3) lens distortion coefficients and between principal point shifts (Cx, Cy) and tangential (p1, p2) lens distortion coefficients (see error reports linked in supplementary section) suggesting potential over-parameterisation. While some parameters are acknowledged to have inherent correlations (Senn et al., 2022), it is suggested to remove individual parameters if their error exceeds the coefficient value (James et al., 2017b). Camera calibration coefficients in this study show errors that are significantly lower than their coefficient values, with errors representing a miniscule fraction of the corrections applied. Although there is not consensus regarding the optimal parameters available in SfM software (Śledź and Ewertowski, 2022), flight design and acceptable error bounds need to be fit for purpose to answer the research objectives considering the scale, resolution, precision, and accuracy of the methods (Anderson, 2019).

In this study, flight planning incorporated a double grid pattern, including nadir and oblique imagery, and distributed RTX control and checks points to ensure reliable geometric camera calibration (Eltner and James, 2022). The inclusion of off-nadir imagery in aerial grid surveys has been shown to improve scale variation within and between images and improves self-calibration within the bundle-block adjustment (Luo et al., 2020, Nesbit and Hugenholtz, 2019, Sanz-Ablanedo et al., 2020). The high relief landscapes of the dune sites also increased the scale variation within and between images which benefits network geometry (Fonstad et al., 2013, Fraser, 2013). In surveys at Snake Lagoon (Site C), flight start locations occurred in an area with clear line of sight of aircraft, but up to 21 metres below surrounding dune ridges. This reduced photo-overlap combined with increasing vegetation resulted in significant elevation errors in the May survey of Site C. Check points were preferentially placed along ridge lines to incorporate apparent doming errors into interpretations of significant change. Accuracy and precision estimates used in the error propagation methods of this work, gives a LoD typically below ~10 cm, except for the last survey of Site C. While the level of detection likely misses some hydrologically driven surface processes (Ellett et al., 2019), illustrated in Figure 21, it reflects the realistic method limitations of using SfM with non-metric consumer grade-cameras in remote rapidly re-vegetating post-fire environments. The inclusion of check points in this work is shown to be vital in assessing and accounting for error, with their omission in some works suggesting inaccurate or incredulous error bounds.

3.6 Conclusions

This study focuses on the post-fire response of burnt coastal dunes on Kangaroo Island, South Australia using a variety of remote sensing techniques and methods. The three sites studied here represent the landscape diversity of both active, partially vegetated, and relict stabilised dune fields in a temperate climate. Fire has been suggested to be an initiator of coastal dunefield transgression, but the results of this work show no evidence of aeolian destabilisation or widespread landscape instability in the months following a wildfire. *In-situ* bi-monthly UAV surveys are used to reconstruct landscapes and compared to describe the significant geomorphic and vegetation changes and assess potential dunefield transgression. The UAV surveys show that negative surface changes associated with aeolian erosion and destabilisation occurred in the coastal sites, predominantly occurring in the spring and early summer months in highly exposed regions. Positive 3D changes show vegetation regrowth occurring across all sites, with distinctly increased rates in sheltered and relatively low-lying regions. The high temporal resolution illustrates the variable vegetation regrowth rates and landscape dynamics related to seasonality, which are observed in the spectral signatures from satellite indices. Errors in this method are reviewed with the limitations of the UAV methods discussed specific to the objective of the research question. Without pre-fire baseline data or rapid post-fire assessments, changes that occurred in the immediate six months following the fire are unknown. The logistics of rapid response surveys in protected wild areas precluded earlier UAV surveys so alternative data was used.

Satellite composite images were computed to calculate spectral indices to assess the groundcover changes that occurred in the years before and following the fire. During the time period of the UAV surveys, spectral indices increased and approached pre-fire baseline values. The results from the satellite time-series agree with the UAV surveys showing that vegetation ground cover in dune sites is steadily increasing and suggests a continued trend of landscape stability and re-vegetation.

Overall, the results of this work correspond to similar recent research in post-fire coastal dune fields showing landscape stability following fire. The literature reviewed here suggesting fire as an initiation mechanism for landscape instability and dunefield transgression is largely sourced from stratigraphic data, suggesting that fire followed by changing or atypical climatic conditions produces instability. The short term of this study illustrates the structural and ground-cover trends changes in these dunefields but demonstrates a trend towards vegetation re-growth and increasing stability over time. We note that the short time period of the drone surveys in this study is a limitation in regard to explaining longer-term landscape dynamism. As reviewed in the introduction, fires are natural and cyclical in Australian landscapes but shifts in fire regimes or climate may alter dunefield structure in the longer term. Following the most extensive fire on record however, the results presented here do not suggest landscape instability or a re-activation of previously stabilised transgressive or parabolic dunefields. This may be due to the occurrence of an immediate post-fire climate which was mild and wet; alternatively, it may indicate that stratigraphic interpretations of widespread landscape instability following fire may need to be re-assessed.

CHAPTER 4.

Paper in press: Geomorphology: Transgressive Coastal Dunefield Evolution as a Response to Prolonged Shoreline Erosion (Corrections returned to journal 09/10/23)

Marcio D. DaSilva (80%), Patrick A. Hesp (10%), David Bruce (5%), Joram Downes, Graziela Miot da Silva (5%)

Statement of co-authorship - I lead the research design of this manuscript in this chapter. I was mentored and aided by my supervisors from the conceptualisation through to realisation. I received field assistance on the 9 multi-day field trips for the data collected for this manuscript from my co-authors but personally led all research field excursions. All text, figures, analysis, and final editorial changes were ultimately my decision after consulting with my PhD committee.

Transgressive Coastal Dunefield Evolution as a Response to Prolonged Shoreline Erosion

Abstract

The Younghusband Peninsula coastal barrier extends ~190 km and is predominantly comprised of a mix of active, semi-stabilised and stabilised (relict) transgressive and parabolic dunefields. Wave driven shoreline erosion has triggered the rapid development of a transgressive dunefield along a portion of the peninsula. This study focuses on a ~2 km region with the highest regional erosion rates (> -2.0 m/year since 1988), and which has experienced rapid destabilisation and subsequent landward translation of the dunefield. Aerial LIDAR derived datasets of the barrier system from 2008 and 2018 and eight drone photogrammetry surveys between August 2020 and April 2022 are used to compare the rates of change across the beach-dune system. The net and intra-survey changes are used to show the short- to medium-term response and illustrate the relationship of sediment dynamics to the developing morphology and structure of the dunefield. Shoreline change

rates (m/yr) are sourced from the Digital Earth Australia coastlines dataset which provides annual rates for continental Australia from a Landsat time series (1988-2021). When the rate of shoreline change is segmented from the total dataset to the study time-period (2008-2021), the average resulting rates show an increase from -2.2 m/yr to -3.3 m/yr, respectively. This coincides with a landward advance rate of >10 m/yr from 2008 of the dunefield edge, with the fastest eroding dune toes corresponding to regions with the highest rate of dunefield translation and transgression. Net volumetric totals and their ratios of gain to loss of sediments show that significant sediment is lost to offshore during the retrogradation of the dunefield as only a fraction of the stoss slope sediment is transferred landwards. All regions of the dunefield exhibit a net loss of sediments but the high-temporal resolution shows that the magnitude of 3D changes varies through time. An adapted model of erosional stoss slope evolution and dunefield development is advanced and a temporal model of transgressive dunefield evolution is synthesised.

4.1. Introduction

Coastal dunes are aeolian landforms characteristic of sandy beaches where there is a sufficient supply of sediment and wind energy (Carter, 1988). They can range in size from small discrete nebkha to extensive transgressive dunefields which can reach tens of metres high and extend for kilometres along- and inshore (Davidson-Arnott et al., 2019). Transgressive coastal dunefields or sand sheets are formed by the downwind movement of sand over prior terrain, often cannibalising and remobilising previously stabilised sediment deposits or landforms (Hesp, 2013). They vary from highly stabilised by vegetation to fully active with mobile dunes, with most dunefields containing both stable and active areas (Barchyn and Hugenholtz, 2013) depending on the climate, sediment supply, age, and stage of evolution (Hesp et al., 2021). While some authors use the term ‘transgressive dune’ to refer to blowouts, parabolics and transgressive dune sheets/fields, for this work the term transgressive dunes will refer either to transgressive sand sheets (no dunes present) or transgressive dunefields as defined in Hesp and Thom (1990) and Hesp and Walker (2022).

Transgressive dunefields occur in phases or episodes where forcing conditions (e.g. wind or wave energy), shifts in environmental factors (sea level changes, sediment supply, or climate), or disturbances (coastal erosion) causes small to large scale destabilisation of the dunefields (Hesp, 2011a). There is an extensive body of research exploring the drivers of transgressive dunefield formation with many initiation mechanisms relating to climate change (Hesp, 2013, Hesp et al., 2022b). Some studies have argued that the initiation or remobilisation of transgressive dunefields in the past was a response to sea level rise, causing shoreline erosion and the translation of sediments as it transgressed inland (Cooper, 1958, Dillenburg et al., 2009, Jelgersma et al., 1970, Pye, 1982). Others have shown the initiation of transgressive dunefields can occur during periods of sea level fall (Andreucci et al., 2010, Christiansen et al., 1990, Ward, 1977). Coastal erosion is understood to drive transgressive dunefield development (Roy et al., 1980) and some authors argue that sustained coastal erosion (Hansen et al., 2020, Jackson et al., 2019b, Short and Hesp, 1982, Hesp et al., 2022b) and/or a single storm (Mathew et al., 2010) can result in the destruction of a foredune system and the initiation of a new transgressive dunefield phase.

Shoreline changes directly influence the morphology and stability of coastal dunes, as factors such as sediment supply are a product of the erosion-recovery equilibrium of beaches and adjacent coastal systems (Castelle et al., 2017). The landward translation of dunefields is one response to shoreline erosion, a negative sediment budget and relative water level increases (van et al., 2021, Davidson et al., 2020, Davidson-Arnott and Bauer, 2021, Davidson-Arnott et al., 2018, Anderton and Loope, 1995), but understanding the relationship between forcing factors and dune evolution is still in its infancy (Walker et al., 2017). The response of beaches and dunes to sea level rise (SLR; including lakes) has been studied and modelled extensively (Davidson-Arnott and Bauer, 2021), with the two prominent equilibrium profile models, the Bruun (1962) rule and RD-A model (Davidson-Arnott, 2005), providing differing shoreline-dune responses. Diverging forecasts of pessimistic global predictions of sandy coast loss (Vousdoukas et al., 2020) and optimistic refutations that sandy coasts will persist with SLR (Cooper et al., 2020) have been presented. The Bruun rule predicts that shoreline loss will occur without an equivalent dune translation as beach sediments are transported to the near-shore profile to maintain its equilibrium, with a resulting net-loss of sediments as water level increases (Rosati et al., 2013). The RD-A model suggests that there is no net loss to the nearshore as eroded sediments from the foredune will be translated landward at an equal or greater rate than the erosion, and that the landward migration of sediment will keep pace with rising water levels (Davidson-Arnott, 2005). With a clear divergence in predictions, more observational studies are required to improve our understandings of present and future coastal dunefield evolution especially in relation to net beach erosion and/or rising sea levels (Farrell et al., 2023, Short, 2022).

Significant research using stratigraphic data has been conducted in the Great Lakes region of North America, where preserved stands of paleosols in dunefields show numerous cycles of dune building and transgression following changes in local water levels and fluctuations in climate (Arbogast et al., 2023). Conceptual models of dunefield remobilisation and transgression following rising water levels in the Great Lakes are developed by Anderton and Loope (1995) and adapted (Loope and Arbogast, 2000) based on stratigraphic dating of mid- to -late Holocene deposits. Various studies have investigated the response of beach-dune environments with contemporary observations of episodic or clustered erosion events (Masselink et al., 2016, Masselink et al., 2022, Castelle et al., 2017) and their longer-term morphological evolution (Turner et al., 2016, Castelle et al., 2018, Robin et al., 2023, Laporte-Fauret et al., 2022, Davidson et al., 2021, Castelle et al., 2019, González-Villanueva et al., 2023). Robin et al. (2023) examined the various stages of development of a transgressive dunefield in southwest France and found that disturbances, such as prolonged shoreline erosion, has led to the recent remobilisation of a semi-stabilised coastal transgressive dunefield. On the SW coast of England, Masselink et al. (2022) explored the relationship between shoreline and dune retreat showing that sediments were often transported landward, as opposed to being lost to the littoral zone. van et al. (2021) shows that along the Dutch coast, the position of the dune toe is translating faster than recorded measurements of SLR, with the dune toe increasing in elevation and relative height to the water line. Similar observations of coastal sand-barriers response to storm events and SLR have been made, showing the importance of sediment supply, antecedent topography and relative exposure to wave energy (Costas, 2022, Ashton and Lorenzo-Trueba, 2018, Shawler et al., 2021). Recent research has reiterated the importance of dune slope as a geomorphic control in determining the evolution of vegetated coastal dunes (Smyth et al., 2023), especially as eroding dunes are scarped and alter wind speed at the toe (Hesp and Smyth, 2021). Longer term and larger geographical scope studies of the evolution of transgressive dunefields show that their stability is a product of a combination of drivers; these include storminess, climate and aeolian activity which vary in importance across latitudes (Jackson et al., 2019b, Costas et al., 2012) and exposure (Costas, 2022).

This study is focused on landform change that has occurred on a recently developing transgressive coastal dunefield in South Australia from datasets that range from 2008 through to 2022. The site is henceforth referred to as 41.5 Mile, as it is approximately a half mile SE of the nearby 42 Mile Crossing track (Fig. 1). The geomorphic evolution of the dunefield is described using 3D datasets with baseline airborne LIDAR and sequential UAV photogrammetry datasets. The objectives are to (1) measure the changes in volume, shoreline position, and the morphological response of the dunefield to long term erosion and (2) quantify the net changes of the sediment profile as remobilised dune sediments transgress landwards. Specifically, this research illustrates the ratio of sediments lost versus those translated during retrogradation. The aim is to contribute to the understanding of how coastal dune systems respond to prolonged shoreline erosion and present the results as a proxy study for some of the forecasted effects associated with climate change on the month to year timescale.

4.2 Study Area - 41.5 Mile

The focus of this study is a site of rapidly eroding coastal dunes (139° 42’E, 36°18’S) on the Younghusband Peninsula (YP) in South Australia (Fig. 1) within the Coorong National Park. The YP is a ~190 km long and 1-2 km wide coastal barrier comprised of active, semi-stabilised and relict transgressive and parabolic coastal dunes of Holocene age. The barrier is morphologically diverse, ranging from highly active and stabilised transgressive dunefields, sand sheets, and parabolics in its northern and mid-sections to multi-ridge foredune plains in the south. The reader is directed to Dillenburg et al. (2020) for a detailed review of regional geological and marine features. The climate is classified Csb (Köppen), with warm and dry summers and cool wet winters and an annual rainfall gradient of 468-586 mm/yr from the north to the south, respectively (Moulton et al., 2018).

The YP barrier is composed of Holocene beach and dune sands. Sediments are carbonate-rich and derived from the adjacent continental shelf (Short and Hesp, 1984). At the 41.5 Mile section of the barrier coarse-grained sediments and significant shell deposits are abundant on the beach (0.31-0.59 mm), while medium through to fine sediments (0.23-0.26 mm) are mostly found in the dunes.

Along the YP, surfzone wave energy increases from southeast to northwest as a result of variations in the width and depth of the inner shelf (Short and Hesp, 1982). Swell waves approach from the SW with an annual average significant wave height of 2.7 m and 12 second period recorded offshore (Hemer et al., 2008) and tides are micro-tidal (Short, 2001). This study is focused on the mid-section of the barrier (Fig. 1), which is oriented perpendicular to the predominant direction of swell waves with a surfzone classified as intermediate rhythmic bar beach (Short, 2001). The wind climate is predominantly influenced by strong south and south-westerly winds off the Southern Ocean, with Fryberger and Dean (1979) resultant drift direction (RDD) of 53°, drift potential (DP) of 125 vector units (vu in m/sec), and resultant drift potential (RDP) of 60 vu (Fig. 1;Hesp et al. (2022b)).

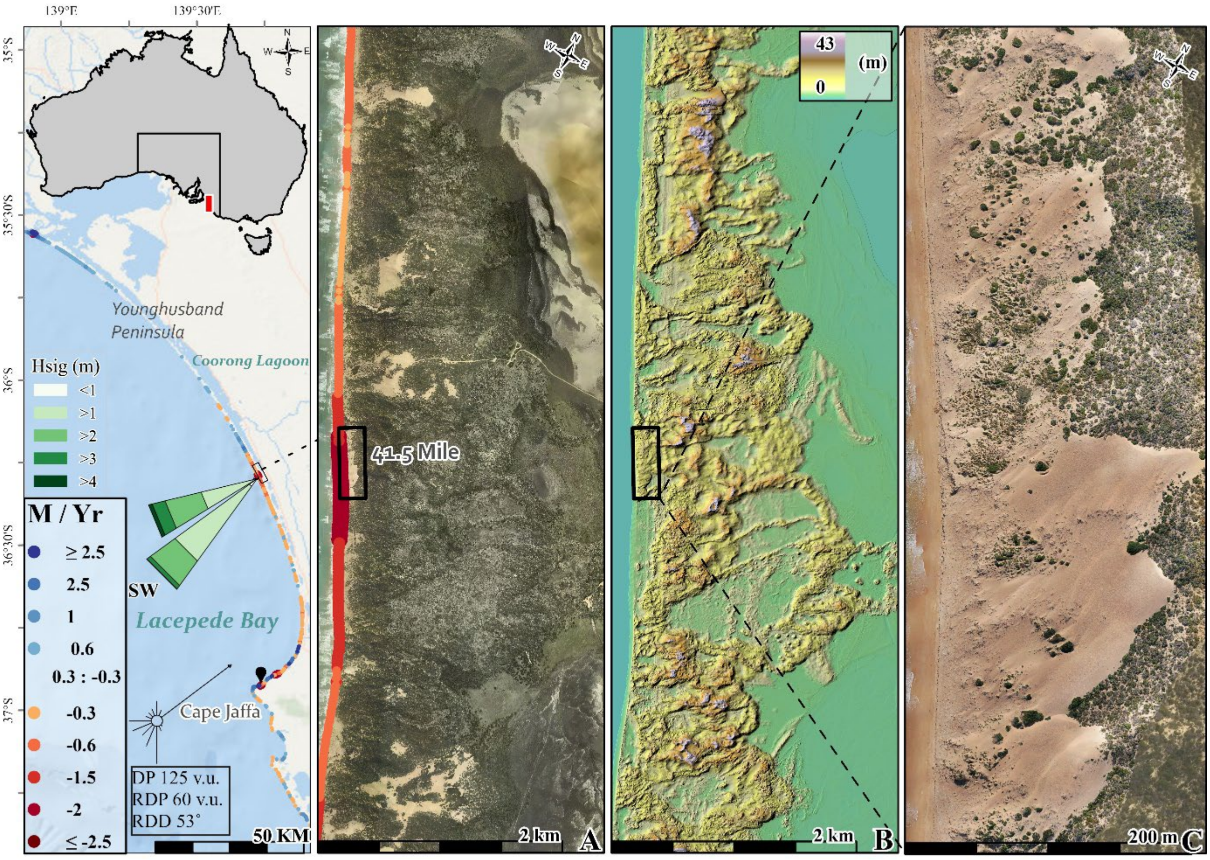

Figure 4-1- Location of the Younghusband Penninsula in South Australia, showing the shoreline change rates (M/Yr) from1988 to 2021 from the Digital Earth Australia (DEA) Coastlines dataset. Significant waveheight (Hsig) is shown according to re-analysis data from 1 km off-shore of study site (https://nationalmap.gov.au/) for 2008 to 2022. Sand rose from wind measurements at the Cape Jaffa met station. Inset maps show an ortho-photo from 2018 overlain with the DEA coastlines (A), shaded colour relief from 2018 LIDAR of the same extent (B), and an orthomosaic from the April 2022 survey of the study site at 41.5 Mile (C).

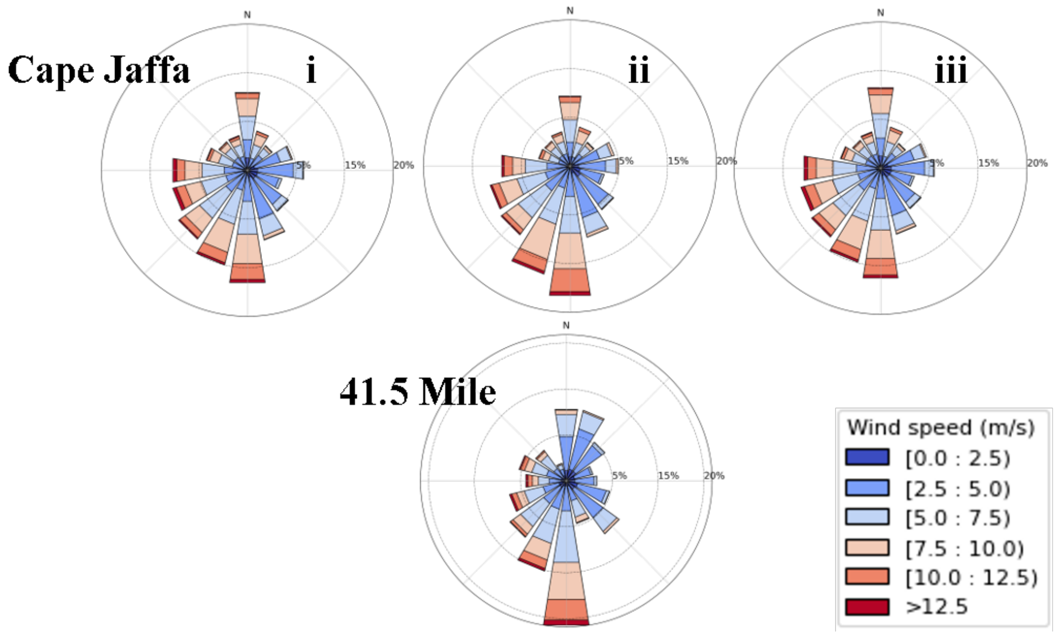

Figure 4-2 - Wind roses for the closest established weather station at Cape Jaffa for three time periods relevant to this study: (i) April 2008 to May 2018, (ii) August 2020 to February 2022, and (iii) April 2008 to February 2022 and from a weather station installed at 41.5 Mile.

The 41.5 Mile region shoreline change trends show significant erosion and barrier retrogradation with national datasets confirming it as a regional erosion hotspot (Bishop-Taylor et al., 2021b). Previous work at this site (Hesp et al., 2022b) explored the barrier retrogradation since 1975, showing the recent development and initiation of rapid landward translation and transgression of a sand sheet (+100 m in 8 years) because of prolonged wave driven erosion. The reasons for this erosion are not known at this time. Fig. 3 summarises the evolution of the transgressive dunefield at 41.5 Mile with aerial ortho-imagery.

Figure 4-3 - ***Aerial imagery of the 41.5 Mile region in 2008, 2013 and 2022 showing the evolution of the new transgressive dunefield post 2008 (modified from Hesp et al. (2022b)).***

4.3 Methods

4.3.1 Satellite Derived Changes and Development of the Dunefield

The Digital Earth Australia (DEA) coastlines (1988-2021) dataset (Bishop-Taylor et al., 2021a) was used to quantify the historical shoreline change trends in the study site. The dataset contains vector shorelines derived from annual median shoreline positions within normal tidal conditions and point data at 30 metre intervals including shoreline change statistics (Bishop-Taylor et al., 2021b). To align the shoreline position data with the survey timeline, an additional annual-median shoreline vector at sea-level was derived for 2022 adapting the DEA workflow from Krause et al. (2021). To extract the edge of the advancing dunefield the sub-pixel contour method (Bishop-Taylor et al., 2019) was used on annual medians of the Normalised Difference Vegetation Index (NDVI) from Landsat (5, 7, 8 and 9) imagery from the years 2008 to 2022, with the threshold (0.2) to derive vector representations of the boundary of sand and vegetation.

The sub-pixel contour method is used to extract boundaries between mixed pixels (Bishop-Taylor et al., 2019) and was adapted here to delineate a boundary between sand and vegetation, but the outputs are limited according to pixel size and the threshold of spectral indices. Inevitably, the static threshold represents an imperfect value and potential mixed pixels should be acknowledged as an indicator of predominant cover (Smyth et al., 2022), and not an absolute measure of dunefield extent. Near-concurrent high-resolution imagery and satellite derived vectors are presented in the results figures to support its use with an NDVI threshold of 0.2 (Fig. 4).

4.3.2 LIDAR datasets and Drone Survey Methods

Two baseline elevation Light Detection and Ranging (LIDAR) datasets were used from 2008 and 2018. These were collected by aircraft with different LIDAR sensors, have varying resolution, precision, and accuracy (see links in Supporting Material - SM). Both datasets were analysed in the Geodetic Datum of Australia 1994 (GDA94), Universal Transverse Mercator (UTM) 54S in the Australian Height Datum (AHD) Ausgeoid09.

Drone flight surveys were designed to cover the 41.5 Mile region site with specific flight information included in the supplementary tables. Variations in photos, ground control, and weather conditions reflect the variable dynamic field conditions in remote locations. A DJI Mavic 2 Pro was used for all flights, equipped with a 3 band (RGB) Hasselblad camera. The camera has a 1” CMOS sensor with 20 Megapixels (MPs), 28 mm (35 mm format equivalent) focal length (FL) and uses an electronic (rolling) shutter. DJI Ground Station Pro was used for flight design and operations, with the sensor collecting images using automatic ISO and focus settings and saving in JPEG format. Drone image collection consisted of multiple flight lines at 50 metres above flight location in a crosshatch pattern with nadir and off-nadir (70 degree) imagery. Forward and lateral overlap of images was set to a minimum of 75/60 respectively, with two orthogonal blocks forming a double grid. The location of Ground Control (GCPs) and Check Points (CCPs) was generally standardised across surveys, see table 6 in SM for specifics. Spatial data was collected with a Trimble RTX-GNSS in the GDA94 within UTM zone 54S and AHD09. Estimates of precision for GNSS points were generated from Trimble Business Center and used for individual GCP and CCP precision.

Surveys were processed in Metashape (1.8.4) with uniform processing parameters (Table 5 in SM) following methods from Over et al. (2021) and outlined in DaSilva et al. (2023). Both LIDAR and photogrammetry derived point clouds were imported into ArcGIS Pro 3.0 and converted to digital surface model rasters at 1 metre resolution using the binning method of the average without void filling. Measurements of accuracy are derived from Metashape's total error, which includes the individual RTX point's precision. The error is calculated by determining the distance between the control/check and its modelled position in space, resulting in the root mean square error (RMSE). The independent check point RMSE were used to propagate error estimates between multi-temporal surveys and datasets.

Drone derived 3D datasets were analysed as digital surface models, these include vegetation regrowth and its loss in subsequent volumetric change analyses. This was done as optically derived photogrammetry datasets reconstruct the top of canopy and many of the vegetation types form discrete accretionary dunes (nebkha) that simultaneously build their sediment and vegetation profiles higher. The results therefore show areas that are accreting sediments and increasing vegetation cover, illustrating the inextricable ecogeomorphic feedback that occurs in coastal dune systems as vegetation type and density follows morphology (Costas et al., 2023).

4.3.3 Transect Generation and Analyses

Transect lines were generated at locations of DEA coastlines shoreline analysis, which are located at 30 metre intervals alongshore. They were oriented to the resultant direction of observed aeolian dunefield translation (53˚) and extended inland to the extent of the UAV surveys covered in this study. The stack profile tool in ArcGIS Pro was used to sample height values for surveys at the same distance along the transects. These distance and height values were plotted and analysed in python and R. Volumetric changes (m^3) for representative profiles were calculated by differencing their extent, with volume above transects considered to be accretion (A), below to be erosion (E) and the ratio (R) their relationship (A/|E|).

Profiles were grouped into north and south sub-analysis groups to investigate their distinct slope evolution and resultant topographic changes. These groups were used to aggregate a mean topographic profile of the groups for comparisons. The dunefield's stoss slope was calculated from 3 m AHD to the first major slope break in degrees ($\Delta Y/\Delta X$) for profiles from 2008, 2018 and 2022. The height of 3 m was chosen to standardise analysis at a point above areas that were inundated across the time series and in recognition that the profiles were aggregated as an average profile from the sub-analysis groups. Slopes from 3 m AHD to the crest or maximum value of the transect were calculated for all LIDAR and drone derived surveys. Additionally, the maximum fractional speed-up ratio by JH75 Jackson and Hunt (1975) was calculated for flow up the dunefield stoss slopes as follows:

$$(\delta_{\max}) = 2H/L \qquad (1)$$

where δ_{max} is the maximum fractional speed of the topographically forced flow acceleration of wind approaching the slope, given by the ratio of dune height (*H)* and the cross-shore half length of the dune (*L*) (Wiggs et al., 1994).

In this study, the cross-shore transects are oriented to the predominant wind direction with their origins arising from points of longer-term shoreline change analysis (Fig. 1 and 4).

The profiles were used for calculating the slope in degrees and the JH75 wind speed up ratio as a proxy for understanding the slope and dunefield evolution. The JH75 was developed for wind flow over hills and is not intended to fully explain more complex computational fluid dynamic concepts such as flow-separation (Michelsen et al., 2015, Walker and Hesp, 2013, Davidson et al., 2022, Smyth, 2016), it is used here to provide an estimate of flow interactions in a progressively retreating slope scenario. JH75 does not incorporate transport-limiting factors such as surface roughness effects from vegetation or ground-debris into its model but has been used widely to estimate boundary-layer airflow in dune settings (Walker, 2020, Walker et al., 2017).

4.3.4 Volumetric Analyses

To analyse the volumetric changes of all pixels within the study area, the Geomorphic Change Detection (GCD) software of Wheaton et al. (2010) was used. This was chosen as it allows for comprehensive error propagation between multi-date time series with varying error estimates and has been used in similar multi-temporal coastal dune studies (Hilgendorf et al., 2021, Hilgendorf et al., 2022, Walker et al., 2023). Within GCD the RMSE from independent check points (Table 6, SM) and the LIDAR's metadata are incorporated into the time-series differences and used to create rasters thresholded to significant changes. Sediment compartments within GCD are used to spatially separate volumetric totals between surveys and were created around each transect with a 15-metre rectangle buffer. The volumetric changes with thresholded error were then used to compare surface lowering and raising through the time-series analyses according to the relative location within the surveys. Differences between drone surveys were segmented between beach (below 3 m) and dune (above 3 m) according to the extent of the April 2022 survey. This was done to show variations in volumetric changes alongshore and across profiles during this study and to compare against concurrent wind data. Results provide normalised volumetric changes to area (m^3m^{-2}) and then to time in months between surveys.

4.3.5 Wind Data

Wind data was obtained from a variety of weather sources during the survey period (Fig. 2). A weather station was installed immediately landward of the 41.5 Mile site shoreline and additional wind observations were sourced from the Cape Jaffa weather station located 70 km south of the study site (Australian Bureau of Meteorology). The wind data was analysed to generate estimates of aeolian sand transport potentials following the methods of Fryberger and Dean (1979). The resultant drift direction (RDD) and resultant drift potential (RDP) are based on the mean grain size (0.26 mm) of the dunefield (Short and Hesp, 1984). A threshold velocity of ~6.0 m/s was estimated (following Miot da Silva and Hesp (2010)) in the calculations of RDD and RDP. Limitations of the Fryberger method are reviewed in Pearce and Walker (2005).

4.4 Results

4.4.1 Shoreline position and Rates of Change

To explore the rates of shoreline change in this study, the DEA coastlines dataset was imported using both vector shorelines and points with associated shoreline change statistics. Fig. 4 shows the evolution of the dunefield in two panels; panel A shows the recession of the shoreline and (panel B) the progression of the dunefield through a simple threshold of NDVI illustrating the translation of the sand/vegetation boundary. In panel A the shoreline change rates from the annual-median shoreline positions from 2008 through to 2021 are labelled and overlain with transects oriented in the direction of the predominant dunefield translation and RDD. Panel B shows the resulting rate of landward dunefield translation along the transects oriented to the predominant dunefield translation path (See methods 3.3).

Table 1 shows the spatially grouped north and south mean shoreline change rates from the total time-series of the DEA coastlines dataset (1988-2021), pre-study time-series (1988-2008), during this study (2008 to 2021) and the average dunefield advance rates (2008 to 2020). Across all the time-series groups, the southern transects of the dunefield

(Fig. 4) show larger negative values indicating higher rates of shoreline erosion and landward translation of the dunefield. Panel B in Fig. 4 illustrates the differential progression of the sand/vegetation boundary as derived from NDVI and the resulting mean annual rate of change along the transects. Both sections exhibit a consistent landward advance until 2020, which reverses seawards in the north and continues landwards in the south. The reversal is related to an increase in vegetation cover post-2020 and is predominantly due to invasion of the area by non-native species *Euphorbia paralias* (Sea spurge) and *Cakile maritima* (Sea rocket). This increase in vegetation cover in the north section is visible in the 2022 image of panel A over transects 6 through 10 and is reflected in the u-shaped vegetation lines of 2020-2022 over the 2019 image in panel B (Fig. 4).

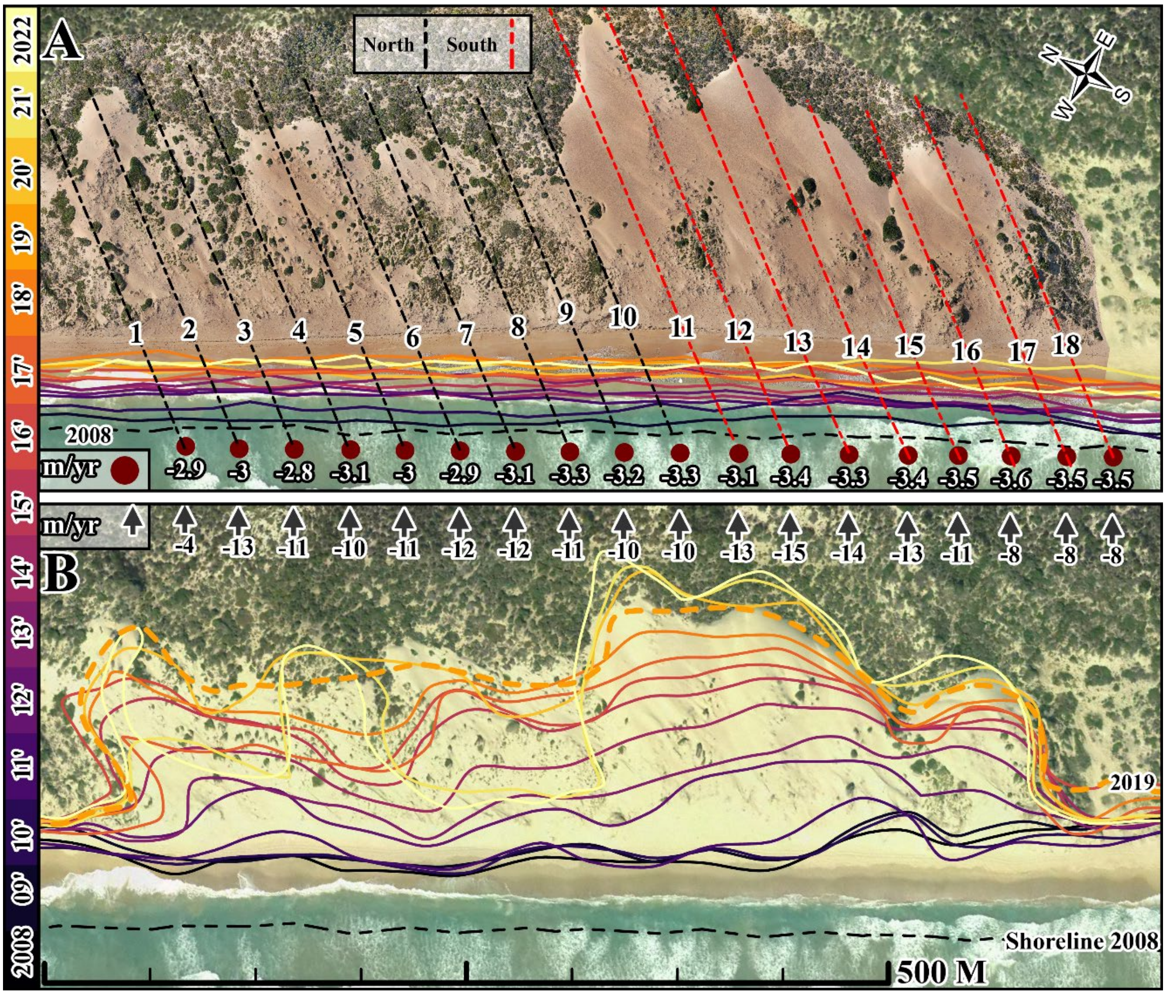

Figure 4-4 – The upper panel (A) shows the cross shore transects, 1-18, oriented to the resultant direction of dunefield translation, classified points representing the shoreline change rates (metres per year) from 2008-2021 from DEA Coastlines v2, and shoreline position vectors from 2008-2022 overlain on an orthomosaic from April 2022. Panel B shows the progression of the landward edge of the dunefield from 2008-2020 with arrows at the top corresponding to Panel A's points with dunefield advance rates in m/yr. Dunefield translation rate is derived from the boundary of annual composites (NDVI threshold 0.2) along oriented transects. Panel B shows the ortho-image and dunefield edge vector (orange dotted line) from 2019. Colour ramp on left side of figure shows classified years for vectors in both A and B panels.

Table 4-1 – Rates of shoreline change (m/year) for 3 periods from the DEA Coastlines dataset. Mean values are calculated for transects 1-10 (north) and 11-18 (south) shown in panel A of Fig. 4. *2008-2020* shows the grouped dunefield advance rates from Panel B of Fig. 4.

	1988 - 2021	1988 - 2008	2008 - 2021	*2008 – 2020*
South	-2.31	-1.5	-3.4	-11.4
North	-2.2	-1.1	-3.1	-10.4

4.3.2 Transect Changes from Elevation Datasets

The following results sections use the derived elevation models from the LIDAR baseline datasets (2008 & 2018) and the 8 successive photogrammetry surveys to compare their volumetric and structural change that occurred between 2008 and 2022.

Fig. 5 shows representative transects from the northern section (transects 2, 3, 7 and 10 in Fig. 4) that show the changes that have occurred during this study period. The 3D models from Apr 2008 and Apr 2022 illustrate the net changes, principally, that the position of the shoreline has retreated landwards and parts of the dunefield have been remobilised or activated. The profiles show the cross-shore landward retreat, illustrating the dunefield's evolution through time. Table 2 gives the volumetric profile changes corresponding to Fig. 5, with accretion and erosion totals showing the gross gain and loss between time periods. Ratio values above 1 indicate a net positive gain of sediment, with values below 1 showing a net loss of sediments. All transects between 2008 and 2018 indicate a negative sediment budget, with a mix of mostly negative and some equal ratios within the other short periods.

This indicates that there is on-going sediment loss and some sediment translation and/or stabilisation across the profiles.

Wave cut scarps are shown by the parallel topographic profiles on the stoss side of the transects (7 and 10) from May 2018 and Apr 2022, with aeolian deflation and cannibalisation flattening the slopes in intervening surveys. Dune height continues to increase past the initial stoss slope, showing the steady increase in elevation and a consistent low slope angle as it approaches the transect maximum high point or crest. Through time, the topographic highs increase slightly in elevation, particularly where vegetation cover has increased since 2020 (Fig. 4). Discrete nebkha form and remnant knobs appear indicated by the increasing roughness in the transects (transects 2 and 3). Remnant knobs and nebkha occur across both northern and southern portions of the dunefield where plants, particularly shrubs and trees, survive the sand inundation. On the lee side, precipitation ridges have formed in profiles 2 and 7, where the dunefields have migrated into leeward topographic lows.

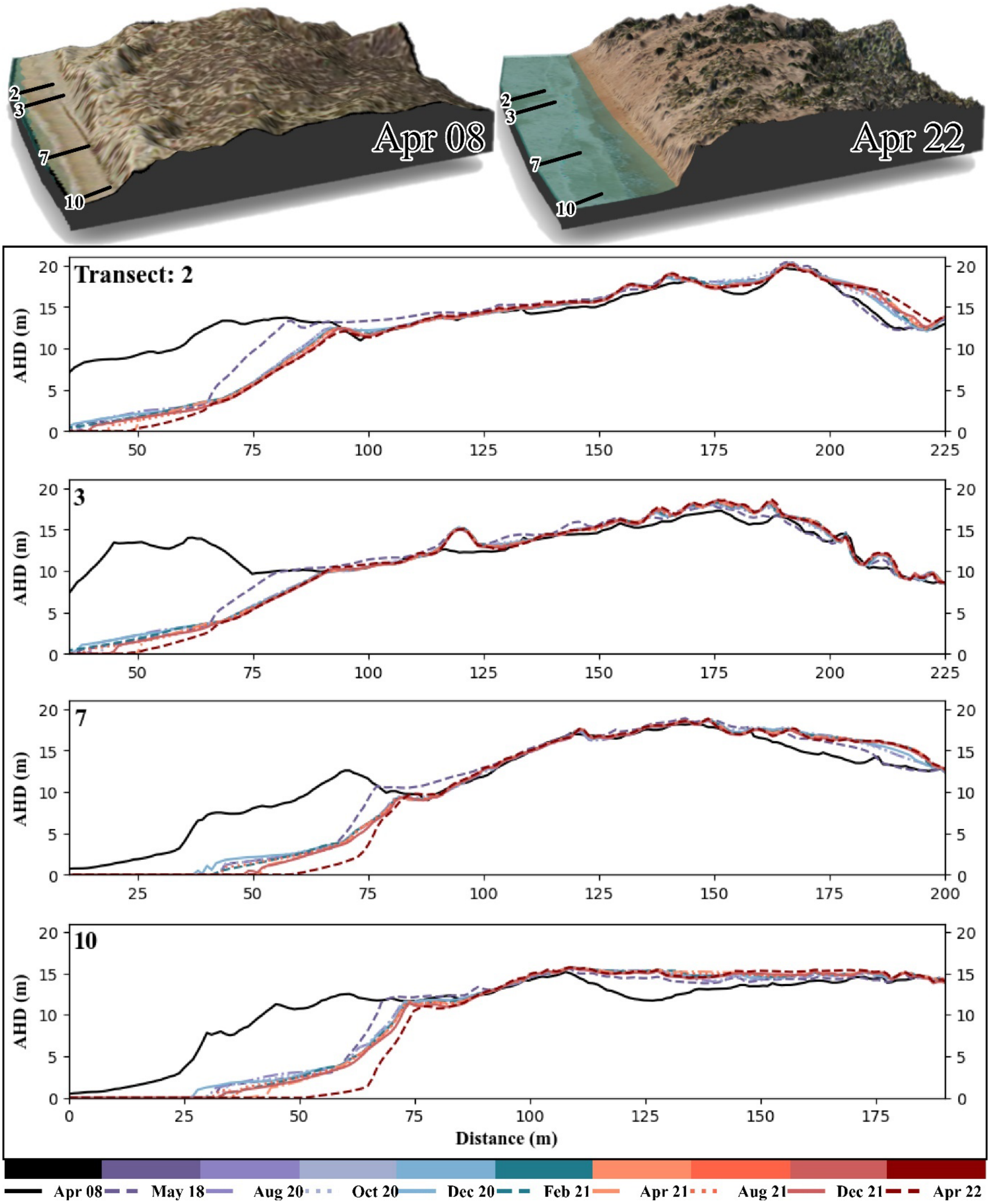

Figure 4-5 – Transects 2, 3, 7, and 10 on the north side of the dunefield, with locations indicated on 3D images (above), and showing the progression of the dunefield through time along the transects. Distance and height in AHD (Australian Height Datum) in metres as generated from elevation datasets.

Table 4-2 – Volumetric changes between transects (Fig. 5) with the Erosion (E), Accretion (A) and Ratio (R) indicated. E and A represent volumetric changes across transects of 1 metre pixels and resulting units are reported in m^3. R shows the ratio between erosion and accretion, where values below 1 indicate a net loss of sediment and values above 1 show a net gain of sediment.

		Apr08-May18	May18 - Aug20	Aug20 - Oct20	Oct20 - Dec20	Dec20 - Feb21	Feb21 - Apr21	Apr21 - Aug21	Aug21 - Dec21	Dec21 - Apr22
2	E	-387	-124	-10	-22	-20	-25	-21	-11	-33
	A	85	47	16	15	16	4	8	20	22
	R	**0.2**	**0.4**	**1.6**	**0.7**	**0.8**	**0.2**	**0.4**	**1.9**	**0.7**
3	E	-461	-78	-10	-14	-12	-27	-14	-13	-25
	A	91	45	8	15	13	5	13	13	15
	R	**0.2**	**0.6**	**0.8**	**1.1**	**1.1**	**0.2**	**0.9**	**1**	**0.6**
7	E	-315	-75	-2	-10	-20	-20	-6	-29	-53
	A	90	41	15	16	16	3	17	1	17
	R	**0.3**	**0.5**	**7.4**	**1.7**	**0.8**	**0.1**	**2.8**	**0**	**0.3**
10	E	-336	-33	-8	-14	-26	-22	-14	-27	-92
	A	86	44	9	18	11	9	18	5	21
	R	**0.3**	**1.4**	**1**	**1.3**	**0.4**	**0.4**	**1.3**	**0.2**	**0.2**

In the southern portion of the dunefield (Fig. 6), the transects show a distinctly different response in comparison to the northern section. Net changes in the southern section show extensive shoreline retreat from the 3D models of 2008 and 2022, but with significant differences in landform change compared to the northern section. There is considerably less vegetation cover with only a few remnant knobs visible in 2022 and more sediment mobilised on the stoss slope and landward regions of the dunefield. Table 3 shows the volumetric profile changes, with accretion and erosion totals indicating the gross gain and loss between time periods. All transects between 2008 and 2018 indicate a negative sediment budget shown by the ratios below 1, with a mix of mostly negative and some balanced (1) ratios within the intra-survey periods indicating mostly net sediment loss but some translation across the profiles.

All transects in Fig. 6 have the parallel scarped profiles from May 2018 and Apr 2022, illustrating the steep scarp slope of 2018 and subsequent flattening through aeolian deflation until scarping recurs in 2022. The dune toe retreats only slightly during the course of the drone surveys between 2020 and 2022. Deflation of the crestal region in transects 14 and 15 occurs, while the topographic highs of transects 11 and 13 remain relatively unchanged. Apart from where topographic lows exist, the inherited topography and vegetation cover on the dunefield crest tends to operate as a sediment translation surface where sediment bypasses it to form downwind precipitation ridges.

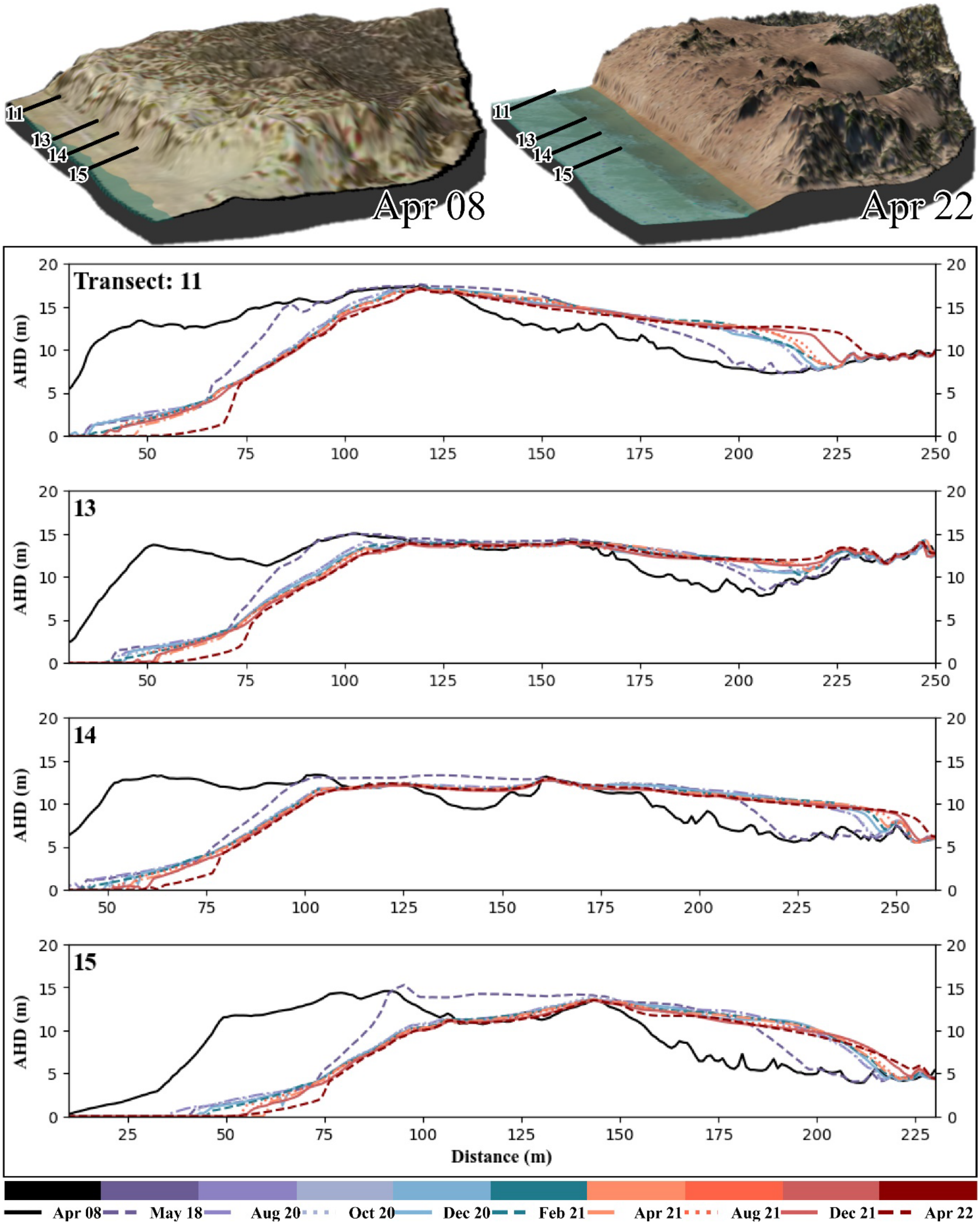

Figure 4-6 – Transects 11, 13, 14, and 15 on the southern section of the dunefield with locations indicated on the 3D images above. The transects show the erosion and translation of the dunefield across the transects. Distance and corresponding height in metres above AHD (Australian Height Datum).

Table 4-3 – Shows resulting volumetric changes between transects (Fig. 6) with the Erosion (E), Accretion (A) and Ratio (R). E and A represent volumetric changes across transects of 1 metre pixels and resulting units are reported in m^3. R shows the ratio between erosion and

accretion, where values below 1 indicate a net loss of sediment and values above 1 show a net gain of sediment.

		Apr08-May18	May18 - Aug20	Aug20 - Oct20	Oct20 - Dec20	Dec20 - Feb21	Feb21 - Apr21	Apr21 - Aug21	Aug21 - Dec21	Dec21 - Apr22
11	E	-484	-148	-12	-29	-24	-28	-21	-34	-91
	A	191	111	10	19	29	14	22	31	37
	R	**0.4**	**0.8**	**0.8**	**0.7**	**1.2**	**0.5**	**1.1**	**0.9**	**0.4**
13	E	-458	-107	-19	-42	-19	-35	-33	-33	-51
	A	136	55	4	13	41	16	16	10	34
	R	**0.3**	**0.5**	**0.2**	**0.3**	**2.1**	**0.5**	**0.5**	**0.3**	**0.7**
14	E	-499	-113	-17	-29	-21	-25	-22	-28	-37
	A	216	116	17	14	19	7	12	11	25
	R	**0.4**	**1**	**1**	**0.5**	**0.9**	**0.3**	**0.5**	**0.4**	**0.7**
15	E	-477	-171	-21	-37	-16	-38	-22	-33	-46
	A	303	116	7	19	19	5	20	11	10
	R	**0.6**	**0.7**	**0.3**	**0.5**	**1.1**	**0.1**	**0.9**	**0.3**	**0.2**

4.3.3 Volumetric Changes

4.3.3.1 Total Changes

Fig. 7 shows the total volumetric changes between the different time-series groups in this study sourced from the elevation datasets. The relief maps illustrate the structural and morphological conditions in each survey and show the changes in roughness as vegetation cover shifts through the dunefield. The 2008 relief image shows the antecedent topography of the relict dunefield before widespread transgression started in the early 2010's (Hesp et al., 2022b), highlighting the differences between the left (north) and right (south) sides of the dunefield. In the north, the stoss slope closest to the waterline has a higher elevation backed by a relatively lower region which increases in height as it extends landwards (profiles 3, 7, and 10 in Fig. 5). The southern dunefield has a more uniform topography in 2008, without noticeable topographic lows in the stoss profile or high elevation in the lee (Fig. 7). Fig. 8 divides the volumetric changes into buffered transects along the profiles of Fig. 4, segmenting the time-series' changes spatially according to the locations of the historical shoreline change analysis. The surface raising and lowering values are normalised to time (m^3 / month) between surveys and show the ratio of sediment gain to loss alongshore of the dunefield, see tables 7 and 8 in SM for exact volumetric totals and ratios. In all time periods of Fig. 8, and especially for the shorter time periods from 2018 to 2022, the transects in the south of the dunefield show the highest rates of volumetric loss on the seaward margin (Fig. 7) and correspond to the highest rates of shoreline erosion and dunefield translation as derived from space (Fig. 4 and Table 1). Profile 10 exists in a boundary zone, where the profile in Fig. 5 is closer to the other north profiles, but the buffer extends into the south and shows the downwind accumulation of sediment through time. The contrasting response in dunefield evolution between the north and south is visible in the difference maps of Fig. 7, with more widespread translation of sediments occurring in the south as sediments are eroded, deflated, and deposited on the landward side of the dunefield.

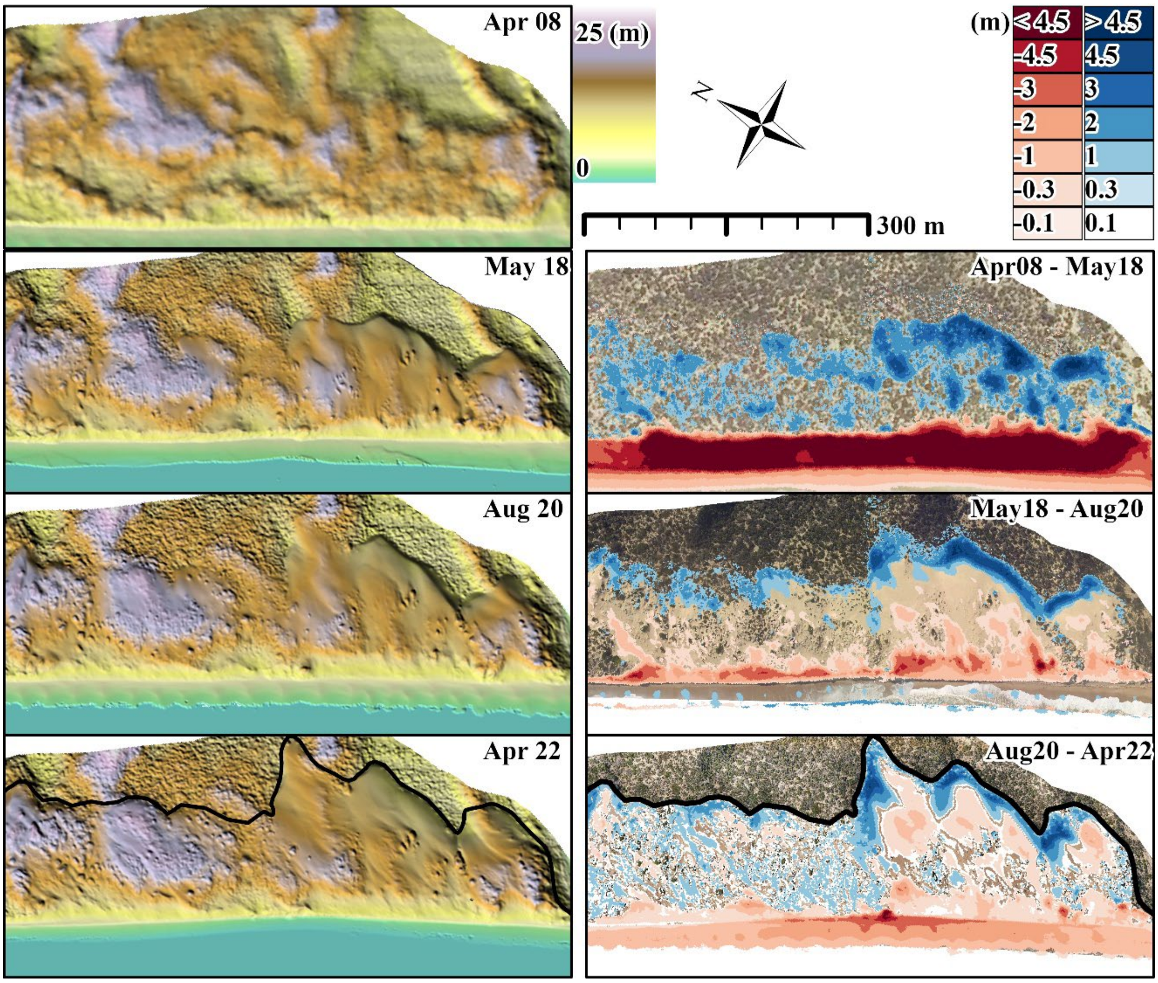

Figure 4-7 – Left side of figure shows the coloured relief and resulting elevation changes that occurred within this study. On the right, the surface changes are shown according to the thresholded (by propagated error) difference between April 2008 and May 2018, May 2018 and August 2020, and August 2020 April 2022. Negative values correspond to surface lowering/erosion, while positive values show surface raising/accretion. The solid black line in April 2022 panels show the extent of dunefield and change analysis.

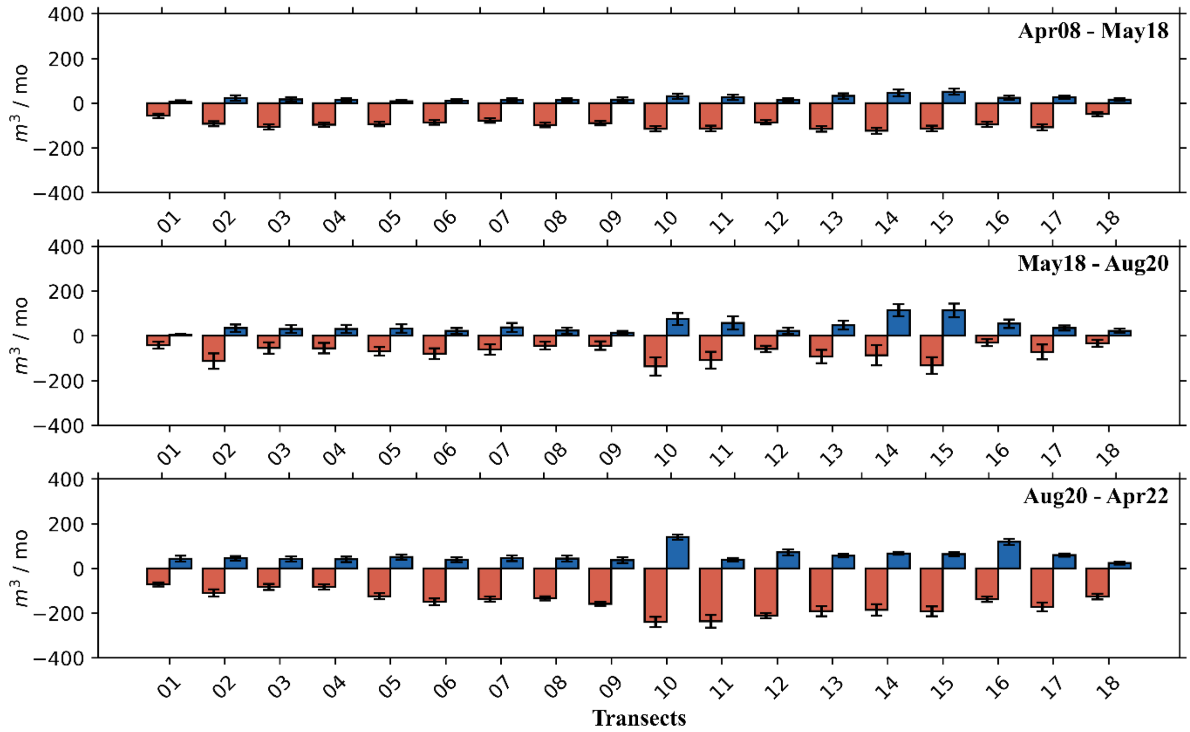

Figure 4-8 – The resulting volumetric changes according to the buffered transects (Fig. 4) showing the dunefield changes normalised to m^3 / month. Transects cover the extent of drone surveys as shown by black extent line in the April 2022 panel in Fig. 7.

4.3.3.2 Intra-survey changes

From August 2020 to April 2022, 8 drone photogrammetry surveys were conducted and are used to generate the topographic changes shown in Fig. 9. These changes are separated between beach and dune changes according to the Apr22 survey, with the resulting normalised volumetric changes (volume/area/time, $m^3m^{-2}m^{-1}$) and wind records presented in table 4 and illustrated in Fig. 10. Through the course of this study, the beach-backshore region fronting the dune system shows both surface raising and lowering between surveys. Over the winter months of 2021, (Aug21-Apr21, Fig. 9), the increase in beach height suggests significant sediment has built up in front of the dune system, either through slumping and debris avalanching off the eroded dune stoss slope or deposited by waves. Our multiple field observations indicate that the former is the dominant process here. The following surveys show surface lowering of the beach and stoss slope from aeolian deflation, and a large wave-cut scarp has formed in the final survey in April 2022 (shown in Fig. 9 from Dec21- Apr22 panel) in the centre of this study area.

The wind records from Cape Jaffa (Fig. 9 i.) and a local met station (Fig. 9 ii. through iv) are used to generate wind roses, as well as a resultant drift direction (RDD) and aeolian resultant drift potential (RDP), to show the variation in local wind patterns and potential sand transport through the time of the surveys. Fig. 9 illustrates the strong relationship between the principal wind direction (RDD), its magnitude (RDP), and the resulting migration of sediments within the dunefield (major deposition locations). In periods where the wind is primarily onshore (Fig. 9 i., ii., v., and vi.) there is a landward migration and building of the precipitation ridges on the northeastern margin of the dunefield. In the periods where the wind is more oblique to alongshore there is substantial northerly accretion and alongshore expansion of the dunefield (Fig. 9, iii., iv., vii. and table 4). The wind patterns throughout this period help illustrate the variability in the predominant forcing mechanism driving the landward translation of sediments in the dunefield, as it compares to the longer-term wind record (Fig. 2) and resultant aeolian drift potential (sand rose in Fig. 1).

Fig. 10 shows the volumetric changes (between drone surveys) along the profiles of Fig. 4 and separated between changes in beach and dune, according to a classification of the Apr 2022 survey. These surface change values illustrate the variable rates of change alongshore and across-profile that are occurring in the areas below (beach) and above (dune) 3 m during this study. Similar to Fig. 8, the highest rates of surface changes are occurring on the right side of the figure in the southern transects 11-18, showing both higher rates of surface loss (erosion) and downwind, landward gain (translation) of sediments. Profile 10 also exhibits high variability in this time-series as its topographic profile exists in the boundary region within the dunefield and extends into the south, with the buffer including the edge of the advancing dunefield in a topographic low (Fig. 4). Certain time periods, such as the winter (Apr21-Aug21) and spring months (Aug20-Oct20) have net positive sediment budgets with predominantly accretional net changes due to sediment accumulation in front of the dune along the beach and leeward accumulation downwind in the dunes (Fig. 10), respectively. Overall, most of the intra-survey changes from transect ratios (Tables 2 and 3) and total volumetric changes (Tables 7 and 8 in SM) indicate a negative sediment budget, with some landward translation but a net loss of sediments and erosion of the dunefield. This is shown especially in Figures 9 and 10 results from the summer (Dec20-Feb 21), autumn (Feb21-Apr 21) and combined time-series (Dec21-Apr22).

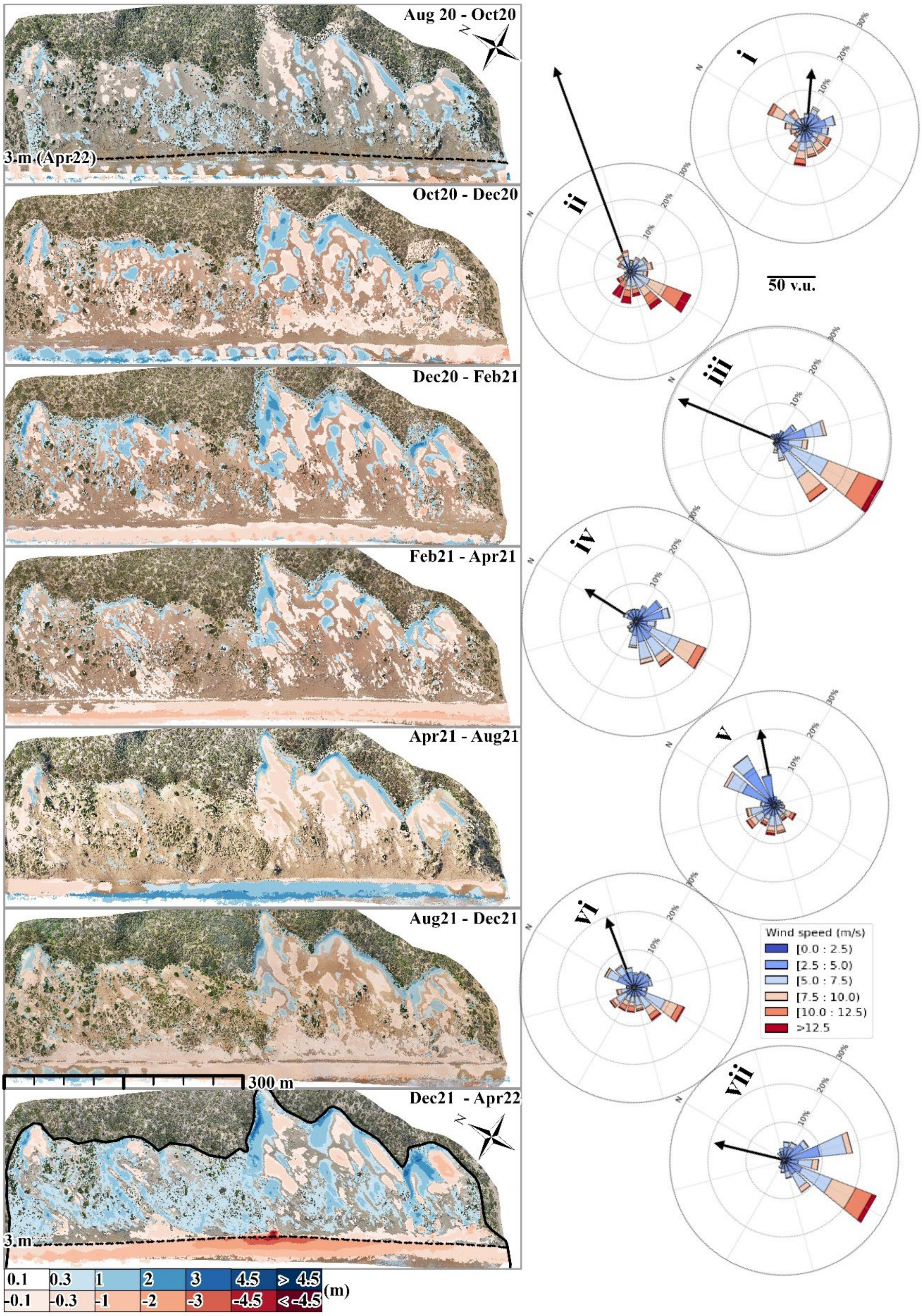

Figure 4-9 – Intra-survey changes of the dunefield as derived from the drone surveys. On the left, surface lowering and raising are shown according to the error thresholded values from the Geomorphic Change Detection (GCD) software from the extent of drone surveys as shown by the black line extent in the final panel. The horizontal dotted line across the first and final

panel show the 3 m contour which is used in further analysis to distinguish beach and dune changes. On the right, wind roses are oriented to the map frame and show the resultant drift potential (vu [in metres/sec]) and direction according to a grain size of 0.26 mm.

Table 4-4 – The net normalised volumetric changes between drone surveys by area and time, ($m^3m^{-2}month^{-1}$) segmented between Beach (B) and Dune (D) areas in the North and South with RDD and RDP for corresponding time periods. Net erosional values are indicated by greyed cells.

Interval	Time (months)	North B	D	South B	D	RDD°	RDP (vu)
Aug20 - Oct20	1.4	-0.055	-0.016	-0.091	0.037	63	36
Oct20 - Dec20	2.5	0.108	0.005	0.021	0.047	41	171
Dec20 - Feb21	1.7	-0.128	0.028	-0.062	0.045	355	78
Feb21 - Apr21	2.6	-0.207	0.013	-0.116	0.045	1	33
Apr21 - Aug21	4.0	0.121	0.002	0.079	0.027	49	49
Aug21 - Dec21	3.5	0.012	-0.014	0.036	0.024	39	54
Dec21 - Apr22	4.2	-0.313	-0.037	-0.293	0.006	344	53

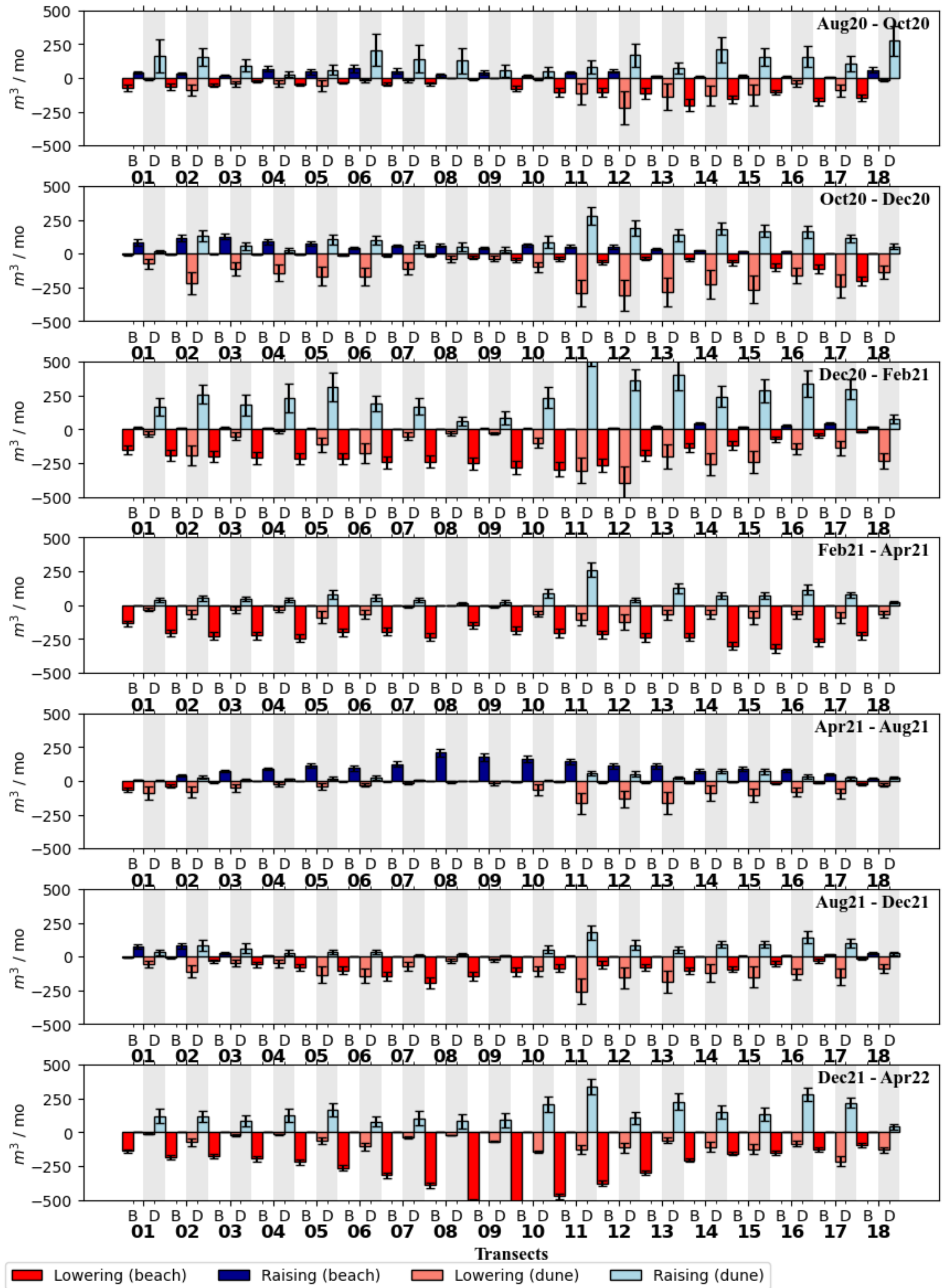

Figure 4-10 - Dunefield changes for the 18 transects illustrated in Fig. 4 during the course of the drone surveys, total volumetric changes are normalised to m3/month and presented in segments according to changes above 3 m (dune) and below 3 m (beach) of the April 2022

survey, see Fig. 9. Dune changes have a light grey background. Compartments are 15 m rectangular buffers from transects.

4.3.4 Relationships between dunefield changes and seaward slope development

The mean topographic profiles oriented in the predominant wind direction are shown in Fig. 11, and illustrate the mean height values at the cross-shore distance in the sub-groups. It illustrates the differences in erosional stoss slope gradients, antecedent topography and their evolution through the course of this study between the north and south profile groups (Fig. 4). Fig. 11, presents the slope in degrees and the fractional speed up ratio (δ_{max}; JH75) for the respective profile groups. On the top left side of each sub-plot is the slope from 3 m AHD to the first major slope break, and in the bottom right from 3 m to the transect crest. The 3 m height point was chosen because it is commonly the dune toe/top of backshore position, to standardise analysis at a point above areas that were inundated across the time series, and in recognition that the profiles were aggregated as an average profile from the sub-analysis groups.

In the north, the stoss slope from 3 m AHD to the first break of slope is steeper with a higher resultant speed up ratio for wind (δ_{max}) than in the south. When measured to the dune crest (at ~142m distance landwards in Fig. 11), both the inclination and resultant fractional speed up ratio decrease compared to the first slope break and become less steep through time from 22.7°/0.83 in 2018 to 7.0°/0.24 in 2022, respectively. This suggests that wind speeds decrease past the first slope break and have a reduced sediment transport potential as they approach the crest. This reduction in wind speed-up has increased local sediment deposition and allowed the vegetation cover to increase, as invasive species that thrive in mild to moderate sand-depositional environments colonise the area. In addition to increasing in height, the slope crest in the north has shifted in time and translated 60 metres landward between 2018 and 2022 as the dunefield builds upwards and landwards.

In contrast to the north, the southern profiles in Fig. 11 display a lower stoss gradient to the first slope break but a relative higher angle slope when measured to the crest. This crestal-slope gradient would allow more sediments in both lower and higher wind velocities to be delivered to the crest and beyond in the south compared to the north. This consistent wind speed-up has maintained the landward translation of sediment across the stoss aeolian sand ramp and deposited it on the leeward side of the dune. The leeward profile in 2008 also shows topographic lows and accommodation space behind the southern crestal region, compared to the higher flatter crestal regions in the north. The crest of the southern profiles has remained consistent in its location across the transect throughout the time-series but has shifted in height; such that it increased from 2008 to 2018 and deflated over the course of the subsequent drone surveys.

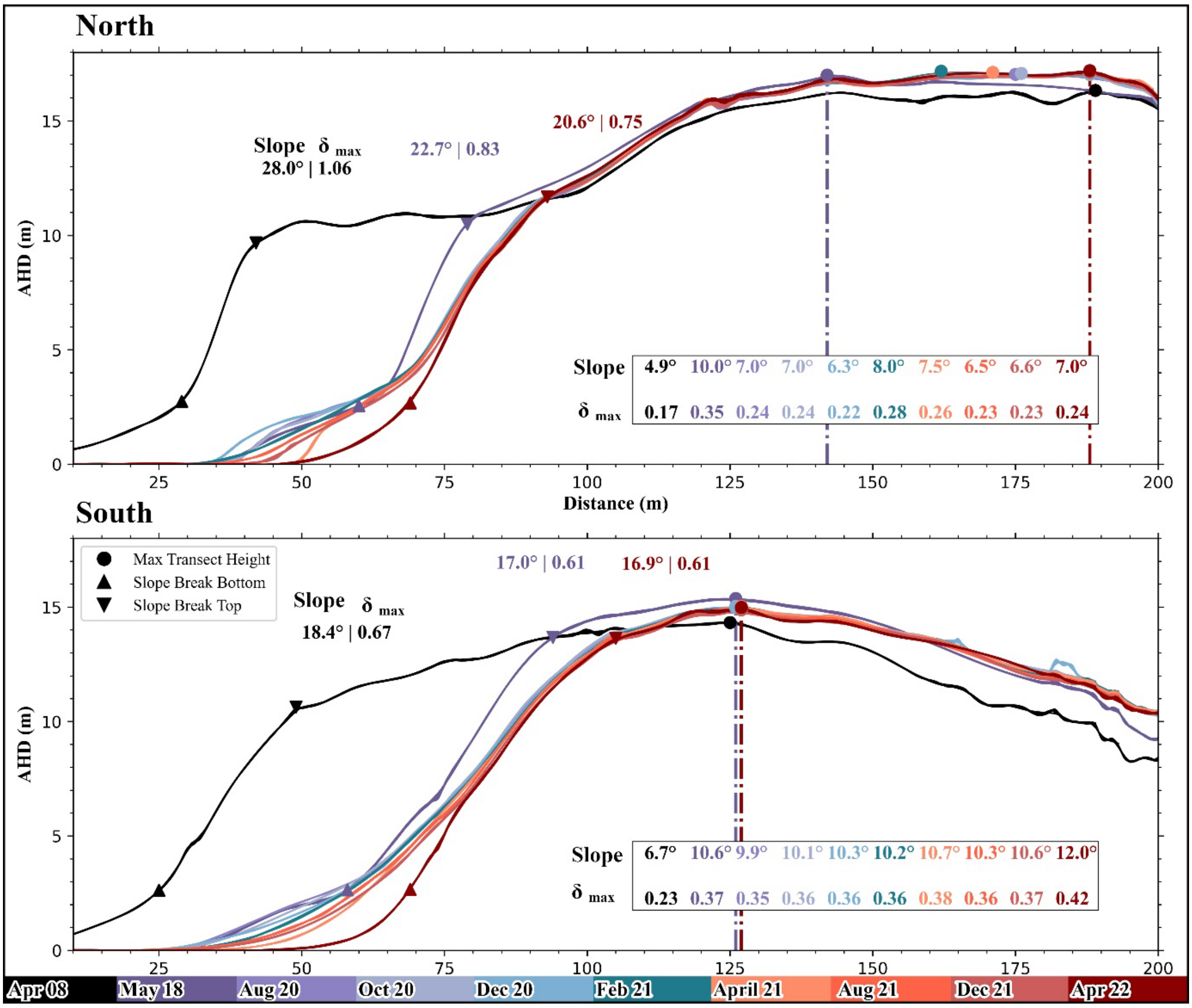

Figure 4-11 – Mean topographic profiles for all transects in the northern and in the southern sections of the study site. Slope (dy/dx) and the maximum flow acceleration (δ_{max}) is calculated for coloured 2008, 2018, and 2022 transects from 3m AHD to the break of slope at the top of the stoss slope (left) side of transect. Below the transect lines, slope and δ_{max} is calculated from 3m AHD to the transect crest (Max Transect Height) for each respective

survey. Max transect height is shown by vertical lines for 2018 and 2022 and by circles on transect lines.

4.5 Discussion

This study documents the recent 3D evolution of a rapidly eroding, translating coastal dunefield. The study site has experienced prolonged retrogradation, with the historical record indicating at least 50 years of retreat (Hesp et al., 2022b), as the translation of sediment comprising the formerly vegetated (relict) transgressive dunefield caused the initiation of a transgressive sand-sheet and eventual formation of a dunefield. In this work, the DEA coastlines dataset was used to show that the increase in the rate of shoreline erosion (table 1) has corresponded to the translation, transgression, and development of a dunefield (Fig. 4). Within the dunefield, differential transgression has occurred post-2020 between the north and south sections of the dunefield. This is linked to the distinct differences in antecedent topography and availability of sediment (Fig. 7) and the evolving stoss slope profiles (Fig. 11). Volumetric changes of the dunefield are presented from representative profiles (Tables 2 and 3) and the buffered sections of transects (Table 4, Fig. 8 and 10) to show that sediments are translating landward, but often at a negative net ratio showing an overall negative system sediment budget. The higher rates of shoreline erosion in the south correspond to the highest rates of dunefield translation and advance of the precipitation ridges (Table 1).

4.5.1 Conceptual Models

The conceptual models developed in the Great Lakes region show that dunefield remobilisation and transgression follow changes in water levels based on stratigraphic dating of dune deposits from the mid- to -late Holocene (Loope and Arbogast, 2000, Anderton and Loope, 1995). These changes are observed in successive deposits of aeolian sediments illustrating the geomorphic response of the adjacent dunefields as rising or high-water levels drive erosion and transgression of dune landforms. In this work, high-resolution 3D datasets are used to quantify the rapid changes as they occur and the model presented in Anderton and Loope (1995) is adapted to provide models for a high wave energy coast undergoing significant wave erosion, not long-term water level changes (Fig. 12 and 13). Fig. 12 shows a cyclical slope model of a retreating coastal dune where wave-driven erosion combined with aeolian cannibalisation has driven its landward translation. The 4 phases of dune retreat and translation according to the model are: (I) waves scarp the dune profile; (II) sediments collapse, slump, and are partially removed by waves; (III) wave erosion continues with aeolian cannibalisation, flattening the slope and depositing sediments at the crest; and then (IV) slope retreat, further flattening, and aeolian cannibalisation continue as sediments are transported downwind and leeward to form a dunefield. An interphase of the scarping, slump, and ramp cycle can occur at any time if/when wave erosion causes a new scarp to develop which is common at this site due to ongoing net erosion. The magnitude and totals of sediment transported to the top and/or lee side of the profile is a product of the interaction of the forcing mechanisms (wind, wave) and evolving transport pathways (slope profiles), as shown by the differential responses in the results of this study.

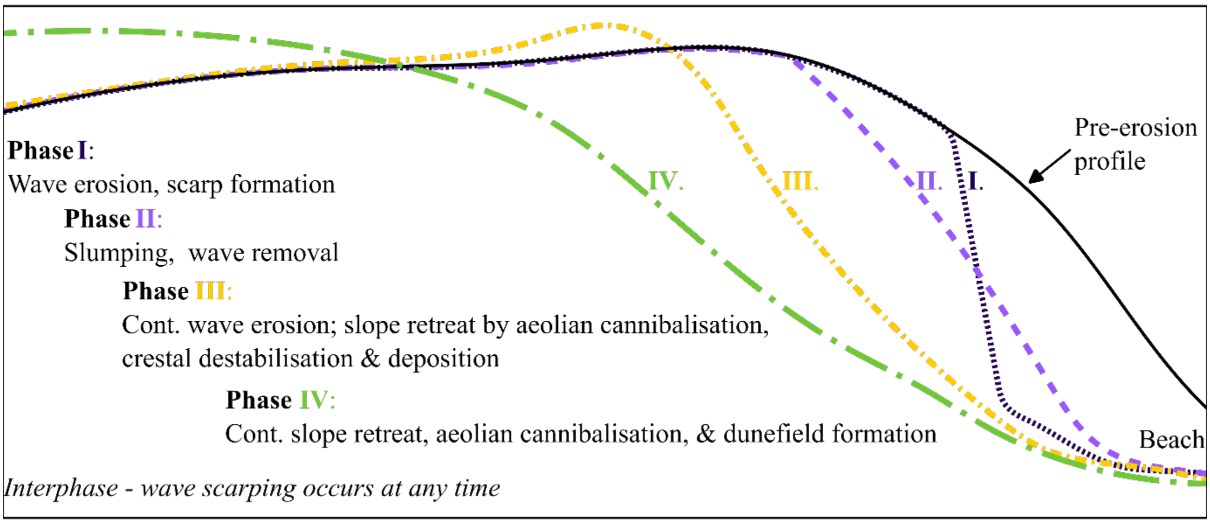

Figure 4-12 – Conceptual slope model of a translating dune experiencing on-going wave driven erosion and aeolian cannibalisation. Phase I occurs as erosion causes the formation of a near-vertical scarp; phase II as the scarp collapses and slumps with sediments removed by waves; phase 3 comprises on-going wave erosion, slope retreat by aeolian cannibalisation paired with crestal deposition. Phase IV as erosion and cannibalisation continues and aeolian processes translate sediments landward and a dunefield is formed.

At the 41.5 Mile section of the barrier, prolonged dunefield erosion is driving the retreat of a dunefield, with the results of this research showing two distinct trajectories for dunefield transgression and the landward translation of sediments. Within this highly erosional section of the barrier, the southern portion is characterised by the formation of downwind sand deposits in slipfaces and precipitation ridges, and in the north a mix of invasive species stabilising and building the dunefield higher. Fig. 13 shows a conceptual model of dunefield retreat and transgression where these two trajectories represent different stages of the dunefield transgression cycle. In the north the profile is characterised by a higher elevation and more gradual stoss-crestal slope which reduces the wind speed-up velocity and sediment transport potential during the erosion in stage 2. This reduction facilitates the aggradation of the dunefield with the growth of species that thrive with moderate sediment deposition and leads to its stabilisation (Stage 3A). As long as beach and dune-toe erosion continue, the retrogradation of the system will continue the scarping, slumping, sand ramping, landward aeolian transport cycle (Fig. 12) until the northern section's topographic profile to the crest is either steeper, shorter in distance, or a combination that facilitates further transgression and translation (stage 3B, Fig. 13). As aeolian cannibalisation continues, the dunefield may form a deflation plain as sediment transgresses landward (stage 4, Fig. 13) and where significant high water/wave events may cause overwash and episodic inundation. After retrogradation and erosion slows or stops, the deflated sand plain may re-vegetate and stabilise (stage 5).

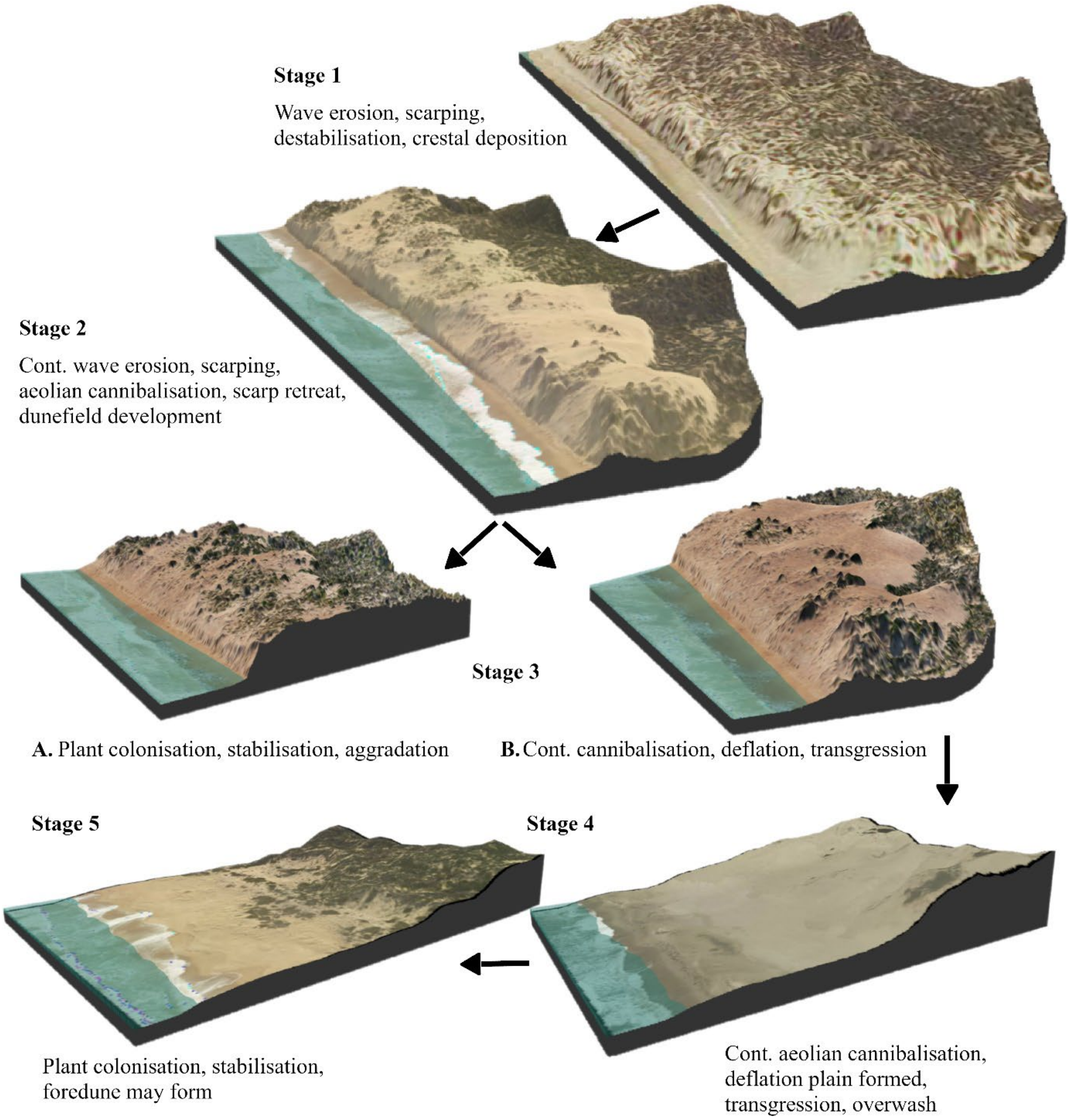

Figure 4-13 – A conceptual model of the evolution stages at 41.5 Mile. In Stage 1, the dunefield enters an early stage of retrogradation, with destabilisation occurring on the stoss slope, accompanied by crestal deposition and vegetation dieback. Stage 2 where continued wave erosion and scarping, paired with aeolian cannibalisation has initiated a sand sheet and then dunefield. Stage 3 where the dunefield may diverge between 3A characterised by vegetation colonisation and stabilisation, or 3B characterised by continued translation and transgression. Stage 4 where aeolian cannibalisation and downwind movement of the dunefield continues and a deflation plain has formed, and stage 5 where plant colonisation and stabilisation take place.

4.5.2 Dunefield Transgression at 41.5 Mile

The 41.5 Mile site has no foredune, as this was removed post-1978 by wave erosion. There is little to no accumulation of wave driven sediments at the base and in front of the stoss slope, and the beach-backshore primarily changes due to alternate processes of scarping and wave removal or stoss slope slumping and temporary accretion (Fig. 12). Eroding coasts with negative local sediment budgets hinder or prevent the recovery or formation of foredunes and result in a perennial sand-ramp and scarp cycle as the beach is in a long-term recession or retrogradation (Davidson et al., 2020).

Figures 14 and 15 shows images of the dunefield, approximately 2 years apart. The label i is located near the origin of transect 10, where wave-cut erosion has degraded the prominent remnant knob in May of 2020 and formed a steep erosional scarp in April 2022. On Fig. 14, label ii is located on a relict parabolic dune ridge, which is acting as a barrier to in-land translation as shown in the profile of transect 13 in Fig. 6. Label iii shows the formation of blowouts on the stoss crest of the eroding dunefield, which have largely flattened and disappeared over time.

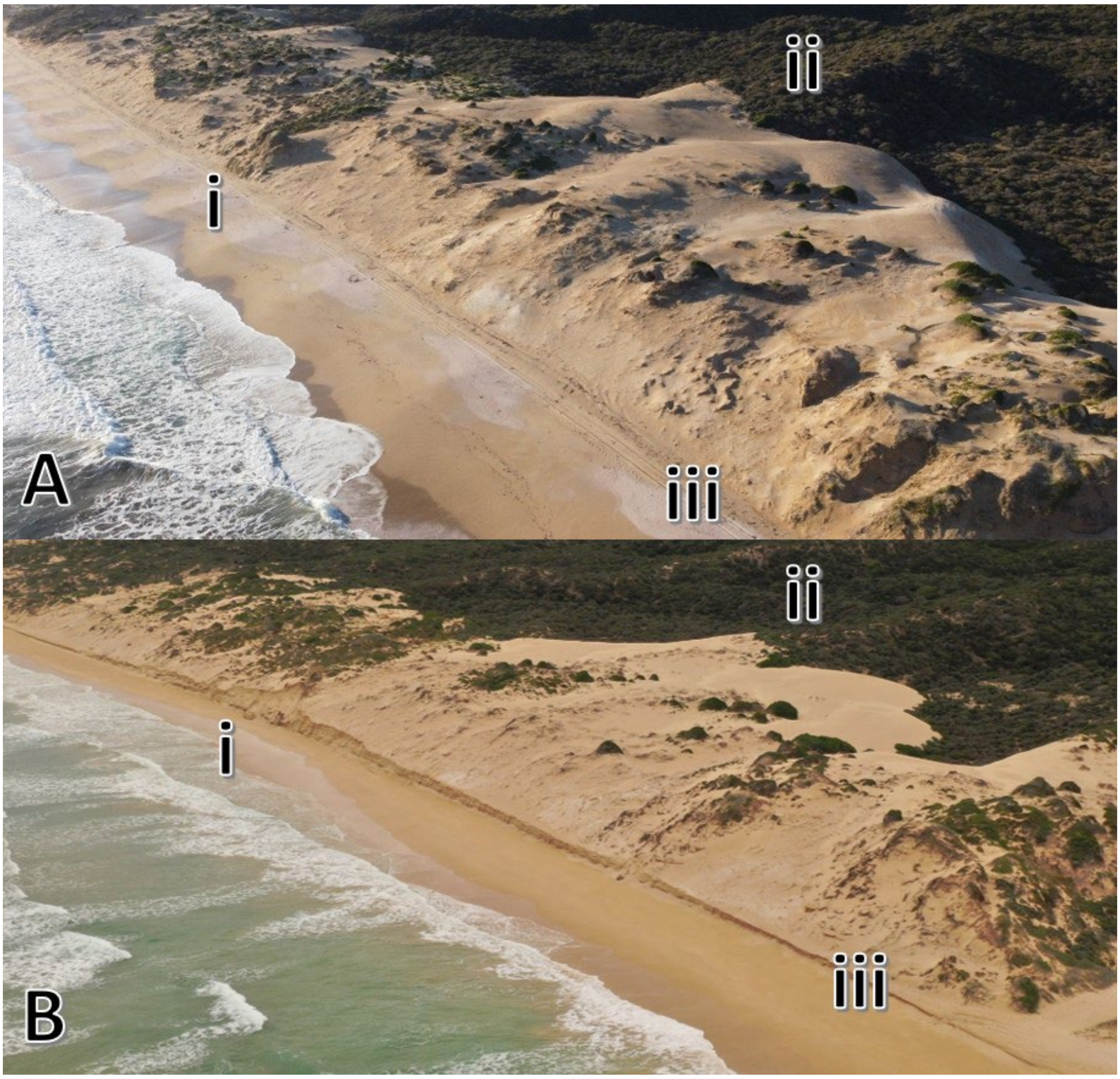

Figure 4-14 - Oblique images of 41.5 Mile from (A) May 2020 and (B) April 2022. Transect 10 crosses i from Figures 4 and 5, showing a remnant knob in (A) and high erosional scarp (B). Transect 13 from Figures 4 and 6 ends approximately at ii, a relict parabolic dune ridge. Location iii shows blowouts forming at the top of the stoss slope (A) and their disappearance (B) as the slope deflates.

The predominant wind direction means that most high-velocity winds capable of sediment transport arrive from the south and southwest from a mix of onshore and oblique alongshore winds (Fig. 1 and 2). Oblique alongshore winds increase the sediment transport potential as it results in increased fetch over (more frequently dry) sandy beach regions (Walker et al., 2017, Bauer and Davidson-Arnott, 2003, Delgado-Fernandez, 2010) and results in less potential wind-speed deceleration (Hesp and Smyth, 2021). Sediment for dunefield translation is often sourced from previous or relict dunes, as opposed to the often-saturated inter-tidal zone which requires higher wind velocities for mobilisation (Hoonhout and de Vries, 2017, Brakenhoff et al., 2019, Walker, 2020, Ruz and Meur-Ferec, 2004, Swann et al., 2021). Fig. 15iv shows a deflated sand plain to the south of the dunefield and is likely a later stage of dunefield transgression as aeolian deflation continues (stage 5 - Fig. 13).

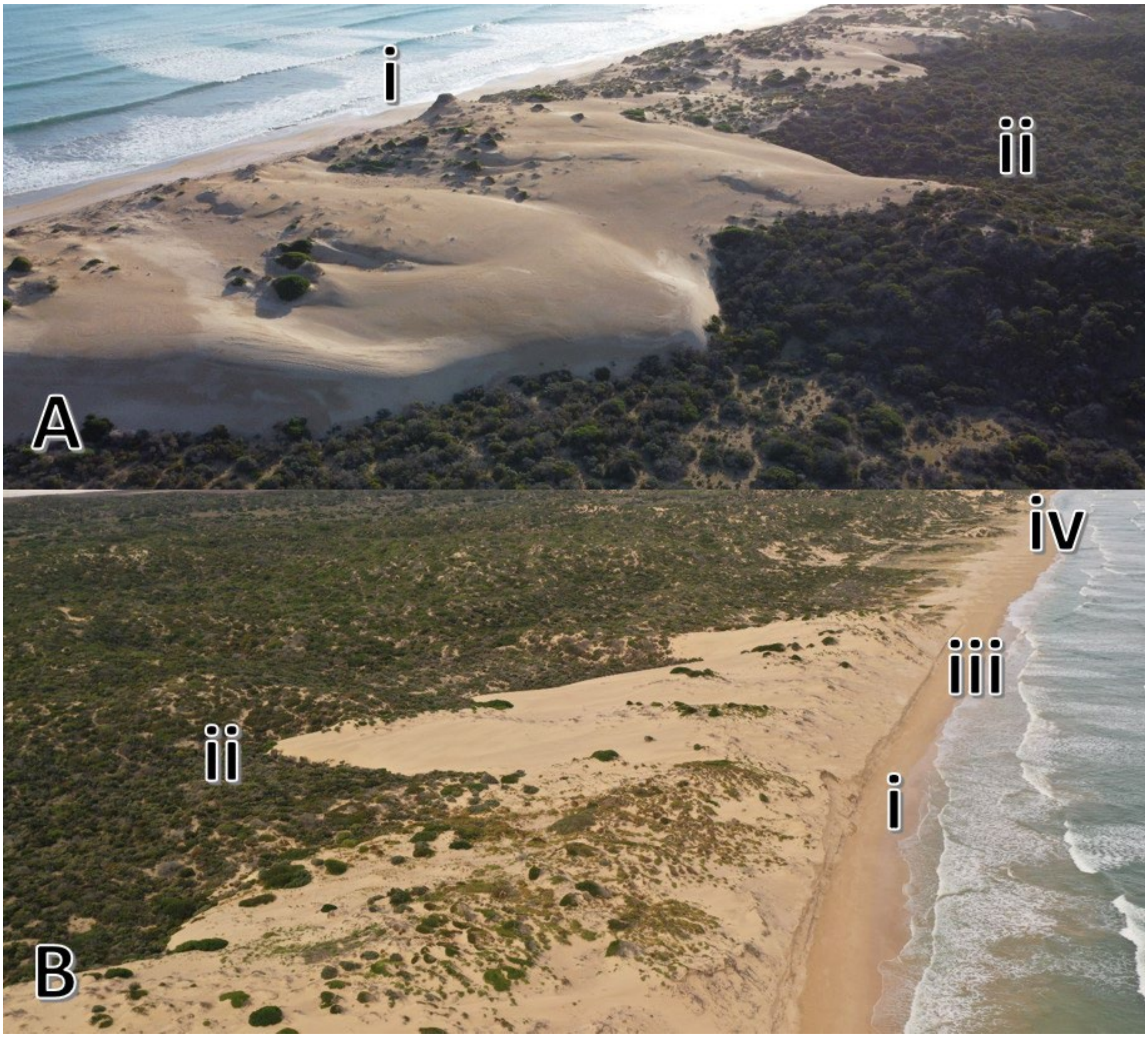

Figure 4-15 - Oblique images of 41.5 from (A) May 2020 and (B) April 2022. Labels i, ii, and iii are landforms shown in Fig. 11. In panel B, the image is oriented to the southeast, showing a deflation plain at label iv which has experienced similar rates of shoreline retrogradation.

4.5.3 Wider Implications and Context

Australian beach and dune systems, including the Younghusband Peninsula are likely far away from a climate change related tipping point that would tilt the barrier into large-scale and prolonged long-term recession (Short, 2022, Short and Cowell, 2009). This study is focused on the landform responses that occur when forcing mechanisms such as beach erosion and aeolian processes combine to drive prolonged retrogradation of coastal systems. However, it acts as a proxy for studying potential effects of a changing climate, as changes in wave energy/direction, storminess, and/or sea level rise may individually or in combination drive the erosion of beaches and dunefields and trigger their destabilisation and transgression.

Our results illustrate the geomorphic response of a dunefield undergoing severe and prolonged retreat and presents quantitative measures of rapid change to the local barrier system. The edge of the dunefield migrates landward about 66 m between 2018 and our last survey 4 years later when measured along the predominant wind direction of the region (Fig. 1, RDD), giving an end point rate of nearly 16.5 m/yr. This rate of landward advance is similar to many of the most rapid rates of dunefield transgression that have been documented (Muckersie and Shepherd, 1995, Shepherd, 1987, Robin et al., 2023). Few contemporary studies of transgressive dunefield initiation exist in the literature (Hesp, 2013) but it is considered that changes in water levels and/or shoreline erosion can trigger a transgressive dunefield phase (Loope and Arbogast, 2000, Anderton and Loope, 1995, Hesp et al., 2022a, Robin et al., 2021, Santos and Latrubesse, 2021, Robin et al., 2023). Recent studies have reiterated the importance of dune stoss slope aerodynamics as a geomorphic control in determining the evolution of vegetated eroding coastal dunes (Smyth et al., 2023, Davidson et al., 2022, Hesp and Smyth, 2021). Recent studies have also documented similar observations to the slope model in Fig. 12, as scarped dunes are unable to be replenished due to frequent wave erosion (Castelle et al., 2017, Laporte-Fauret et al., 2022). The drivers of dunefield and coastal changes in embayments have been shown to be closely aligned with longer-term wind, wave, and climate patterns (González-Villanueva et al., 2023) but also subject to significant changes from storm events (Kennedy et al., 2023). More work is needed to study the potential effects of sea level rise, changes in wind regimes, and altered wave patterns that are acting on the Younghusband Peninsula (YP) as the changes at the 41.5 Mile site represent a regional hotspot of erosion within a highly dynamic barrier system. Within the 190 kms of the YP, shoreline trends range from highly accretional, stable, through to highly erosional as at our study site (Fig. 1) and all of these long-term trends exist within only a few kms to the north and south.

The role of invasive species in the stabilisation of dunefields is difficult to isolate but were observed to be dominant in the post-2020 vegetation stabilisation that occurred in the northern portion of the 41.5 Mile site (Fig. 4). *Cakile maritima* was observed to form seasonal nebkha fields, and dense stands of *Euphorbia paralias* colonised the area (Fig. 12B). These species and *Thinopyrum Junceiforme* have been shown to dominate in South Australian re-vegetating dunefields (DaSilva et al., 2023, Hilton et al., 2006), are predominant in other coastal dunes within the region (DaSilva et al., 2021a, Moulton et al., 2021) and have rapidly spread, altering dune morphology across the Australian coastal dune landscape (Giulio et al., 2022, Garcia-Romero et al., 2019b).

4.6. Conclusions

This study is focused on a coastal dune site which is an erosional hotspot on the Younghusband Peninsula in South Australia. After a period of prolonged erosion, aeolian cannibalisation led to the initiation and development of a transgressive sand sheet in the early 2010's. This study examines the evolutionary trajectory of that coastal sand sheet as it responds to sustained erosion and describes those changes as the dunesheet transitions to a dunefield.

National satellite datasets are used to explore how the rates of shoreline change relate to the landward dunefield translation. The data shows an increase in the rate of change of shoreline erosion from -2.2 m/yr to -3.3 m/yr when segmenting the national datasets from the total (1988-2021) to our time-period (2008-2021). The 2D dunefield evolution from annual satellite derived proxies is compared to high-resolution 3D datasets and quantifies the sediment dynamics of the retreating dunefield. 3D observations are sourced from two LIDAR datasets (2008, 2018) and sequential drone photogrammetry surveys provide a high-resolution time-series of the dunefield's morphological evolution. The volumetric changes show that the cross-shore dune profile is translating but at a system level net loss, indicating a negative sediment budget, with significant removal of sediment to the nearshore and beyond. Within the dunefield, the analysis is separated into two sub-groups based on their respective evolution, rates of shoreline erosion, and landward translation.

The sub-groups are in the north and south of the dunefield, with the results showing their differential evolution is attributed to distinctive differences in antecedent topography, stoss slope morphology, and sediment supply. In the south, higher shoreline erosion is related to higher rates of landward dunefield translation as aeolian cannibalisation, transgression, and deflation results in large downwind accumulations of sediments. The north section has experienced relatively lower rates of erosion and displays a trend towards aggradation, as sediment and vegetation build the dunefield higher and stabilises it. Two adapted conceptual models are presented, one of stoss slope erosion as a cycle of dune scarping, slumping, and ramping drives the retreat of the dunefield, and the other as a dunefield translation evolutionary model where prolonged erosion may lead to a deflated and stabilised sand plain and downwind vegetated dunefield phase.

Dunefield transgression and translation occurs as a response to factors associated with a changing climate, such as sea level rise and increased wave erosion. The results presented here show that as dunefields translate, there can be a net loss of sediments from the system when exposed to prolonged retrogradation. This local dunefield translation has occurred at an incredibly rapid rate over the span of a few years as the contemporary 3D datasets show. The results show that these geomorphological processes possibly occur more frequently than has been observed by dating or stratigraphic studies of Holocene barriers.

CHAPTER 5.

5.1 Summary of Findings

The three studies in this thesis investigate the response and evolution of transgressive coastal dunefields to disturbances with remote sensing and geospatial methods. The studies document the landscape's response to two disturbance types that are considered to be initiation mechanisms or drivers of landscape instability within coastal dunefields in South Australia, Australia. These disturbances may become more prevalent, severe, and/or widespread with a changing climate (East and Sankey, 2020, Warrick et al., 2022) and their study within this thesis helps understand their current state and response to two potential drivers of change, namely, fire and coastal erosion. The chapters apply and develop methods to inform our knowledge of the past, present, and potential future of these natural systems. The core findings contribute to the understanding of the complex interactions of fire severity, landscape stability, ecogeomorphic adaptations of temperate dunefields, and their response to prolonged shoreline erosion. I examine these at different spatial, spectral, and temporal resolutions and study their changes at scales ranging from the broader landscape down to the individual landforms. The key findings from each of the specific chapters and studies are as follows:

1. Chapter 2 has shown how the predominant method of assessing fire severity from space is heavily influenced by the exact characteristics of coastal dunes, namely bright exposed soils/sands and discontinuous canopies. This has led to desktop studies from government and academia suggesting that fire severity within the coastal dune regions of Kangaroo Island was relatively lower than surrounding regions. Chapter 2 develops an improved index for determining fire severity and gives an updated assessment showing that dunefields of Kangaroo Island have been severely burnt by the 2020 Black Summer fires.

This method is an improvement for monitoring the severity of fires with optical remote sensing in dunefields and similar environments with significant potential for wider applications. It combines the available bands within multi-spectral satellite imagery (i.e., Sentinel 2) using the Tasselled Cap Transformation and measures the transformed spectral distance in a temporal sequence as an indication of severity. This alternative method allows the scaling of characteristics such as greenness or soil brightness for calibrated fire severity estimates and could be more suited for large scale assessments of heterogenous landscapes.

2. Chapter 3 examines the response of 3 burnt coastal dunefields on Kangaroo Island. Landscape stability and vegetation dynamics are explored in the year after the fire in relation to their local topography and variability. Wide-spread instability and dunefield transgression is suggested in the literature to follow severe fires, but the results indicate resiliency and re-vegetation.

The results from the drone observations are compared against a time-series of satellite indices, including the index developed in chapter 2, to expand the temporal range of the study. The satellite derived time-series data is used to assess a pre-fire spectral-temporal baseline to compare with the post-fire trajectory and show that the dunefield is approaching the spectral characteristics of the pre-fire unburnt dune system. This combination of sources shows the re-vegetation and ecogeomorphic response of the post-fire dunefields in the year following fire. Its main contribution is to provide a very high spatial and temporal resolution study of the re-vegetation that further aligns with contemporary studies suggesting landscape instability does not always follow fire in coastal dunefields.

3. Chapter 4 illustrates the evolution of a rapidly eroding and transgressing coastal dune system and the differential responses with the studied area. National datasets of the historical and recent erosion trends are compared to the 3D sources to illustrate the evolution of the dunefield profile through time. The results indicate that the translation of sediments is occurring, but at a differential rate related to the antecedent topography, sediment supply, and magnitude of shoreline erosion. This study shows that the highest

rates of translation (from stoss to lee) occur in regions with the highest rates of erosion and larger supplies of sediment (higher volume in pre-erosion stoss slope). Additionally, the translation of the dunefield has occurred at a rapid rate (>10 m/yr) and the cannibalisation process is likely to continue as long as the retrogradation of the shoreline and barrier continues. Two modified conceptual models are advanced on transgressive dunefield retreat and evolution based on the observations of this study. The stoss-slope model shows the cycle of scarp, sand ramp, and retreat during prolonged erosion and the transgressive dunefield translation model illustrates the landform changes that can occur. To date, this is the only study to my knowledge to track the rapid retreat of a coastal landform, and in particular, a transgressive dunefield, in high resolution 3D and 2D scales and measures the total amounts of sediments lost vs gained as a ratio through time. This study quantifies the rapid morphological changes that have occurred and advances conceptual models that improve our understanding of dunefield dynamics and change.

5.2 Future Work

All observations made in this thesis were a product of the resolution of the datasets used, the ability to process those outputs, and the scope of the specific research aim of the studies. Within each chapter there were methods or processes that warrant more investigation. This section will review and expand upon the next steps to advance understanding of these processes, methods, and opportunities. These further areas of work include the following:

5.2.1 Improved Resolutions, Transformations and Sensors

This section will cover two areas of remote sensing applied within this thesis by discussing their limitations and opportunities for future work, these are separated into two sections below: (1) satellite remote sensing and (2) drone derived photogrammetry datasets.

(1) Chapters 2 and 3 investigate the response of burnt coastal dunefields as measured from multi-spectral satellite imagery and progresses an application of an adapted index for broad-scale assessments of heterogenous environments. The ever-evolving technology and expanding knowledge derived from Earth Observation will continue to facilitate significant opportunities for advancements in some of the methods used in this thesis. Specifically, the spatial, temporal, and spectral resolutions of emerging platforms with improved sensors and innovative methods of processing existing datasets will expand the capabilities of space-based observations and analysis. The development of datasets such as the combined harmonised Sentinel 2 and Landsat archives (Claverie et al., 2018) will result in significantly more images available within contiguous time-series for investigations into the past, present, and future. Widely available (and accessible) multi-spectral satellite missions provide data across the natural world and planned missions will be released with improvements in resolutions. The current capabilities of very high-resolution imagery (sub metre) to measure and track fine-scale changes which exists currently have limited widespread application (continental or regional scale) due to their prohibitive costs. The improvement in freely accessible data from improved sensor resolutions or processing of that data will provide a more accurate snapshot of on-ground conditions across huge swaths of extensive natural systems such as coastal environments and dunefields. The spatial resolutions of sensors used in this thesis limited the ability to track specific landforms through time, instead, composites and landscape level statistics showed predominant landcover trends (Chapters 2 and 3) or vector derivations of shorelines (chapters 4 and Appendix 1). Advancements in the processing of spectral information and derivations from medium resolution imagery will progress current techniques, such as fractional cover (Shumack et al., 2021, Beutel et al., 2019) and linear transformations (DaSilva et al., 2021b), and will aid significantly in future studies.

One such method which could be improved, used in Chapters 2 and 3, is the Tasselled Cap Transformation (TCT), initially developed to tailor the spectral resolution available within multi-spectral imagery to specific agricultural crops (Kauth and Thomas, 1976), and has been adapted for detecting environmental disturbances in time-series applications (Viana-Soto et al., 2020, Khodaee et al., 2020, Liu et al., 2018, Healey et al., 2005). There is considerable potential to tailor the coefficients of the individual indices of greenness, brightness, and wetness (TCG, TCB, and TCG) to target landscapes or vegetation types and improve the precision of them in a time-series. Chapter 2 illustrates its use with the general coefficients, but with the accessibility of large-scale computing and extensive repositories of multi-spectral imagery, tailored coefficients for individual pixels, regional landcover types, or local features in a time-series is possible. The extensive datasets of high-resolution satellite and aerial imagery could be leveraged to supplement and support their validity depending on the target ecosystem or environment and would reduce the coarseness that comes with applying uncalibrated methods in a broad application. Existing global or state classifications could be used to augment coefficients for particular applications. Future work should explore the Barest Earth (Roberts et al., 2019) for soil brightness and/or the fractional cover datasets (Beutel et al., 2019) for percent canopy, which could be used to scale multi-temporal indices or observations based on the unique signature of individual pixels.

In chapter 2, one limitation of the methods is that it infers severity as a difference of spectral changes from optical images which are directly influenced by changes in object chemistry. This limits the usefulness of the index in certain situations where large spectral changes do not necessarily discern high fire severity, as Chapter 2 shows with the example of grass fires indicating high severity. Future work could explore the changes that can be derived from near-simultaneous SAR imagery, particularly in cross-polarised backscatter as they can give indications of structural changes (Addison and Oommen, 2018, Tanase et al., 2015, Ban et al., 2020, Havivi et al., 2018). There is considerable interest in developing methods for estimating above-ground biomass from space-borne active remote sensing, either from LIDAR or SAR sensors. Specifically, SAR interferometry (InSAR) which uses multiple images can give estimates of vegetation height and/or structural components of woody branches (Khati and Singh, 2022). The launch of new SAR platforms (Biomass, NISAR) with additional frequencies (P, S, and L) will build extensive global datasets capable of use in InSAR pairs or time-series and facilitate observations of textural information at an unprecedented scale.

(2) Chapters 3 and 4 apply structure from motion methods with images from consumer grade cameras to recreate landforms and track their changes through time. The use of relatively high precision spatial information (GNSS) allowed for the errors that exist in the elevation datasets to be quantified and propagated between surveys, showing the realistic error bounds of the methods (James et al., 2019, James et al., 2020). But the non-metric cameras on the drone, and the unmitigated field conditions within my study sites meant that the resulting ortho-images had limited use in objective time-series analysis. The highly exposed coastal dunefields that were the subject of this thesis experienced dynamic conditions that changed the illumination (cloudy/diffuse vs sunny/shadows), and the landscape's stability (wind affecting sand or vegetation position) which precluded the use of traditional objective image segmentation methods. These limitations could be addressed with an improved classification approach such as a Deep Learning algorithm which are optimal for detecting patterns in nonlinear time-series data (Jansen et al., 2023). These machine learning algorithms have significant potential to be applied to 2D high-resolution images from drones (Joyce et al., 2023) and to their 3D derivative in point clouds for pattern recognition and classification (Guo et al., 2020).

The resulting 3D surface generated from structure from motion gives a top of canopy (digital surface model) dataset, which I used to measure changes in chapters 3 and 4. These optically derived datasets are often used to generate digital terrain (or ground) models by filtering above ground vegetation and other debris through various classification methods (Anders et al., 2019). But within aeolian dune systems there are ecogeomorphic feedbacks where discrete dunes that are aggrading do not have a clear ground/vegetation profile. These accretionary dune types, like nebkha, build their profile up by accumulating or trapping sands. Additionally, the regions explored in chapter 3 and 4, were observed to be dominated by invasive sand trapping plants and grasses (Giulio et al., 2022, Garcia-Romero et al., 2019b), which meant that as these areas aggraded and/or stabilised they became dominated by vegetation that were mostly smaller than the pixels of drone imagery (~1 cm). This was overcome by measuring aggregated changes in the point clouds (Chapter 3) within DSMs (Chapter 4) and interpreting these resulting changes as accretionary. Others have used similar interpretations in dune systems to explore their changes through time and quantify their stability, dynamism, or transgression (Hilgendorf et al., 2022, Hilgendorf et al., 2021, Konlechner and Hilton, 2022). Future work could investigate the structural evolution of vegetation in either eroding or post-fire dunefields by applying Deep Learning (or alternative machine learning algorithms) methods focused on segmentation (vegetation, ground, etc) to track discrete landforms and their changes in these aeolian shaped landscapes.

5.2.2 Longer term studies in burnt dunefields

Chapters 2 and 3 focus on the short-term responses of the post-fire dunefield, observing change on a scale from months to years. In chapter 2, the results illustrate the near-immediate spectral changes that occur post-fire from differenced images before and after the fire. Chapter 3 expands the temporal resolution by using seasonal composites from multi-spectral satellite imagery and 5 drone surveys in the year following the fire. The relatively short time periods of these studies are illustrative of the local changes, but more study is needed to look at both the response (short-term) and longer-term evolution of fire-affected dunefields. This is important as the consequences of repeat and severe burns are less understood as established vegetation communities are prevented from returning to their mature state (Bennett et al., 2016). On Kangaroo Island, the frequency of fire events appears to be increasing as the time between major fires is shortening, as observed in records dating to the 1930's (Bonney et al., 2020). The regions that were the focus of my study were last burnt in 2008 (Bonney et al., 2020), and if this trend of increased frequency continues then re-visiting of these study sites should be considered. Spatial datasets (airborne LIDAR and imagery) were collected following the fire, and future studies could leverage these existing datasets when new spatial data is collected by various government agencies.

In chapter 3, I investigate the post-fire weather patterns and show that monthly temperature and rainfall suggests mild and wet summer months followed the large fire. This coincided with a run of La Niña years (2020-2023), translating to wetter and cooler conditions, which may have been more conducive to the rapid re-vegetation observed in chapter 3. Longer term studies focused on the biodiversity and ecogeomorphic evolution of the dunefield may show decreased resiliency to fires and increasing landscape destabilisation. The use of time-series from satellite remote sensing could be used in future work to evaluate changes in land cover as a consequence of inter-annual shifts in precipitation, weather, or climate indices.

5.2.3 Regional investigations in the Coorong

Chapter 4 focuses on an erosional hotspot within the Younghusband Peninsula (YP) and it represents a response of a temperate dunefield to rapid rates of wave driven erosion. But the changes that are occurring in other regions of the YP barrier are deserving of further investigation. The YP region's environmental conditions, besides wave energy and shoreline orientation, vary only slightly but dunefield stability, structure, and form differ considerably from south to north. Additionally, its 20th century history is similar to many dunefields around the globe that have undergone greening or widespread stabilisation, with studies showing human/animal interventions have further contributed to the vegetation colonisation in the region (Moulton et al., 2018). Across the ~190 km barrier, shoreline change trends vary from highly erosional (chapter 4), to stable, to accretional, with all of these trends exhibited within a few kms of the study site of chapter 4. Further study of the region comparing the evolution of the stable and accretionary portions is necessary to better understand the current differences within these extensive dunefields and how they may change in the future. The foundational work of national agencies have provided a useful repository of 30 years of shoreline trends (Nanson et al., 2022) which can be accessed with relative ease. There is considerable potential to contribute to our understanding of coastal dune responses to a range of shoreline trends by building on the foundations of existing projects such as those from DEA (Krause et al., 2021). Future investigations could use these datasets in conjunction with regional 3D datasets such as the high-resolution 3D (LiDAR) and 2D (Aerial and satellite imagery) datasets that cover the entire region. Larger scale 3D datasets will be able to be generated from InSAR pairs to generate DSMs or DGMs depending on the sensor's wavelength (Amitrano et al., 2021), this capability exists currently but applicable wavelengths are only available through commercial providers with significant costs. Studies could examine the structural changes from the regional datasets that have occurred on the Younghusband Peninsula and investigate their relationship to the regional gradients of wave energy and direction (Moulton et al., 2021).

5.2.4 Improvements in sediment transport models and resulting volumetric changes

In chapter 4, I use local wind data to create models of the resulting sediment transport potential as a means of exploring the relationship between aeolian forces and resulting dunefield changes. Additionally, I orient the 3D volumetric and profile changes along transects in the direction of the predominant wind transport direction. This was done to explore the sediment dynamics of an eroding dunefield and measure how much sediment is sourced from cannibalising relict landforms versus of the intermittently exposed inter-tidal beach area. Within the methods that I used, there are specific limitations and opportunities that could be advanced in future work. These are listed as follows and explained below, (1) limitations of the Fryberger (1979) methods and (2) shifting axis of dunefield extent changes between multi-temporal surveys.

(1) In Chapter 4 the Fryberger method was used to estimate the potential sand transport between time steps. This method has acknowledged limitations, mainly that it does not include supply-limiting factors such as fetch or surface moisture and does not incorporate transport-limiting factors such as surface roughness from vegetation or ground-debris (Pearce and Walker, 2005, Walker, 2020) . As a result, the estimates of potential sediment transport from the Fryberger method are considered to be an over-estimation, with measured results typically much lower than estimates (Walker et al., 2017). In spite of its acknowledged limitations it provides a valuable and widely used method for estimating the sediment transport from wind patterns (Miot da Silva and Hesp, 2010). Further work in this area could incorporate estimates at varying grain sizes into the resulting sand rose estimations, essentially providing a spatially variant estimate of sand transport. This could improve estimates as sediments in coastal dunes are often highly sorted according to their relative topographic position within the beach and dune system. Within chapter 4, I show that the surf-zone sediment size is on-average double the size to that found in the dunes. This means that significantly stronger wind would be needed to mobilise these sediments. Additionally, the Fryberger method assumes dry conditions, but transport over wet sands is significantly different than dry beds (Swann et al., 2021) and the often inundated and larger grain size sediments on the beach are not incorporated into resulting sediment transport models. See the following for recent advancements in dynamic sediment transport models (Shen et al., 2023, Kolesar et al., 2022, Zhao et al., 2021, Yizhaq et al., 2020, Yang et al., 2019, Shen et al., 2019).

(2) The topographic and volumetric changes between surveys in chapter 4 were measured along a fixed orientation from the predominant direction of regional wind records (the resultant drift direction, RDD) across all temporal steps. The wind records illustrate the

intra-annual shifts in dominant direction and magnitude of the wind, and further studies focused on the intricacies of wind-flow patterns, steering, or computational fluid dynamics (CFD) could adjust the direction of topographic or 3D changes accordingly. It is well understood that the slope of a landform affects the resulting wind speed and pathways for sediment transport, (Smyth et al., 2023, Davidson et al., 2022, Bauer and Wakes, 2022, Hesp and Smyth, 2021, Walker, 2020) but to my knowledge no studies have used a shifting principal axis direction according to wind records in a multi-temporal 3D change time-series study. Essentially, showing that 3D topographic and volumetric changes within a region are explained by the variations in the wind record. In chapter 4, I used wind data to interpret the differential 3D dune changes through time with an objective focus on the resulting dunefield's evolution and morphological response. Further work could focus on more detailed analysis (i.e., CFD) and resulting topographic changes alongst a shifting principal axis to better explain the effects of environmental forcing conditions.

5.3 Concluding Remarks

Transgressive coastal dunefields are landscapes that reflect their environmental conditions in their current stability, form, vegetation, and extent. Through the course of this thesis, I have explored some of the mechanisms (fire) and processes (transgression) that are thought to alter dunefield stability (chapters 2 and 3) and the rapid transgression occurring in a dunefield experiencing prolonged coastal erosion and retrogradation (chapter 4). These processes are expected to occur in a world with a changed climate, as temperate regions experience more frequent severe fires, longer windows of conducive seasonal conditions, and sea level rise potentially combined with increased storminess. The research within this thesis has contributed by advancing a multi-spectral method of assessing fire severity in heterogenous landscapes and illustrating the acknowledged but often overlooked or ignored limitation of pre-fire (spectral signature) conditions. This work further explored a contemporary example of post-fire coastal dunefield response, contributing to the growing body of research showing that a severe fire does not necessarily equate to widespread landscape instability. In its final chapter, a very high-resolution example of dunefield retreat is presented, contextualising the rapid pace that dunefields can respond to retrogradation, just as stratigraphic based research has explained from chrono sequences. The remotely sensed observations in this work advance the understanding of the Earth's geomorphological processes and contributes to our understanding of how we can better measure those changes. These dunefields landscapes are products of their environment, and the processes and methods used and developed here give us the capability to measure them as their conditions potentially change, evolve, and/or stabilise.

BIBLIOGRAPHY

AAGAARD, T., ORFORD, J. & MURRAY, A. S. 2007. Environmental controls on coastal dune formation; Skallingen Spit, Denmark. *Geomorphology,* 83**,** 29-47.

ADDISON, P. & OOMMEN, T. 2018. Utilizing satellite radar remote sensing for burn severity estimation. *International Journal of Applied Earth Observation and Geoinformation,* 73**,** 292-299.

ADELEYE, M. A., CONNOR, S. E., HABERLE, S. G., HERBERT, A. & BROWN, J. 2021. European colonization and the emergence of novel fire regimes in southeast Australia. *Anthropocene Review,* 9**,** 537-549.

ALVAREZ-VANHARD, E., HOUET, T., MONY, C., LECOQ, L. & CORPETTI, T. 2020. Can UAVs fill the gap between in situ surveys and satellites for habitat mapping? *Remote Sensing of Environment,* 243**,** 111780.

AMITRANO, D., DI MARTINO, G., GUIDA, R., IERVOLINO, P., IODICE, A., PAPA, M. N., RICCIO, D. & RUELLO, G. 2021. Earth Environmental Monitoring Using Multi-Temporal Synthetic Aperture Radar: A Critical Review of Selected Applications. *Remote Sensing,* 13**,** 604.

ANDERS, N., VALENTE, J., MASSELINK, R. & KEESSTRA, S. 2019. Comparing Filtering Techniques for Removing Vegetation from UAV-Based Photogrammetric Point Clouds. *Drones,* 3**,** 61.

ANDERSON, K., WESTOBY, M. J. & JAMES, M. R. 2019. Low-budget topographic surveying comes of age: Structure from motion photogrammetry in geography and the geosciences. *Progress in Physical Geography-Earth and Environment,* 43**,** 163-173.

ANDERSON, S. W. 2019. Uncertainty in quantitative analyses of topographic change: error propagation and the role of thresholding. *Earth Surface Processes and Landforms,* 44**,** 1015-1033.

ANDERTON, J. B. & LOOPE, W. L. 1995. Buried Soils in a Perched Dunefield as Indicators of Late Holocene Lake-Level Change in the Lake-Superior Basin. *Quaternary Research,* 44**,** 190-199.

ANDREUCCI, S., CLEMMENSEN, L. B. & PASCUCCI, V. 2010. Transgressive dune formation along a cliffed coast at 75 ka in Sardinia, Western Mediterranean: a record of sea-level fall and increased windiness. *Terra Nova,* 22**,** 424-433.

APONTE, C., DE GROOT, W. J. & WOTTON, B. M. 2016. Forest fires and climate change: causes, consequences and management options. *International Journal of Wildland Fire,* 25**,** I-Ii.

ARBOGAST, A. F., LOVIS, W. A., MCKEEHAN, K. G. & MONAGHAN, G. W. 2023. A 5500-year record of coastal dune evolution along the shores of Lake Michigan in the North American Great Lakes: The relationship of lake-level fluctuations and climate. *Quaternary Science Reviews,* 307**,** 108042.

ARBOGAST, A. F. & PACKMAN, S. C. 2004. Middle-Holocene mobilization of aeolian sand in western upper Michigan and the potential relationship with climate and fire. *Holocene,* 14**,** 464-471.

ARKIN, J., COOPS, N. C., HERMOSILLA, T., DANIELS, L. D. & PLOWRIGHT, A. 2019. Integrated fire severity-land cover mapping using very-high-spatial-resolution aerial imagery and point clouds. *International Journal of Wildland Fire,* 28**,** 840-860.

ASH, J. & WASSON, R. 1983. Vegetation and sand mobility in the Australian desert dunefield. *Zeitschrift fur Geomorphologie,* 45**,** 7-25.

ASHTON, A. D. & LORENZO-TRUEBA, J. 2018. Morphodynamics of Barrier Response to Sea-Level Rise. *Barrier Dynamics and Response to Changing Climate.* Springer International Publishing.

AXEL, A. C. 2018. Burned Area Mapping of an Escaped Fire into Tropical Dry Forest in Western Madagascar Using Multi-Season Landsat OLI Data. *Remote Sensing,* 10**,** 371.
BALL, D. 2002. Vegetation. *In:* TYLER, M. J., DAVIES, M. & TWIDALE, C. R. (eds.) *Natural history of Kangaroo Island.* 2nd ed. ed. Adelaide: Royal Society of South Australia.
BAN, Y., ZHANG, P., NASCETTI, A., BEVINGTON, A. R. & WULDER, M. A. 2020. Near Real-Time Wildfire Progression Monitoring with Sentinel-1 SAR Time Series and Deep Learning. *Sci Rep,* 10**,** 1322.
BARBERO, R., ABATZOGLOU, J. T., PIMONT, F., RUFFAULT, J. & CURT, T. 2020. Attributing Increases in Fire Weather to Anthropogenic Climate Change Over France. *Frontiers in Earth Science,* 8**,** 104.
BARCHYN, T. E. & HUGENHOLTZ, C. H. 2013. Reactivation of supply-limited dune fields from blowouts: A conceptual framework for state characterization. *Geomorphology,* 201**,** 172-182.
BARRINEAU, P., WERNETTE, P., WEYMER, B., TRIMBLE, S., HAMMOND, B. & HOUSER, C. 2015. The Critical Zone of Coastal Barrier Systems. *In:* GIARDINO, J. R. & HOUSER, C. (eds.) *Developments in Earth Surface Processes.* Elsevier.
BAUER, B. O. & DAVIDSON-ARNOTT, R. G. D. 2003. A general framework for modeling sediment supply to coastal dunes including wind angle, beach geometry, and fetch effects. *Geomorphology,* 49**,** 89-108.
BAUER, B. O. & WAKES, S. J. 2022. CFD simulations of wind flow across scarped foredunes: Implications for sediment pathways and beach-dune recovery after storms. *Earth Surface Processes and Landforms,* 47**,** 2989-3015.
BAUER, F. H. 1959. The regional geography of Kangaroo Island, South Australia.
BAUMANN, M., OZDOGAN, M., WOLTER, P. T., KRYLOV, A., VLADIMIROVA, N. & RADELOFF, V. C. 2014. Landsat remote sensing of forest windfall disturbance. *Remote Sensing of Environment,* 143**,** 171-179.
BECK, H. E., ZIMMERMANN, N. E., MCVICAR, T. R., VERGOPOLAN, N., BERG, A. & WOOD, E. F. 2018. Present and future Koppen-Geiger climate classification maps at 1-km resolution. *Sci Data,* 5**,** 180214.
BELL, D. T. 2001. Ecological response syndromes in the flora of southwestern Western Australia: Fire resprouters versus reseeders. *Botanical Review,* 67**,** 417-440.
BENNETT, L. T., BRUCE, M. J., MACHUNTER, J., KOHOUT, M., TANASE, M. A. & APONTE, C. 2016. Mortality and recruitment of fire-tolerant eucalypts as influenced by wildfire severity and recent prescribed fire. *Forest Ecology and Management,* 380**,** 107-117.
BERTIN, S., STÉPHAN, P. & AMMANN, J. 2022. Assessment of RTK Quadcopter and Structure-from-Motion Photogrammetry for Fine-Scale Monitoring of Coastal Topographic Complexity. *Remote Sensing,* 14**,** 1679.
BEUTEL, T. S., TREVITHICK, R., SCARTH, P. & TINDALL, D. 2019. VegMachine.net. online land cover analysis for the Australian rangelands. *Rangeland Journal,* 41**,** 355-362.
BIGARELLA, J. J. 1972. Eolian Environments their Characteristics Recognition and Importance.
BIGARELLA, J. J., BECKER, R. D. & DUARTE, G. M. 1969. Coastal dune structures from Parana (Brazil). *Marine Geology,* 7**,** 5-55.
BISHOP-TAYLOR, R., NANSON, R., SAGAR, S. & LYMBURNER, L. 2021a. Digital Earth Australia Coastlines. Geoscience Australia Canberra.
BISHOP-TAYLOR, R., NANSON, R., SAGAR, S. & LYMBURNER, L. 2021b. Mapping Australia's dynamic coastline at mean sea level using three decades of Landsat imagery. *Remote Sensing of Environment,* 267**,** 112734.
BISHOP-TAYLOR, R., SAGAR, S., LYMBURNER, L., ALAM, I. & SIXSMITH, J. 2019. Sub-Pixel Waterline Extraction: Characterising Accuracy and Sensitivity to Indices and Spectra. *Remote Sensing,* 11**,** 2984.

BLAKE, D., NYMAN, P., NICE, H., D'SOUZA, F. M. L., KAVAZOS, C. R. J. & HORWITZ, P. 2020. Assessment of post-wildfire erosion risk and effects on water quality in south-western Australia. *International Journal of Wildland Fire,* 29**,** 240-257.

BONNEY, M. T., HE, Y. H. & MYINT, S. W. 2020. Contextualizing the 2019-2020 Kangaroo Island Bushfires: Quantifying Landscape-Level Influences on Past Severity and Recovery with Landsat and Google Earth Engine. *Remote Sensing,* 12**,** 3942.

BOUCHER, J., BEAUDOIN, A., HÉBERT, C., GUINDON, L. & BAUCE, É. 2017. Assessing the potential of the differenced Normalized Burn Ratio (dNBR) for estimating burn severity in eastern Canadian boreal forests. *International Journal of Wildland Fire,* 26**,** 32-45.

BOURMAN, R. P. 2016. *Coastal landscapes of South Australia*, Adelaide : The University of Adelaide Press.

BOYD, M. 2010. Identification of Anthropogenic Burning in the Paleoecological Record of the Northern Prairies: A New Approach. *Annals of the Association of American Geographers,* 92**,** 471-487.

BRADSTOCK, R. A. 2008. Effects of large fires on biodiversity in south-eastern Australia: disaster or template for diversity? *International Journal of Wildland Fire,* 17**,** 809-822.

BRAKENHOFF, L. B., SMIT, Y., DONKER, J. J. A. & RUESSINK, G. 2019. Tide-induced variability in beach surface moisture: Observations and modelling. *Earth Surface Processes and Landforms,* 44**,** 317-330.

BRANDOLINI, F., GUILLEM, ZERBONI, A. & TURNER, S. 2020. A Google Earth Engine-enabled Python approach to improve identification of anthropogenic palaeo-landscape features. *arXiv pre-print server*.

BRIGHT, B. C., HUDAK, A. T., KENNEDY, R. E., BRAATEN, J. D. & KHALYANI, A. H. 2019. Examining post-fire vegetation recovery with Landsat time series analysis in three western North American forest types. *Fire Ecology,* 15**,** 8.

BROOKE, B. P., HUANG, Z., NICHOLAS, W. A., OLIVER, T. S. N., TAMURA, T., WOODROFFE, C. D. & NICHOL, S. L. 2019. Relative sea-level records preserved in Holocene beach-ridge strandplains - An example from tropical northeastern Australia. *Marine Geology,* 411**,** 107-118.

BRUUN, P. 1962. Sea-level rise as a cause of shore erosion. *Journal of the Waterways and Harbors division,* 88**,** 117-132.

BURNINGHAM, H. & FERNANDEZ-NUNEZ, M. 2020. Shoreline Change Analysis. *Sandy Beach Morphodynamics.* San Diego: Elsevier.

CAMPBELL, M. 1915. Movement of sand dunes on the California coast. *Journal of the Washington Academy of Science,* 5**,** 328.

CARTER, B. 1988. *Coastal environments : an introduction to the physical, ecological, and cultural systems of coastlines*, New York : Academic Press.

CARTER, R., HESP, P. & NORDSTROM, K. 1990. Geomorphology of erosional dune landscapes. *Coastal dunes: Processes and morphology***,** 217-250.

CARVAJAL-RAMÍREZ, F., MARQUES DA SILVA, J. R., AGÜERA-VEGA, F., MARTÍNEZ-CARRICONDO, P., SERRANO, J. & MORAL, F. J. 2019. Evaluation of Fire Severity Indices Based on Pre- and Post-Fire Multispectral Imagery Sensed from UAV. *Remote Sensing,* 11**,** 993.

CARY, G. 2003. *Australia Burning: Fire Ecology, Policy and Management Issues*, Victoria: CSIRO Publishing.

CASELLA, E., DRECHSEL, J., WINTER, C., BENNINGHOFF, M. & ROVERE, A. 2020. Accuracy of sand beach topography surveying by drones and photogrammetry. *Geo-Marine Letters,* 40**,** 255-268.

CASTELLE, B., BUJAN, S., FERREIRA, S. & DODET, G. 2017. Foredune morphological changes and beach recovery from the extreme 2013/2014 winter at a high-energy sandy coast. *Marine Geology,* 385**,** 41-55.

CASTELLE, B., GUILLOT, B., MARIEU, V., CHAUMILLON, E., HANQUIEZ, V., BUJAN, S. & POPPESCHI, C. 2018. Spatial and temporal patterns of shoreline change of a 280-

km high-energy disrupted sandy coast from 1950 to 2014: SW France. *Estuarine Coastal and Shelf Science,* 200**,** 212-223.
CASTELLE, B., LAPORTE-FAURET, Q., MARIEU, V., MICHALET, R., ROSEBERY, D., BUJAN, S., LUBAC, B., BERNARD, J. B., VALANCE, A., DUPONT, P., EL MOCTAR, A. O. & NARTEAU, C. 2019. Nature-Based Solution along High-Energy Eroding Sandy Coasts: Preliminary Tests on the Reinstatement of Natural Dynamics in Reprofiled Coastal Dunes. *Water,* 11**,** 2518.
CHEN, X. X., VOGELMANN, J. E., ROLLINS, M., OHLEN, D., KEY, C. H., YANG, L. M., HUANG, C. Q. & SHI, H. 2011. Detecting post-fire burn severity and vegetation recovery using multitemporal remote sensing spectral indices and field-collected composite burn index data in a ponderosa pine forest. *International Journal of Remote Sensing,* 32**,** 7905-7927.
CHRISTIANSEN, C., DALSGAARD, K., MOLLER, J. & BOWMAN, D. 1990. Coastal dunes in Denmark chronology in relation to sea level in Dunes of the European Coasts. Geomorphology-Hydrology-Soils. *Catena. Supplement (Giessen)***,** 61-70.
CHUVIECO, E., AGUADO, I., SALAS, J., GARCÍA, M., YEBRA, M. & OLIVA, P. 2020. Satellite Remote Sensing Contributions to Wildland Fire Science and Management. *Current Forestry Reports,* 6**,** 81-96.
CHUVIECO, E., MOUILLOT, F., VAN DER WERF, G. R., SAN MIGUEL, J., TANASE, M., KOUTSIAS, N., GARCÍA, M., YEBRA, M., PADILLA, M., GITAS, I., HEIL, A., HAWBAKER, T. J. & GIGLIO, L. 2019. Historical background and current developments for mapping burned area from satellite Earth observation. *Remote Sensing of Environment,* 225**,** 45-64.
CLAVERIE, M., JU, J., MASEK, J. G., DUNGAN, J. L., VERMOTE, E. F., ROGER, J. C., SKAKUN, S. V. & JUSTICE, C. 2018. The Harmonized Landsat and Sentinel-2 surface reflectance data set. *Remote Sensing of Environment,* 219**,** 145-161.
COLLINS, L., BRADSTOCK, R. A. & PENMAN, T. D. 2014. Can precipitation influence landscape controls on wildfire severity? A case study within temperate eucalypt forests of south-eastern Australia. *International Journal of Wildland Fire,* 23**,** 9-20.
COLOMINA, I. & MOLINA, P. 2014. Unmanned aerial systems for photogrammetry and remote sensing: A review. *Isprs Journal of Photogrammetry and Remote Sensing,* 92**,** 79-97.
COOPER, H. M., WASKLEWICZ, T., ZHU, Z., LEWIS, W., LECOMPTE, K., HEFFENTRAGER, M., SMABY, R., BRADY, J. & HOWARD, R. 2021. Evaluating the Ability of Multi-Sensor Techniques to Capture Topographic Complexity. *Sensors (Basel),* 21**,** 2105.
COOPER, J. A. G., MASSELINK, G., COCO, G., SHORT, A. D., CASTELLE, B., ROGERS, K., ANTHONY, E., GREEN, A. N., KELLEY, J. T., PILKEY, O. H. & JACKSON, D. W. T. 2020. Sandy beaches can survive sea-level rise. *Nature Climate Change,* 10**,** 993-+.
COOPER, W. S. 1958. *Coastal sand dunes of Oregon and Washington*, Geological Society of America.
COOPER, W. S. 1967. Coastal dunes of California.
COPPOLETTA, M., MERRIAM, K. E. & COLLINS, B. M. 2016. Post-fire vegetation and fuel development influences fire severity patterns in reburns. *Ecol Appl,* 26**,** 686-99.
CORDOVA, C. E., KIRSTEN, K. L., SCOTT, L., MEADOWS, M. & LÜCKE, A. 2019. Multi-proxy evidence of late-Holocene paleoenvironmental change at Princessvlei, South Africa: The effects of fire, herbivores, and humans. *Quaternary Science Reviews,* 221**,** 105896.
COSTAS, S. 2022. Evolutionary Trajectories of Coastal Sand Barriers along the West Portuguese Coast during the Holocene. *Journal of Marine Science and Engineering,* 10**,** 1894.

COSTAS, S., GALLEGO-FERNÁNDEZ, J. B., DE SOUSA, L. B. & KOMBIADOU, K. 2023. Ecogeomorphic response of a coastal dune in southern Portugal regulated by extrinsic factors. *CATENA,* 221**,** 106796.

COSTAS, S., JEREZ, S., TRIGO, R. M., GOBLE, R. & REBÊLO, L. 2012. Sand invasion along the Portuguese coast forced by westerly shifts during cold climate events. *Quaternary Science Reviews,* 42**,** 15-28.

COSTAS, S., NAUGHTON, F., GOBLE, R. & RENSSEN, H. 2016. Windiness spells in SW Europe since the last glacial maximum. *Earth and Planetary Science Letters,* 436**,** 82-92.

COWLING, R. M. & PIERCE, S. M. 1988. Secondary Succession in Coastal Dune Fynbos - Variation Due to Site and Disturbance. *Vegetatio,* 76**,** 131-139.

CRIST, E. P. 1985. A Tm Tasseled Cap Equivalent Transformation for Reflectance Factor Data. *Remote Sensing of Environment,* 17**,** 301-306.

CRIST, E. P. & CICONE, R. C. 1984. A Physically-Based Transformation of Thematic Mapper Data - the Tm Tasseled Cap. *Ieee Transactions on Geoscience and Remote Sensing,* 22**,** 256-263.

CSIRO 2020. State of the Climate 2020. Bureau of Meteorology.

CUNLIFFE, A. M., ANDERSON, K., BOSCHETTI, F., BRAZIER, R. E., GRAHAM, H. A., MYERS-SMITH, I. H., ASTOR, T., BOER, M. M., CALVO, L. G., CLARK, P. E., CRAMER, M. D., ENCINAS-LARA, M. S., ESCARZAGA, S. M., FERNANDEZ-GUISURAGA, J. M., FISHER, A. G., GDULOVA, K., GILLESPIE, B. M., GRIEBEL, A., HANAN, N. P., HANGGITO, M. S., HASELBERGER, S., HAVRILLA, C. A., HEILMAN, P., JI, W., KARL, J. W., KIRCHHOFF, M., KRAUSHAAR, S., LYONS, M. B., MARZOLFF, I., MAURITZ, M. E., MCINTIRE, C. D., METZEN, D., MENDEZ-BARROSO, L. A., POWER, S. C., PROSEK, J., SANZ-ABLANEDO, E., SAUER, K. J., SCHULZE-BRUNINGHOFF, D., SIMOVA, P., SITCH, S., SMIT, J. L., STEELE, C. M., SUAREZ-SEOANE, S., VARGAS, S. A., VILLARREAL, M., VISSER, F., WACHENDORF, M., WIRNSBERGER, H. & WOJCIKIEWICZ, R. 2022. Global application of an unoccupied aerial vehicle photogrammetry protocol for predicting aboveground biomass in non-forest ecosystems. *Remote Sens Ecol Conserv,* 8**,** 57-71.

DASILVA, M., DA SILVA, G. M., HESP, P. A., BRUCE, D., KEANE, R. & MOORE, C. 2021a. Assessing Shoreline Change using Historical Aerial and RapidEye Satellite Imagery (Cape Jaffa, South Australia). *Journal of Coastal Research,* 37**,** 468-483.

DASILVA, M. D., BRUCE, D., HESP, P. A. & DA SILVA, G. M. 2021b. A New Application of the Disturbance Index for Fire Severity in Coastal Dunes. *Remote Sensing,* 13**,** 4739.

DASILVA, M. D., BRUCE, D., HESP, P. A., DA SILVA, G. M. & DOWNES, J. 2023. Post-wildfire coastal dunefield response using photogrammetry and satellite indices. *Earth Surface Processes and Landforms,* 48**,** 1845-1868.

DAVIDSON-ARNOTT, R., BAUER, B. & HOUSER, C. 2019. *Introduction to coastal processes and geomorphology*, Cambridge university press.

DAVIDSON-ARNOTT, R. G. D. 2005. Conceptual model of the effects of sea level rise on sandy coasts. *Journal of Coastal Research,* 21**,** 1166-1172.

DAVIDSON-ARNOTT, R. G. D. & BAUER, B. O. 2021. Controls on the geomorphic response of beach-dune systems to water level rise. *Journal of Great Lakes Research,* 47**,** 1594-1612.

DAVIDSON-ARNOTT, R., HESP, P., OLLERHEAD, J., WALKER, I., BAUER, B., DELGADO-FERNANDEZ, I. & SMYTH, T. 2018. Sediment budget controls on foredune height: Comparing simulation model results with field data. *Earth Surface Processes and Landforms,* 43**,** 1798-1810.

DAVIDSON, S. G., HESP, P. & MIOT DA SILVA, G. 2021. Rapid shoreline erosion and dunefield Change, Salmon Hole, South Australia. *Sci Total Environ,* 767**,** 145406.

DAVIDSON, S. G., HESP, P. A., DASILVA, M. & DA SILVA, G. M. 2022. Flow dynamics over a high, steep, erosional coastal dune slope. *Geomorphology,* 402**,** 108111.

DAVIDSON, S. G., HESP, P. A. & SILVA, G. M. D. 2020. Controls on dune scarping. *Progress in Physical Geography: Earth and Environment,* 44**,** 923-947.
DAVIES, J. L. 1980. *Geographical variation in coastal development,* New York, Hafner Pub. Co.
DELGADO-FERNANDEZ, I. 2010. A review of the application of the fetch effect to modelling sand supply to coastal foredunes. *Aeolian Research,* 2**,** 61-70.
DELGADO-FERNANDEZ, I. & DAVIDSON-ARNOTT, R. 2011. Meso-scale aeolian sediment input to coastal dunes: The nature of aeolian transport events. *Geomorphology,* 126**,** 217-232.
DELGADO-FERNANDEZ, I., O'KEEFFE, N. & DAVIDSON-ARNOTT, R. G. D. 2019. Natural and human controls on dune vegetation cover and disturbance. *Sci Total Environ,* 672**,** 643-656.
DEPARTMENT OF AGRICULTURE, W. A. T. E. 2020. Australian Google Earth Engine Burnt Area Map. *In:* DEPARTMENT OF AGRICULTURE, W. A. T. E. (ed.) *A Rapid, National Approach to Fire Severity Mapping.* Canberra.
DEROSE, R. J., LONG, J. N. & RAMSEY, R. D. 2011. Combining dendrochronological data and the disturbance index to assess Engelmann spruce mortality caused by a spruce beetle outbreak in southern Utah, USA. *Remote Sensing of Environment,* 115**,** 2342-2349.
DEVRIES, B., PRATIHAST, A. K., VERBESSELT, J., KOOISTRA, L. & HEROLD, M. 2016. Characterizing Forest Change Using Community-Based Monitoring Data and Landsat Time Series. *PLoS One,* 11**,** e0147121.
DILLENBURG, S. R., BARBOZA, E. G., TOMAZELLI, L. J., AYUP-ZOUAIN, R. N., HESP, P. A. & CLEROT, L. C. 2009. The Holocene Coastal Barriers of Rio Grande do Sul. *Geology and Geomorphology of Holocene Coastal Barriers of Brazil.* Springer.
DILLENBURG, S. R., HESP, P. A., KEANE, R., DA SILVA, G. M., SAWAKUCHI, A. O., MOFFAT, I., BARBOZA, E. G. & BITENCOURT, V. J. B. 2020. Geochronology and evolution of a complex barrier, Younghusband Peninsula, South Australia. *Geomorphology,* 354**,** 107044.
DRAPER, N. 2015. Islands of the dead? Prehistoric occupation of Kangaroo Island and other southern offshore islands and watercraft use by Aboriginal Australians. *Quaternary International,* 385**,** 229-242.
DRUMMOND, C. D., HARLEY, M. D., TURNER, I. L., A MATHEEN, A. N. & GLAMORE, W. C. UAV applications to coastal engineering. Australasian Coasts & Ports Conference 2015: 22nd Australasian Coastal and Ocean Engineering Conference and the 15th Australasian Port and Harbour Conference, 2015. Engineers Australia and IPENZ, 267.
EAST, A. E. & SANKEY, J. B. 2020. Geomorphic and Sedimentary Effects of Modern Climate Change: Current and Anticipated Future Conditions in the Western United States. *Reviews of Geophysics,* 58.
ELLETT, N. G., PIERCE, J. L. & GLENN, N. F. 2019. Partitioned by process: Measuring post-fire debris-flow and rill erosion with Structure from Motion photogrammetry. *Earth Surface Processes and Landforms,* 44**,** 3128-3146.
ELTNER, A. & JAMES, M. R. 2022. 1.5 Guidelines for flight operations. *UAVs for the Environmental Sciences.*
EPTING, J. & VERBYLA, D. 2005. Landscape-level interactions of prefire vegetation, burn severity, and postfire vegetation over a 16-year period in interior Alaska. *Canadian Journal of Forest Research,* 35**,** 1367-1377.
ESCUIN, S., NAVARRO, R. & FERNÁNDEZ, P. 2007. Fire severity assessment by using NBR (Normalized Burn Ratio) and NDVI (Normalized Difference Vegetation Index) derived from LANDSAT TM/ETM images. *International Journal of Remote Sensing,* 29**,** 1053-1073.

FARRELL, E. J., FERNANDEZ, I. D., SMYTH, T., LI, B. L. & SWANN, C. 2023. Contemporary research in coastal dunes and aeolian processes. *Earth Surface Processes and Landforms*.

FASSNACHT, F. E., SCHMIDT-RIESE, E., KATTENBORN, T. & HERNÁNDEZ, J. 2021. Explaining Sentinel 2-based dNBR and RdNBR variability with reference data from the bird's eye (UAS) perspective. *International Journal of Applied Earth Observation and Geoinformation,* 95**,** 102262.

FEAGIN, R. A., SHERMAN, D. J. & GRANT, W. E. 2005. Coastal erosion, global sea-level rise, and the loss of sand dune plant habitats. *Frontiers in Ecology and the Environment,* 3**,** 359-364.

FERNÁNDEZ-GUISURAGA, J. M., SANZ-ABLANEDO, E., SUÁREZ-SEOANE, S. & CALVO, L. 2018. Using Unmanned Aerial Vehicles in Postfire Vegetation Survey Campaigns through Large and Heterogeneous Areas: Opportunities and Challenges. *Sensors,* 18**,** 586.

FILION, L. 1984. A Relationship between Dunes, Fire and Climate Recorded in the Holocene Deposits of Quebec. *Nature,* 309**,** 543-546.

FILION, L. 2017. Holocene Development of Parabolic Dunes in the Central St. Lawrence Lowland, Québec. *Quaternary Research,* 28**,** 196-209.

FILION, L., SAINT-LAURENT, D., DESPONTS, M. & PAYETTE, S. 1991. The late Holocene record of aeolian and fire activity in northern Québec, Canada. *The Holocene,* 1**,** 201-208.

FISHER, A. & HESSE, P. P. 2019. The response of vegetation cover and dune activity to rainfall, drought and fire observed by multitemporal satellite imagery. *Earth Surface Processes and Landforms,* 44**,** 2957-2967.

FISHER, T. G., DEVRIES-ZIMMERMAN, S. J., HANSEN, E. C., WOLIN, J. A., LEPPER, K. & SPANBAUER, T. 2021. Drought coincident with aeolian activity in a Great Lakes coastal dune setting during the Algoma Phase (3.1-2.4 ka), southwest Michigan. *Journal of Great Lakes Research,* 47**,** 1468-1484.

FLANNIGAN, M. D., KRAWCHUK, M. A., DE GROOT, W. J., WOTTON, B. M. & GOWMAN, L. M. 2009. Implications of changing climate for global wildland fire. *International Journal of Wildland Fire,* 18**,** 483-507.

FONSTAD, M. A., DIETRICH, J. T., COURVILLE, B. C., JENSEN, J. L. & CARBONNEAU, P. E. 2013. Topographic structure from motion: a new development in photogrammetric measurement. *Earth Surface Processes and Landforms,* 38**,** 421-430.

FORMAN, S. L. 2015. Episodic eolian sand deposition in the past 4000 years in Cape Cod National Seashore, Massachusetts, USA in response to possible hurricane/storm and anthropogenic disturbances. *Frontiers in Earth Science,* 3**,** 3.

FRASER, C. S. 2013. Automatic Camera Calibration in Close Range Photogrammetry. *Photogrammetric Engineering and Remote Sensing,* 79**,** 381-388.

FRASER, R. H., VAN DER SLUIJS, J. & HALL, R. J. 2017. Calibrating Satellite-Based Indices of Burn Severity from UAV-Derived Metrics of a Burned Boreal Forest in NWT, Canada. *Remote Sensing,* 9**,** 279.

FRENCH, N. H. F., KASISCHKE, E. S., HALL, R. J., MURPHY, K. A., VERBYLA, D. L., HOY, E. E. & ALLEN, J. L. 2008. Using Landsat data to assess fire and burn severity in the North American boreal forest region: an overview and summary of results. *International Journal of Wildland Fire,* 17**,** 443-462.

FRYBERGER, S., G. & DEAN, G. 1979. Dune forms and wind regime. *A study of global sand seas,.* Washington, D.C.

G. POLEY, L. & J. MCDERMID, G. 2020. A Systematic Review of the Factors Influencing the Estimation of Vegetation Aboveground Biomass Using Unmanned Aerial Systems. *Remote Sensing,* 12**,** 1052.

GAO, J. J., KENNEDY, D. M. & KONLECHNER, T. M. 2020. Coastal dune mobility over the past century: A global review. *Progress in Physical Geography-Earth and Environment,* 44**,** 814-836.
GAO, J. J., KENNEDY, D. M., KONLECHNER, T. M., MCSWEENEY, S., CHIARADIA, A. & MCGUIRK, M. 2022. Changes in the vegetation cover of transgressive dune fields: A case study in Cape Woolamai, Victoria. *Earth Surface Processes and Landforms,* 47**,** 778-792.
GARCIA-ROMERO, L., DELGADO-FERNANDEZ, I., HESP, P. A., HERNANDEZ-CALVENTO, L., HERNANDEZ-CORDERO, A. I. & VIERA-PEREZ, M. 2019a. Biogeomorphological processes in an arid transgressive dunefield as indicators of human impact by urbanization. *Sci Total Environ,* 650**,** 73-86.
GARCIA-ROMERO, L., HESP, P. A., PENA-ALONSO, C., MIOT DA SILVA, G. & HERNANDEZ-CALVENTO, L. 2019b. Climate as a control on foredune mode in Southern Australia. *Sci Total Environ,* 694**,** 133768.
GARDNER, D. 1955. *Beach-sand heavy-mineral deposits of eastern Australia*, Department of National Development, Bureau of Mineral Resources, Geology and ….
GASCON, F., BOUZINAC, C., THÉPAUT, O., JUNG, M., FRANCESCONI, B., LOUIS, J., LONJOU, V., LAFRANCE, B., MASSERA, S., GAUDEL-VACARESSE, A., LANGUILLE, F., ALHAMMOUD, B., VIALLEFONT, F., PFLUG, B., BIENIARZ, J., CLERC, S., PESSIOT, L., TRÉMAS, T., CADAU, E., DE BONIS, R., ISOLA, C., MARTIMORT, P. & FERNANDEZ, V. 2017. Copernicus Sentinel-2A Calibration and Products Validation Status. *Remote Sensing,* 9**,** 584.
GIBSON, R., DANAHER, T., HEHIR, W. & COLLINS, L. 2020. A remote sensing approach to mapping fire severity in south-eastern Australia using sentinel 2 and random forest. *Remote Sensing of Environment,* 240**,** 111702.
GILL, T., JOHANSEN, K., PHINN, S., TREVITHICK, R., SCARTH, P. & ARMSTON, J. 2016. A method for mapping Australian woody vegetation cover by linking continental-scale field data and long-term Landsat time series. *International Journal of Remote Sensing,* 38**,** 679-705.
GIRARDI, J. D. & DAVIS, D. M. 2010. Parabolic dune reactivation and migration at Napeague, NY, USA: Insights from aerial and GPR imagery. *Geomorphology,* 114**,** 530-541.
GIULIO, S., PINNA, L. C., CARBONI, M., MARZIALETTI, F., ACOSTA, A. T. R., GARBOLINO, E. & JUCKER, T. 2022. Invasion dynamics and potential future spread of sea spurge (Euphorbia paralias) across Australia's coastal dunes. *Journal of Biogeography,* 49**,** 378-390.
GOLDSMITH, V. 1973. Internal Geometry and Origin of Vegetated Coastal Sand Dunes. *Journal of Sedimentary Petrology,* 43**,** 1128-1142.
GONÇALVES, G., GONÇALVES, D., GÓMEZ-GUTIÉRREZ, Á., ANDRIOLO, U. & PÉREZ-ALVÁREZ, J. A. 2021. 3D Reconstruction of Coastal Cliffs from Fixed-Wing and Multi-Rotor UAS: Impact of SfM-MVS Processing Parameters, Image Redundancy and Acquisition Geometry. *Remote Sensing,* 13**,** 1222.
GONÇALVES, J. A. & HENRIQUES, R. 2015. UAV photogrammetry for topographic monitoring of coastal areas. *ISPRS Journal of Photogrammetry and Remote Sensing,* 104**,** 101-111.
GONZÁLEZ-VILLANUEVA, R., PASTORIZA, M., HERNÁNDEZ, A., CARBALLEIRA, R., SÁEZ, A. & BAO, R. 2023. Primary drivers of dune cover and shoreline dynamics: A conceptual model based on the Iberian Atlantic coast. *Geomorphology,* 423**,** 108556.
GRAY, P. C., RIDGE, J. T., POULIN, S. K., SEYMOUR, A. C., SCHWANTES, A. M., SWENSON, J. J. & JOHNSTON, D. W. 2018. Integrating Drone Imagery into High Resolution Satellite Remote Sensing Assessments of Estuarine Environments. *Remote Sensing,* 10**,** 1257.

GROHMANN, C. H., GARCIA, G. P. B., AFFONSO, A. A. & ALBUQUERQUE, R. W. 2020. Dune migration and volume change from airborne LiDAR, terrestrial LiDAR and Structure from Motion-Multi View Stereo. *Computers & Geosciences,* 143, 104569.
GUERSCHMAN, J. P., SCARTH, P. F., MCVICAR, T. R., RENZULLO, L. J., MALTHUS, T. J., STEWART, J. B., RICKARDS, J. E. & TREVITHICK, R. 2015. Assessing the effects of site heterogeneity and soil properties when unmixing photosynthetic vegetation, non-photosynthetic vegetation and bare soil fractions from Landsat and MODIS data. *Remote Sensing of Environment,* 161, 12-26.
GUO, Y., WANG, H., HU, Q., LIU, H., LIU, L. & BENNAMOUN, M. 2020. Deep learning for 3d point clouds: A survey. *IEEE transactions on pattern analysis and machine intelligence,* 43, 4338-4364.
HANSEN, E., DEVRIES-ZIMMERMAN, S., DAVIDSON-ARNOTT, R., VAN DIJK, D., BODENBENDER, B., KILIBARDA, Z., THOMPSON, T. & YURK, B. 2020. Dunes of the Laurentian Great Lakes. *Inland Dunes of North America.* Springer International Publishing.
HANSEN, E. C., FISHER, T. G., ARBOGAST, A. F. & BATEMAN, M. D. 2010. Geomorphic history of low-perched, transgressive dune complexes along the southeastern shore of Lake Michigan. *Aeolian Research,* 1, 111-127.
HAVIVI, S., AMIR, D., SCHVARTZMAN, I., AUGUST, Y., MAMAN, S., ROTMAN, S. R. & BLUMBERG, D. G. 2018. Mapping dune dynamics by InSAR coherence. *Earth Surface Processes and Landforms,* 43, 1229-1240.
HAYES, J. J. & ROBESON, S. M. 2011. Relationships between fire severity and post-fire landscape pattern following a large mixed-severity fire in the Valle Vidal, New Mexico, USA. *Forest Ecology and Management,* 261, 1392-1400.
HEALEY, S. P., COHEN, W. B., YANG, Z. Q. & KRANKINA, O. N. 2005. Comparison of Tasseled Cap-based Landsat data structures for use in forest disturbance detection. *Remote Sensing of Environment,* 97, 301-310.
HEALEY, S. P., YANG, Z. Q., COHEN, W. B. & PIERCE, D. J. 2006. Application of two regression-based methods to estimate the effects of partial harvest on forest structure using Landsat data. *Remote Sensing of Environment,* 101, 115-126.
HEMER, M. A., SIMMONDS, I. & KEAY, K. 2008. A classification of wave generation characteristics during large wave events on the Southern Australian margin. *Continental Shelf Research,* 28, 634-652.
HESP, P. 1988. Morphology, Dynamics and Internal Stratification of Some Established Foredunes in Southeast Australia. *Sedimentary Geology,* 55, 17-41.
HESP, P. 1999. Barrier morphodynamics. *Handbook of beach and shoreface morphodynamics*, 307-333.
HESP, P. 2002. Foredunes and blowouts: initiation, geomorphology and dynamics. *Geomorphology,* 48, 245-268.
HESP, P. 2011a. Dune Coasts. *Treatise on Estuarine and Coastal Science.*
HESP, P. & THOM, B. 1990. Geomorphology and evolution of active transgressive dunefields. *Coastal dunes. Form and process.*
HESP, P. & WALKER, I. 2021. 11.17 Coastal Dunes (V2). *Treatise on Geomorphology*.
HESP, P. A. 2011b. A review of biological and geomorphological processes involved in the initiation and development of incipient foredunes. *Proceedings of the Royal Society of Edinburgh. Section B. Biological Sciences,* 96, 181-201.
HESP, P. A. 2013. Conceptual models of the evolution of transgressive dune field systems. *Geomorphology,* 199, 138-149.
HESP, P. A., DASILVA, M., DA SILVA, G. M., BRUCE, D. & KEANE, R. 2022a. Review and direct evidence of transgressive aeolian sand sheet and dunefield initiation. *Earth Surface Processes and Landforms,* 47, 2660-2675.
HESP, P. A., DASILVA, M., MIOT DA SILVA, G., BRUCE, D. & KEANE, R. 2022b. Review and direct evidence of transgressive aeolian sand sheet and dunefield initiation. *Earth Surface Processes and Landforms,* 47, 2660-2675.

HESP, P. A., HERNÁNDEZ-CALVENTO, L., GALLEGO-FERNÁNDEZ, J. B., MIOT DA SILVA, G., HERNÁNDEZ-CORDERO, A. I., RUZ, M.-H. & ROMERO, L. G. 2021. Nebkha or not? -Climate control on foredune mode. *Journal of Arid Environments,* 187**,** 104444.
HESP, P. A. & MARTÍNEZ, M. L. 2007. Disturbance Processes and Dynamics in Coastal Dunes. *In:* JOHNSON & MIYANISHI (eds.) *Plant Disturbance Ecology.* Elsevier.
HESP, P. A. & SMYTH, T. A. 2021. CFD flow dynamics over model scarps and slopes. *Physical Geography,* 42**,** 1-24.
HESP, P. A. & WALKER, I. J. 2013. 11.17 Coastal Dunes. *In:* SHRODER, J. F. (ed.) *Treatise on Geomorphology.* San Diego: Academic Press.
HESP, P. A. & WALKER, I. J. 2022. Coastal Dunes. *In:* SHRODER, J. F. (ed.) *Treatise on Geomorphology.* Oxford: Academic Press.
HILGENDORF, Z., MARVIN, M. C., TURNER, C. M. & WALKER, I. J. 2021. Assessing Geomorphic Change in Restored Coastal Dune Ecosystems Using a Multi-Platform Aerial Approach. *Remote Sensing,* 13**,** 354.
HILGENDORF, Z., WALKER, I. J., PICKART, A. J. & TURNER, C. M. 2022. Dynamic restoration and the impact of native versus invasive vegetation on coastal foredune morphodynamics, Lanphere Dunes, California, USA. *Earth Surface Processes and Landforms,* 47**,** 3083-3099.
HILLMAN, S., HALLY, B., WALLACE, L., TURNER, D., LUCIEER, A., REINKE, K. & JONES, S. 2021. High-Resolution Estimates of Fire Severity-An Evaluation of UAS Image and LiDAR Mapping Approaches on a Sedgeland Forest Boundary in Tasmania, Australia. *Fire-Switzerland,* 4**,** 14.
HILTON, M., HARVEY, N., HART, A., JAMES, K. & ARBUCKLE, C. 2006. The Impact of Exotic Dune Grass Species on Foredune Development in Australia and New Zealand: a case study ofAmmophila arenariaandThinopyrum junceiforme. *Australian Geographer,* 37**,** 313-334.
HINKEL, J., NICHOLLS, R. J., TOL, R. S. J., WANG, Z. B., HAMILTON, J. M., BOOT, G., VAFEIDIS, A. T., MCFADDEN, L., GANOPOLSKI, A. & KLEIN, R. J. T. 2013. A global analysis of erosion of sandy beaches and sea-level rise: An application of DIVA. *Global and Planetary Change,* 111**,** 150-158.
HINKLEY, E. A. & ZAJKOWSKI, T. 2011. USDA forest service-NASA: unmanned aerial systems demonstrations - pushing the leading edge in fire mapping. *Geocarto International,* 26**,** 103-111.
HISLOP, S., JONES, S., SOTO-BERELOV, M., SKIDMORE, A., HAYWOOD, A. & NGUYEN, T. H. 2018. Using Landsat Spectral Indices in Time-Series to Assess Wildfire Disturbance and Recovery. *Remote Sensing,* 10**,** 460.
HOONHOUT, B. & DE VRIES, S. 2017. Field measurements on spatial variations in aeolian sediment availability at the Sand Motor mega nourishment. *Aeolian Research,* 24**,** 93-104.
HOSSEINI, M. & LIM, S. 2023. Burned area detection using Sentinel-1 SAR data: A case study of Kangaroo Island, South Australia. *Applied Geography,* 151**,** 102854.
HUANG, Z. B., CAO, C. X., CHEN, W., XU, M., DANG, Y. F., SINGH, R. P., BASHIR, B., XIE, B. & LIN, X. J. 2020. Remote Sensing Monitoring of Vegetation Dynamic Changes after Fire in the Greater Hinggan Mountain Area: The Algorithm and Application for Eliminating Phenological Impacts. *Remote Sensing,* 12**,** 156.
HUGENHOLTZ, C. H., LEVIN, N., BARCHYN, T. E. & BADDOCK, M. C. 2012. Remote sensing and spatial analysis of aeolian sand dunes: A review and outlook. *Earth-Science Reviews,* 111**,** 319-334.
JACKSON, D. W. T., COSTAS, S., GONZÁLEZ-VILLANUEVA, R. & COOPER, A. 2019a. A global 'greening' of coastal dunes: An integrated consequence of climate change? *Global and Planetary Change,* 182**,** 103026.

JACKSON, D. W. T., COSTAS, S. & GUISADO-PINTADO, E. 2019b. Large-scale transgressive coastal dune behaviour in Europe during the Little Ice Age. *Global and Planetary Change,* 175**,** 82-91.

JACKSON, P. S. & HUNT, J. C. R. 1975. Turbulent Wind Flow over a Low Hill. *Quarterly Journal of the Royal Meteorological Society,* 101**,** 929-955.

JAMES, M. R., ANTONIAZZA, G., ROBSON, S. & LANE, S. N. 2020. Mitigating systematic error in topographic models for geomorphic change detection: accuracy, precision and considerations beyond off-nadir imagery. *Earth Surface Processes and Landforms,* 45**,** 2251-2271.

JAMES, M. R., CHANDLER, J. H., ELTNER, A., FRASER, C., MILLER, P. E., MILLS, J. P., NOBLE, T., ROBSON, S. & LANE, S. N. 2019. Guidelines on the use of structure-from-motion photogrammetry in geomorphic research. *Earth Surface Processes and Landforms,* 44**,** 2081-2084.

JAMES, M. R., ROBSON, S., D'OLEIRE-OLTMANNS, S. & NIETHAMMER, U. 2017a. Optimising UAV topographic surveys processed with structure-from-motion: Ground control quality, quantity and bundle adjustment. *Geomorphology,* 280**,** 51-66.

JAMES, M. R., ROBSON, S. & SMITH, M. W. 2017b. 3-D uncertainty-based topographic change detection with structure-from-motion photogrammetry: precision maps for ground control and directly georeferenced surveys. *Earth Surface Processes and Landforms,* 42**,** 1769-1788.

JANSEN, A. J., NICHOLSON, J. D., ESPARON, A., WHITESIDE, T., WELCH, M., TUNSTILL, M., PARAMJYOTHI, H., GADHIRAJU, V., VAN BODEGRAVEN, S. & BARTOLO, R. E. 2023. Deep Learning with Northern Australian Savanna Tree Species: A Novel Dataset. *Data,* 8**,** 44.

JELGERSMA, S., DE JONG, J. & ZAGWIJN, W. T. 1970. *The coastal dunes of the western Netherlands; geology, vegetational history and archeology*.

JENNINGS, J. N. 1957. On the Orientation of Parabolic or U-Dunes. *Geographical Journal,* 123**,** 474-480.

JOYCE, K. E., FICKAS, K. C. & KALAMANDEEN, M. 2023. The unique value proposition for using drones to map coastal ecosystems. *Cambridge Prisms: Coastal Futures,* 1**,** e6.

KAUTH, R. J. & THOMAS, G. S. 1976. The tasselled cap - a graphic description of the spectraltemporal development of agricultural crops as seen by Landsat. *Procs. Symposium on Machine Processing of Remotely Sensed Data***,** 41-51.

KEELEY, J. & SYPHARD, A. 2016. Climate Change and Future Fire Regimes: Examples from California. *Geosciences,* 6**,** 37.

KEELEY, J. E. 1995. Seed-Germination Patterns in Fire-Prone Mediterranean-Climate Regions. *In:* ARROYO, M. T. K., ZEDLER, P. H. & FOX, M. D. (eds.) *Ecology and Biogeography of Mediterranean Ecosystems in Chile, California, and Australia.* New York, NY: Springer New York.

KEELEY, J. E. 2009. Fire intensity, fire severity and burn severity: a brief review and suggested usage. *International Journal of Wildland Fire,* 18**,** 116-126.

KENNEDY, D. M., MCCARROLL, R. J., FELLOWES, T. E., GALLOP, S. L., PUCINO, N., MCSWEENEY, S. L., VILA-CONCEJO, A., REEF, R., YUAN, R., CARVALHO, R., QUANG, T. H. & IERODIACONOU, D. 2023. Drivers of seasonal and decadal change on an estuarine beach in a fetch-limited temperate embayment. *Marine Geology,* 463**,** 107130.

KENNEDY, D. M., OLIVER, T. S. N., TAMURA, T., MURRAY-WALLACE, C. V., THOM, B. G., ROSENGREN, N. J., IERODIACONOU, D., AUGUSTINUS, P., LEACH, C., GAO, J. J., MCSWEENEY, S. L., KONLECHNER, T. & WOODROFFE, C. D. 2020. Holocene evolution of the Ninety Mile Beach sand barrier, Victoria, Australia: The role of sea level, sediment supply and climate. *Marine Geology,* 430**,** 106366.

KENNEDY, R. E., YANG, Z. G. & COHEN, W. B. 2010. Detecting trends in forest disturbance and recovery using yearly Landsat time series: 1. LandTrendr - Temporal segmentation algorithms. *Remote Sensing of Environment,* 114**,** 2897-2910.

KEY, C. & BENSON, N. 2005. Landscape assessment: ground measure of severity, the Composite Burn Index; and remote sensing of severity, the Normalized Burn Ratio. *FIREMON: Fire effects monitoring and inventory system.* Fort Collins, CO: US Department of Agriculture, Forest Service, Rocky Mountain Research Station.

KEY, C. H. & BENSON, N. C. 2006. Landscape assessment (LA). *In: Lutes, Duncan C.; Keane, Robert E.; Caratti, John F.; Key, Carl H.; Benson, Nathan C.; Sutherland, Steve; Gangi, Larry J. 2006. FIREMON: Fire effects monitoring and inventory system. Gen. Tech. Rep. RMRS-GTR-164-CD. Fort Collins, CO: US Department of Agriculture, Forest Service, Rocky Mountain Research Station. p. LA-1-55,* 164.

KHATI, U. & SINGH, G. 2022. Combining L-band SAR backscatter and TanDEM-X canopy height for forest aboveground biomass estimation. *Frontiers in Forests and Global Change***,** 156.

KHODAEE, M., HWANG, T., KIM, J., NORMAN, S. P., ROBESON, S. M. & SONG, C. H. 2020. Monitoring Forest Infestation and Fire Disturbance in the Southern Appalachian Using a Time Series Analysis of Landsat Imagery. *Remote Sensing,* 12**,** 2412.

KLINGER, R. & BROOKS, M. 2017. Alternative pathways to landscape transformation: invasive grasses, burn severity and fire frequency in arid ecosystems. *Journal of Ecology,* 105**,** 1521-1533.

KLINGER, R., MCKINLEY, R. & BROOKS, M. 2019. An evaluation of remotely sensed indices for quantifying burn severity in arid ecoregions. *International Journal of Wildland Fire,* 28**,** 951-968.

KOLESAR, K. R., MAVKO, M., BURGESS, E., NGUYEN, N. & SCHAAF, M. D. 2022. A modified resultant drift potential for more accurate prediction of sand transportation in the vicinity of the Keeler Dunes, California. *Aeolian Research,* 58**,** 100819.

KONLECHNER, T. M. & HILTON, M. J. 2022. Post-disturbance evolution of a prograded foredune barrier during a sustained dynamic restoration project-the role of wind speed, wind direction and vegetation. *Earth Surface Processes and Landforms,* 47**,** 3435-3452.

KOTILAINEN, M. 2004. *Dune stratigraphy as an indicator of Holocene climatic change and human impact in Northern Lapland, Finland.* PhD, University of Helsinki.

KRAUSE, C., DUNN, B., BISHOP-TAYLOR, R., ADAMS, C., BURTON, C., ALGER, M., CHUA, S., PHILLIPS, C., NEWEY, V. & KOUZOUBOV, K. 2021. Digital Earth Australia notebooks and tools repository. *In:* AUSTRALIA, G. (ed.). Canberra, Australia. : Geoscience Australia.

LAGUE, D., BRODU, N. & LEROUX, J. 2013. Accurate 3D comparison of complex topography with terrestrial laser scanner: Application to the Rangitikei canyon (NZ). *ISPRS journal of photogrammetry and remote sensing,* 82**,** 10-26.

LAMPERT, R. J. 1981. The Great Kartan Mystery. *Australian Archaeology,* 12**,** 107-109.

LANDSBERG, S. Y. 1956. The Orientation of Dunes in Britain and Denmark in Relation to Wind. *Geographical Journal,* 122**,** 176-189.

LANORTE, A., DANESE, M., LASAPONARA, R. & MURGANTE, B. 2013. Multiscale mapping of burn area and severity using multisensor satellite data and spatial autocorrelation analysis. *International Journal of Applied Earth Observation and Geoinformation,* 20**,** 42-51.

LAPORTE-FAURET, Q., CASTELLE, B., MARIEU, V., BUJAN, S., MICHALET, R. & ROSEBERY, D. 2020. Coastal Dune Morphology Evolution Combining Lidar and UAV Surveys, Truc Vert beach 2011-2019. *Journal of Coastal Research,* 95**,** 163-167.

LAPORTE-FAURET, Q., CASTELLE, B., MARIEU, V., NICOLAE-LERMA, A. & ROSEBERY, D. 2022. Foredune blowout formation and subsequent evolution along a chronically eroding high-energy coast. *Geomorphology,* 414**,** 108398.

LAPORTE-FAURET, Q., MARIEU, V., CASTELLE, B., MICHALET, R., BUJAN, S. & ROSEBERY, D. 2019. Low-Cost UAV for High-Resolution and Large-Scale Coastal

Dune Change Monitoring Using Photogrammetry. *Journal of Marine Science and Engineering,* 7**,** 63.
LASTOVICKA, J., SVEC, P., PALUBA, D., KOBLIUK, N., SVOBODA, J., HLADKY, R. & STYCH, P. 2020. Sentinel-2 Data in an Evaluation of the Impact of the Disturbances on Forest Vegetation. *Remote Sensing,* 12**,** 1914.
LEVIN, N., LEVENTAL, S. & MORAG, H. 2012. The effect of wildfires on vegetation cover and dune activity in Australia's desert dunes: a multisensor analysis. *International Journal of Wildland Fire,* 21**,** 459-475.
LEVIN, N., YEBRA, M. & PHINN, S. 2021. Unveiling the Factors Responsible for Australia's Black Summer Fires of 2019/2020. *Fire-Switzerland,* 4**,** 58.
LI, C. M., SHAO, Z. F., ZHANG, L., HUANG, X. & ZHANG, M. 2021. A Comparative Analysis of Index-Based Methods for Impervious Surface Mapping Using Multiseasonal Sentinel-2 Satellite Data. *Ieee Journal of Selected Topics in Applied Earth Observations and Remote Sensing,* 14**,** 3682-3694.
LIU, Q. S., LIU, G. H. & HUANG, C. 2018. Monitoring desertification processes in Mongolian Plateau using MODIS tasseled cap transformation and TGSI time series. *Journal of Arid Land,* 10**,** 12-26.
LIU, Z. 2016. Effects of climate and fire on short-term vegetation recovery in the boreal larch forests of Northeastern China. *Sci Rep,* 6**,** 37572.
LOOPE, W. L. & ARBOGAST, A. F. 2000. Dominance of an ~150-year cycle of sand-supply change in late Holocene dune-building along the eastern shore of Lake Michigan. *Quaternary Research,* 54**,** 414-422.
LOOPE, W. L. & ARBOGAST, A. F. 2017. Dominance of an ~150-Year Cycle of Sand-Supply Change in Late Holocene Dune-Building along the Eastern Shore of Lake Michigan. *Quaternary Research,* 54**,** 414-422.
LOPES, A. R., GIRONA-GARCÍA, A., CORTICEIRO, S., MARTINS, R., KEIZER, J. J. & VIEIRA, D. C. S. 2020. What is wrong with post-fire soil erosion modelling? A meta-analysis on current approaches, research gaps, and future directions. *Earth Surface Processes and Landforms,* 46**,** 205-219.
LUCAS, R., MUELLER, N., SIGGINS, A., OWERS, C., CLEWLEY, D., BUNTING, P., KOOYMANS, C., TISSOTT, B., LEWIS, B., LYMBURNER, L. & METTERNICHT, G. 2019. Land Cover Mapping using Digital Earth Australia. *Data,* 4**,** 143.
LUIJENDIJK, A., HAGENAARS, G., RANASINGHE, R., BAART, F., DONCHYTS, G. & AARNINKHOF, S. 2018. The State of the World's Beaches. *Sci Rep,* 8**,** 6641.
LUO, W. Y., SHAO, M., CHE, X. H., HESP, P. A., BRYANT, R. G., YAN, C. Z. & XING, Z. P. 2020. Optimization of UAVs-SfM data collection in aeolian landform morphodynamics: a case study from the Gonghe Basin, China. *Earth Surface Processes and Landforms,* 45**,** 3293-3312.
LUTZ, J. A., KEY, C. H., KOLDEN, C. A., KANE, J. T. & VAN WAGTENDONK, J. W. 2011. Fire Frequency, Area Burned, and Severity: A Quantitative Approach to Defining a Normal Fire Year. *Fire Ecology,* 7**,** 51-65.
MANDANICI, E. & BITELLI, G. 2016. Preliminary Comparison of Sentinel-2 and Landsat 8 Imagery for a Combined Use. *Remote Sensing,* 8**,** 1014.
MANGAN, J. M., OVERPECK, J. T., WEBB, R. S., WESSMAN, C. & GOETZ, A. F. H. 2004. Response of Nebraska Sand Hills natural vegetation to drought, fire, grazing, and plant functional type shifts as simulated by the century model. *Climatic Change,* 63**,** 49-90.
MANN, D. H., HEISER, P. A. & FINNEY, B. P. 2002. Holocene history of the Great Kobuk Sand Dunes, northwestern Alaska. *Quaternary Science Reviews,* 21**,** 709-731.
MARCOS, B., GONÇALVES, J., ALCARAZ-SEGURA, D., CUNHA, M. & HONRADO, J. P. 2021. A Framework for Multi-Dimensional Assessment of Wildfire Disturbance Severity from Remotely Sensed Ecosystem Functioning Attributes. *Remote Sensing,* 13**,** 780.

MARTÍNEZ, M. L., PSUTY, N. P. & LUBKE, R. A. 2008. A Perspective on Coastal Dunes. *Coastal Dunes.* Springer Berlin Heidelberg.
MARTINHO, C. T., DILLENBURG, S. R. & HESP, P. A. 2008. Mid to late Holocene evolution of transgressive dunefields from Rio Grande do Sul coast, southern Brazil. *Marine Geology,* 256**,** 49-64.
MARTINHO, C. T., HESP, P. A. & DILLENBURG, S. R. 2010. Morphological and temporal variations of transgressive dunefields of the northern and mid-littoral Rio Grande do Sul coast, Southern Brazil. *Geomorphology,* 117**,** 14-32.
MASEK, J. G., HUANG, C. Q., WOLFE, R., COHEN, W., HALL, F., KUTLER, J. & NELSON, P. 2008. North American forest disturbance mapped from a decadal Landsat record. *Remote Sensing of Environment,* 112**,** 2914-2926.
MASSELINK, G., BROOKS, S., POATE, T., STOKES, C. & SCOTT, T. 2022. Coastal dune dynamics in embayed settings with sea-level rise - Examples from the exposed and macrotidal north coast of SW England. *Marine Geology,* 450**,** 106853.
MASSELINK, G., SCOTT, T., POATE, T., RUSSELL, P., DAVIDSON, M. & CONLEY, D. 2016. The extreme 2013/2014 winter storms: hydrodynamic forcing and coastal response along the southwest coast of England. *Earth Surface Processes and Landforms,* 41**,** 378-391.
MASSETTI, A., RÜDIGER, C., YEBRA, M. & HILTON, J. 2019. The Vegetation Structure Perpendicular Index (VSPI): A forest condition index for wildfire predictions. *Remote Sensing of Environment,* 224**,** 167-181.
MATHEW, S., DAVIDSON-ARNOTT, R. G. D. & OLLERHEAD, J. 2010. Evolution of a beach-dune system following a catastrophic storm overwash event: Greenwich Dunes, Prince Edward Island, 1936-2005. *Canadian Journal of Earth Sciences,* 47**,** 273-290.
MATHEWS, L. E. H. & KINOSHITA, A. M. 2020. Vegetation and Fluvial Geomorphology Dynamics after an Urban Fire. *Geosciences,* 10**,** 317.
MATTHEWS, J. A. & SEPPÄLÄ, M. 2013. Holocene environmental change in subarctic aeolian dune fields: The chronology of sand dune re-activation events in relation to forest fires, palaeosol development and climatic variations in Finnish Lapland. *The Holocene,* 24**,** 149-164.
MAUN, M. A. 2009. *The biology of coastal sand dunes*, Oxford University Press.
MAZZIA, V., COMBA, L., KHALIQ, A., CHIABERGE, M. & GAY, P. 2020. UAV and Machine Learning Based Refinement of a Satellite-Driven Vegetation Index for Precision Agriculture. *Sensors (Basel),* 20**,** 2530.
MCKEEHAN, K. G. & ARBOGAST, A. F. 2021. Repeat photography of Lake Michigan coastal dunes: Expansion of vegetation since 1900 and possible drivers. *Journal of Great Lakes Research,* 47**,** 1518-1537.
MCKENNA, P., ERSKINE, P. D., LECHNER, A. M. & PHINN, S. 2017. Measuring fire severity using UAV imagery in semi-arid central Queensland, Australia. *International Journal of Remote Sensing,* 38**,** 4244-4264.
MEHRTENS, B., LOJEK, O., KOSMALLA, V., BOELKER, T. & GOSEBERG, N. 2023. Foredune growth and storm surge protection potential at the Eiderstedt Peninsula, Germany. *Frontiers in Marine Science,* 9**,** 2698.
MENTASCHI, L., VOUSDOUKAS, M. I., PEKEL, J. F., VOUKOUVALAS, E. & FEYEN, L. 2018. Global long-term observations of coastal erosion and accretion. *Sci Rep,* 8**,** 12876.
MICHELSEN, B., STROBL, S., PARTELI, E. J. & POSCHEL, T. 2015. Two-dimensional airflow modeling underpredicts the wind velocity over dunes. *Sci Rep,* 5**,** 16572.
MILLER, J. D., KNAPP, E. E., KEY, C. H., SKINNER, C. N., ISBELL, C. J., CREASY, R. M. & SHERLOCK, J. W. 2009a. Calibration and validation of the relative differenced Normalized Burn Ratio (RdNBR) to three measures of fire severity in the Sierra Nevada and Klamath Mountains, California, USA. *Remote Sensing of Environment,* 113**,** 645-656.

MILLER, J. D. & THODE, A. E. 2007. Quantifying burn severity in a heterogeneous landscape with a relative version of the delta Normalized Burn Ratio (dNBR). *Remote Sensing of Environment,* 109, 66-80.
MILLER, J. D. & YOOL, S. R. 2002. Mapping forest post-fire canopy consumption in several overstory types using multi-temporal Landsat TM and ETM data. *Remote Sensing of Environment,* 82, 481-496.
MILLER, T. E., GORNISH, E. S. & BUCKLEY, H. L. 2009b. Climate and coastal dune vegetation: disturbance, recovery, and succession. *Plant Ecology,* 206, 97-104.
MIOT DA SILVA, G. & HESP, P. 2010. Coastline orientation, aeolian sediment transport and foredune and dunefield dynamics of Moçambique Beach, Southern Brazil. *Geomorphology,* 120, 258-278.
MIOT DA SILVA, G. & SHULMEISTER, J. 2016. A Review of Coastal Dunefield Evolution in Southeastern Queensland. *Journal of Coastal Research,* 75, 308-312.
MORGAN, B. E., CHIPMAN, J. W., BOLGER, D. T. & DIETRICH, J. T. 2020. Spatiotemporal Analysis of Vegetation Cover Change in a Large Ephemeral River: Multi-Sensor Fusion of Unmanned Aerial Vehicle (UAV) and Landsat Imagery. *Remote Sensing,* 13, 51.
MOULTON, M. A. B., HESP, P. A., DA SILVA, G. M., KEANE, R. & FERNANDEZ, G. B. 2020. Effects of the Increase in Vegetation Cover and Impact of Rabbits on the Geomorphology of Parabolic Dunes (Younghusband Peninsula - SA, Australia). *Journal of Coastal Research,* 95, 108-112.
MOULTON, M. A. B., HESP, P. A., DA SILVA, G. M., KEANE, R. & FERNANDEZ, G. B. 2021. Surfzone-beach-dune interactions along a variable low wave energy dissipative beach. *Marine Geology,* 435, 106438.
MOULTON, M. A. B., HESP, P. A., MIOT DA SILVA, G., BOUCHEZ, C., LAVY, M. & FERNANDEZ, G. B. 2018. Changes in vegetation cover on the Younghusband Peninsula transgressive dunefields (Australia) 1949–2017. *Earth Surface Processes and Landforms,* 44, 459-470.
MUCKERSIE, C. & SHEPHERD, M. J. 1995. Dune Phases as Time-Transgressive Phenomena, Manawatu, New-Zealand. *Quaternary International,* 26, 61-67.
MYERSCOUGH, P. J. & CLARKE, P. J. 2007. Burnt to blazes: landscape fires, resilience and habitat interaction in frequently burnt coastal heath. *Australian Journal of Botany,* 55, 91.
NANSON, R., BISHOP-TAYLOR, R., SAGAR, S. & LYMBURNER, L. 2022. Geomorphic insights into Australia's coastal change using a national dataset derived from the multi-decadal Landsat archive. *Estuarine Coastal and Shelf Science,* 265, 107712.
NEDKOV, R. 2017. Orthogonal Transformation of Segmented Images from the Satellite Sentinel-2. *Comptes Rendus De L Academie Bulgare Des Sciences,* 70, 687-692.
NELSON, N. A. & PIERCE, J. 2010. Late-Holocene relationships among fire, climate and vegetation in a forest-sagebrush ecotone of southwestern Idaho, USA. *Holocene,* 20, 1179-1194.
NESBIT, P. R. & HUGENHOLTZ, C. H. 2019. Enhancing UAV-SfM 3D Model Accuracy in High-Relief Landscapes by Incorporating Oblique Images. *Remote Sensing,* 11, 239.
NICHOLLS, R. J., WONG, P. P., BURKETT, V., CODIGNOTTO, J., HAY, J., MCLEAN, R., RAGOONADEN, S., WOODROFFE, C. D., ABUODHA, P. & ARBLASTER, J. 2007. Coastal systems and low-lying areas. *Climate change 2007: Impacts, adaptation and vulnerability. Contribution of working group II to the fourth assessment report of the Intergovernmental Panel on Climate Change.* Cambridge, UK and New York, USA: Cambridge University Press.
NORTHCOTE, K. H. 2002. Soils. *In:* ROYAL SOCIETY OF SOUTH, A. (ed.) *Natural history of Kangaroo Island.* 2nd ed. ed. Adelaide: Royal Society of South Australia.
NORTON, J., GLENN, N., GERMINO, M., WEBER, K. & SEEFELDT, S. 2009. Relative suitability of indices derived from Landsat ETM+ and SPOT 5 for detecting fire

severity in sagebrush steppe. *International Journal of Applied Earth Observation and Geoinformation,* 11**,** 360-367.
OVER, J.-S. R., RITCHIE, A. C., KRANENBURG, C. J., BROWN, J. A., BUSCOMBE, D. D., NOBLE, T., SHERWOOD, C. R., WARRICK, J. A. & WERNETTE, P. A. 2021. Processing coastal imagery with Agisoft Metashape Professional Edition, version 1.6—Structure from motion workflow documentation. US Geological Survey.
PÁDUA, L., GUIMARÃES, N., ADÃO, T., SOUSA, A., PERES, E. & SOUSA, J. J. 2020. Effectiveness of Sentinel-2 in Multi-Temporal Post-Fire Monitoring When Compared with UAV Imagery. *ISPRS - International Journal of Geo-Information,* 9**,** 225.
PAMMENTER, N. W., BERJAK, M. & MACDONALD, I. A. W. 1985. Regeneration of a Natal Coastal Dune Forest after Fire. *South African Journal of Botany,* 51**,** 453-459.
PARKS, S. A., DILLON, G. K. & MILLER, C. 2014. A new metric for quantifying burn severity: the relativized burn ratio. *Remote Sensing,* 6**,** 1827-1844.
PEACE, M. 2012. *A case study of the 2007 Kangaroo Island bushfires,* Melbourne, Melbourne : Centre for Australian Weather and Climate Research.
PEARCE, K. I. & WALKER, I. J. 2005. Frequency and magnitude biases in the 'Fryberger' model, with implications for characterizing geomorphically effective winds. *Geomorphology,* 68**,** 39-55.
PÉREZ-ALBERTI, A., GÓMEZ-PAZO, A. & OTERO, X. 2021. Natural and Anthropogenic Variations in the Large Shifting Dune in the Corrubedo Natural Park, NW Iberian Peninsula (1956–2017). *Applied Sciences,* 11**,** 34.
PÉREZ-CABELLO, F., MONTORIO, R. & ALVES, D. B. 2021. Remote Sensing Techniques to assess Post-Fire Vegetation Recovery. *Current Opinion in Environmental Science & Health***,** 100251.
PÉREZ-RODRÍGUEZ, L. A., QUINTANO, C., MARCOS, E., SUAREZ-SEOANE, S., CALVO, L. & FERNÁNDEZ-MANSO, A. 2020. Evaluation of Prescribed Fires from Unmanned Aerial Vehicles (UAVs) Imagery and Machine Learning Algorithms. *Remote Sensing,* 12**,** 1295.
PETERSON, C. D., STOCK, E., PRICE, D. M., HART, R., RECKENDORF, F., ERLANDSON, J. M. & HOSTETLER, S. W. 2007. Ages, distributions, and origins of upland coastal dune sheets in Oregon, USA. *Geomorphology,* 91**,** 80-102.
PETROVA, P. G., DE JONG, S. M. & RUESSINK, G. 2023. A Global Remote-Sensing Assessment of the Intersite Variability in the Greening of Coastal Dunes. *Remote Sensing,* 15**,** 1491.
PICKART, A. J. & HESP, P. A. 2019. Spatio-temporal geomorphological and ecological evolution of a transgressive dunefield system, Northern California, USA. *Global and Planetary Change,* 172**,** 88-103.
PICKELL, P. D., HERMOSILLA, T., FRAZIER, R. J., COOPS, N. C. & WULDER, M. A. 2015. Forest recovery trends derived from Landsat time series for North American boreal forests. *International Journal of Remote Sensing,* 37**,** 138-149.
PIERCE, S. M. & COWLING, R. M. 1991. Dynamics of Soil-Stored Seed Banks of Six Shrubs in Fire-Prone Dune Fynbos. *The Journal of Ecology,* 79**,** 731.
PROVOOST, S., JONES, M. L. M. & EDMONDSON, S. E. 2011. Changes in landscape and vegetation of coastal dunes in northwest Europe: a review. *Journal of Coastal Conservation,* 15**,** 207-226.
PSUTY, N. P. & SILVEIRA, T. M. 2010. Global climate change: an opportunity for coastal dunes?? *Journal of Coastal Conservation,* 14**,** 153-160.
PUCINO, N., KENNEDY, D. M., CARVALHO, R. C., ALLAN, B. & IERODIACONOU, D. 2021. Citizen science for monitoring seasonal-scale beach erosion and behaviour with aerial drones. *Sci Rep,* 11**,** 3935.
PYE, K. 1982. Morphological Development of Coastal Dunes in a Humid Tropical Environment, Cape Bedford and Cape Flattery, North Queensland. *Geografiska Annaler Series a-Physical Geography,* 64**,** 213-227.

PYE, K. 1983. Coastal Dunes. *Progress in Physical Geography-Earth and Environment,* 7**,** 531-557.
RADOČAJ, D., OBHOĐAŠ, J., JURIŠIĆ, M. & GAŠPAROVIĆ, M. 2020. Global Open Data Remote Sensing Satellite Missions for Land Monitoring and Conservation: A Review. *Land,* 9**,** 402.
RANASINGHE, R. 2016. Assessing climate change impacts on open sandy coasts: A review. *Earth-Science Reviews,* 160**,** 320-332.
RANASINGHE, R., CALLAGHAN, D. & STIVE, M. J. F. 2011. Estimating coastal recession due to sea level rise: beyond the Bruun rule. *Climatic Change,* 110**,** 561-574.
RANWELL, D. 1958. Movement of Vegetated Sand Dunes at Newborough-Warren, Anglesey. *Journal of Ecology,* 46**,** 83-100.
RAVI, S., BADDOCK, M. C., ZOBECK, T. M. & HARTMAN, J. 2012. Field evidence for differences in post-fire aeolian transport related to vegetation type in semi-arid grasslands. *Aeolian Research,* 7**,** 3-10.
RAVI, S., D'ODORICO, P., BRESHEARS, D. D., FIELD, J. P., GOUDIE, A. S., HUXMAN, T. E., LI, J. R., OKIN, G. S., SWAP, R. J., THOMAS, A. D., VAN PELT, S., WHICKER, J. J. & ZOBECK, T. M. 2011. Aeolian Processes and the Biosphere. *Reviews of Geophysics,* 49.
RAVI, S., D'ODORICO, P., ZOBECK, T. M. & OVER, T. M. 2009. The effect of fire-induced soil hydrophobicity on wind erosion in a semiarid grassland: Experimental observations and theoretical framework. *Geomorphology,* 105**,** 80-86.
RICH, J., RITTENOUR, T. M., NELSON, M. S. & OWEN, J. 2015. OSL chronology of middle to late Holocene aeolian activity in the St. Anthony dune field, southeastern Idaho, USA. *Quaternary International,* 362**,** 77-86.
ROBERTS, D., MUELLER, N. & MCINTYRE, A. 2017. High-Dimensional Pixel Composites From Earth Observation Time Series. *Ieee Transactions on Geoscience and Remote Sensing,* 55**,** 6254-6264.
ROBERTS, D., WILFORD, J. & GHATTAS, O. 2019. Exposed soil and mineral map of the Australian continent revealing the land at its barest. *Nature Communications,* 10**,** 1-11.
ROBIN, N., BILLY, J., CASTELLE, B., HESP, P., LERMA, A. N., LAPORTE-FAURET, Q., MARIEU, V., ROSEBERY, D., BUJAN, S., DESTRIBATS, B. & MICHALET, R. 2021. 150 years of foredune initiation and evolution driven by human and natural processes. *Geomorphology,* 374**,** 107516.
ROBIN, N., BILLY, J., LERMA, A. N., CASTELLE, B., HESP, P. A., ROSEBERY, D., FAUNY, C., DEPARIS, J., MARIEU, V., BOUCHET, C. & DA SILVA, G. M. 2023. Natural remobilization and historical evolution of a modern coastal transgressive dunefield. *Earth Surface Processes and Landforms,* 48**,** 1064-1083.
ROBINSON, A. C., ARMSTRONG, D. M., NATIONAL ESTATE GRANTS, P., SOUTH AUSTRALIA. DEPT. FOR ENVIRONMENT, H. & ABORIGINAL, A. 1999. *A biological survey of Kangaroo Island South Australia in November 1989 and 1990,* Adelaide, Adelaide : Dept. for Environment, Heritage and Aboriginal Affairs.
RODRÍGUEZ-SANTALLA, I., GOMEZ-ORTIZ, D., MARTÍN-CRESPO, T., SÁNCHEZ-GARCÍA, M. J., MONTOYA-MONTES, I., MARTÍN-VELÁZQUEZ, S., BARRIO, F., SERRA, J., RAMÍREZ-CUESTA, J. M. & GRACIA, F. J. 2021. Study and Evolution of the Dune Field of La Banya Spit in Ebro Delta (Spain) Using LiDAR Data and GPR. *Remote Sensing,* 13**,** 802.
ROSATI, J. D., DEAN, R. G. & WALTON, T. L. 2013. The modified Bruun Rule extended for landward transport. *Marine Geology,* 340**,** 71-81.
ROY, P. S., THOM, B. G. & WRIGHT, L. D. 1980. Holocene Sequences on an Embayed High-Energy Coast - an Evolutionary Model. *Sedimentary Geology,* 26**,** 1-19.
ROYAL-COMMISSION 2020. Royal Commission into National Natural Disaster Arrangements. Interim Observations.

RUSSELL-SMITH, J. & EDWARDS, A. C. 2006. Seasonality and fire severity in savanna landscapes of monsoonal northern Australia. *International Journal of Wildland Fire,* 15**,** 541-550.

RUZ, M. H. & MEUR-FEREC, C. 2004. Influence of high water levels on aeolian sand transport: upper beach/dune evolution on a macrotidal coast, Wissant Bay, northern France. *Geomorphology,* 60**,** 73-87.

SAMIAPPAN, S., HATHCOCK, L., TURNAGE, G., MCCRAINE, C., PITCHFORD, J. & MOORHEAD, R. 2019. Remote Sensing of Wildfire Using a Small Unmanned Aerial System: Post-Fire Mapping, Vegetation Recovery and Damage Analysis in Grand Bay, Mississippi/Alabama, USA. *Drones,* 3**,** 43.

SANKEY, J. B., GERMINO, M. J. & GLENN, N. F. 2009a. Aeolian sediment transport following wildfire in sagebrush steppe. *Journal of Arid Environments,* 73**,** 912-919.

SANKEY, J. B., GERMINO, M. J. & GLENN, N. F. 2009b. Relationships of post-fire aeolian transport to soil and atmospheric conditions. *Aeolian Research,* 1**,** 75-85.

SANKEY, J. B., GERMINO, M. J., SANKEY, T. T. & HOOVER, A. N. 2012. Fire effects on the spatial patterning of soil properties in sagebrush steppe, USA: a meta-analysis. *International Journal of Wildland Fire,* 21**,** 545-556.

SANKEY, J. B., GLENN, N. F., GERMINO, M. J., GIRONELLA, A. I. N. & THACKRAY, G. D. 2010. Relationships of aeolian erosion and deposition with LiDAR-derived landscape surface roughness following wildfire. *Geomorphology,* 119**,** 135-145.

SANTOS, L. A. & LATRUBESSE, E. M. 2021. Aeolian mobility in the Middle Sao Francisco Dune Field, Northeast Brazil, as a response to Caatinga's droughts and land-use changes. *Geomorphology,* 393**,** 107940.

SANZ-ABLANEDO, E., CHANDLER, J. H., BALLESTEROS-PÉREZ, P. & RODRÍGUEZ-PÉREZ, J. R. 2020. Reducing systematic dome errors in digital elevation models through better UAV flight design. *Earth Surface Processes and Landforms,* 45**,** 2134-2147.

SCHOENNAGEL, T., SMITHWICK, E. A. & TURNER, M. G. 2009. Landscape heterogeneity following large fires: insights from Yellowstone National Park, USA. *International Journal of Wildland Fire,* 17**,** 742-753.

SEIDL, R., THOM, D., KAUTZ, M., MARTIN-BENITO, D., PELTONIEMI, M., VACCHIANO, G., WILD, J., ASCOLI, D., PETR, M., HONKANIEMI, J., LEXER, M. J., TROTSIUK, V., MAIROTA, P., SVOBODA, M., FABRIKA, M., NAGEL, T. A. & REYER, C. P. O. 2017. Forest disturbances under climate change. *Nat Clim Chang,* 7**,** 395-402.

SENN, J. A., MILLS, J., WALSH, C. L., ADDY, S. & PEPPA, M. V. 2022. On-site geometric calibration of RPAS mounted sensors for SfM photogrammetric geomorphological surveys. *Earth Surface Processes and Landforms,* 47**,** 1615-1634.

SEPPÄLÄ, M. 1995. Deflation and redeposition of sand dunes in finnish lapland. *Quaternary Science Reviews,* 14**,** 799-809.

SEYDI, S. T., AKHOONDZADEH, M., AMANI, M. & MAHDAVI, S. 2021. Wildfire Damage Assessment over Australia Using Sentinel-2 Imagery and MODIS Land Cover Product within the Google Earth Engine Cloud Platform. *Remote Sensing,* 13**,** 220.

SHAKESBY, R. A., WALLBRINK, P. J., DOERR, S. H., ENGLISH, P. M., CHAFER, C. J., HUMPHREYS, G. S., BLAKE, W. H. & TOMKINS, K. M. 2007. Distinctiveness of wildfire effects on soil erosion in south-east Australian eucalypt forests assessed in a global context. *Forest Ecology and Management,* 238**,** 347-364.

SHAWLER, J. L., CIARLETTA, D. J., CONNELL, J. E., BOGGS, B. Q., LORENZO-TRUEBA, J. & HEIN, C. J. 2021. Relative influence of antecedent topography and sea-level rise on barrier-island migration. *Sedimentology,* 68**,** 639-669.

SHEN, Y. P., ZHANG, C. L., HUANG, X. Q., WANG, X. S. & CEN, S. B. 2019. The effect of wind speed averaging time on sand transport estimates. *Catena,* 175**,** 286-293.

SHEN, Y. P., ZHANG, C. L. & ZHANG, Y. J. 2023. Assessment of wind erosivity based on wind speed conversion over different averaging times. *Journal of Soils and Sediments,* 23**,** 2037-2047.

SHEPHERD, M. J. 1987. Holocene Alluviation and Transgressive Dune Activity in the Lower Manawatu-Valley, New-Zealand. *New Zealand Journal of Geology and Geophysics,* 30**,** 175-185.
SHI, T. T. & XU, H. Q. 2019. Derivation of Tasseled Cap Transformation Coefficients for Sentinel-2 MSI At-Sensor Reflectance Data. *Ieee Journal of Selected Topics in Applied Earth Observations and Remote Sensing,* 12**,** 4038-4048.
SHIN, J. I., SEO, W. W., KIM, T., PARK, J. & WOO, C. S. 2019. Using UAV Multispectral Images for Classification of Forest Burn Severity-A Case Study of the 2019 Gangneung Forest Fire. *Forests,* 10**,** 1025.
SHORT, A. & COWELL, P. 2009. Coorong Sea Level Rise Vulnerability Study Report No. CS 0902. South Australian Department of Environment and Heritage.
SHORT, A. D. 1988. Holocene Coastal Dune Formation in Southern Australia - a Case-Study. *Sedimentary Geology,* 55**,** 121-142.
SHORT, A. D. 2001. *Beaches of the South Australian Coast and Kangaroo Island : a guide to their nature, characteristics, surf and safety,* [Sydney], Australian Beach Safety and Management Program.
SHORT, A. D. 2022. Australian beach systems: Are they at risk to climate change? *Ocean & Coastal Management,* 224**,** 106180.
SHORT, A. D. & FOTHERINGHAM, D. 1986. *Coastal morphodynamics and Holocene evolution of the Kangaroo Island coast, South Australia*, Coastal Studies Unit, Department of Geography, University of Sydney.
SHORT, A. D. & HESP, P. A. 1982. Wave, Beach and Dune Interactions in Southeastern Australia. *Marine Geology,* 48**,** 259-284.
SHORT, A. D. & HESP, P. A. 1984. Beach and Dune Morphodynamics of the South East Coast of South Australia. *In:* HESP, P. A. & UNIVERSITY OF SYDNEY. COASTAL STUDIES, U. (eds.) *Technical Report 84/2.* Sydney: Coastal Studies Unit, Dept. Geography, Univ. Sydney.
SHUMACK, S., FAREBROTHER, W. & HESSE, P. 2022. Quantifying vegetation and its effect on aeolian sediment transport: A UAS investigation on longitudinal dunes. *Aeolian Research,* 54**,** 100768.
SHUMACK, S., FISHER, A. & HESSE, P. P. 2021. Refining medium resolution fractional cover for arid Australia to detect vegetation dynamics and wind erosion susceptibility on longitudinal dunes. *Remote Sensing of Environment,* 265**,** 112647.
SHUMACK, S. & HESSE, P. 2018. Assessing the geomorphic disturbance from fires on coastal dunes near Esperance, Western Australia: Implications for dune de-stabilisation. *Aeolian Research,* 31**,** 29-49.
SHUMACK, S., HESSE, P. & TURNER, L. 2017. The impact of fire on sand dune stability: Surface coverage and biomass recovery after fires on Western Australian coastal dune systems from 1988 to 2016. *Geomorphology,* 299**,** 39-53.
ŚLEDŹ, S. & EWERTOWSKI, M. W. 2022. Evaluation of the Influence of Processing Parameters in Structure-from-Motion Software on the Quality of Digital Elevation Models and Orthomosaics in the Context of Studies on Earth Surface Dynamics. *Remote Sensing,* 14**,** 1312.
SMITH, A., LUNARDI, B., GEORGE, E., LEHNER, J. & HOUSER, C. 2022. Coastal Dune Eco-geomorphology: sUAS Applications and Opportunities. *sUAS Applications in Geography.* Springer.
SMYTH, A. G. T., WILSON, R., ROONEY, P. & YATES, L. K. 2022. Extent, accuracy and repeatability of bare sand and vegetation cover in dunes mapped from aerial imagery is highly variable. *Aeolian Research,* 56**,** 100799.
SMYTH, T. A., ROONEY, P. & YATES, K. L. 2023. Dune slope, not wind speed, best predicts bare sand in vegetated coastal dunes. *Journal of Coastal Conservation,* 27**,** 27.
SMYTH, T. A. G. 2016. A review of Computational Fluid Dynamics (CFD) airflow modelling over aeolian landforms. *Aeolian Research,* 22**,** 153-164.

SOFAN, P., BRUCE, D., JONES, E., KHOMARUDIN, M. R. & ROSWINTIARTI, O. 2020. Applying the Tropical Peatland Combustion Algorithm to Landsat-8 Operational Land Imager (OLI) and Sentinel-2 Multi Spectral Instrument (MSI) Imagery. *Remote Sensing,* 12**,** 3958.

SOVEREL, N. O., PERRAKIS, D. D. B. & COOPS, N. C. 2010. Estimating burn severity from Landsat dNBR and RdNBR indices across western Canada. *Remote Sensing of Environment,* 114**,** 1896-1909.

STARK, M., HECKMANN, T., PIERMATTEI, L., DREMEL, F., KAISER, A., MACHOWSKI, P., HAAS, F. & BECHT, M. 2021. From consumer to enterprise grade: How the choice of four UAS impacts point cloud quality. *Earth Surface Processes and Landforms,* 46**,** 2019-2043.

STOREY, E. A., STOW, D. A., O'LEARY, J. F., DAVIS, F. W. & ROBERTS, D. A. 2021. Does short-interval fire inhibit postfire recovery of chaparral across southern California? *Science of the Total Environment,* 751**,** 142271.

STOUT, J. 2012a. A field study of wind erosion following a grass fire on the Llano Estacado of North America. *Journal of Arid Environments,* 82**,** 165-174.

STOUT, J. E. 2012b. A field study of wind erosion following a grass fire on the Llano Estacado of North America. *Journal of Arid Environments,* 82**,** 165-174.

SWANN, C., LEE, D., TRIMBLE, S. & KEY, C. 2021. Aeolian sand transport over a wet, sandy beach. *Aeolian Research,* 51**,** 100712.

SZPAKOWSKI, D. M. & JENSEN, J. L. R. 2019. A Review of the Applications of Remote Sensing in Fire Ecology. *Remote Sensing,* 11**,** 2638.

TANASE, M. A., KENNEDY, R. & APONTE, C. 2015. Radar Burn Ratio for fire severity estimation at canopy level: An example for temperate forests. *Remote Sensing of Environment,* 170**,** 14-31.

THOMAS, D. S. G. & LEASON, H. C. 2005. Dunefield activity response to climate variability in the southwest Kalahari. *Geomorphology,* 64**,** 117-132.

TICEHURST, C., ZHOU, Z. S., LEHMANN, E., YUAN, F., THANKAPPAN, M., ROSENQVIST, A., LEWIS, B. & PAGET, M. 2019. Building a SAR-Enabled Data Cube Capability in Australia Using SAR Analysis Ready Data. *Data,* 4**,** 100.

TOLKSDORF, J. F., KLASEN, N. & HILGERS, A. 2013. The existence of open areas during the Mesolithic: evidence from aeolian sediments in the Elbe-Jeetzel area, northern Germany. *Journal of Archaeological Science,* 40**,** 2813-2823.

TRAN, B., TANASE, M., BENNETT, L. & APONTE, C. 2019. *Fire-severity classification across temperate Australian forests: random forests versus spectral index thresholding*.

TRAN, B. N., TANASE, M. A., BENNETT, L. T. & APONTE, C. 2018. Evaluation of Spectral Indices for Assessing Fire Severity in Australian Temperate Forests. *Remote Sensing,* 10**,** 1680.

TRAN, B. N., TANASE, M. A., BENNETT, L. T. & APONTE, C. 2020a. High-severity wildfires in temperate Australian forests have increased in extent and aggregation in recent decades. *PLoS One,* 15**,** e0242484.

TRAN, D. Q., PARK, M., JUNG, D. & PARK, S. 2020b. Damage-Map Estimation Using UAV Images and Deep Learning Algorithms for Disaster Management System. *Remote Sensing,* 12**,** 4169.

TRIDAWATI, A., WIKANTIKA, K., SUSANTORO, T. M., HARTO, A. B., DARMAWAN, S., YAYUSMAN, L. F. & GHAZALI, M. F. 2020. Mapping the Distribution of Coffee Plantations from Multi-Resolution, Multi-Temporal, and Multi-Sensor Data Using a Random Forest Algorithm. *Remote Sensing,* 12**,** 3933.

TURNER, I. L., HARLEY, M. D., SHORT, A. D., SIMMONS, J. A., BRACS, M. A., PHILLIPS, M. S. & SPLINTER, K. D. 2016. A multi-decade dataset of monthly beach profile surveys and inshore wave forcing at Narrabeen, Australia. *Scientific Data,* 3**,** 1-13.

TURNER, M. G., HARGROVE, W. W., GARDNER, R. H. & ROMME, W. H. 1994. Effects of Fire on Landscape Heterogeneity in Yellowstone-National-Park, Wyoming. *Journal of Vegetation Science,* 5**,** 731-742.

TURNER, M. G., ROMME, W. H. & GARDNER, R. H. 1999. Prefire heterogeneity, fire severity, and early postfire plant reestablishment in subalpine forests of Yellowstone National Park, Wyoming. *International Journal of Wildland Fire,* 9**,** 21-36.

TURTON, S. M. 2017. Expansion of the tropics: revisiting frontiers of geographical knowledge. *Geographical Research,* 55**,** 3-12.

TURTON, S. M. 2020. Geographies of bushfires in Australia in a changing world. *Geographical Research,* 58**,** 313-315.

VALENTI, V. L., CARCELEN, E. C., LANGE, K., RUSSO, N. J. & CHAPMAN, B. 2020. Leveraging Google Earth Engine User Interface for Semiautomated Wetland Classification in the Great Lakes Basin at 10 m With Optical and Radar Geospatial Datasets. *Ieee Journal of Selected Topics in Applied Earth Observations and Remote Sensing,* 13**,** 6008-6018.

VAN, I. C. O., DE VRIES, S., HALLIN, C. & HESP, P. A. 2021. Sea level rise outpaced by vertical dune toe translation on prograding coasts. *Sci Rep,* 11**,** 12792.

VAN OLDENBORGH, G. J., KRIKKEN, F., LEWIS, S., LEACH, N. J., LEHNER, F., SAUNDERS, K. R., VAN WEELE, M., HAUSTEIN, K., LI, S. & WALLOM, D. 2021. Attribution of the Australian bushfire risk to anthropogenic climate change. *Natural Hazards and Earth System Sciences,* 21**,** 941-960.

VERAVERBEKE, S., GITAS, I., KATAGIS, T., POLYCHRONAKI, A., SOMERS, B. & GOOSSENS, R. 2012. Assessing post-fire vegetation recovery using red-near infrared vegetation indices: Accounting for background and vegetation variability. *Isprs Journal of Photogrammetry and Remote Sensing,* 68**,** 28-39.

VERAVERBEKE, S. & HOOK, S. J. 2013. Evaluating spectral indices and spectral mixture analysis for assessing fire severity, combustion completeness and carbon emissions. *International Journal of Wildland Fire,* 22**,** 707-720.

VERMEIRE, L. T., WESTER, D. B., MITCHELL, R. B. & FUHLENDORF, S. D. 2005. Fire and grazing effects on wind erosion, soil water content, and soil temperature. *J Environ Qual,* 34**,** 1559-65.

VESTERGAARD, P. & HASTINGS, A. 2001. Recovery of Danish coastal dune vegetation after a wildfire. *Journal of Coastal Conservation,* 7**,** 117-128.

VIANA-SOTO, A., AGUADO, I., SALAS, J. & GARCÍA, M. 2020. Identifying Post-Fire Recovery Trajectories and Driving Factors Using Landsat Time Series in Fire-Prone Mediterranean Pine Forests. *Remote Sensing,* 12**,** 1499.

VOUSDOUKAS, M. I., RANASINGHE, R., MENTASCHI, L., PLOMARITIS, T. A., ATHANASIOU, P., LUIJENDIJK, A. & FEYEN, L. 2020. Sandy coastlines under threat of erosion. *Nature Climate Change,* 10**,** 260-+.

WALKER, I. J., DAVIDSON-ARNOTT, R. G. D., BAUER, B. O., HESP, P. A., DELGADO-FERNANDEZ, I., OLLERHEAD, J. & SMYTH, T. A. G. 2017. Scale-dependent perspectives on the geomorphology and evolution of beach dune systems. *Earth-Science Reviews,* 171**,** 220-253.

WALKER, I. J. & HESP, P. A. 2013. 11.7 Fundamentals of Aeolian Sediment Transport: Airflow Over Dunes. *In:* SHRODER, J. F. (ed.) *Treatise on Geomorphology.* San Diego: Academic Press.

WALKER, I. J., HILGENDORF, Z., GILLIES, J. A., TURNER, C. M., FURTAK-COLE, E. & NIKOLICH, G. 2023. Assessing performance of a "nature-based" foredune restoration project, Oceano Dunes, California, USA. *Earth Surface Processes and Landforms,* 48**,** 143-162.

WALKER, J. 2020. Aeolian (windblown) sand transport over beaches. *Sandy Beach Morphodynamics.* San Diego: Elsevier.

WANG, C. & GLENN, N. F. 2009. Estimation of fire severity using pre- and post-fire LiDAR data in sagebrush steppe rangelands. *International Journal of Wildland Fire,* 18**,** 848-856.
WANG, J., DING, J., YU, D., TENG, D., HE, B., CHEN, X., GE, X., ZHANG, Z., WANG, Y., YANG, X., SHI, T. & SU, F. 2020. Machine learning-based detection of soil salinity in an arid desert region, Northwest China: A comparison between Landsat-8 OLI and Sentinel-2 MSI. *Sci Total Environ,* 707**,** 136092.
WARD, W. 1977. Sand movement on Fraser Island: a response to changing climates. *University of Queensland, Occasional Papers in Anthropology* 8**,** 113-126.
WARD, W. T. 2006. Coastal dunes and strandplains in southeast Queensland: Sequence and chronology. *Australian Journal of Earth Sciences,* 53**,** 363-373.
WARRICK, J. A., EAST, A. E. & DOW, H. 2022. Fires, floods and other extreme events – How watershed processes under climate change will shape our coastlines. *Cambridge Prisms: Coastal Futures,* 1**,** e2.
WASSON, R. J. & NANNINGA, P. M. 1986. Estimating Wind Transport of Sand on Vegetated Surfaces. *Earth Surface Processes and Landforms,* 11**,** 505-514.
WATER, D. F. E. A. 2000. *Soil Landscape Map Units of southern South Australia*. Adelaide, South Australia: Government of South Australia.
WELLINGTON, A. & NOBLE, I. 1985. Post-fire recruitment and mortality in a population of the mallee Eucalyptus incrassata in semi-arid, south-eastern Australia. *The Journal of Ecology***,** 645-656.
WHEATON, J. M., BRASINGTON, J., DARBY, S. E. & SEAR, D. A. 2010. Accounting for uncertainty in DEMs from repeat topographic surveys: improved sediment budgets. *Earth Surface Processes and Landforms,* 35**,** 136-156.
WHICKER, J. J., PINDER, J. E., 3RD & BRESHEARS, D. D. 2006. Increased wind erosion from forest wildfire: implications for contaminant-related risks. *J Environ Qual,* 35**,** 468-78.
WHITE, J. C., WULDER, M. A., HERMOSILLA, T., COOPS, N. C. & HOBART, G. W. 2017. A nationwide annual characterization of 25 years of forest disturbance and recovery for Canada using Landsat time series. *Remote Sensing of Environment,* 194**,** 303-321.
WIGGS, G., LIVINGSTONE, I., THOMAS, D. & BULLARD, J. 1994. Effect of vegetation removal on airflow patterns and dune dynamics in the southwest Kalahari Desert. *Land Degradation & Development,* 5**,** 13-24.
WIGGS, G. F. S., THOMAS, D. S. G. & BULLARD, J. E. 1995. Dune Mobility and Vegetation Cover in the Southwest Kalahari Desert. *Earth Surface Processes and Landforms,* 20**,** 515-529.
WILLIAMS, J. G., ANDERS, K., WINIWARTER, L., ZAHS, V. & HÖFLE, B. 2021. Multi-directional change detection between point clouds. *Isprs Journal of Photogrammetry and Remote Sensing,* 172**,** 95-113.
WITTKE, S., YU, X. W., KARJALAINEN, M., HYYPPÄ, J. & PUTTONEN, E. 2019. Comparison of two-dimensional multitemporal Sentinel-2 data with three-dimensional remote sensing data sources for forest inventory parameter estimation over a boreal forest. *International Journal of Applied Earth Observation and Geoinformation,* 76**,** 167-178.
WRIGHT, B. R. & CLARKE, P. J. 2007. Fire regime (recency, interval and season) changes the composition of spinifex (

spp.)-dominated desert dunes. *Australian Journal of Botany,* 55**,** 709-724.
YAN, N. & BAAS, A. C. W. 2015. Parabolic dunes and their transformations under environmental and climatic changes: Towards a conceptual framework for understanding and prediction. *Global and Planetary Change,* 124**,** 123-148.
YANG, Z. L., QIAN, G. Q., HAN, Z. W., DONG, Z. B., LUO, W. Y., ZHANG, Z. C., LU, J. F., LIANG, A. M. & TIAN, M. 2019. Variation in grain-size characteristics as a function of

wind direction and height in the Sanlongsha dune field of the northern Kumtagh Desert, China. *Aeolian Research,* 40**,** 53-64.
YE, Z. L., LONG, J. P., ZHENG, H. N., LIU, Z. H., ZHANG, T. C. & WANG, Q. Y. 2023. Mapping Growing Stem Volume Using Dual-Polarization GaoFen-3 SAR Images in Evergreen Coniferous Forests. *Remote Sensing,* 15**,** 2253.
YIZHAQ, H., XU, Z. W. & ASHKENAZY, Y. 2020. The effect of wind speed averaging time on the calculation of sand drift potential: New scaling laws. *Earth and Planetary Science Letters,* 544**,** 116373.
ZENKOVICH, V. P., STEERS, J. A., KING, C. A. & FRY, D. 1967. Processes of coastal development. *(No Title)*.
ZHANG, F., HASSANZADEH, A., KIKKERT, J., PETHYBRIDGE, S. J. & VAN AARDT, J. 2021. Comparison of UAS-Based Structure-from-Motion and LiDAR for Structural Characterization of Short Broadacre Crops. *Remote Sensing,* 13**,** 3975.
ZHAO, Y., ZHOU, Q. Z., GAO, G. L., DING, G. D., ZHANG, Y. & ZHOU, J. X. 2021. A new methodological framework coupling computational fluid dynamics and fingerprinting for assessment of aeolian sediment transport processes. *Catena,* 204**,** 105372.
ZHOU, Y., RUPNIK, E., MEYNARD, C., THOM, C. & PIERROT-DESEILLIGNY, M. 2019. Simulation and Analysis of Photogrammetric UAV Image Blocks—Influence of Camera Calibration Error. *Remote Sensing,* 12**,** 22.
ZHOU, Y. L., DAAKIR, M., RUPNIK, E. & PIERROT-DESEILLIGNY, M. 2020. A two-step approach for the correction of rolling shutter distortion in UAV photogrammetry. *Isprs Journal of Photogrammetry and Remote Sensing,* 160**,** 51-66.

APPENDICES

Appendix 1 - Assessing Shoreline Change using Historical Aerial and RapidEye Satellite Imagery (Cape Jaffa, South Australia)

DASILVA, M., MIOT DA SILVA, G., HESP, P. A., BRUCE, D., KEANE, R. & MOORE, C. 2021. Journal of Coastal Research, 37, 468-483.

The coastal zone is a dynamic area which can experience substantial natural change in short time periods, but changes are also associated with human modifications to the coastline. This case study is focused around assessing shoreline change associated with the Cape Jaffa Marina and canal estate in South Australia. The research comprises a GIS based analysis of shoreline change utilising aerial imagery from 1975 to 2005, which provides information of the morphological coastal trends prior to construction in 2008 of the marina/canal estate. In addition, imagery collected by the RapidEye satellite constellation was used to assess shoreline changes in the decade since construction, 2009 to 2019. The shoreline change statistics over the past few decades were calculated using the Digital Shoreline Analysis System extension of ESRI's ArcGIS. The image analysis workflow is based on the objective extraction of shoreline proxies from individual image statistics in a semi-automated process and is used to identify the waterline and edge of vegetation shoreline proxies in a time series analysis. The results provide a case study of a historically progradational sandy coastline experiencing substantial amounts of alongshore sediment transport, the corresponding obstruction from coastal infrastructure, and the resulting morphological changes to the Cape Jaffa shoreline. Shoreline change trends were altered from a predominantly accretional shoreline before the construction of the marina to one oscillating between extremes of erosion and accretion. The results showed significant accretion occurring updrift (Net Shore Movement (NSM) of 106 m) and significant erosion downdrift (NSM of80 m) of the marina’s training walls and entrance. The information derived from Earth observation satellites, such as RapidEye, can provide valuable insights into trend analysis due to their relatively high spatial (5 metre) and temporal resolution (5.5-day revisit).

Appendix 2 - Review and direct evidence of transgressive aeolian sand sheet and dunefield initiation

HESP, P. A., **DASILVA, M**., MIOT DA SILVA, G., BRUCE, D. & KEANE, R. 2022. Review and direct evidence of transgressive aeolian sand sheet and dunefield initiation. Earth Surface Processes and Landforms, 47, 2660-2675.

Abstract

The multiple hypotheses which exist to explain the initiation of transgressive aeolian sand sheets and dunefields, are reviewed and discussed. Direct evidence supporting many of these hypotheses is largely lacking. In South Australia, the Younghusband Peninsula coastal barrier extends 180 km and predominantly comprises transgressive and parabolic dunefields. The 42 Mile Crossing area on the barrier is undergoing significant erosion at variable rates of 0.5 to 5.0 m/yr, and a new transgressive aeolian sand sheet has rapidly developed in 1 year and is extending landwards at an average rate of 13 m/yr. This research provides unequivocal evidence that large-scale shoreline and dunefield erosion does lead to the development of a new transgressive aeolian sand sheet (and eventual dunefield) phase thereby demonstrating an initiation mechanism that is likely linked to future sea level rise and climate change. We also show that the initiation process, and, in particular, the subsequent rate of sand sheet transgression occurs at an incredibly rapid rate (+100m in 8 years). Plain Language Summary: Coastal sand dunes border many of the world's coastlines and are highly adapted to local climate and conditions. How coastal dunes transition from predominantly vegetated and stable systems to wind-blown sand sheets and dunefields transgressing prior terrain is a research area of pressing relevance due to forecasts of sea level rise and climate change. The factors or triggers that are considered to initiate transgressive aeolian sand sheets and dunefields are reviewed. The formation and evolution of a new transgressive aeolian sand sheet phase triggered by large-scale shoreline erosion in South Australia is presented. According to the results from historical and satellite images, local shoreline erosion began in the late 1970s and has continued at highly variable rates. We show that once the foredune was removed, the high scarp created by wave erosion of the relict, vegetated transgressive dunefield destabilized and was then eroded by wind processes leading to the rapid development of a transgressive aeolian sand sheet. The initiation and evolution of the sand sheet provides an excellent example of how dunefields might respond to future sea level rise and climate change.

Appendix 3 - Flow dynamics over a high, steep, erosional coastal dune slope

DAVIDSON, S. G., HESP, P. A., **DASILVA, M**. & DA SILVA, G. M. 2022. Flow dynamics over a high, steep, erosional coastal dune slope. Geomorphology, 402, 108111.

Abstract

Flow dynamics over a high, unvegetated, and steep scarp slope that fronts a severely eroded relict transgressive dunefield were investigated at Salmon Hole (also known as Post Office Rock), a small headland-bay beach located near Beachport, southeast South Australia. The ~15-metre-high steep dune at Salmon Hole provided the opportunity to conduct a wind flow experiment on a larger, higher and longer stoss slope than previously studied. The scarp slope is comprised of segments of varying slope that have a significant impact on flow dynamics over the dune. Percentage speed up and a decrease in turbulence were recorded up the stoss slope due to streamline convergence and flow compression. However, flow expansion at a change in gradient on the upper stoss slope caused a significant drop in wind speed and an increase in turbulence, contrary to what has previously been found in the literature where maximum percentage speed up is primarily recorded at the crest. Topographic steering typically seen in wind flow over scarps and foredunes was observed at Salmon Hole along with flow separation and the formation of a reversing vortex on the lee slope. This study also demonstrates how a lack of sediment delivery back to the beach and thence to the dune between storm events results in the inability for dune recovery or translation. However, the Salmon Hole study shows that blowouts can still develop and grow through dune cannibalization regardless of the lack of sediment supply from the beach and the recession of the shoreline.

Appendix 4 - Scientific and Industry Conferences and Community Presentations

Locate 2023 (May 2023) – Abstract accepted titled, “SAR-SXXC: what can we see from SAR S, X, X, C bands? Multi-polarisation, multi-platform, multi-date SAR with multi-platform-LIDAR over Plantation-Forestry.”

Coorong Sand And Silt 2023 – Oral Presentation titled, “Eroding Coastal Dunes at 42 Mile Crossing”

Advancing Earth Observation Forum (AEO22), Brisbane 2022, EO360 Interactive session titled, ‘Generating an automated early warning system for Australian plantation forest health issues’

**Advancing Earth Observation Forum (AEO22), Brisbane 2022, EO360 Interactive session titled, ‘What is Burn Severity a discussion focused on Kangaroo Island’

EEE HDR conference 2021—Oral presentation titled, ‘Applications of Remote Sensing to Study Coastal Dune Disturbance’

EEE conference 2022 – Oral presentation titled, ‘UAV SfM and LIDAR applied to Rapidly Transgressing Coastal Dunes in Southeast, South Australia’

Windy Day Down Under 2020 – Online presentation titled, ‘Shoreline Recession and the Landward Translation of Coastal Dunes at 42 Mile Crossing in South Australia’

Ecology, Environment and Evolution (EEE) Research Group ECR Talk 2021: Oral presentation titled, ‘Post-Fire Coastal Dune Evolution on Kangaroo Island’

Spatial Information Day 2022 – Oral presentation titled, ‘Applications of Remote Sensing to Study Coastal Dune’

Spatial Information Day 2021 – Oral presentation titled, ‘Remote sensing of fire affected coastal dunes on Kangaroo Island, UAV photogrammetry and tasselled caps’

Spatial Information Day 2019 – Oral presentation titled, ‘Assessing Shoreline Change with a GIS of Aerial, Satellite and UAV Sources’

South Australian Coastal Conference 2019 – Oral presentation titled, ‘Assessing Shoreline Change at the Cape Jaffa Marina SE South Australia’

** Indicates co-author

SUPPLEMENTARY MATERIAL

Supplementary Material to Chapter 2

Table B– Pearson's R correlation coefficient as derived from the Welch's t-test comparing Z scores for index values grouped by Landsystem (LS) Soil groups. Index values from the differenced Disturbance Index (dDI), differenced Normalised Burn Ratio (NBR) and the relativised differenced Normalised Burn Ratio (rdNBR) are compared in pairs to show significant differences in population means (all pairs assessed to be significant by p value 0.05 except highlighted and bold). Higher values indicate larger deviations from the compared means of individual indices.

LS	dDI - dNBR	dDI - rdNBR	dNBR - rdNBR
GOS	0.08	0.18	0.11
BKR	0.28	0.04	0.27
CTO	0.11	0.20	0.10
FLC	0.00	0.31	0.32
RIT	0.25	0.12	0.16
ROR	0.09	0.12	0.03
SAB	0.55	0.65	0.07
CDC	0.64	0.80	0.38
CBO	0.27	0.44	0.20

Supplementary Material to Chapter 3

Supplementary data located at DOI: 10.25451/flinders.22138379, Includes Metashape error reports for Sites A, B and C.

Table B-9– Results of M3C2-PM changes during Time Period of Figure 10, grouped according to satellite derived thresholds of areas that were predominantly exposed sand before the fire (NDVI > 0.15) and areas that were burnt and unburnt (dNBR > 0.2). Total area of Sand, Burnt and Unburnt is shown and their percent of the surveyed area. M3C2-PM changes are shown according to volumetric (m3) Loss and Gain with estimated error (±). The area of pixels where significant change has occurred are reported as the Total (m2) of the classification (Sand, Burnt, Unburnt) and as the ratio of classified pixels showing significant loss or gain.

	Sand: 68,394 m^2 (27%)			Burnt: 140,391 m^2 (55%)			Unburnt: 48,614 m^2 (18%)		
	Vol. (m^3)		Area	Vol. (m^3)		Area	Vol. (m^3)		Area
Time Period	Loss -	Gain +	Total (m^2) -/+ (%)	Loss -	Gain +	Total (m^2) -/+ (%)	Loss -	Gain +	Total (m^2) -/+ (%)
Aug20-May21	567 ±129	4648 ±760	11578 15/85	241 ±66	8470 ±1114	15362 6/94	328 ±95	1252 ±339	5647 22/78

Table 3-10 – Results of M3C2-PM changes during Time Period of Figure 11, grouped according to satellite derived thresholds of areas that were predominantly exposed sand before the fire (NDVI > 0.15) and areas that were burnt and unburnt (dNBR > 0.2). Total area of Sand, Burnt and Unburnt is shown and their percent of the surveyed area. M3C2-PM changes are shown according to volumetric (m3) Loss and Gain with estimated error (±). The area of pixels where

significant change has occurred are reported as the Total (m2) of the classification (Sand, Burnt, Unburnt) and as the ratio of classified pixels showing significant loss or gain.

	Sand: 68,394 m² (27%)			Burnt: 140,391 m² (55%)			Unburnt: 48,614 m² (18%)		
	Vol. (m^3)		Area	Vol. (m^3)		Area	Vol. (m^3)		Area
Time Period	Loss -	Gain +	Total (m^2) -/+ (%)	Loss -	Gain +	Total (m^2) -/+ (%)	Loss -	Gain +	Total (m^2) -/+ (%)
Aug20-Oct20	351 ±84	787 ±232	4854 26/74	-361 ±86	481 ±113	3071 43/57	-308 ±82	363 ±106	2880 44/56
Oct20-Dec20	925 ±180	548 ±118	5647 60/40	-517 ±85	597 ±153	4510 36/64	-699 ±144	196 ±61	3879 70/30
Dec20- Feb21	152 ±34	2413 ±276	7130 11/89	-28 ±9	3862 ±604	14114 2/98	-120 ±37	856 ±185	5111 17/83
Feb21-May21	244 ±53	1949 ±355	5815 13/87	-360 ±81	3422 ±572	9313 12/88	-70 ±29	311 ±87	1663 25/75

Table 3-11 - Results of M3C2-PM changes during Time Period of Figure 13, grouped according to satellite derived thresholds of areas that were predominantly exposed sand before the fire (NDVI > 0.15) and areas that were burnt and unburnt (dNBR > 0.2). Total area of Sand, Burnt and Unburnt is shown and their percent of the surveyed area. M3C2-PM changes are shown according to volumetric (m3) Loss and Gain with estimated error (±). The area of pixels where significant change has occurred are reported as the Total (m2) of the classification (Sand, Burnt, Unburnt) and as the ratio of classified pixels showing significant loss or gain.

	Sand: 41,999 m² (28%)			Burnt: 60,510m² (41%)			Unburnt: 44,957 m² (30%)		
	Vol. (m^3)		Area	Vol. (m^3)		Area	Vol. (m^3)		Area
Time Period	Loss -	Gain +	Total (m^2) -/+ (%)	Loss -	Gain +	Total (m^2) -/+ (%)	Loss -	Gain +	Total (m^2) -/+ (%)
Aug20-May21	528 ±112	5710 ±1078	16022 9/91	390 ±90	1201 ±252	4598 26/74	122 ±33	844 ±215	3331 13/87

Table 3-12 - Results of M3C2-PM changes during Time Period of Figure 14, grouped according to satellite derived thresholds of areas that were predominantly exposed sand before the fire (NDVI > 0.15) and areas that were burnt and unburnt (dNBR > 0.2). Total area of Sand, Burnt and Unburnt is shown and their percent of the surveyed area. M3C2-PM changes are shown according to volumetric (m3) Loss and Gain with estimated error (±). The area of pixels where significant change has occurred are reported as the Total (m2) of the classification (Sand, Burnt, Unburnt) and as the ratio of classified pixels showing significant loss or gain.

	Sand: 41,999 m² (28%)			Burnt: 60,510m² (41%)			Unburnt:44,957 m² (30%)		
	Vol. (m^3)		Area	Vol. (m^3)		Area	Vol. (m^3)		Area
Time Period	Loss -	Gain +	Total (m^2) -/+ (%)	Loss -	Gain +	Total (m^2) -/+ (%)	Loss -	Gain +	Total (m^2) -/+ (%)
Aug20-Oct20	794 ±100	320 ±96	2722 51/49	370 ±83	471 ±140	3105 37/63	42 ±17	259 ±83	1390 17/83
Oct20-Dec20	1122 ±250	436 ±77	5710 76/24	150 ±42	249 ±65	1873 39/61	196 ±55	140 ±39	1644 59/41
Dec20-Feb21	535 ±82	1117 ±215	5118 28/72	427 ±87	220 ±60	2523 59/41	477 ±101	191 ±51	2623 66/34

Feb21-May21	190 ±42	1884 ±374	6192 10/90	31 ±11	876 ±190	2989 5/95	18 ±7	380 ±88	1423 8/92

Table 3-13 - Results of M3C2-PM changes during Time Period of Figure 13, grouped according to satellite derived thresholds of areas that were predominantly exposed sand before the fire (NDVI > 0.15) and areas that were burnt and unburnt (dNBR > 0.2). Total area of Sand, Burnt and Unburnt is shown and their percent of the surveyed area. M3C2-PM changes are shown according to volumetric (m^3) Loss and Gain with estimated error (±). The area of pixels where significant change has occurred are reported as the Total (m2) of the classification (Sand, Burnt, Unburnt) and as the ratio of classified pixels showing significant loss or gain.

	Unburnt: 172,629 m^2 (100%)		
	Vol. (m^3)		Area
Time Period	Loss -	Gain +	Total (m^2) -/+ (%)
Aug20-May21	84 ±34	16592 ±3046	21725 1/99

Table 3-14 - Results of M3C2-PM changes during Time Period of Figure 14, grouped according to satellite derived thresholds of areas that were predominantly exposed sand before the fire (NDVI > 0.15) and areas that were burnt and unburnt (dNBR > 0.2). Total area of Sand, Burnt and Unburnt is shown and their percent of the surveyed area. M3C2-PM changes are shown according to volumetric (m3) Loss and Gain with estimated error (±). The area of pixels where significant change has occurred are reported as the Total (m2) of the classification (Sand, Burnt, Unburnt) and as the ratio of classified pixels showing significant loss or gain.

	Unburnt: 172,629 m^2 (100%)		
	Vol. (m^3)		Area
Time Period	Loss -	Gain +	Total (m^2) -/+ (%)
Aug20-Oct20	132 ±37	1858 ±662	9290 5/95
Oct20-Dec20	153 ±50	2071 ±437	7886 10/90
Dec20-Feb21	299 ±152	7849 ±1194	23902 1/99
Feb21-May21	84 ±34	3831 ±1149	9481 12/88

Supplementary Material to Chapter 4

Table C-5 - Outline of workflow and processing parameters for Agisoft Metashape (MS 1.8.4) with internal Orientation Parameters (IOP).

MS Workflow	Parameters	Values
Align Photos	Accuracy	Medium

	Generic Preselection	Source
	Key/Tie Points Limit	60,000/10,000
	Rolling Shutter Compensation	True
	Adaptive Camera Model Fitting	False
Gradual Selection	Reconstruction Uncertainty	10
	Projection Accuracy	5
	Reprojection Error	0.4
Camera Alignment	IOP (f, cx, cy, k1, k2, k3)	True
	Rolling Shutter XYZ	True
	Adaptive Model Fitting	False
	Image Quality	>0.7
Build Dense Cloud	Quality	High
	Depth Filtering	Mild

Table C-6 - Information on surveys flown over 41.5 Mile survey site (Fig. 1) and LIDAR surveys sourced from https://elevation.fsdf.org.au/. Showing the survey date, total number of images and ground Control, and independent Check Points (in Bold). LIDAR RMSE show vertical and horizontal RMSE from sourced metadata.

Date	Images	GCP|CCP	RMSE (cm)
30/04/08	**LIDAR**	**N/A**	**15|50**
30/05/18	**LIDAR**	**N/A**	**15/27**
24/08/20	**933**	**12|6**	**4.0|4.5**
06/10/20	**996**	**16|8**	**2.0|3.6**
20/12/20	**1244**	**17|8**	**1.7|4.2**
08/02/21	**1126**	**17|8**	**1.8|2.9**
27/04/21	**1109**	**14|8**	**3.9|5.7**
			2.4|2.8
25/08/21	**1233**	**17|8**	
			2.1|3.4

08/12/21	**1317**	**18|9**	**2.5|3.2**
13/04/22	**1664**	**18|8**	

Table C-7 – shows the 3D change totals segmented according to transects (Figure 4) as derived from the Geomorphic Change Detection (GCD) Software. The Erosion (E) and Accretion (A) with their respective thresholded error margins and the resulting net Ratio (R) of E/|A|. Values below 1 show a net loss, and above 1 indicate a net gain of sediments.

		1	**2**	**3**	**4**	**5**	**6**	**7**	**8**	**9**	**10**
Apr08 - May18	E	6845 ± 1214	11211 ± 1404	12895 ± 1393	11696 ± 1269	11353 ± 1213	10460 ± 1214	9464 ± 1315	11817 ± 1313	10844 ± 1200	13985 ± 1441
	A	902 ± 579	2830 ± 1528	2056 ± 1215	1762 ± 994	1056 ± 690	1327 ± 774	1600 ± 893	1615 ± 933	1942 ± 1105	3831 ± 1359
	R	**0.1**	**0.3**	**0.2**	**0.2**	**0.1**	**0.1**	**0.2**	**0.1**	**0.2**	**0.3**
May18 - Aug20	E	1138 ± 414	3079 ± 934	1485 ± 687	1508 ± 643	1883 ± 520	2160 ± 639	1668 ± 631	1201 ± 461	1199 ± 526	3707 ± 1095
	A	105 ± 80	924 ± 442	820 ± 487	832 ± 508	867 ± 506	587 ± 351	1004 ± 538	630 ± 361	381 ± 220	2031 ± 718
	R	**0.1**	**0.3**	**0.6**	**0.6**	**0.5**	**0.3**	**0.6**	**0.5**	**0.3**	**0.5**
Aug20 - Oct20	E	120 ± 47	215 ± 90	136 ± 43	88 ± 52	153 ± 72	77 ± 25	92 ± 34	62 ± 15	19 ± 10	315 ± 150
	A	285 ± 190	264 ± 105	155 ± 73	134 ± 52	150 ± 80	394 ± 210	272 ± 176	213 ± 148	131 ± 84	177 ± 80
	R	**2.4**	**1.2**	**1.1**	**1.5**	**1**	**5.1**	**3**	**3.4**	**6.9**	**0.6**
Oct20 - Dec20	E	202 ± 93	550 ± 206	276 ± 123	365 ± 153	427 ± 178	451 ± 170	305 ± 134	121 ± 72	156 ± 82	823 ± 275
	A	260 ± 76	619 ± 159	446 ± 119	285 ± 92	444 ± 125	355 ± 107	312 ± 96	272 ± 108	169 ± 71	822 ± 199
	R	**1.3**	**1.1**	**1.6**	**0.8**	**1**	**0.8**	**1**	**2.3**	**1.1**	**1**

Dec20 - Feb21	E	306 ± 85	632 ± 195	413 ± 115	374 ± 83	546 ± 147	640 ± 189	482 ± 118	434 ± 96	458 ± 93	983 ± 238
	A	299 ± 113	452 ± 119	319 ± 138	404 ± 181	531 ± 180	322 ± 97	283 ± 102	101 ± 56	152 ± 83	1004 ± 225
	R	**1**	**0.7**	**0.8**	**1.1**	**1**	**0.5**	**0.6**	**0.2**	**0.3**	**1**
Feb21 - Apr21	E	430 ± 85	700 ± 152	676 ± 130	663 ± 133	857 ± 188	682 ± 159	532 ± 91	611 ± 72	412 ± 82	795 ± 185
	A	95 ± 45	132 ± 56	119 ± 51	98 ± 46	202 ± 85	145 ± 57	102 ± 40	42 ± 22	56 ± 36	669 ± 140
	R	**0.2**	**0.2**	**0.2**	**0.1**	**0.2**	**0.2**	**0.2**	**0.1**	**0.1**	**0.8**
Apr21 - Aug21	E	596 ± 259	459 ± 212	250 ± 151	101 ± 65	177 ± 108	128 ± 64	75 ± 46	46 ± 32	67 ± 53	684 ± 311
	A	34 ± 10	275 ± 68	323 ± 55	404 ± 72	527 ± 115	468 ± 127	516 ± 100	830 ± 116	705 ± 114	801 ± 150
	R	**0.1**	**0.6**	**1.3**	**4**	**3**	**3.6**	**6.9**	**18.2**	**10.5**	**1.2**
Aug21 - Dec21	E	208 ± 90	407 ± 180	275 ± 120	373 ± 169	735 ± 289	846 ± 281	750 ± 232	772 ± 193	586 ± 152	1184 ± 424
	A	359 ± 115	564 ± 193	319 ± 152	123 ± 77	122 ± 64	123 ± 61	42 ± 26	61 ± 32	29 ± 18	631 ± 176
	R	**1.7**	**1.4**	**1.2**	**0.3**	**0.2**	**0.1**	**0.1**	**0.1**	**0**	**0.5**
Dec21 - Apr22	E	615 ± 77	1058 ± 184	796 ± 104	872 ± 98	1172 ± 165	1515 ± 194	1477 ± 105	1699 ± 89	2418 ± 116	2469 ± 227
	A	505 ± 210	493 ± 169	355 ± 177	532 ± 210	680 ± 204	326 ± 152	434 ± 222	343 ± 214	381 ± 222	1399 ± 224
	R	**0.8**	**0.5**	**0.4**	**0.6**	**0.6**	**0.2**	**0.3**	**0.2**	**0.2**	**0.6**

Table C-8 - shows the 3D change totals segmented according to transects (Figure 4) as derived from the Geomorphic Change Detection (GCD) Software. The Erosion (E) and

Accretion (A) with their respective thresholded error margins and the resulting net Ratio (R) of E/|A|. Values below 1 show a net loss, and above 1 indicate a net gain of sediments.

		11	**12**	**13**	**14**	**15**	**16**	**17**	**18**
Apr08 - May18	E	13784 ± 1528	10436 ± 1214	14040 ± 1523	14960 ± 1640	13707 ± 1492	11623 ± 1423	13101 ± 1640	5876 ± 1134
	A	3113 ± 1463	1622 ± 901	3874 ± 1445	5618 ± 1759	6210 ± 1659	2891 ± 1111	3163 ± 906	1955 ± 859
	R	**0.2**	**0.2**	**0.3**	**0.4**	**0.5**	**0.2**	**0.2**	**0.3**
May18 - Aug20	E	2960 ± 1016	1612 ± 392	2524 ± 809	2371 ± 1235	3599 ± 1009	843 ± 421	1971 ± 891	905 ± 419
	A	1546 ± 811	596 ± 397	1280 ± 534	3093 ± 735	3059 ± 823	1458 ± 525	925 ± 307	607 ± 255
	R	**0.5**	**0.4**	**0.5**	**1.3**	**0.8**	**1.7**	**0.5**	**0.7**
Aug20 - Oct20	E	458 ± 224	124 ± 37	359 ± 192	472 ± 168	402 ± 151	210 ± 60	378 ± 109	232 ± 42
	A	314 ± 138	90 ± 64	125 ± 62	306 ± 144	244 ± 102	238 ± 116	162 ± 85	475 ± 180
	R	**0.7**	**0.7**	**0.3**	**0.6**	**0.6**	**1.1**	**0.4**	**2**
Oct20 - Dec20	E	913 ± 325	364 ± 128	790 ± 299	658 ± 301	815 ± 304	646 ± 222	858 ± 285	832 ± 194
	A	592 ± 174	378 ± 136	427 ± 136	511 ± 126	463 ± 115	447 ± 112	289 ± 67	129 ± 49
	R	**0.6**	**1**	**0.5**	**0.8**	**0.6**	**0.7**	**0.3**	**0.2**
Dec20 - Feb21	E	1085 ± 277	619 ± 139	648 ± 214	640 ± 194	589 ± 193	354 ± 109	298 ± 119	415 ± 103
	A	617 ± 136	398 ± 127	695 ± 196	469 ± 141	504 ± 144	608 ± 169	567 ± 132	440 ± 86
	R	**0.6**	**0.6**	**1.1**	**0.7**	**0.9**	**1.7**	**1.9**	**1.1**

Feb21 - Apr21	E	877 ± 218	643 ± 127	799 ± 178	780 ± 164	1005 ± 190	1000 ± 151	939 ± 180	747 ± 137
	A	105 ± 42	233 ± 84	326 ± 96	185 ± 61	186 ± 58	299 ± 84	198 ± 58	59 ± 26
	R	**0.1**	**0.4**	**0.4**	**0.2**	**0.2**	**0.3**	**0.2**	**0.1**
Apr21 - Aug21	E	573 ± 263	293 ± 170	681 ± 334	402 ± 234	455 ± 200	402 ± 138	425 ± 166	218 ± 84
	A	635 ± 162	662 ± 102	536 ± 116	578 ± 141	655 ± 144	433 ± 113	281 ± 82	164 ± 51
	R	**1.1**	**2.3**	**0.8**	**1.4**	**1.4**	**1.1**	**0.7**	**0.8**
Aug21 - Dec21	E	738 ± 359	760 ± 259	915 ± 368	772 ± 305	840 ± 333	630 ± 221	620 ± 254	342 ± 139
	A	313 ± 134	197 ± 91	197 ± 84	334 ± 92	331 ± 92	520 ± 166	402 ± 138	164 ± 66
	R	**0.4**	**0.3**	**0.2**	**0.4**	**0.4**	**0.8**	**0.6**	**0.5**
Dec21 - Apr22	E	2035 ± 242	2820 ± 134	1480 ± 158	1290 ± 214	1155 ± 199	964 ± 146	1416 ± 227	912 ± 160
	A	439 ± 194	858 ± 242	939 ± 249	618 ± 202	568 ± 196	1158 ± 211	910 ± 142	178 ± 82
	R	**0.2**	**0.3**	**0.6**	**0.5**	**0.5**	**1.2**	**0.6**	**0.2**